



Dipl.-Ing. Arno Meingast

Analytical TEM Investigations of Nanoscale Magnetic Materials

DOCTORAL THESIS

to achieve the university degree of
Doktor der technischen Wissenschaften
submitted to

Graz University of Technology

Supervisor

Ao.Univ.-Prof. Dipl.-Ing. Dr.techn. Gerald Kothleitner

Institute for Electron Microscopy and Nanoanalysis

AFFIDAVIT

I declare that I have authored this thesis independently, that I have not used other than the declared sources/resources, and that I have explicitly indicated all material which has been quoted either literally or by content from the sources used. The text document uploaded to TUGRAZonline is identical to the present doctoral thesis.

14. 10. 2015

Date

A handwritten signature in blue ink, written in a cursive style, positioned above a horizontal line.

Signature

Contents

Contents.....	4
1. Acknowledgement.....	6
2. Abstract	7
3. Kurzfassung.....	9
4. Motivation	11
4.1 Highly defined nanocrystals.....	12
4.2 Gallium nitride doped with transition metals	14
4.3 Spin polarizing contacts: the case of Heusler-films on GaAs	17
5. Publications	19
5.1 Highly defined nanocrystals.....	19
5.2 Gallium nitride doped with transition metals	19
5.3 Heusler alloys.....	20
6. Practical aspects about transmission electron microscopy	21
6.1 Utilized electron microscopical instrumentation.....	21
6.2 Benefits of transmission electron microscopy.....	22
6.3 The transmission electron microscope and its working modes	23
6.3.1 TEM-imaging mode	25
6.3.2 Diffraction mode	26
6.3.3 STEM imaging mode	26
6.3.4 ABF imaging	30
6.4 The monochromator	33
6.5 Correction of the spherical aberration	35
6.6 Electron energy loss spectroscopy.....	42
6.6.1 The post-column energy filter GIF QuantumERS.....	43
6.6.2 The DualEELS mode and its synchronization.....	44
6.6.3 EFTEM imaging.....	46
6.7 Characteristics and analytical aspects of EELS.....	46
6.8 Energy dispersive X-ray spectroscopy	49
6.9 STEM image simulation using multislice	51
6.10 Electron trajectory simulation in materials.....	52
7. TEM Specimen preparation.....	53
7.1 Specimen preparation of nanocrystals.....	53
7.2 Specimen preparation of GaN	54
7.2.1 Standardized TEM specimen preparation.....	54
7.2.2 Focused ion beam processing of GaN	59
7.2.3 Wedge polishing of GaN grown on sapphire.....	62
7.2.4 Advanced cross-section preparation of GaN	64

7.3	Conclusion of TEM specimen preparation.....	67
8.	Analytical results and discussion.....	68
8.1	Phase determination of Fe_xO_y reference nanocrystals	68
8.2	Composition analysis of core-shell nanocrystals	71
8.3	Compound semiconductor gallium nitride	79
8.3.1	STEM resolution improvement in GaN.....	79
8.3.2	GaN – image simulations.....	81
8.3.3	GaN – analytical investigations	85
8.3.4	Determination of the origin of the oxygen	88
8.4	Manganese-doped GaN semiconductors	90
8.4.1	Homogeneously Mn-doped GaN.....	90
8.4.2	δ -doped (GaMn)N	93
8.5	Iron-doped GaN semiconductors.....	99
8.6	Diffusion characterizations of Heusler-alloys on GaAs	109
9.	Summary	113
10.	Abbreviations	116
11.	References	117
12.	Peer reviewed papers.....	126
12.1	Highly defined nanocrystals.....	126
12.2	Gallium nitride doped with transition metals	134
12.3	Heusler-films on GaAs.....	154

1. Acknowledgement

This work would not have been possible without the support of many people, for which I want to express my gratitude at this point.

First of all I want to thank my supervisor Gerald Kothleitner for his guidance, the support and the patience which was very important to me throughout the whole thesis.

I would like to thank the whole team of the FELMI for fruitful discussions, their friendliness, all technical support and the inspiring atmosphere at the institute. I would like to mention Mihaela Albu for the help regarding strain measurements, Thomas Ganner for “borrowing” his AFM skills and Johannes Rattenberger for the help with electron trajectory simulations. Furthermore, I want to thank Martina Dienstleder and Sebastian Rauch for their contribution regarding specimen preparation. Especially I would like to thank Harald Plank for the countless coffees we had together and the inspiring discussions at these occasions. Birgit Kunert from the Institute of Solid State Physics of the Graz University of Technology contributed with XRD measurements of nanocrystals.

My sincere thanks go to the colleagues in Linz for not only providing the material to be investigated and the technological aspects behind it but also for the fruitful collaboration. Thanks go to Alberta Bonanni and her Magic Spin group, Wolfgang Heiss and the Nanocrystal group and Reinhold Koch from the Magnetic Heterostructures group.

I want to thank András Kovács from the Ernst Ruska-Centre for the advice regarding TEM specimen preparation of GaN and helping me with my first “steps” within aberration corrected electron microscopy. Thanks go to Doris Mertens from the Ernst Ruska-Centre, who helped fabricating GaN specimens by means of FIB.

Christoph Mitterbauer and Sorin Lazar, both from FEI Company, who were providing support regarding annular bright field imaging and EDXS mappings of GaN. Credit goes also to Stefan Löffler from the Vienna University of Technology for performing the annular bright field image simulation of GaN. My special thanks go to Martina Lattemann for her effort and inspiration during the composition of this thesis.

Most importantly, I want to thank my wife Anna-Lena for her backup, her mental support, her infinite love and her endless patience with me. Also Ellie and Isabelle for turning my life upside down and thereby making it complete.

This work has been supported by the Austrian NANO Initiative within the project number 819702. Special thanks are expressed to the FFG for funding of the ASTEM microscope within the COIN Aufbau Programm (project number: 821074).

2. Abstract

Analytical transmission electron microscopy has been applied within this thesis to investigate several novel approaches to design and fabricate nanoscale magnetic materials. As the size of the features of interest rank in the sub-nanometer range, it is necessary to employ techniques with a resolution – both spatial and analytical – well below this magnitude. Only at this performance level it is possible to examine material properties, necessary for the further tailoring of materials. Within this work two key aspects have been covered: First, analytical TEM (transmission electron microscopy) investigations were carried out to get insight into novel magnetic materials with high detail. Second, new analytical and imaging possibilities enabled with the commissioning of the new ASTEM (Austrian scanning transmission electron microscope) were explored.

The aberration corrected TITAN[®] microscope (© FEI Company) allows resolving features in scanning transmission mode (STEM) with 70 pm distance. Thereby, direct imaging of light elements in STEM mode by using the annular bright field method becomes possible. Facilitated through high beam currents within the electron probe, an increased acquisition speed of analytical signals is possible. For energy dispersive X-ray spectroscopy (EDXS) a new four detector disc geometry around the specimen was implemented, which increases the accessible collection angle. With the integration of the latest generation of image filter and electron spectrometer (GIF QuantumERS), electron energy loss spectroscopy (EELS) is boosted through the high acquisition speed and the dual spectroscopy mode. The high acquisition speed allows to record up to 1000 spectra per second and the possibility to record atomically resolved EELS maps is at hand. Hereby it is important to avoid beam damage and alteration of the material during imaging and analysis. With the simultaneous acquisition of the low and the high loss spectral region, an extended range for element identification or, an absolute quantification is possible. Moreover, the parallel acquisition of EDXS and EELS signals allows combining the strength of each respective technique. A careful and precise sample preparation is crucial and knowledge and suitable methods had to be developed. Preparation induced modifications of the investigated material was minimized by identifying changes to the material during thinning to electron transparency. Reducing surface amorphization of TEM specimens and moreover identifying and quantifying surface oxidation was an important factor.

Questions regarding the structural architecture of three diverse magnetic materials down to the atomic level have been addressed, and elemental distributions have been determined quantitatively. The first part of the results treats structural and analytical results of crystalline nanocubes. These cubes have dimensions below 30 nm, and represent a class of materials to exploit magnetic exchange coupling on a nanometer scale. Knowledge about the elemental distribution on a nanometer basis within a nanocube is necessary to tailor the magnetic properties. Analytical investigations deal with the determination of the oxidation state of iron oxide reference nanocrystals and the elemental distribution within a multi-component system.

Transition metal doped gallium nitride (GaN) falling into the class of dilute magnetic semiconductors was investigated by various high resolution imaging techniques and spectroscopic methods for resolving morphologies and dopant concentrations. The doping of GaN is intended to provide additional magnetic functionalities to the semiconducting material used for future spintronic devices. Quantitative EELS measurements resolved that Mn was incorporated either in a homogeneous way or added to GaN in a pulsed way, leading to a layered doping. Iron was used as another potential dopant for GaN. Hereby specific growth procedures enabled the formation of a layer of iron-rich nanocrystals. Samples with two different nominal iron concentrations were investigated where prior magnetization measurements indicated different composition of nanocrystals. Various imaging techniques were applied to probe if the embedment of the nanocrystals within the matrix is coherent. Analytical investigations proved a confinement of iron solely within the nanocrystals. Compositional analyses on a per-nanocrystal basis reveal large fluctuations of the individual constituents. Elaborate data processing allows extracting general trends regarding the nanocrystal composition despite the large fluctuations in composition. In rare cases even an inner structure within the nanocrystals could be visualized. A common problem to analytical investigations is surface oxidation, complicating interpretation of the results, in addition to electron beam induced sputtering of nitrogen. Both influences are described in this work and accounted for it during analysis.

The third investigated material group where layers of a specific type of Heusler alloy grown, on a gallium arsenide (GaAs) substrate. This magnetic layer is intended to act as an electron spin-filter in future spintronic devices. Due to the nature of the fabrication process, an interdiffusion between substrate and Heusler alloy takes place. To technically exploit the spin filtering property the interdiffusion needed to be identified. EDXS linescans revealed the elemental distribution within this zone.

3. Kurzfassung

Im Rahmen dieser Arbeit wurden verschiedene Typen von magnetischen Materialien mit transmissions-elektronenmikroskopischen Methoden untersucht. Da die Strukturgröße der untersuchten Objekte im Subnanometerbereich liegt ist es notwendig auch Techniken mit einer Auflösung – sowohl räumlich als auch analytisch – zu verwenden, die diese Größenordnung bedienen. Nur auf diesem Auflösungslevel ist es möglich Materialeigenschaften zu untersuchen, und daraufhin Materialien weiter zu verbessern. Im Rahmen dieser Arbeit wurden zwei Schlüsselaspekte abgedeckt: erstens wurden analytische TEM (Transmissionselektronenmikroskop) Untersuchungen durchgeführt um Einblick in neuartige magnetische Materialien in großer Detailliertheit zu bekommen. Zweitens wurden neue analytische und abbildende Methoden, welche mit der Kommissionierung des neuen ASTEM (Austrian Scanning Transmission Electron Microscope) Transmissionselektronenmikroskops eingeführt wurden, erkundet.

Das Aberrations-korrigierte TITAN[®] Mikroskop (© FEI Company) erlaubt Strukturen im Rastertransmissionsmodus (STEM) mit 70 pm Distanz aufzulösen. Als Novum wird dadurch die direkte Abbildung von leichten Elementen in einer Hellfeldtechnik mittels ringförmigem Detektor möglich. Eine erhöhte Aufnahmegeschwindigkeit analytischer Signale wird erstmals durch die hohe Helligkeit des Elektronenstrahls zugänglich. Im Fall der energiedispersiven Röntgenspektroskopie (EDXS) wurde eine neue Vierdetektorgeometrie rund um und oberhalb der Probe implementiert, wodurch der Auffangwinkel und damit die Detektionseffizienz vergrößert wird. Durch die Integration eines Elektronenspektrometers neuester Generation (GIF QuantumERS, [®]Gatan Inc.) wird die Elektronenverlustspektroskopie (EELS) durch eine hohe Aufnahmegeschwindigkeit und einen neuen Doppelspektroskopiemodus verbessert. Die hohe Aufnahmegeschwindigkeit erlaubt es hierbei 1000 Spektren pro Sekunde und mehr aufzunehmen und daraus atomar aufgelöste EELS Verteilungsbilder zu errechnen. Hierbei ist es wichtig Strahlenschäden und Veränderungen des Materials während des Abbildens und der analytischen Untersuchung zu vermeiden. Durch die gleichzeitige Aufnahme der spektralen Niederverlust- und Hochverlustregion ist es möglich einen erweiterten Bereich für Elementanalysen sowie absolute Elementquantifizierungen durchzuführen. Außerdem erlaubt die parallele Aufnahme von EDXS und EELS Signalen die jeweiligen Vorteile der Techniken besser zu nutzen. Eine sorgfältige und präzise Probenpräparation ist essentiell, Kenntnisse und passende Methoden mussten entwickelt werden. Präparationsinduzierte, strukturelle Änderungen des untersuchten Materials wurden durch Identifizieren von Veränderungen während des Dünnens zur Elektronentransparenz minimiert. Die Reduktion von Oberflächenamorphisierung von TEM Proben und weiters die Ermittlung des Ausmaßes an Oberflächenoxidation waren wichtige Faktoren.

In dieser Arbeit wurden Fragen bezüglich des strukturellen Aufbaus und der chemischen Zusammensetzung von drei verschiedenen magnetischen Materialklassen behandelt. Der erste Teil der Resultate behandelt die Ergebnisse von kristallinen Nanowürfeln. Die Würfel besitzen Dimensionen von unter 30 nm und stellen eine neue Möglichkeit dar um die magnetische Austauschwechselwirkung

auf einer Nanometerskala auszunutzen. Kenntnisse über die Verteilung von Elementen innerhalb eines Nanowürfels sind notwendig um die magnetischen Eigenschaften maßzuschneidern. Die analytischen Untersuchungen behandeln die Bestimmung der Oxidationsstufe von Referenznanokristallen und die Elementverteilung innerhalb eines Mehrkomponentensystems.

Übergangsmetalldotiertes Galliumnitrid (GaN), welches in die Klasse der verdünnten magnetischen Halbleiter fällt, wurde mit verschiedenen hochauflösenden Abbildungstechniken und spektroskopischen Methoden untersucht um die Morphologie und Dotierkonzentration aufzuklären. Das Dotieren von GaN zielt darauf ab, magnetische Funktionalitäten in den Halbleiter einzubauen, um ihn für zukünftige spintronische Anwendungen zugänglich zu machen. Die durchgeführten quantitativen EELS Messungen sollten sicherstellen, dass Mangan in Galliumnitrid entweder zu homogener oder –wenn gepulst abgeschieden– zu geschichteter Dotierung führt. Als zweites Dotiersystem wurde Eisen untersucht, dessen spezifische Wuchsbedingungen die Formation einer Schicht von eisenreichen Nanokristallen begünstigte. Proben mit verschiedenen nominellen Eisenkonzentrationen wurden untersucht, an denen bereits erfolgte Magnetisierungsmessungen verschiedene Zusammensetzungen der Nanokristalle nahelegten. Verschiedene Abbildungstechniken wurden angewendet um eine kohärente Einbettung der Nanokristalle in der Matrix festzustellen. Analytische Untersuchungen bestätigten die Inkorporation von Eisen ausschließlich innerhalb der Nanokristalle. Zusammensetzungsanalysen auf Einzelkristallbasis zeigten Fluktuationen der einzelnen Bestandteile. In seltenen Fällen konnten auch Änderungen innerhalb der Nanokristalle sichtbar gemacht werden. Ein gemeinsames Problem aller analytischen Untersuchungen ist die Oberflächenoxidation, welche die Interpretation der Resultate zusätzlich zur elektronenstrahlinduzierten Schädigung verkomplizierte. Beide Einflüsse wurde in der Arbeit so gut wie möglich Rechnung getragen.

Die dritte untersuchte Materialgruppe war eine spezifische Heuslerlegierung, welche auf einem Substrat aus Galliumarsenid (GaAs) aufgewachsen wurde, und die als Elektronenspinfilter für zukünftige Spin-gesteuerte Bauteile fungiert sollte. Durch die Art des Herstellungsprozesses findet unweigerlich Vermischung und Interdiffusion zwischen Substrat und Legierung statt, die identifiziert werden musste. EDXS Linienabtastungen zeigten die Elementverteilung innerhalb dieser kritischen Zone.

4. Motivation

In this work analytical transmission electron microscopy (AEM) has been used to investigate materials that represent different approaches to design, fabricate and structure novel magnetic materials on a nanoscale basis. In order to exploit the properties of these magnetic nanocomposites in (future) commercial products, it is inevitable to accurately characterize them in order to establish correlations between fabrication parameters, crystallographic properties and magnetic response of the systems with structural and analytical findings on a highly spatially resolved basis. Such spatial resolution for TEM (transmission electron microscopy) can only be achieved with spherical aberration correction. Moreover, the combination of the elements within the materials itself is rather challenging for analytical investigations. This is the case for light elements such as nitrogen (which suffers from sputtering due to the knock on with highly accelerated electrons during imaging and analysis) but also for elements that are close to each other in the periodic table, making the extraction of signals and quantification difficult due to overlapping signals in the different analytical techniques. This makes it necessary to invoke EELS (electron energy loss spectroscopy) and EDXS (energy dispersive X-ray spectroscopy) simultaneously, and harness their respective strengths. The stringent demands regarding lateral resolution and analytical diversity were accounted for with the commissioning of the “ASTEM” (Austrian scanning transmission electron microscope) microscope at the FELMI.

The scientific frame for this thesis was the “NanoProbe” project, part of the research project-cluster “Nanostructured Surfaces and Interfaces” (NSI¹). NanoProbe comprised of two branches performing characterizations. The one group was performing optical-analytical techniques comprising reflectance difference spectroscopy, spectroscopic ellipsometry and magneto-optical Kerr effect. Electron beam-based analytical techniques were performed by the second group, i.e. the FLEMI.

Pre-characterizations have been done by the project partners themselves beforehand allowing the selection of relevant samples for advanced investigations. These investigations left open questions regarding the structural buildup of materials, homogeneity within the material, elemental distributions and quantitative composition information in a relative or absolute manner on an atomically resolved basis. Hereby aberration corrected TEM, energy filtered TEM (EFTEM), EDXS, EELS, aberration corrected Z-contrast imaging in scanning transmission electron microscopy mode (STEM HAADF imaging) and annular bright field imaging (ABF) provided answers. The investigated materials from our partners were: highly defined nanocrystalline cubes (section 4.1), transition metal doped GaN layers (section 4.2) and Heusler alloys (section 4.3). The following sections describe the potential application of those materials and to sketch their interesting physical properties.

¹ please refer to: <http://www.nanoscience.at/nsi.html>

4.1 Highly defined nanocrystals

The investigated samples were provided by the project partner “NanoShape”, led by Prof. Wolfgang Heiss from the Nanocrystal group of the Solid State Physics Division at the JKU Linz.

Nanometer sized magnetic materials, showing exchange coupling, are currently intensively researched for their magnetic phenomena [1]. Exchange coupling is a general term for a multitude of magnetic interactions in magnetic materials with two or more magnetic phases. At the nanometer length scale this is governed by interface interactions [2]. To understand this phenomenon it is not sufficient to image but also to analytically investigate the interface. It is necessary to not only determine the elemental distribution below one nanometer but also to also deliver a complete picture of the interface. Metal ferrites are one of the most prominent magnetic material classes. They are widely used in commercial applications (e.g. magnets in household goods) as well as in fundamental research due to the fact that they are environmentally friendly, cheap and chemically stable [3]. Metal ferrites can expose different chemical compositions, which exhibit exchange coupling at room temperature. This class of material might help overcoming some fundamental limitations such as the superparamagnetic limit of nanocrystals (NCs) [1]. Therefore, it is attractive to use them in applications such as magnetic storage devices, allowing to lower the critical size measures [2], in magneto-electronics, in ferrofluidic systems as components of a analytes used in biotechnology and medicine [4,5]. Within the last years a multitude of single-phase and multi-phase magnetic particles have been published by the group of Prof. Heiss, which has been done by means of solution phase chemical synthesis [3,5]. The particles have been synthesized by a one-pot reaction based on the thermal decomposition of metal oleates [3]. Very often such multicomponent architectures suffer from a variety of drawbacks [3,5]:

- Insufficient control of stoichiometry and phase composition.
- Inhomogeneity of morphology and size of each component.
- Multiple number of steps required for synthesis.

Owing to the work of Prof. Heiss and his group it has been possible to develop more reliable synthesis routes, which reduce the mentioned difficulties [5]. Due to the strong dependence of the magnetic properties on size, shape, composition and interface properties, there is a strong demand for further improvements. This comprises not only the improvement of already existing methods or the search for novel approaches in designing magnetic nanostructures, but especially a deepened characterization. Particles with an apparent core-shell structure in the form of cubes and spheres have been synthesized by the group of Prof. Heiss. The structure has been pre-characterized by conventional TEM, electron diffraction (ED), dark-field (DF) imaging and X-ray diffraction (XRD) to screen for their shape, size and structural buildup [3]. DF imaging indicated a core-shell structure as visible in Figure 1. By using HR-TEM imaging it was possible to outline a coherent interface between the core and the shell. Electron diffraction, conventional EDXS and XRD are interpreted in such way that the core consists of an antiferromagnetic (AFM) material of ferrous oxide (wüstite, Fe_xO with $x=0.83 - 0.95$) which is

surrounded by a ferrimagnetic (FiM) shell of a metal ferrite (MeFe_2O_4), the latter being dependent on the used precursor type.

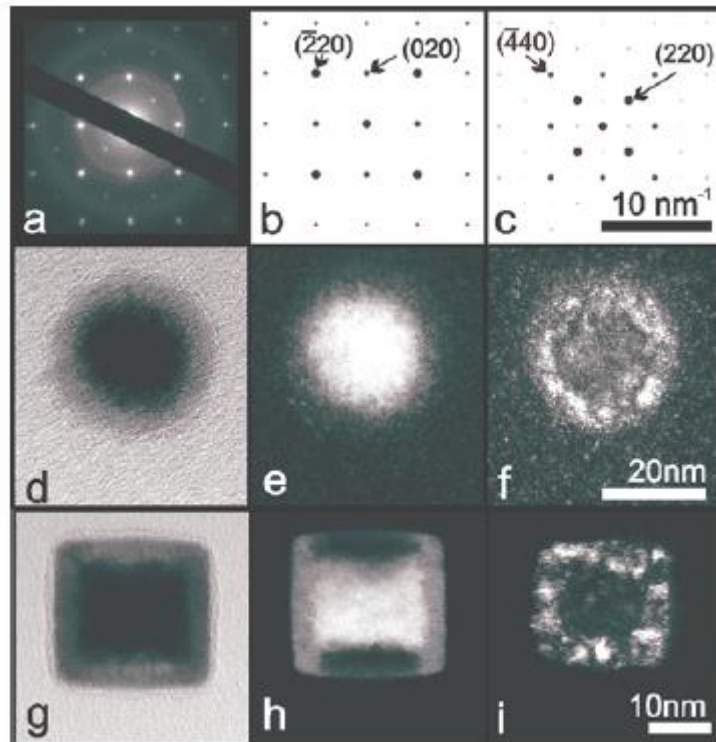


Figure 1: (a) TEM diffraction pattern obtained in two beam condition from a single $\text{Fe}_x\text{O}/\text{CoFe}_2\text{O}_4$ nanocube and the corresponding simulated patterns for rock-salt wuestite (b) and for inverse-spinel metal ferrite (c), for the [100] zone axis. (d) and (g) are bright field images of spherical and cubical particles at the two beam condition of the (020) wuestite diffraction spot and the complementary dark-field images (e) and (h). (f) and (i) are dark field images, showing the origin of the (220) reflection from the metal ferrite shell. (Figure taken with permission from [3].)

However, for determining the arrangement of chemical elements within a nanometer sized cube less ambiguous techniques are needed. This is due to the similarity of reflections for FeO , Fe_2O_3 and Fe_3O_4 – in the case for XRD and ED. Conventional EDXS lacks sensitivity to distinguish between phases, having such a similar stoichiometry. Applicable techniques are Z-contrast imaging in HAADF-STEM geometry, STEM-EELS and EFTEM imaging for mapping and visualizing different chemical elements.

Investigated particle samples:

The first sample investigated in this work consisted of cubic particles without core-shell structure. These particles exhibited a side length of ~ 15 nm and investigations focused on the determination of the oxidation state of the iron oxide particles. This was also the model system to gain firsthand information about the electron beam sensitivity. The second, and more intensively studied class, was a core-shell particle type with the core assumed to consist of Fe_xO_y , surrounded by a ferrimagnetic shell of CoFe_2O_4 [3]. To analyze these crystals, exhibiting a side length of ~ 26 nm, a pronounced

investigational effort was put on the EELS fine-structure analysis by means of electron beam monochromation.

4.2 Gallium nitride doped with transition metals

These samples were provided by the group of Prof. Alberta Bonanni from the Magic Spin group of the JKU Linz.

Gallium nitride (GaN) is a wide bandgap semiconductor [6] and an appealing material for both, basic research and commercial production of integrated circuits [7]. At the moment, GaN is widely used within the field of optoelectronics, lightning [8], high-speed wireless communication [9], high-voltage switching [10] and energy efficient power conversion applications [11]. Unfortunately, it is not a material that can be processed as easily as silicon, since GaN is a very hard and mechanically stable semiconductor [6]. Currently one of the main problems is to fabricate large enough single crystals that can be used as wafers in commercial production and basic research [12]. To overcome this drawback today, GaN is deposited as a thin film on different substrates such as sapphire, silicon or silicon carbide [13]. The lattice mismatch between these different substrate materials and GaN leads to a high defect density in the order of a $100 \cdot 10^6 - 10 \cdot 10^9$ defects/cm². Doping moreover induces tensile stress in GaN, making it prone for further fracture during processing [14,15]. Regardless of these processing difficulties it is desired to incorporate additional functionalities into GaN. It is expected that the addition of magnetic capabilities through doping with transition metals (TM) or rare earths will extend the functionality of these materials systems to applications in spintronics, quantum information and magneto-optics [16–19]. Devices made of magnetic semiconductors are able to take advantage of the spin together with the charge of electrons [20,21]. By combining various magnetic materials it is furthermore anticipated to obtain multifunctional devices. New functionalities for electronics and photonics become possible if injection, transfer and detection of carrier spins can be controlled reliably above room temperature (RT) [20]. Therefore a lot of research interest is focused onto the fabrication of materials suitable for spintronic devices [22]. Currently the search for magnetic semiconductors with a Curie temperature (TC) above RT is one of the major challenges in research on semiconductor spintronic [23]. Of special interest are so-called diluted magnetic semiconductors (DMS). These are semiconducting materials where a fraction of the host cations are substitutionally replaced by magnetic ions. Transition metals like Sc, Ti, V, Cr, Mn, Fe, Co, Ni and Cu are commonly used during synthesis [23]. Furthermore, rare earths like Sm, Eu, Gd, Tb, Dy, Er can be used to synthesize DMS. Technically applicable DMS materials must exhibit ferromagnetic ordering with a Curie temperature above RT, which represents a key task for these materials systems [17]. In the past, II-VI and IV-VI semiconductors with TM as substitution elements have been studied extensively [24], for instance for such fundamental phenomena like the onset of carrier-mediated ferromagnetic coupling [25]. These compounds though are less attractive for technical applications. Conventional

III–V semiconductors are already commercially used and the discovery of hole-mediated ferromagnetism in (GaMn)As [26] rendered these material class interesting for both fundamental research and for actual use in micro- and optoelectronics [27]. So far the highest Curie temperature reported for (GaMn)As lies by far below a practical limit and overcoming hole and spin compensation by defect formation is still an actual challenge [28,29]. The work of Dietl and co-workers has increased awareness on wide bandgap DMS since it predicts that GaN-based DMS should show ferromagnetism above RT upon doping with TM in the order of 5%, while simultaneously containing a large density of holes ($\sim 10^{20} \text{ cm}^{-3}$) [30]. Studies have been carried out over the last years, highlighting the distribution of magnetic dopants in the semiconducting matrix and how it affects the structural, magnetic, electrical and optical properties of the resulting material substantially [31–33]. In particular, the recent advancements in fabrication and characterization of magnetically doped nitrides have made clear that depending on the growth conditions (and eventually post-growth treatment) the introduction of magnetic ions can essentially result in:

- i. A dilute (homogeneous) system [34].
- ii. A chemically inhomogeneous system (chemical phase separation) [32].
- iii. A crystallographically inhomogeneous system (crystallographic phase separation, secondary phases, embedded nanocrystals) [35].
- iv. A system with magnetic complexes [36] (not investigated within this work).

For the design and functionality of the next generation of devices one needs to control the formation, structure, arrangement and effect of homogeneity, as they influence the chemical and physical behavior within the host material. One of the fundamental questions is whether the TM-dopant is incorporated in its desired state, regarding dilution and chemical or crystallographic inhomogeneity. This is essential since the incorporation can influence the charge state of the dopant and lead to a paramagnetic behavior of the material [37].

To monitor the desired incorporation within GaN C_S -corrected TEM and STEM imaging as well as elemental quantification on a highly localized basis by using STEM-EELS was necessary for in-depth understanding of the material. Prior to the involvement of FELMI in the project, information on the concentration levels have been obtained by superconducting quantum interference device (SQUID) measurements. This technique allows estimating a concentration indirectly through the resulting magnetization of the material. Hereby local fluctuations in the dopant concentration, such as in inhomogeneous doped system, might lead to a locally different magnetic response of the content resulting in an different TM content measured by SQUID than actually present [23]. STEM-EELS is able to deliver spatially resolved concentration values and direct probing of the dopant concentration is achieved by detecting localized excitations within the material of the TEM specimen. Particularly in the case of embedded magnetic nanocrystals it was essential to establish a correlation between the growth parameters and the local chemical composition and size of the nanostructures, considering that these figures have been shown to determine the magnetic properties of the whole system e.g. in the

case of Fe-rich nanocrystals embedded in GaN, it has been found that by modifying the composition of the nanostructures, it was possible to tune the system from ferromagnetic to antiferromagnetic, even up to room temperature [38]. Through aggregation of iron-rich precipitates a phase-separated material system was made suitable as building-block not only for FM spintronic devices but also for AF spintronic devices, the latter being an appealing perspective, due to the fact that a minimal critical current is needed to modify the magnetic order of an AF system [39]. The resistance to external magnetic fields and the absence of stray fields make antiferromagnets particularly promising materials for ultrafast and ultrahigh-density spintronics [40]. Investigational focus was put on the assurance of an epitaxial relationship between nanocrystal and matrix and the determination of the chemical composition of individual precipitates within the matrix. Thereby it was crucial not to modify the precipitates during TEM specimen preparation or investigations.

Investigated GaN samples:

The basic structuring of all investigated materials is shown in Figure 2. A 1 μm thick GaN buffer layer was grown by metalorganic vapor phase epitaxy (MOVPE) on a c-plane sapphire substrate according to a standard growth procedure established within the group of Prof. Bonanni [41]. All GaN samples have been fabricated using an AIXTRON 200RF horizontal tube reactor equipped with ellipsometry and reflectometry for in situ process control. The buffer layer reduces the dislocation density and strain caused by the lattice mismatch between sapphire and GaN. In a subsequent step doped GaN layer was grown on top of the buffer layer.

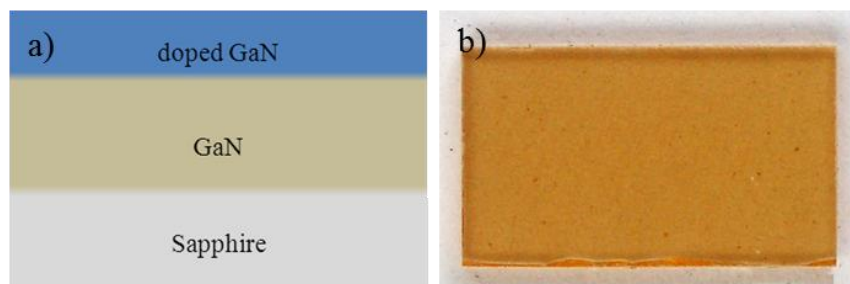


Figure 2: a) General scheme of the doped GaN samples; b) as-received GaN sample (here: Fe-doped; side measures: $\sim 3 \times 5$ mm).

The different types of doped GaN layers are schematically depicted in Figure 3 (including STEM HAADF overview images).

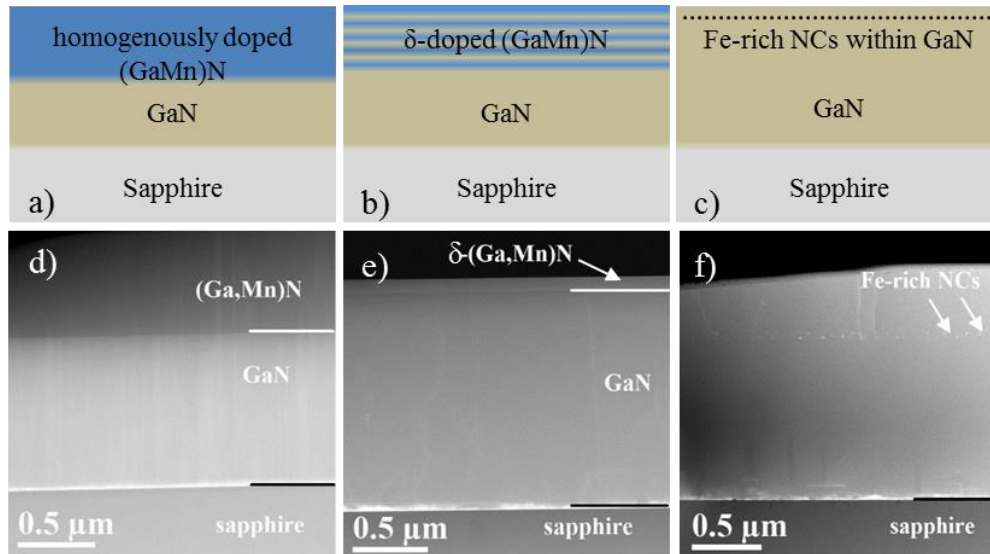


Figure 3: Schematic cross section of the investigated GaN samples depicted in a) – c); corresponding STEM HAADF overview images below (d – e). This figure was composed by the author of this thesis and taken from [42].

4.3 Spin polarizing contacts: the case of Heusler-films on GaAs

The Heusler films were provided by Prof. Reinhold Koch from the Magnetic Heterostructures group of the JKU Linz.

A general prerequisite for the successful realization of spin-sensitive devices is the controlled injection of spin polarized charge carriers into a semiconductor [43]. One possible way to obtain spin injection is through ferromagnetic layers with a high spin polarization. Such spin injecting layers can be fabricated on semiconductor substrates and are therefore attracting increasing interest in research [44]. Such a material can be furthermore exploited in magnetoresistive elements for magnetoelectronic devices [45]. One approach to obtain spin-dependent injection is by depositing Fe on a semiconductor substrate such as GaAs. The Fe contacts are usually grown at or below room temperature in order to avoid interfacial reactions between the metal and semiconductor thereby deteriorating the spin injection [46]. Unfortunately highest spin injection efficiencies have been obtained through an post-growth step at temperatures $\sim 250^\circ\text{C}$ in order to anneal device hetero-structures [47]. This temperature leads to a modification of the Fe/GaAs interface enabling an annealing-induced spin injection enhancement. One explanation is that annealing promotes a more ordered and abrupt Fe/GaAs interface. However, the interface between Fe and GaAs is thermodynamically not stable [48]. Therefore, annealing should promote interfacial reactions and an intermixed interfacial region rather than an ordered-phase-separated interface. Heusler compounds, such as Fe_3Si or Co_2FeSi , are a further attractive material type to obtain high spin-polarization. Theoretical calculations of Heusler compounds state that perfect crystallographic order is essential for achieving high spin polarization [49]. It has been shown that Heusler alloys can provide a spin-injection of $\sim 45\%$ which is similar to pure Fe contacts [50]. For efficient spin injection the interface has to be abrupt and it seems

to strongly depend on the type of atoms forming the contact layer [51]. Therefore, an in-depth knowledge about the interface disorder due to inter-diffusion or interface reactions between applied film and substrate is crucial. It has been reported that during deposition of Co_2FeSi onto GaAs(001) Co, Fe, and Si diffuse about 50 nm deep into the substrate through a thermally activated process [52]. Since the metal atoms may act as paramagnetic spin-scattering centers, the obtained spin injection has been low, even though abrupt interfaces have been revealed by HR-TEM [53]. Experimentally, binary Heusler alloys have been chosen for research. The fewer constituents of this system allowed a straightforward interpretation of the ongoing interface reactions [54]. Analytical transmission electron microscopy provides the possibility to track down diffusion profiles well below 1 nm even when a sharp interface can be imaged in HR-TEM. It was applied in combination with other complementary techniques such as XRD, reflection high- and low-energy electron diffraction (RHEED and LEED), atomic force microscopy (AFM), cantilever beam magnetometry (CBM) and Auger depth profiling. A calibrated quartz crystal microbalance (QCM) has been used to directly measure the mass equivalent of deposited Fe and Si for determining film thickness and composition [54].

Investigated Heusler-film samples:

Within this work two layers of ferromagnetic FeSi films grown on GaAs(001) were investigated [54]. They have been grown by molecular beam epitaxy (MBE) at a temperature of 200°C in a multichamber ultra-high vacuum (UHV) system. The films have been grown with a nominal thickness of 7 nm in order to enhance sensitivity towards interdiffusion effects. The films were composed of $\text{Fe}_{0.84}\text{Si}_{0.16}$ and $\text{Fe}_{0.76}\text{Si}_{0.24}$ which is close to the nominal Heusler alloy consisting of $\text{Fe}_{0.75}\text{Si}_{0.25}$. By the application of a multitude of other analysis techniques as mentioned above it has been known that inter-diffusion took place during fabrication. However, with those techniques it has not been possible to determine accurately the width of the diffusion zone and the composition profile. This was addressed by analytical transmission electron microscopy.

5. Publications

Several peer reviewed papers were published as a result of this thesis. A description of the performed work within these publications is given in the following.

5.1 Highly defined nanocrystals

Journal contribution: “Tuning the Magnetic Properties of Metal Oxide Nanocrystal Heterostructures by Cation Exchange” published in NANO Letters **13**, 586 – 593 (2013). Authors: M. Sytnyk, R. Kirchschlager, M. I. Bodnarchuk, D. Primetzhofer, D. Kriegner, H. Enser, J. Stangl, P. Bauer, M. Voith, A. Walter Hassel, F. Krumeich, F. Ludwig, A. Meingast, G. Kothleitner, M. V. Kovalenko and W. Heiss. The paper is presented in full length in section 12.1.

Analytical electron microscopy results on core-shell nanocrystals delivered the basic understanding for the work presented in this paper. The results of the STEM EELS measurements presented in section 8.2 were the basis for the work presented in the paper.

5.2 Gallium nitride doped with transition metals

Journal contribution: “Experimental probing of exchange interactions between localized spins in the dilute magnetic insulator (Ga,Mn)N” published in PHYSICAL REVIEW B **84**, 035206 (11 pages) (2011). Authors: A. Bonanni, M. Sawicki, T. Devillers, W. Stefanowicz, B. Faina, Tian Li, T. E. Winkler, D. Sztenkiel, A. Navarro-Quezada, M. Rovezzi, R. Jakiela, A. Grois, M. Wegscheider, W. Jantsch, J. Suffczynski, F. D’Acapito, A. Meingast, G. Kothleitner and T. Dietl. The paper is presented in full length in section 12.2.

The contribution originating from this thesis was the analytical TEM investigation, the composition of Figure 6, its legend and the accompanying text within the paper: “The HAADF-STEM on (Ga,Mn)N [...] between the substrate and the intensity modulated lines.”.

Journal contribution: “Analytical electron microscopy study on gallium nitride systems doped with manganese and iron” published in Semiconductor Science and Technology **30**, 035002 (9 pages) (2015) [42]. Authors: A. Meingast, A. Navarro Quezada, T. Devillers, A. Kovács, M. Albu, S. Fladischer, A. Bonanni and G. Kothleitner. The paper is presented in full length in section 12.2.

This paper was mainly carried out by the PhD student. All TEM investigations and the resulting figures were acquired and composed by the student. Analysis, data interpretation and text writing was done by the PhD student in close collaboration with the supervisor. The manuscript was discussed with the remaining co-authors for correct interpretation and correlation of findings with already published information prior to submission.

5.3 Heusler alloys

Journal contribution: “Interdiffusion in Heusler film epitaxy on GaAs(001)” published in PHYSICAL REVIEW B **83**, 035319 (8 pages) (2011). Authors: C. Gusenbauer, T. Ashraf, J. Stangl, G. Hesser, T. Plach, A. Meingast, G. Kothleitner and R. Koch. The paper is presented in full length in section 12.3. The analytical investigations by STEM-EDXS linescans were carried out by the PhD student. The composition of Figure 9 and the accompanying quantification was carried out by the PhD student. The interpretation of results and the text presented in section “F” of the paper was composed by the PhD student in collaboration with the supervisor.

6. Practical aspects about transmission electron microscopy

6.1 Utilized electron microscopical instrumentation

In this work two types of electron microscopes both manufactured by FEI Company, a Tecnai 200 kV microscope located in Graz and various TITAN® microscopes operated at 200 and 300kV were used. They are located in Copenhagen, Eindhoven, Jülich and Graz. This section provides an overview of the technical specifications for the two microscopes located at the FELMI in Graz. Both are displayed in Figure 4 and important characteristics of them are listed in Table 1. The specialties of the other utilized microscopes will be mentioned together with the results obtained on these microscopes.

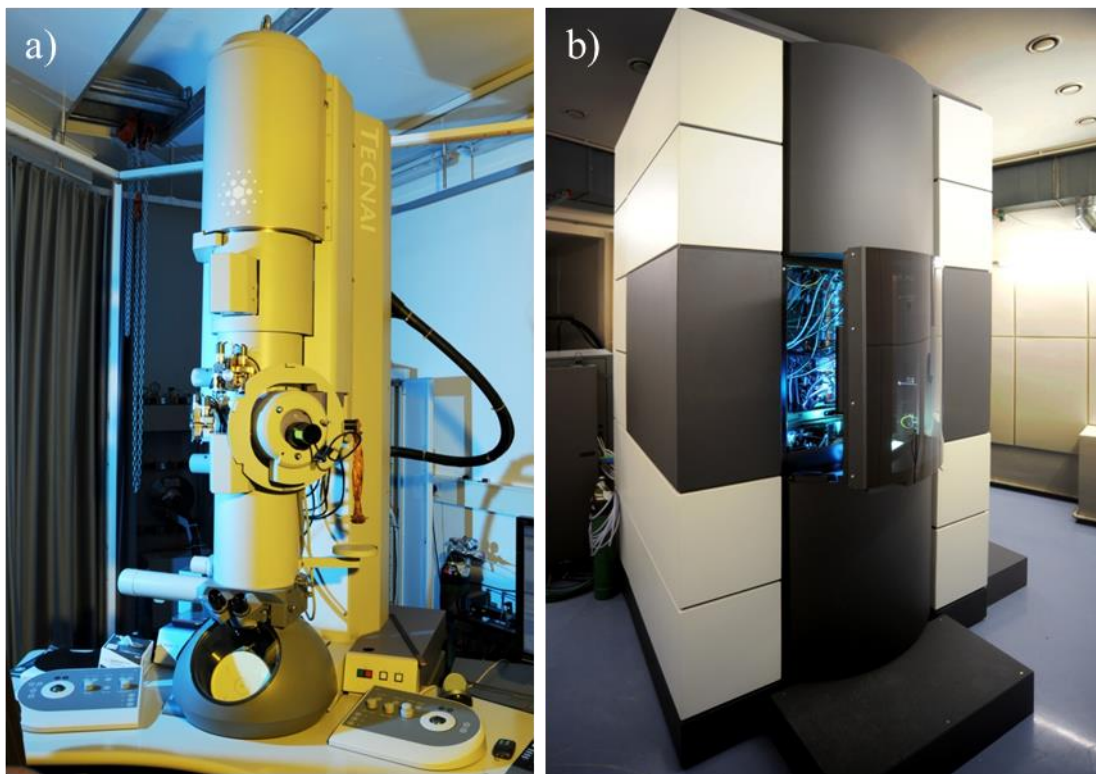


Figure 4: Electron microscopes mainly used within this thesis at the FELMI in Graz: a) FEI Tecnai 200 kV b) FEI TITAN 60 – 300 kV.

Table 1: Key facts about the electron microscopes located at the FELMI.

Microscope type	Tecnai	TITAN
Accelerating voltage	200 kV	60 – 300 kV
Electron source	Schottky FEG	X-FEG
Monochromator	Yes	Yes
C_s probe-corrector	No (C _s : 1.2 mm)	Hexapole type (Ceos GmbH)
EDXS-detector	Si(Li) with Moxtec window (from Edax Inc.)	4 x windowless SDD detectors (from Bruker Corporation)
HAADF / ADF / BF	1 / 1 / 1	2 / 3 / 2
Digiscan II Unit	Yes	Yes
GIF	HR-Triditem	QuantumERS
CCD	2x2 k Ultrascan	2x2 k Ultrascan
DualEELS	No	Yes
GIF Hardware Synchronized	No	Yes

The Tecnai system has been installed at FELMI in 2001 being one of the most advanced analytical systems at that time. Its monochromator and the – at that time – excellent resolution (spatially and energetically) has enabled FELMI to obtain numerous outstanding results such as [55–58]. Subsequent developments have led to advances regarding microscope stability, spatial resolution, beam current, analytical quality and speed. Most notably, large improvements regarding resolution in TEM and STEM imaging have been achieved through the correction of the spherical aberration (C_s correction). To take advantage of this development a probe corrected TITAN system was installed at FELMI in 2011. In section 6.5 a theoretical introduction to C_s correction is given and in section 8.3.1 the improvements are depicted by STEM HAADF images of GaN.

6.2 Benefits of transmission electron microscopy

Transmission electron microscopy allows for identification and quantification of nanostructured features within a material. Since roughly 15 years, with the event of aberration correction of electron beams [59,60], it is possible to routinely observe features down to the atomic level [61]. Such a development has boosted the understanding of materials and provided the possibility to influence structures on an atomic level. The following introduction to transmission electron microscopy and the used analytical techniques is compact and meant to provide the reader with a basic understanding. For a more comprehensive description the reader is referred to the references. Furthermore, due to the multitude of techniques and potentials connected with (analytical) transmission electron microscopy it is neither possible nor intended to describe all possibilities with various modes available in the TEM.

6.3 The transmission electron microscope and its working modes

Transmission electron microscopy makes use of an accelerated beam of electrons with typical accelerating energies ranging from 60 to 300 kV [62]. This beam is used to image electron transparent TEM specimens which in materials science are usually <100 nm thick [63]. This is done in principle by using a number of round electromagnetic lenses for focus and magnification. Apertures block electrons too far away from the optical axis due to the strong increase of the spherical aberration [62]. Figure 5 shows the lens configuration of a TITAN transmission electron microscope with the denotation of the various lenses and apertures. In addition, a more detailed schematic of the spherical aberration probe corrector (C_s probe corrector; denoted by “I”; manufactured by CEOS GmbH) and the Gatan image filter (GIF; denoted by “II”; © Gatan Inc.) are shown in the inserts of Figure 5. The C_s probe corrector is described in section 6.5. More information about the GIF can be found in section 6.6.

A thorough and rather complete introduction to transmission electron microscopy can be found in the standard textbook for electron microscopy [62].

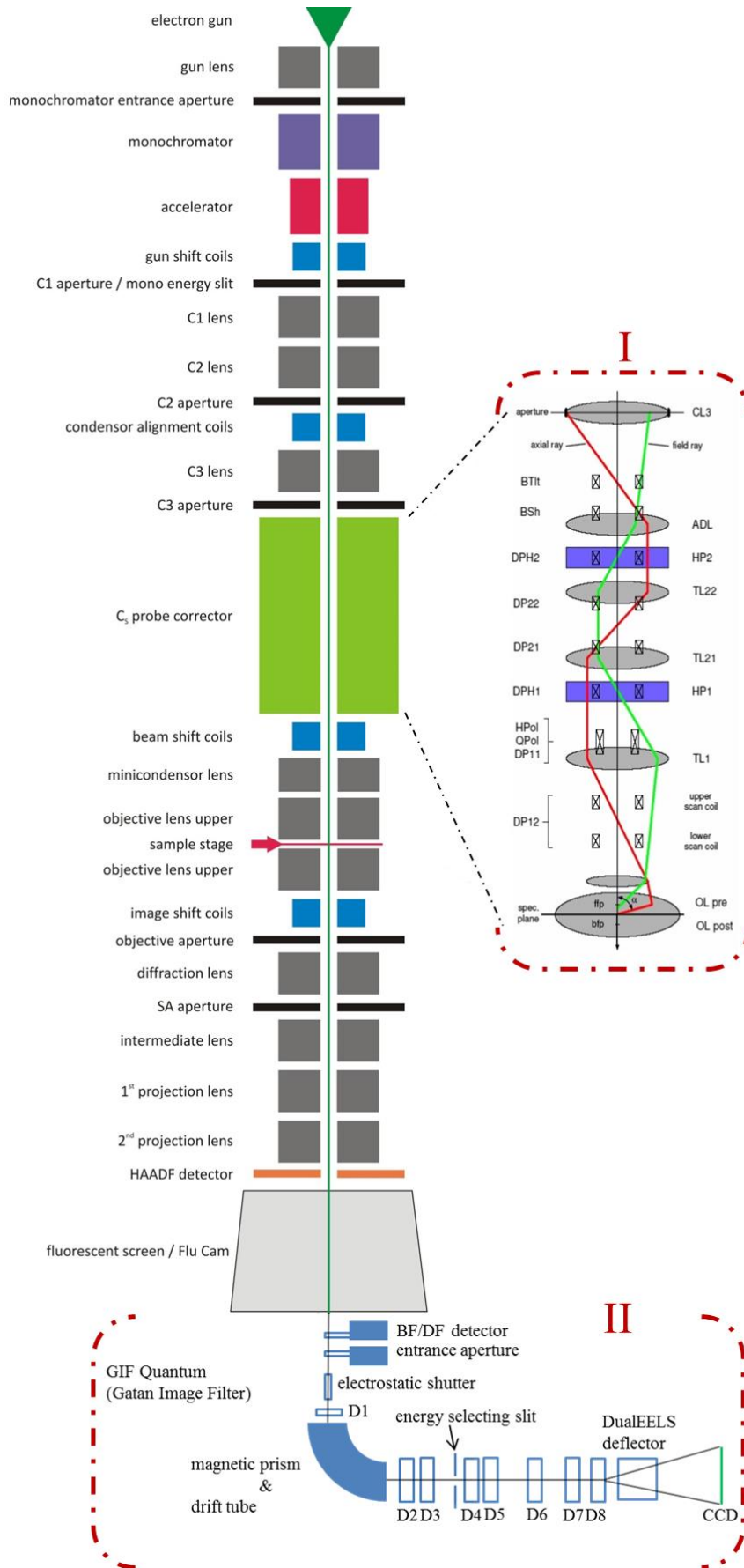


Figure 5: Schematic cross-section through a TITAN transmission electron microscope and its various components; a more detailed scheme of a C_s probe-corrector (denoted by “I”; © CEOS GmbH) is shown in the insert to the right; a schematic drawing of a GIF Quantum is furthermore shown (denoted by “II”).

Figure 5 shows the lenses, apertures and coils that the electrons have to pass after they have been extracted from the electron gun (topmost part). If the electron source is a cold or thermally assisted field emission gun (FEG) the mathematical description of the electrons can be done as coherent electron waves [62]. After the electrons have passed through the monochromator, which is described in detail in section 6.4, they are accelerated. In the case of the TITAN microscope the electron acceleration voltage can be adjusted from 60 kV to 300 kV. Thereafter the electrons pass through the condenser system, consisting in principle of three lenses and three apertures where a demagnification of the electron source is achieved, the convergence angle is selected and the illuminated TEM specimen area is adjusted. Next the electrons pass through the probe corrector system which reduces spherical aberrations when the beam is focused to a fine probe. A detailed description of the probe corrector is given in section 6.5. In the case of TEM imaging, the objective lens system is used to magnify the image after the electrons have interacted with the TEM specimen. Hereby an objective aperture can block electrons scattered too far away from the optical axis thereby enhancing image contrast. Electrons can interact elastically or inelastically when passing through the TEM specimen. These electrons can not only be used for imaging but also for analytical purposes as outlined in section 6.6. In the following, common operating modes of a TEM are described.

6.3.1 TEM-imaging mode

This is the most commonly used mode of a TEM. Hereby a TEM specimen area is illuminated with a parallel electron beam. The electron beam and the TEM specimen interact and the resulting image is then magnified by projector lenses. The contrast within an image can usually be either interpreted as mass-thickness, diffraction or phase contrast. Mass-thickness contrast describes the attenuation of the electron beam due to an increased TEM specimen thickness or a higher mass within a certain region of the TEM specimen. Diffraction contrast gives rises to phenomena such as bend and thickness contours in crystalline materials. Phase contrast mathematically explains the interaction of the electron waves with very thin specimen as it is used for high resolution (HR) TEM imaging [62]. The TEM imaging mode allows a rather direct observation of the TEM specimen by either looking at the phosphorous viewing-screen or using a CCD camera. Crystalline TEM specimens can exhibit diffraction contrast. Hereby the electron beam is scattered according to Bragg's law. Electrons are dispersed into discrete points if a single crystal is illuminated or rings if polycrystalline area is illuminated. The objective aperture is used to select or exclude certain reflexes. The observation is called bright field imaging, when the undiffracted beam is used for forming an image. In contrast, dark field imaging only a specifically selected diffracted beam is used for imaging. This allows imaging of, e.g. specifically oriented crystals. A third possibility is the usage of energy filtered imaging where only electrons with a specific energy loss (such as 0 eV or 400 eV) are used for imaging [64]. This is possible if the microscope is equipped with an image filter (section 6.6). TEM images in this thesis, which are not

explicitly mentioned to be obtained through an aberration corrected instrument, are all zero loss filtered. Zero loss filtering means that the width of the energy selecting slit was set to 10 eV and centered on the zero loss peak (see also section 6.6.3). Thereby the total amount of detectable electrons is reduced. Electrons with lower energy than the primary energy lead to a chromatic aberration within an image causing blur [62]. By blocking these electrons with a slit it is possible to record images with greater detail.

Today, in the case of high resolution TEM imaging, the transmitted beam can be corrected by a C_s (see section 6.5) and possibly a C_c corrector [65–68]. The latter correction enables imaging of features of around 50 pm provided that the TEM specimen is adequate.

6.3.2 Diffraction mode

In this mode, the excitation currents of the projection system are altered such that electrons with the same angular deflection are imaged in the same point on the viewing screen or CCD [62]. Hereby, the diffraction pattern of a TEM specimen area (e.g. a crystal) can be recorded. In the case of a suitably oriented single crystal the diffraction pattern comes in the form of dots. For polycrystalline TEM specimen areas the pattern consists of series of rings. By comparison with reference data an identification of the material is possible [62]. Moreover, diffraction enables one to select specific diffraction spots for TEM imaging to identify crystals with a specific orientation and phase via their diffraction pattern [69] or to orient TEM specimens relatively to the electron beam. The diffraction mode can be setup in two ways within the microscope. The first one uses a parallel electron beam with a rather large diameter (so called microprobe mode) for illumination of the TEM specimen and selecting the region of interest (ROI) for diffraction via an aperture, also called selected area electron diffraction (SAED) [62]. Sample areas with a diameter of a few hundred nanometers can be selected. The second mode uses the so called nano-probe mode of the TEM where the beam diameter (with nearly parallel illumination) can be reduced to a few nanometers. In this mode, the beam diameter determines the selected TEM specimen area used for diffraction [70].

6.3.3 STEM imaging mode

Scanning transmission electron microscopy (STEM) has become increasingly popular in the past ten years [62,71–74]. Generally, there exist two types of transmission electron microscopes: “conventional” TEMs and dedicated STEMs [75]. The first type is a microscope which can be operated basically in two modes, TEM imaging mode and STEM imaging mode. To be able to perform STEM imaging the electron microscope has to be equipped with a scanning unit. Commercial producers of conventional TEMs are e.g.: FEI Company, Jeol Ltd. or Hitachi High-Technologies Corporation. The second type is a microscope which is designed to be operated in STEM imaging mode. On this type of instrument the objective lens system is not present and hence no TEM imaging

mode (as described in section 6.3.1) is possible. Commercial producers of dedicated stems are e.g.: Nion Company or Hitachi High-Technologies Corporation. Since only the first type of TEM has been used for this work all technical details are referred to this type of instrument.

In STEM imaging mode a convergent electron beam is formed before the TEM specimen using the condensor system. For the TITAN system this is done by adjusting the strength of the C3 lens such that the beam has a crossover before the minicondensor lens as depicted in Figure 6 [76]. Thus, the minicondensor lens parallelizes the beam. The convergent beam (so called probe) is then formed to a small spot by the upper objective lens. The position of the crossover between C1 and C2 lens is called spot number and sets the range for the accessible beam current. The interval of the convergence angle is defined by the size of the C2 aperture. The actual convergence angle of the probe is defined by the position of the crossover between the C2 and C3 lens. This allows for a continuous adjustment of the convergence angle within the range given by the C2 aperture.

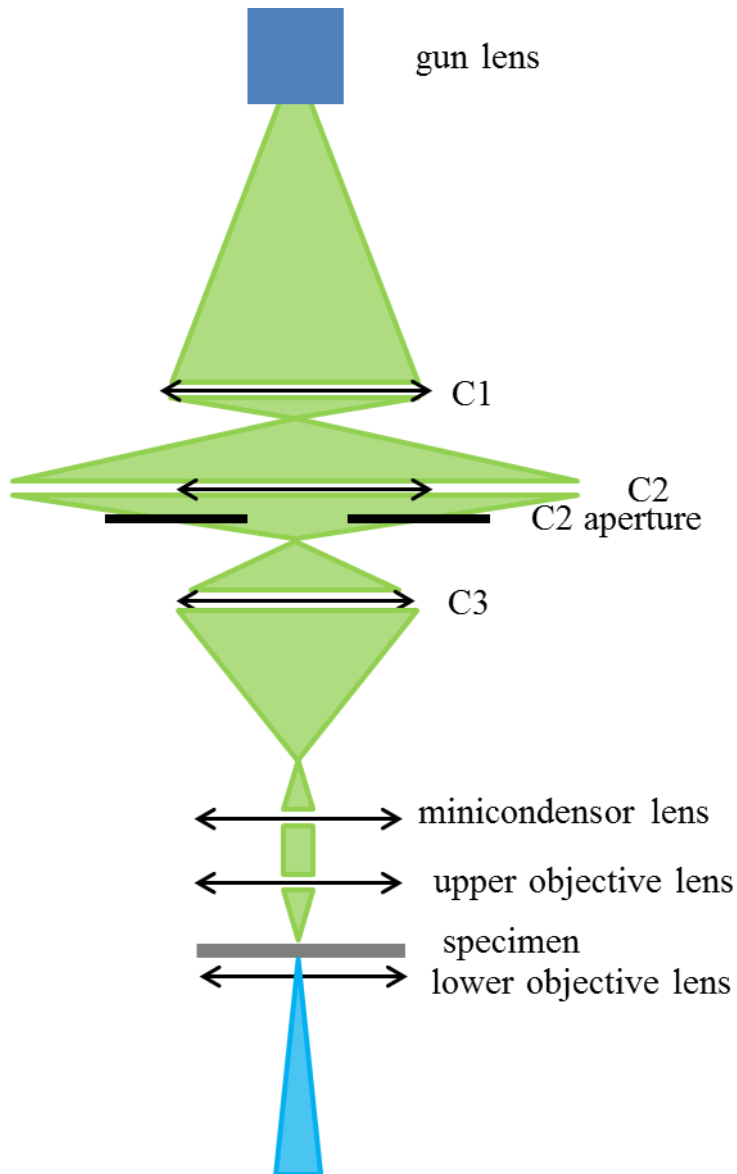


Figure 6: Illumination setting for probe mode: the C3 lens illuminates the probe forming lens (minicondensor lens) with a low convergent beam.

The so formed illuminating spot (i.e. probe) is scanned point by point across the TEM specimen by beam deflector coils [62,77–79]. This is done in a similar mode as in a scanning electron microscope (SEM) [79]. A difference between SEM and STEM is that a thin, electron transparent specimen is used in STEM. This allows that transmitted electrons can be detected. Scattering of the electrons in a thin sample is lower, less beam spreading occurs and the spatial resolution is mainly controlled by the illuminating probe size [77,79]. Typically, the beam diameter illuminating the TEM specimen is around 1 nm. If spherical aberration correction is used the diameter can be reduced even further (see section 6.5). Magnification in STEM mode is done by deflecting the probe and not by lenses. If the probe is deflected far from the optical axis during the rasterizing, the scanned area is large and thus the STEM magnification low. If the probe is deflected slightly from the optical axis the scanned area is small and the STEM magnification high.

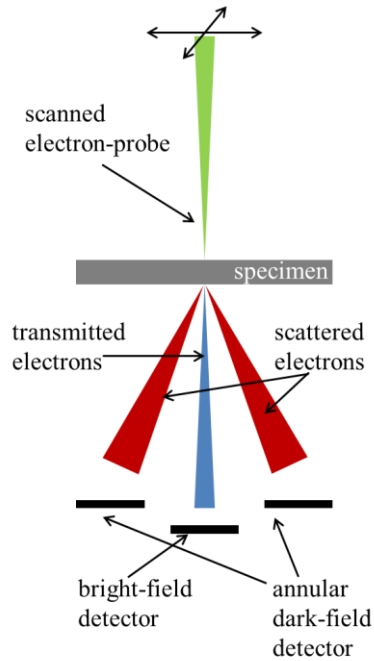


Figure 7: Schematics of STEM imaging with the scanned electron probe and various detectors to collect different types of electrons (scattered or transmitted).

Figure 7 schematically depicts the situation when the focused electron beam is scanned across the TEM specimen. Various detectors can be used (if available on the specific microscope) to collect transmitted or scattered electrons. For each pixel the amount of electrons is translated to a grey value per pixel [62,80]. For scattered electrons the annular shaped detectors, the annular dark field (ADF) and the high angle annular dark-field (HAADF), are used and for transmitted electrons the circular-shaped bright field (BF) detector is used. Hereby all detectors cover various angular ranges. The different detectors allow to image different properties of the TEM specimen. Coherent bright field contrast is used to describe the contrast obtained in bright field images [81,82]. These images show in the absence of material (e.g.: vacuum or a hole) bright pixels as the detector collects the direct beam. Consequently, TEM specimen regions with higher thickness or heavier elements are displayed in grey values. Contrast in images recorded with an ADF detector can be influenced by coherently scattered Bragg beams. Therefore, the contrast cannot purely be related to the atomic number of the imaged material [83]. The contrast in images recorded with a HAADF detector is proportional to the atomic number Z of the illuminated material:

$$I \sim f(\alpha) \sim Z^x \quad (1)$$

with x depending on α (up to $x=2$); I being the intensity, α being the beam convergence angle, Z being the atomic number and x being a constant.

This is due to the fact that HAADF imaging can be described by incoherent thermal diffuse scattering [79,81,82,84,85]. Today atomically resolved HAADF-STEM images can be obtained providing an appropriate TEM specimen [86,87]. If C_s correction to the finely focused electron probe

is applied a spatial resolution of 70 pm can be reached [88,89]. It is possible to record combinations of different signals simultaneously giving comprehensive image information of the material. Moreover, it is possible to acquire analytical information in the form of energy dispersive X-ray spectroscopy (EDXS) and electron energy loss spectroscopy (EELS) from each point imaged.

6.3.4 ABF imaging

Annular bright field (ABF) imaging is a rather new technique applicable when the TEM is operated in STEM mode [90–94]. In the past, transmission electron microscopes have successfully provided images of heavy-atom positions, especially by using HAADF imaging [62,71,95]. However, the detection of light atoms using the annular dark-field method is difficult as light atoms scatter beam electrons poorly [62]. When applying conventional parallel illumination onto a TEM specimen a hollow-cone illumination (HCI) allows improving significantly the resolution as well as the signal-to-noise ratio of a phase contrast image. The hollow-cone illumination minimizes the effect of wavelength fluctuations of the incident electron beam [92,96–98]. This is done in practice by employing a series of off-axial illuminations over a certain angle ranges of the incident beams as schematically depicted in Figure 8a). Based on reciprocity this can be equivalently realized by locating an annular detector within the direct-beam disc in STEM mode [96,99]. Figure 8b) depicts schematically the setup for ABF imaging where the ABF detector covers an angular range from θ_{\min} to θ_{\max} . θ_{\max} is determined by the convergence semi-angle α of STEM probe and θ_{\min} is half the convergence angle α [92].

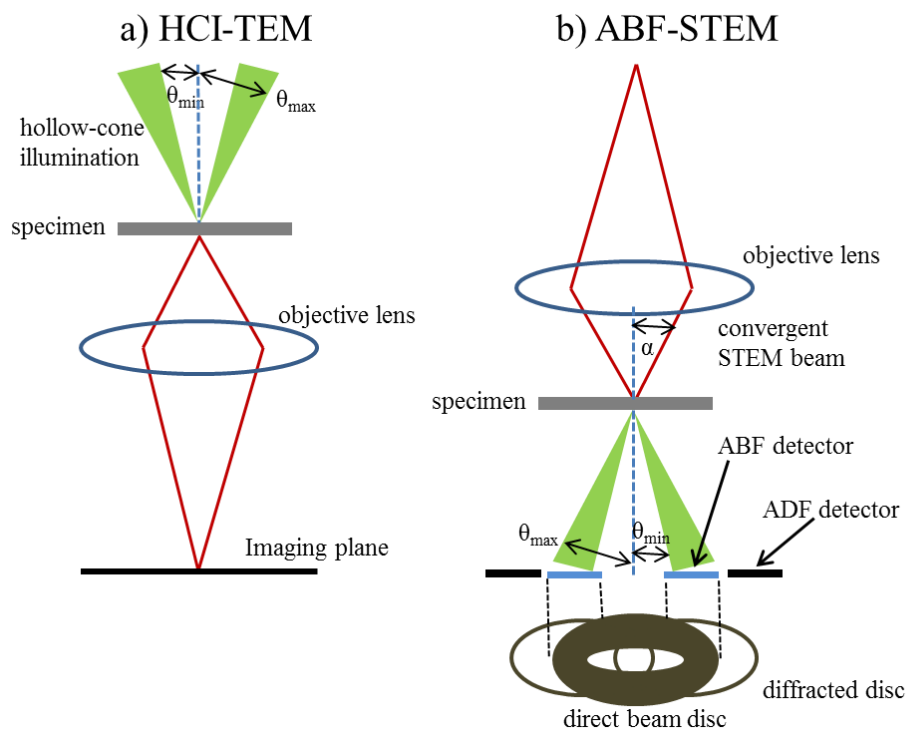


Figure 8: Schematic description of a) HCI-TEM illumination with the cone angle ranging from minimum θ_{\min} to θ_{\max} ; b) equivalent ABF-STEM imaging with the detector angle ranging from θ_{\min} to θ_{\max} where θ_{\max} is set to the convergent semiangle α .

In an early setup the center of the BF detector has been covered with a circular shaped beamstop to form an annular shaped ABF detector [94]. An eased experimental setup for this imaging mode can be realized by choosing the camera length (CL) in such way that the beam diameter of the transmitted electron disc corresponds to the diameter of the inner hole of an ADF detector. Then this camera length is doubled to record only the outer ring of the transmitted electrons using the ADF detector. To be able to do so an appropriate convergence angle α has to be chosen beforehand. The convergence angle α for ABF imaging is usually between 20 – 30 mrad [92]. Thereby, a good signal intensity can be expected for elements up to $Z = 30$ with decreasing but not vanishing signal intensity for heavier elements [90]. The observed ABF intensity I scales approximately with:

$$I \sim Z^{1/3} \quad (2)$$

with Z being the atomic number.

Figure 9 shows a schematic description of a setup using an ADF detector for ABF imaging. Both mentioned setups allow that a HAADF detector can be utilized to identify an appropriate specimen position, orient this specimen position into a suitable zone axis and record simultaneously with the ABF image a conventional HAADF image. In this way the positions of heavy constituents can be identified and an eased ABF image interpretation can be done.

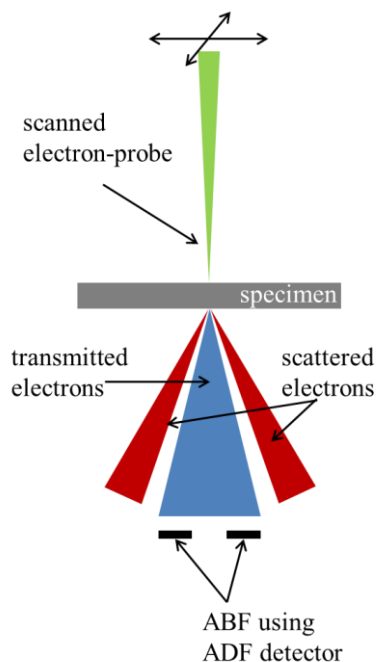


Figure 9: Schematic setup to record ABF images using an ADF detector to collect electrons from the outer ring of the undeflected beam.

ABF images with atomic resolution usually show a bright background with atomic columns appearing dark [90–92,94]. This is the reverse situation of common HAADF images where atomic columns appear bright. The advantage of ABF imaging is that it allows simultaneous imaging of columns of light elements, e.g. hydrogen, nitrogen, oxygen, and heavy atoms columns such as titanium, zinc, strontium or gallium [90,94]. This is beneficial compared to conventional HAADF imaging where only heavier constituent(s) of a material are well imaged. ABF imaging has been successfully employed to a variety of materials to image atomic columns of light and heavy constituents such as:

- Oxygen columns in SrTiO_3 oriented in [001] [94].
- Oxygen columns in Fe_3O_4 [94].
- Nitrogen columns in Si_3N_4 [94].
- Oxygen columns in ZnO [93].
- Hydrogen columns in YH_2 [92].

Theoretical calculations show that ABF imaging has similar focusing characteristics to conventional STEM imaging. It is also less sensitive to TEM specimen thickness variations compared to HR-TEM imaging. In practice this means that specimen positions with a thickness range closer to practical thicknesses suitable for analytical investigations can be used for ABF imaging [90].

6.4 The monochromator

The energy resolution in EELS (section 6.6) is besides other factors (such as high tension stability, stray fields etc.) mainly limited by the energy spread of the electron source. This energy spread is around 1 eV in the case of a Schottky field emission gun (Schottky FEG) [62]. In the case of transmission electron microscopy with low accelerating voltages the usage of a monochromator is important to reduce the effects of chromatic aberration [100–102]. To reduce the energy spread of the FEG it is possible to install a monochromator after the electron source [103]. Figure 10 shows the schematic setup of the field emission gun and the monochromator of a TITAN microscope. The field emission gun consists of the electron emitting tip, the extractor providing the necessary high voltage and the gun lens, which makes a focus of the dispersion in the plane of the energy selection slit (C1 aperture).

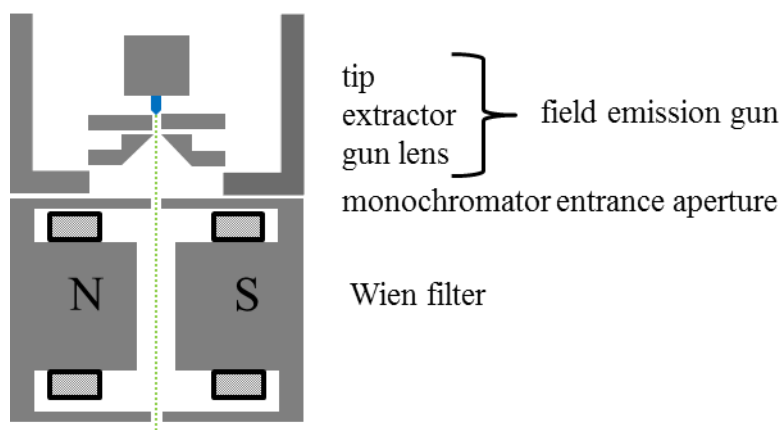


Figure 10: Schematic setup of the field emission gun and the monochromator of a TITAN microscope. The monochromator works according to the Wien filter principle.

If a monochromator is installed on a TITAN and Tecnai microscope it works according to the Wien filter principle [76]. The electric and magnetic fields are normal to each other and both of them are perpendicular to the electron beam. The strength of the electric and magnetic field is constant along the length of the monochromator. The forces of the electric field ($-eE$) and the magnetic field ($-evB$) cancel only for electrons with average velocity $v_0 = E/B$. Electrons with deviating velocity are dispersed according to their energy. To block those electrons an energy selecting slit is used. The amount of dispersion can be adjusted by the excitation strength of the monochromator. This means that a higher excitation of the monochromator leads to an improved energy dispersion of the beam electrons. For a better alignment a point focus at the monochromatizing slit is preferred [76]. Therefore, an electric quadrupole field is added over the whole length of the monochromator. This setup is called double focusing Wien filter [104]. Figure 11 shows a comparison between an electron energy loss spectrum of a “standard” zero-loss peak (ZLP) and a ZLP with a moderately excited monochromator acquired with the Tecnai microscope in Graz. It shows that the full width at half maximum (FWHM) of the ZLP can be decreased by more than a factor of 4.

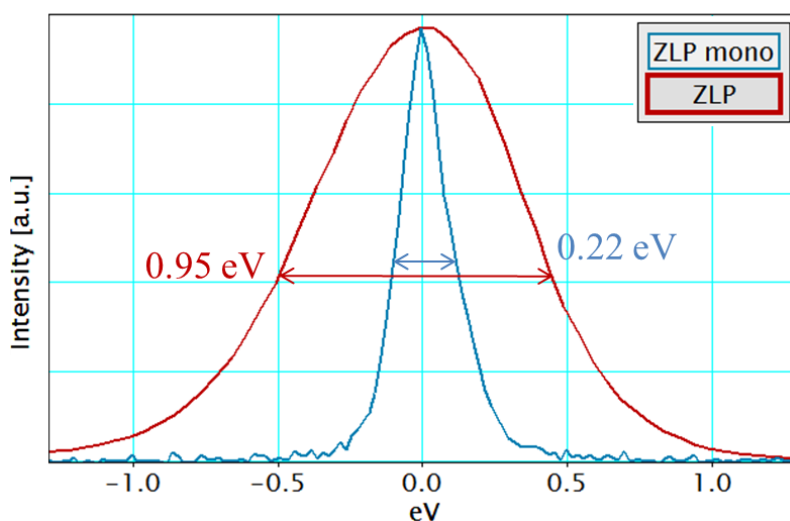


Figure 11: Comparison of the FWHM of zero-loss peaks (“standard” and monochromated) measured on a Tecnai F20 equipped with a Schottky emitter, a monochromator and a GIF QuantumERS with 0.02 eV/pixel dispersion.

With the TITAN microscope it is possible to achieve an energy resolution of the electron beam < 150 meV [103,105,106]. However, with increasing monochromator excitation the amount of beam current drops severely as only a fraction of it passes through the monochromator slit [107]. At high beam currents, the statistical Coulomb interactions in the monochromator broaden the energy distribution (so called Boersch effect) and blur the apparent source. This increases with the length of the monochromator as electrons have a low potential within it. As a result, the energy resolution and spatial resolution of the microscope are limited [104]. For short exposure times the energy resolution is determined by high frequency ripples, aberrations and the point spread of the detector. For longer exposure times contributions come from stray magnetic fields (50, 150Hz), noise and drift (e.g.: high voltage) which can deteriorate the energy resolution [108].

Practical steps to set up a monochromated illumination on a TITAN microscope are:

- Adjust gun lens excitement to focus beam within C2 aperture; use monochromator shifts to center illumination inside the C2 aperture; spread illumination slightly bigger than C2 aperture using the gun lens.
- Focus C2 lens on plane of energy selecting slit using the “slit wobbler” function; this accounts for the modified illumination conditions through excitement of the monochromator.
- Stigmatize beam with monochromator stigmator so that beam broadens with change of monochromator focus symmetrically.
- Increase monochromator excitation; set up excitation to the desired value with small increases in excitation; after each increase re-center beam with monochromator shift.
- Correct for remaining astigmatism and focus dispersed illumination.

- For best energy resolution move the line of dispersed electrons over the GIF entrance aperture and optimize stigmator and gunlens using the spectroscopy mode of the GIF.
- Store the values in a FEG-register and proceed with optimization of the remaining microscope column.

Electron probe monochromation has been successfully applied to various materials. A small selection shall be listed:

- The effect of planar defects in the superconductor $Y_1Ba_2Cu_3O_{7-\delta}$ [109].
- Comparison of the V L and O K ELNES with NEXAFS data of a V_2O_5 crystal [110].
- A study of the ELNES structure of TiO_2 , V_2O_5 , Cr_2O_3 , Fe_2O_3 , CoO and NiO [108].
- To study the surface valency of cerium nanoparticles of the $CeM_{4,5}$ edge [111].
- A study of localized plasmon modes in silver nanoparticles [112].

6.5 Correction of the spherical aberration

In 1936 Otto Scherzer published a proof that the spherical aberration coefficient (C_s) of any rotationally symmetric, static, space-charge-free, dioptric lens can be written as a sum of non-negative definite terms [113]. This aberration can therefore not be eliminated by a thorough lens design as in contrast to glass lenses. He proposed to use quadrupoles lenses to create an asymmetric electron beam and octopole lenses to cancel the aberrations [114]. Already in 1951 it was proven by Scherzer and his co-worker Seeliger that a correction of the electron beam is possible [115]. However, it took nearly 50 years until a usable device to correct for the spherical aberration was realized. The correcting device must be capable of creating an aberration similar to spherical aberration of a round lens but opposite in sign (i.e. a negative C_s). Hawkes showed in 1963 that also hexapole lenses are capable to generate a negative C_s [116]. Furthermore, it was shown that a suitably orientated and excited pair of hexapole lenses can be used to cancel the spherical aberration of a round lens without influencing the lateral resolution. This type of setup for C_s correction provides eased alignment demands and less mechanical precision [117]. All three types of multipole lenses are schematically depicted in Figure 12. For thin multipole lenses, the magnetic field is mainly perpendicular to the electron beam [118]. Therefore, the deflection of the electrons is simply given by the Lorentz force, which is proportional to the field strength at the position of the electron [62].

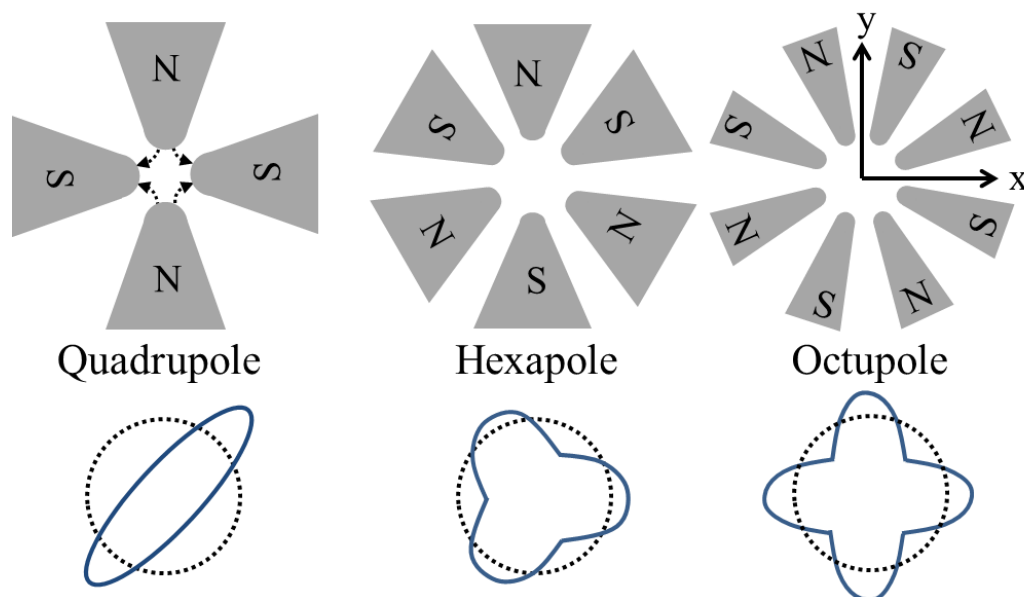


Figure 12: Schematic drawing of multipole lenses with the z-axis, along which the electrons travel, into the page; the geometry of the field lines is indicated on the quadrupole lens; below each multipole lens is the beam cross section shown as original round beam (black dotted line) and multipole lens influenced beam (blue line). Figure in analogy to [118].

Working correctors have been built in the second half of the 1990ies with two different multipole lens configurations:

A group around Krivanek in Cambridge worked to reduce the spot size in a STEM beam using the quadrupole-octopole approach. In a quadrupole lens the field variation is linearly from the optic axis. Along one transverse axis as shown in Figure 12 it focuses the beam and along the perpendicular axis it defocuses the beam. The quadrupole lens works as an optical element that can form a line focus from a round beam and vice versa. This is required to exploit the properties of the octupole lens [118]. The octupole field varies cubically from the optic axis thereby directly influencing the third-order aberrations. In addition it distorts the roundness of the beam. Along one pair of axes (e.g. x and y axis as depicted in Figure 12), it has negative spherical aberration. Along a pair at 45° to those two axes the hexapole has a positive spherical aberration. The quadrupole-octopole corrector works according to the following setup: A first quadrupole to put a line focus along the negative spherical aberration axis of the first octupole. Two subsequent quadrupoles form a line focus in the perpendicular direction for a second octupole. Finally, a fourth quadrupole forms a round electron beam. The two octupoles do not only apply a negative spherical aberration in x and y direction to the electron beam, they also cause a four-fold distortion. To correct for the four-fold distortion a third octupole influences the round beam [118]. For their actual working corrector Krivanek and his group modified the principal quadrupole–octopole configuration. They included six instead of four quadrupoles and designed an antisymmetric lens configuration to obtain more degrees of freedom on the cost of increasing the complexity of the system [119].

Haider and colleagues in Darmstadt and Jülich used hexapoles to build a working corrector [120]. This approach utilizes two electromagnetic hexapoles and four additional lenses [121]. The principle operation mode is as follows: The first hexapole lens creates non-rotationally symmetric second-order aberrations. These aberrations are corrected by the second hexapole. The combination of the two hexapoles introduces also a secondary third-order spherical aberration (C_s). This aberration is rotationally symmetric and proportional to the square of the hexapole strength [122]. The resulting spherical aberration is opposite to that of the objective lens. Therefore, the spherical aberration of a system can be eliminated. This type of hexapole corrector was first proposed for a scanning transmission electron microscope. For this type of instrument off-axial aberrations do not need to be taken into account [123,124]. Haider and colleagues built the working corrector with additional multipole elements to correct the also the TEM imaging mode [59]. This was done to ensure aplanatism (elimination of third-order coma) and to cancel any parasitic aberrations [59,120,125]. Regardless which correction principle is used, to be able to perform aberration correction a very stable electron microscope and a fast response on the field modification within the corrector is necessary. The latter requires high computing power which became accessible at the above mentioned time [118,126]. Mathematically, the wave aberration function χ is defined as the phase difference between a perfect spherical wave and the actual wave front for a given lens:

$$\chi = \frac{2\pi}{\lambda} W \quad (3)$$

with λ being the wavelength and W the error in the wavefront measured as a distance. χ is zero for a perfect lens. In a real, aberrated lens this is a 2-dimensional surface:

$$\chi = \chi(\theta, \varphi) \quad (4)$$

with θ being the angle to the optic axis and φ being the azimuthal angle around the optic axis as schematically depicted in Figure 13

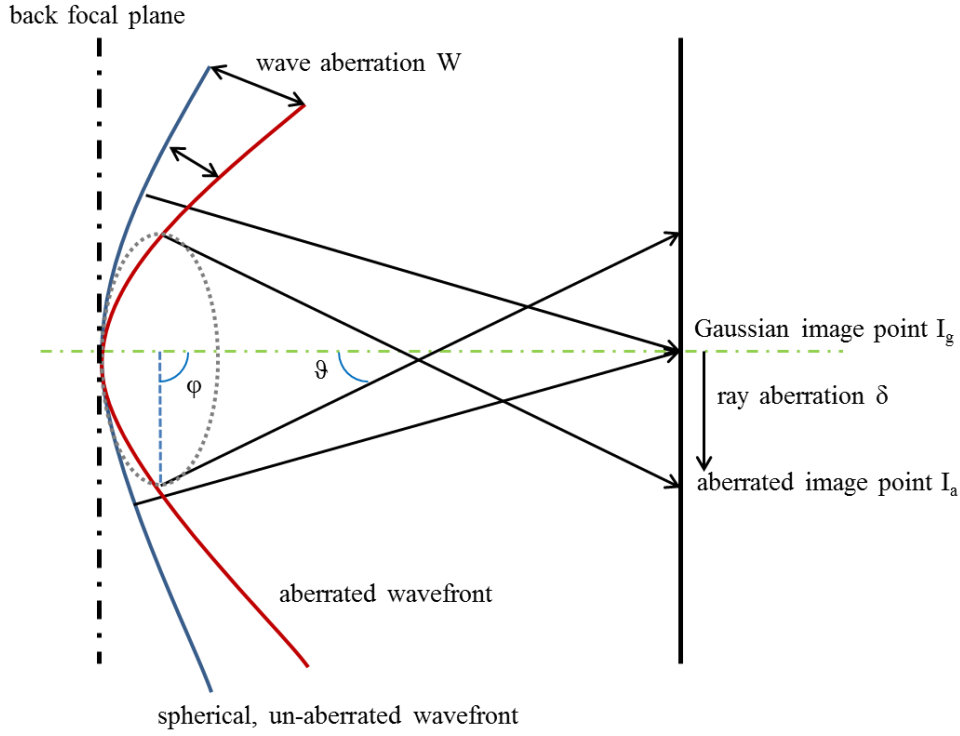


Figure 13: Schematic description of the spherical aberration of a wavefront by a round lens with the denotation of the angles.

In practice $\chi(\vartheta, \varphi)$ is close to zero near the optic axis, but increases rapidly as high order aberrations come to dominate away from the optic axis. The wave aberration function χ can be written in polar coordinates as a polynomial expansion [127]:

$$\begin{aligned}
 \chi(\vartheta, \varphi) = & \text{const} + \vartheta\{C_{01a} \cos(\varphi) + C_{01b} \sin(\varphi)\} + \frac{\vartheta^2}{2}\{C_{10} + \\
 & C_{12a} \cos(2\varphi) + C_{12b} \sin(2\varphi)\} + \frac{\vartheta^3}{3}\{C_{23a} \cos(3\varphi) + \\
 & C_{23b} \sin(3\varphi) + C_{21a} \cos(\varphi) + C_{21b} \sin(\varphi)\} + \frac{\vartheta^4}{4}\{C_{30} + \\
 & C_{34a} \cos(4\varphi) + C_{34b} \sin(4\varphi) + C_{32a} \cos(2\varphi) + C_{32b} \sin(2\varphi)\} + \quad (5) \\
 & \frac{\vartheta^5}{5}\{C_{45a} \cos(5\varphi) + C_{45b} \sin(5\varphi) + C_{43a} \cos(3\varphi) + C_{43b} \sin(3\varphi) + \\
 & C_{41a} \cos(\varphi) + C_{43b} \sin(\varphi)\} + \frac{\vartheta^6}{6}\{C_{50} + C_{56a} \cos(6\varphi) + \\
 & C_{56b} \sin(6\varphi) + C_{45a} \cos(4\varphi) + C_{45b} \sin(4\varphi) + C_{52a} \cos(2\varphi) + \\
 & C_{52b} \sin(2\varphi)\} + \dots
 \end{aligned}$$

with C_{XY} being the aberration coefficients.

The aberration function is a smooth and continuous two dimensional surface. Close to the optical axis dominate low order aberrations the aberration function. At angles further away from the optical axis the steep slopes of the higher order aberrations have more influence [127]. The aberrations and their azimuthal symmetry are listed in Table 2 with the notations of Krivanek et al [128] and Uhlemann & Haider [60].

Table 2: List of the aberration coefficients with their azimuthal symmetry and their respective names according to Krivanek et al. and Uhlemann and Haider.

Aberration coefficient [Krivanek]	Aberration coefficient [Uhlemann and Haider]	Name	Azimuthal symmetry
C_{01}	C_1	Image shift	1
C_{10}		Defocus	0 (Round)
C_{12}	A_1	Twofold astigmatism	2
C_{21}		Axial Coma	1
C_{23}	B_2	Threefold astigmatism	3
C_{30}	$C_S \equiv C_3$	Spherical aberration	0
C_{32}		Twofold astigmatism of C_S (or Third order twofold astigmatism)	2
C_{34}	A_2	Fourfold astigmatism of C_S	4
C_{41}		Fourth order coma	1
C_{43}	A_3	Fourth order threefold astigmatism	3
C_{45}	S_3	Fivefold astigmatism	5
C_{50}	D_4	Fifth order spherical aberration	0
C_{52}		Twofold astigmatism of C_5	2
C_{54}	B_4	Fourfold astigmatism of C_5	4
C_{56}		Sixfold astigmatism of C_5	6

The shape of the distortion introduced to the wavefront through aberrations can be visualized as depicted in Figure 14.

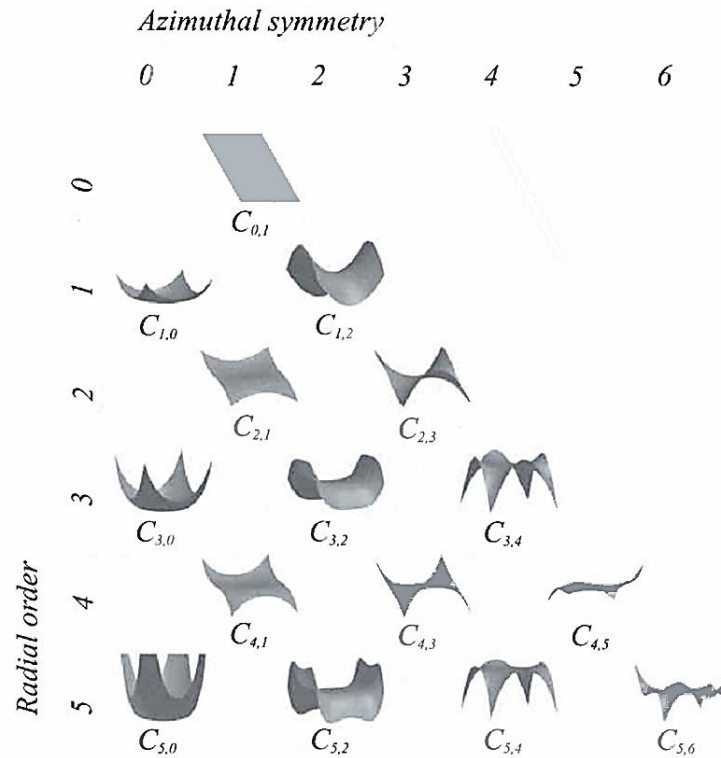


Figure 14: Visualization of the distortions introduced to the wavefront by distortions up to the 5th order. (Figure taken with permission from [127].)

The work for this thesis took mainly advantage of the hexapole corrector type adjusted for a correction of the probe [106]. A schematic description of the lenses and ray paths is given in Figure 5. The alignment strategy to achieve a spatial resolution $< 1 \text{ \AA}$ for this type of corrector is as follows:

- Decision on the used convergence angle of the probe before corrector tuning; this determines the size of the C2:
 - a) High convergence angle such as 25 mrad or higher use $C2 = 70 \mu\text{m}$; this is suitable for imaging with high spatial resolution.
 - b) Medium convergence angle around 20 mrad use $C2 = 50\mu\text{m}$; this is suitable for EELS & EDXS investigations; the probe diameter is rather small and therefore prone to channeling effects [129].
 - c) Low convergence angle around 15 mrad use $C2 = 50\mu\text{m}$; this is suitable to obtain high beam current in a slightly larger spot (suitable for e.g. analytical investigation of nanoparticles).
- Manual centering of C2 aperture and emission spot in diffraction off mode:
 1. Center C2 aperture that it opens symmetrically when defocusing the probe.
 2. Move caustic spot to the center of the probe and center probe along the optical axis.
- Correct manually for A1 and B2 in diffraction on mode:
 1. Move to an amorphous area of the TEM specimen.
 2. Correct for A1 (twofold astigmatism) and B2 (threefold astigmatism) while observing the probe on the FluCam.

- Perform the semi-automated probe correction using the DCOR software package as shown in Figure 15:
 1. Automatically correct for C1 (image shift) and A1 (twofold astigmatism).
 2. Use a “Fast Tableau” (Zemlin tableau [126]; see Figure 15 a and b) choosing a low convergence angle (e.g.: 18 mrad) to correct for A2 and B2 by choosing the respective strength of correction in %; after each correction correct for C1 and A1 again.
 - Criterion for satisfaction: measured values shown in Figure 15 c are in the range as listed in Table 3.
 3. When A2 and B2 values are satisfying use “Standard Tableau” and increase tilt angle (e.g.: 25 mrad; Figure 15 a).
 - Correct now preferentially for S3 (fivefold astigmatism) then carefully for A3 (fourth order threefold astigmatism) and finally C3 (spherical aberration); when all values are within the confidence interval or below the correction is sufficient.
 - The aberration free zone should be >20 mrad to obtain a resolution $<1 \text{ \AA}$ which is visualized in Figure 15 d.

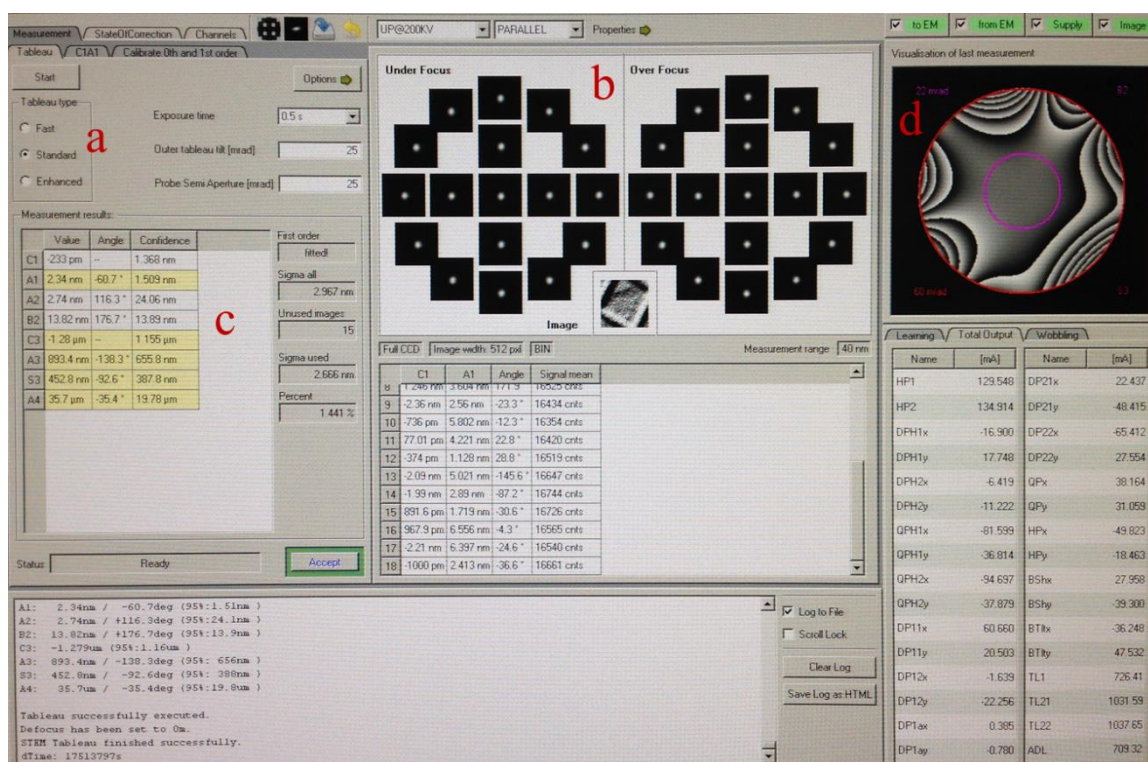


Figure 15: Screenshot of the DCOR probe correction software with indication of important components; a: selection of tableau type; b: visual representation of Zemlin tableau; c: list of aberration and its values; d: visualization of the aberration free zone and its value.

Table 3: List of achievable values for the measurement and confidence of each aberration for 300 kV acceleration voltage of a probe corrected TITAN microscope.

Aberration	Measured value	Confidence level
A1	< 5 nm	< 5 nm
A2	< 50 nm	< 50 nm
B2	< 50 nm	< 50 nm
C3	< 1.5 μm	< 1.5 μm
A3	< 500 nm	< 500 nm
S3	< 500 nm	< 500 nm

6.6 Electron energy loss spectroscopy

Electrons that interact with the TEM specimen inelastically can be used to obtain analytical information as they reflect atomic information [62,130]. This is done in principle by dispersing the inelastically scattered electrons according to their energy loss after they have been transmitted through the TEM specimen. Electron energy loss spectroscopy can be performed by dedicated systems (e.g. Model 977 EnfiniumTMER; © Gatan Inc.) or as a so called post-column energy filter (e.g.: GIF Quantum; © Gatan Inc.). The latter type is discussed in more detail in chapter 6.6.1 as it has been used extensively for the work in this thesis. Figure 16 shows an example image of the post-column energy filter GIF QuantumERS.



Figure 16: Image of the post-column energy filter GIF QuantumERS (© Gatan Inc.).

The result of an EELS experiment is usually shown in a histogram as the number of electrons with certain energy loss versus the energy. EELS is a highly sensitive measurement technique for (especially) light elements and due to the scattering in forward direction also very collection efficient [131]. In combination with energy dispersive X-ray spectroscopy (EDXS) (details on EDXS are given in section 6.8) one can gather a broad range of analytical information. Moreover, EELS spectra can be evaluated in a quantitative way. This is based on the theory of scattering cross sections of inner shell ionization of the illuminated atom(s) [131] which is discussed in section 6.7.

6.6.1 The post-column energy filter GIF QuantumERS

In this work, analytical instruments being equipped with post-column image filters (GIFs) have been used. The advantage of a post-column filter compared to in-column filters (e.g. OMEGA filter; © Zeiss) is that the microscope can be used without insertion of additional components into the optical path. Additionally, it is easier to attach a post-column filter to a microscope or modify/upgrade the system (microscope or energy filter) since both are two inter-connected components rather than one unit. This work took mainly advantage of the latest generation of post-column image filter, the GIF Quantum [132]. The most important parts of this energy filter are (see also Figure 17):

1. Entrance aperture: the filter incorporates three apertures: a 9 mm for imaging and two for spectroscopy (2.5 mm and 5 mm); the aperture diameter for spectroscopy defines the angular acceptance angle for scattered electrons; larger diameter means more signal but less accuracy in spectral resolution.
2. Electrostatic shutter: it allows deflecting the focused spectrum onto a beam trap at the slit; due to its fast and hysteresis free beam blanking a minimum exposure time of 1 μ sec can be achieved.
3. a) Magnetic prism: it bends the electron beam and disperses electrons according to their energy; electrons with lower energy get more bended whereas electrons with higher energy get less bended; the dispersion at the plane of the slit is 2.5 μ m/eV; for the GIF Quantum the dispersion radius is reduced from 100 mm to 75 mm to enable spectroscopy from 60 kV to 300 kV accelerating voltage of the electron beam; the magnetic prism furthermore focuses the generated spectrum onto the plane of the energy selecting slit; it is one of the most important parts since a precise deflection of electrons is required for high resolution imaging and high quality spectroscopy results.
3. b) Fast drift tube: this electrically isolated tube is located inside the magnetic prism; it allows to offset the energy of an energy loss spectrum through the application of a voltage; the drift tube within the GIF Quantum allows a 2 kV offset with a switching time of 20 μ sec; the accuracy is 100 mV with a 30 mV root mean square noise.
4. Energy selecting slit: this insertable element allows to select electrons with certain energy; it is inserted when energy filtered TEM images (EFTEM) are recorded; its adjustable width and a precise defined slit-width are crucial for EFTEM imaging.
5. Dodecapole lenses: the GIF Quantum has altogether 8 multipole lenses where each pole can be excited individually; in principle the lenses can be operated in two ways: imaging mode or spectroscopy mode; they are furthermore used to adjust an image or spectrum, magnify dispersions and compensate aberrations in image or spectroscopy mode.
6. DualEELS deflector: this electrostatic shutter is located in front of the CCD; it allows to deflect the spectrum on the upper or lower half of the CCD with 1 μ sec switching time; the shutter enables to record the low and high loss spectrum sequentially with individual exposure

times on the CCD; between the acquisition of the low and high loss the voltage of the drift tube is adjusted accordingly; with this deflector it is possible to record up to 1000 spectra per second.

7. CCD: it records an image or a spectrum depending on the operation mode; the GIF Quantum consists of 2 k x 2 k pixels with a size of 14 μm per pixel; the readout of the CCD can be performed with 1 MHz (high quality readout) or 10 MHz (high speed readout) which determines the quality of the analog to digital conversion; a description of both read out modes is given in section 6.6.2.

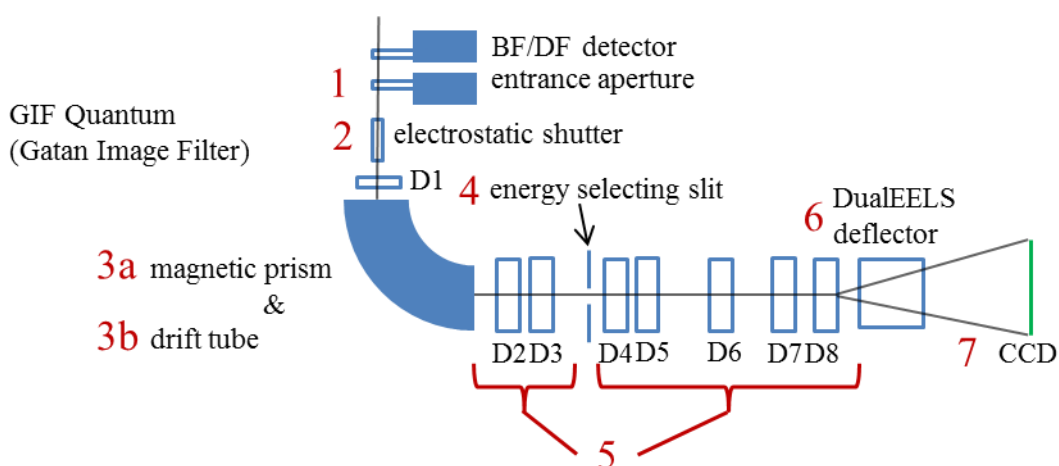


Figure 17: Schematic cross-section through a GIF Quantum with labeling of its most important components (red numbers): 1: entrance aperture; 2: fast electrostatic shutter; 3a: magnetic prism; 3b: drift tube; 4: energy selecting slit; 5: dodecapole lenses (D 1 – 8); 6: DualEELS deflector; 7: CCD.

6.6.2 The DualEELS mode and its synchronization

The GIF Quantum enables a new method how to record EEL spectra in STEM mode: DualEELS (© Gatan Inc.). Hereby, the low and high loss (see also section 6.7) is recorded subsequently from the same TEM specimen area. Since exposure times of high loss and low loss usually differ significantly the exposure time for each type of loss needs to be adjusted. The way DualEELS works is as follows:

1. Blank the beam with the electrostatic shutter; adjust the voltage of the drift tube according to the set value for the high loss; adjust the voltage of the DualEELS deflector such that it project the spectrum onto the upper half of the CCD.
2. Unblank the beam and expose the CCD to the electron beam for the set time of the high loss.
3. Blank the beam with the electrostatic shutter; adjust the voltage of the drift tube according to the set value for the low loss; adjust the voltage of the DualEELS deflector such that it projects the spectrum onto the upper half of the CCD.
4. Unblank the beam and expose the CCD to the electron beam for the set time of the low loss.
5. Blank the beam with the electrostatic shutter; read out each half of the CCD individually.

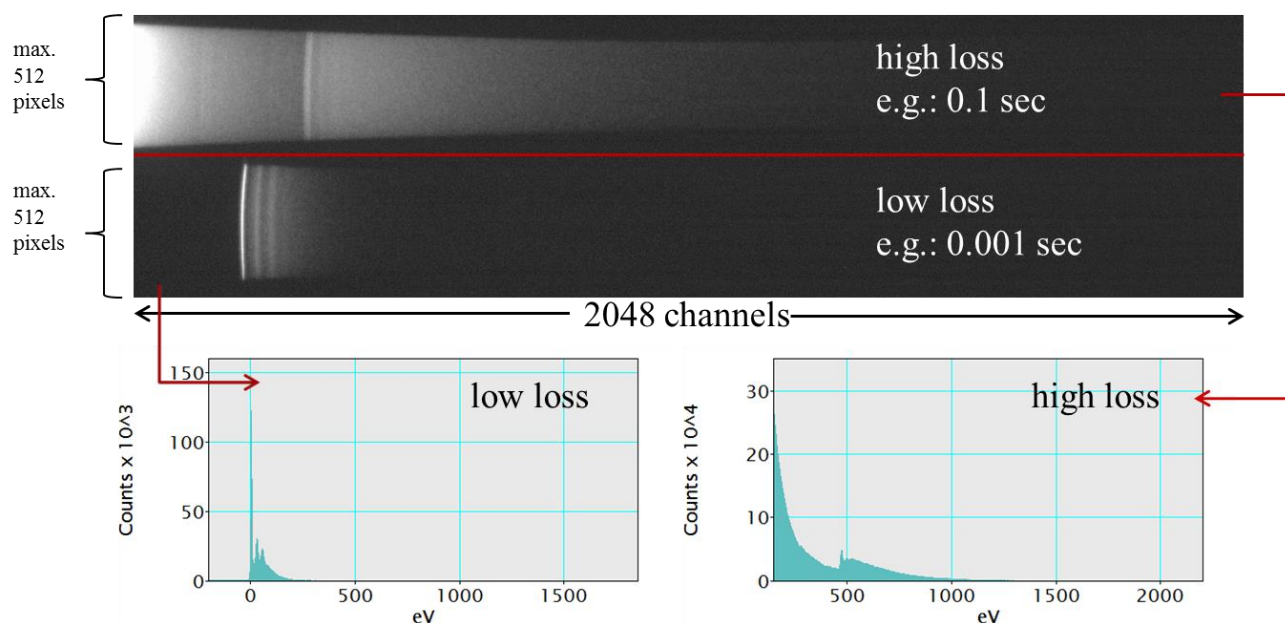


Figure 18: 2D DualEELS spectrum view on the CCD with a high loss and a low loss with the resulting spectra; red horizontal line: indication for the upper and lower half of the CCD.

Figure 18 shows a spectrum view of a DualEELS exposure with the high loss in the upper CCD half and the low loss in the lower CCD half. The red line indicates the middle of the CCD. Commonly the exposure times of the high loss (e.g.: nitrogen, iron, gallium...) are significantly longer than for the low loss (e.g.: zero loss, plasmon region...). Through the individual adjustment of the exposure time of each loss an optimized signal collection time can be set. This is especially beneficial for quantitative analyses since spectra can be further processed (such as spliced together or low-loss deconvoluted [132]). It is also possible to acquire two spectra with different energies of the loss region enabling a signal collection of element combinations that have large differences in energy. The way how the spectrometer CCD is read out is crucial for STEM-EELS spectrum imaging (SI). A SI is a data type where a STEM image (BF, ADF, HAADF or a suitable combination) is recorded pixel by pixel. The control over the beam (X and Y positioning and the exposure time for each pixel) is defined by the investigated area and the acquisition time(s) for a single EEL spectrum, a DualEELS spectrum, an EDX spectrum or a suitable combination of them. In this way a data cube is produced where spatial information (X and Y axis) is correlated with spectroscopic information (Z axis) on a per pixel basis [62]. It is possible to perform the readout of the CCD in two different ways: software synchronized and hardware synchronized. In the software synchronized mode all necessary timings for positioning of the beam, the exposure times for the spectra and the read out of the CCD are controlled by the steering software. This means that a considerable amount of time overhead can be present for each pixel due to the time needed for communication and data transfer. This increases the total acquisition time. Such a read out mode is not favorable for e.g. beam sensitive materials where a total short dwell time per pixel is necessary. In the hardware synchronized mode the necessary timing signal is steered by the CCD. This means that as soon as the exposure time is reached the CCD triggers the re-positioning of the beam on the subsequent pixel, necessary beam blanking, change of

voltages, read out of STEM detectors... This allows reducing the total acquisition time significantly. To reach the speed of 1000 spectra/sec the CCD read out mode has to be changed from high quality to high speed. Both read out mode differ significantly from each other. In the high quality read out mode the spectrum (DualEELS spectra) are read out individually. This means that after each exposure a certain time is necessary to shift the spectrum from a central position on the CCD to the side (top and bottom for DualEELS) of the CCD and perform an analog to digital conversion. In the high speed mode the spectrum is shifted away from the exposed region. This shift is dependent on the used binning. After the shift a new spectrum is acquired. In this way are the individual spectra “stacked” in not exposed areas of the CCD. When a spectrum reaches a side of the CCD (top and bottom for DualEELS) it is read out and digitalized. This mode allows for a faster read out of the CCD at the cost of precision.

6.6.3 EFTEM imaging

By having a post column-energy filter one has not only the option to perform EELS measurements but also record energy filtered TEM images (EFTEM imaging) as described in section 6.3. In this mode the currents of the multipole lenses are modified to project a TEM image onto the CCD. The actual energy filtering is achieved by inserting the slit into the optical path, thereby selecting electrons of certain energies. This allows improving image quality of BF images or diffraction images by omitting electrons that experienced an energy loss (zero loss filtering) as they contribute contrast due to chromatic aberration [62] as described in section 6.3. Furthermore, one can obtain images with material specific contrast, i.e. elemental maps, or to create maps with analytical information of electrons with different energy losses (EFTEM-SI) [133]. The benefit of EFTEM imaging is that a relatively large area can be imaged. However, with increasing energy loss the recording time increases and TEM specimen drift and beam damage can become severe [55].

6.7 Characteristics and analytical aspects of EELS

Figure 19 shows the most prominent features of an EEL spectrum comprising the low loss region and the high loss region. The low loss region comprises the intense zero-loss peak (ZLP) containing electrons with “no” (i.e. usually 0 – 10 eV) energy loss and the plasmon peak which is the collective oscillation of the free electron gas of a material [62].

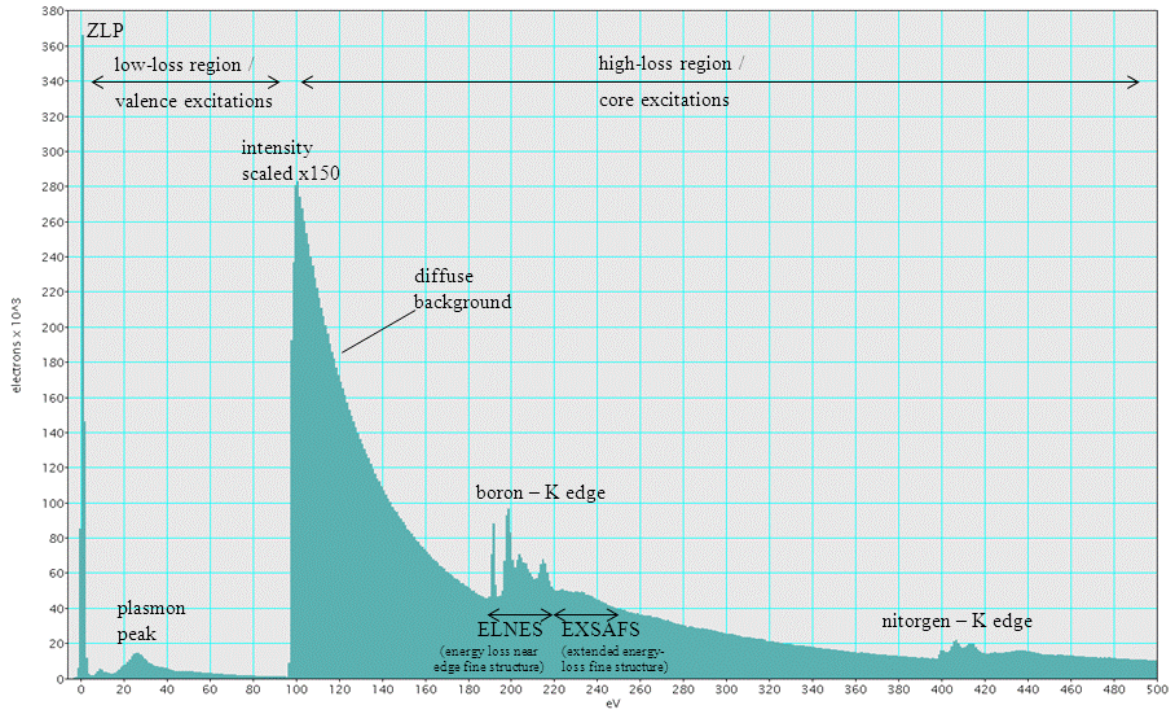


Figure 19: Most prominent features of an EEL spectrum (taken from [134] and modified; © Gatan).

The high loss region contains the element specific edges superimposed on a diffuse, exponentially decaying background. Edges themselves can be split up into the energy loss near edge fine structure (ELNES) and the extended loss fine structure (EXAFS) as shown in Figure 19 [56,135]. ELNES allows gaining information about bonding and valence states whereas EXAFS provides information about interatomic distances and coordination numbers [130]. It is possible to improve the energy resolution of a spectrum by a monochrome electron beam as mentioned in section 6.4. If the electron beam is satisfyingly monochrome a mapping of the energy loss near edge fine structure is possible [108]. Figure 20 shows a comparison between a non-monochromated acquisition of the Fe L_{23} edge and a monochromated one using the Tecnai F20 microscope in Graz. The FWHM of the ZLP in the non monochromated case was ~ 1 eV whereas the FWHM of the ZLP in the monochromated case was ~ 0.3 eV. Only in the monochromated case a subtle split-up of the Fe L_2 edge into two separate peaks is observable (left and right of 724 eV energy loss). The signal in the monochromated case is noisier originating from the lower beam current.

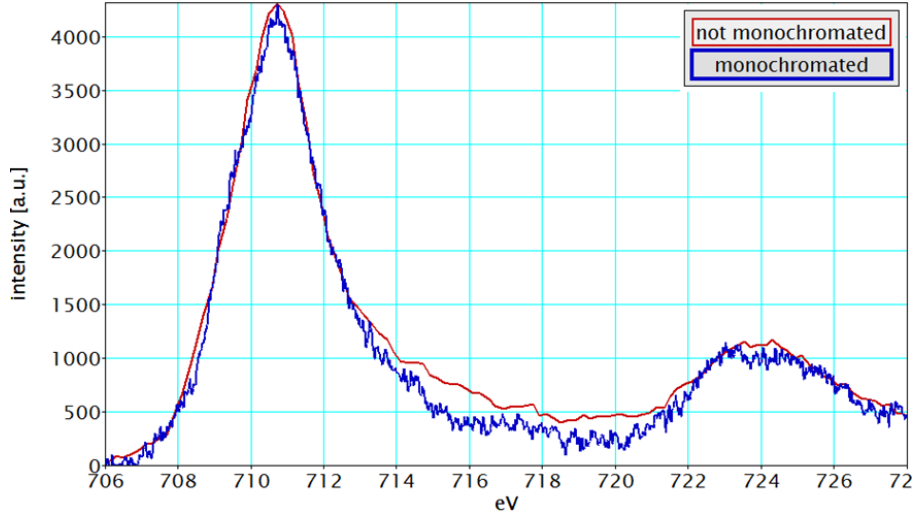


Figure 20: Comparison between a monochromated and a not monochromated recording of the Fe L_{23} edge of Fe_3O_4 nanocrystals; the monochromated spectrum reveals a fine structure of the Fe L_2 edge.

Quantitative evaluation of spectra with high sensitivity for low concentration elements is one of the benefits of EELS [62]. To do so EELS puts higher demands on TEM specimen thickness compared to quantitative EDXS analyses. With increasing TEM specimen thickness a diffuse multiple scattering is added to the spectrum as increasing diffuse background which increasingly hinders deeper analysis. Therefore not the absolute thickness of a TEM specimen ROI is important firsthand but the t/λ value which is a quotient of the usually unknown absolute specimen thickness t over the inelastic mean-free path λ_i . The t/λ value is computed as [62]:

$$\frac{t}{\lambda_i} = \ln\left(\frac{I_t}{I_0}\right) \quad (6)$$

with t being the absolute thickness, λ_i the inelastic mean free path, I_t the total intensity in the spectrum and I_0 the zero-loss peak intensity.

For best analytical results, the t/λ should therefore be around 0.5 [56,135]. The t/λ value can also be calculated from images allowing a determination of this value for a ROI. Hereby an unfiltered (representing I_t) and a zero-loss filtered image (representing I_0) are recorded and processed according to formula (6). This generates rather quick maps with a t/λ value in each pixel. If scattering cross sections are well known through theoretical calculations or preferably through experimental measurements, a relative quantification in at% of the various constituents is possible through [62]:

$$\frac{N_X}{N_Y} = \frac{I_X(\beta, \Delta_1)}{I_Y(\beta, \Delta_2)} * \frac{\sigma_Y(\beta, \Delta_2)}{\sigma_X(\beta, \Delta_1)} \quad (7)$$

with N_X , N_Y are the relative concentrations of element X and Y, $I_X(\beta, \Delta_1)$, $I_Y(\beta, \Delta_2)$ the background subtracted intensities for element X and Y, $\sigma_X(\beta, \Delta_1)$ and $\sigma_Y(\beta, \Delta_2)$ the cross-sections of element X and Y. β denotes the dependency of the collection angle and Δ the size of the used energy window.

If the zero-loss is recorded in addition an absolute quantification in number of atoms per nm² can be performed:

$$N_x = \frac{I_x(\beta, \Delta)}{I_L(\beta, \Delta)} * \frac{1}{\sigma_x(\beta, \Delta)} \quad (8)$$

with $I_L(\beta, \Delta)$ being the intensity of the zero-loss peak.

If the measurement conditions are appropriate and the partial cross sections are well known absolute quantification of trace elements down to the ppm region is possible [56].

A more detailed theoretical description of the quantification of EEL spectra is given in [62,130].

6.8 Energy dispersive X-ray spectroscopy

Energy dispersive X-ray spectroscopy (EDXS) is an analytical technique used for elemental analysis or chemical characterization [136]. It is commonly used in scanning electron microscopes and transmission electron microscopes. An X-ray is generated by an incident beam electron exciting a core-electron into an unoccupied state of an atom while the incident electron loses an element specific amount of energy. In EELS this electron is subsequently analyzed whereas in EDXS the generated X-rays are detected as function of their energy. The X-rays are emitted nonspecificly regarding their angular distribution and only a fraction of them get collected by a solid state detector [62]. Typical detection materials are Si(Li), high purity Ge (HPGe) or silicon drift detectors (SDD). Within the detection material, electron-hole pairs are created and their amount is used to estimate the energy of the incoming X-ray photon [62,137]. The calculated energy of the photon is added as a count to an energy channel within the spectrum. A drawback is that the collection efficiency of EDXS detection systems are much lower compared to EELS systems due to several reasons [62]:

- X-rays are not emitted into a specific direction as in the case for EELS.
- Low-energy X-rays (generated by low Z materials; roughly emission energies below 1 keV) can easily be absorbed within the material or within windows or layers in front of the detection material.
- The actual detection area is rather small.
- Energy conversion is rather an estimation than a precise measurement (precision > 130 eV).
- Artifacts within the spectrum (escape peaks, sum peaks, fluorescence peaks of Si or contact layer etc.) can complicate data evaluation.

EDXS however, has the advantage of tolerating thicker TEM specimens compared to EELS. By mounting several EDXS detectors around the TEM signal collection becomes more efficient. This is commercially available as ChemiSTEM® Technology within some of the FEI transmission electron microscopes. Compared to single detector systems, the larger effective detector area of the ChemiSTEM allows acquiring the same amount of counts within a shorter time or more counts within

the same time. A difficulty regarding quantification is that now several detectors generate the spectrum. Therefore care has to be taken since detectors can be shadowed by the TEM holder itself or a tilted TEM specimen. Therefore, some of the detectors might only collect X-rays with higher energy or fewer counts compared to other detectors. The EDXS detectors can also have differences regarding their detection characteristics. The sum of these effects can lead to erroneous quantification values. As an advantage, however, it has been demonstrated that atomic resolution within elemental maps is possible by acquiring EDXS signals [138].

To obtain quantitative results with EDXS the relatively new ζ -factor method has been used within this work [139]. This method overcomes two major limitations of the conventional Cliff-Lorimer method [140]:

1. It allows the use of multielement, thin-TEM specimen standards rather than pure-element standards.
2. It includes a built-in X-ray absorption correction with simultaneous thickness determination.

These two aspects allow a more precise quantification of especially light elements. The calculation is given by:

$$\rho t = \sum_j^N \frac{\zeta_j I_j AC_j}{D_e}, c_a = \frac{\zeta_A I_A AC_A}{\sum_j^N \zeta_j I_j AC_j}, \dots, c_a = \frac{\zeta_N I_N AC_N}{\sum_j^N \zeta_j I_j AC_j} \quad (9)$$

with ρt denotes the mass thickness (ρ is the density and t the thickness), ζ_x the proportionality factor, I_x the intensity of the characteristic X-ray line of element X and AC_x the absorption correction term of the element X.

The necessary ζ -factors can be either calculated on a theoretical basis or using a standard. Hereby pure element standards or a multi element standard such as the NIST SRM 2063a standard can be used. The ζ -factors used within this work have been experimentally determined for a Tecnai 200 kV instrument installed at the FELMI in Graz [141,142]. It is necessary to iteratively solve equation (9) for composition and thickness, with the resulting mass-thickness being used for the next absorption correction term. It is straightforward to do this and the equation converges very quickly (usually 10 – 15 iterations) until a precision of less than 0.001 wt% in the composition differences and 0.01 nm for the TEM specimen thickness are obtained.

6.9 STEM image simulation using multislice

Simulating images of high resolution, both for TEM and STEM, is a widely used technique to complement, compare and interpret experimental data [143–147]. To describe the interaction of an electron with a crystal one has to solve the Schrödinger equation [62]:

$$\left[-\frac{\hbar}{2m} \nabla^2 - eV(\vec{x}) \right] \psi(\vec{x}) = E\psi(\vec{x}) \quad (10)$$

with $\psi(\vec{x})$ being the wave function of the electron at the position \vec{x} , \hbar being Planck's constant, m being the electron mass, $e = |e|$ being the magnitude of the charge of the electron, E being the total energy of the electron and $-eV(\vec{x})$ being the potential energy of the electron.

This equation describes the behavior of the electron by its quantum mechanical wave nature within the potential of a crystal. One of the most important approaches for simulating finite thickness materials is the multislice method [148]. The first theoretical description thereof was given already in 1957 by Cowley and Moodie [149]. The multislice method simulates the interaction of an electron beam with matter, including all multiple elastic (and recently inelastic) scattering effects. This is done using a plane wave approach for conventional HR TEM images or as a small focused probe at each position of the specimen for HR STEM images. For the simulation a crystalline specimen is approximated by dividing it into many thin slices [148]. The term “thin” in this context means that the interaction of the electron beam can be approximated as a simple phase shift of the electron beam [144]. The amplitudes and phases of all beams which are generated by the incident beam(s) interacting with a single slice are calculated. The electron beam is then transmitted between the individual slices in near field diffraction (Fresnel diffraction) within the vacuum [79]. As a result, the multislice method can be reduced to a sequence of transmit and propagation operations, which can be efficiently handled via the Fast Fourier Transformation (FFT). Thereby the mathematical problem scales with:

$$N \cdot \log(N) \quad (11)$$

with N being the number of Fourier components.

This allows increasing the resolution with a reasonable increase of computed Fourier components. So far the vibration of the atoms around their equilibrium position (i.e. thermal diffuse scattering, TDS) has not been taken into account. This is necessary as the STEM signal consist to a large part of TDS [143]. With the inclusion of the frozen phonon model [148] on each position of the beam many features observed in the thermal diffuse background of STEM images can be simulated [79,150].

6.10 Electron trajectory simulation in materials

Information about the electron beam trajectories within a material is a very helpful tool for planning or evaluating electron microscopical investigations [151]. It allows estimating a variety of parameters e.g.: beam spreading, interaction volume, mean free path of electrons or the spatial resolution of X-ray analysis. These information are important for both, SEM and TEM investigations (not necessarily all at once) [62,152]. The simulation of the individual electron trajectories is performed using the Monte Carlo method [153]. Thereby random numbers are used to predict the scattering angles of an electron through a solid. The quality of the simulation depends on the accurate description of the physics behind the scattering events and taking into account a large enough number of electrons for the simulation [153]. Today these processes are well enough understood and desktop computers are powerful enough to perform such a simulation within a short time [151].

7. TEM Specimen preparation

In order to be able to achieve desired results through TEM investigations a precise control over the TEM specimen² fabrication is important [62,154]. Furthermore, the required resolution is achieved only for ultra-thin samples with amorphous-free surfaces. It is easily possible to introduce preparation artifacts during thinning which later leads to an artificial interpretation. Many techniques for the preparation of TEM specimens for transmission electron microscopy exist such as polishing/ion-milling of cross-sectional TEM specimens, electropolishing, extraction replication, wedge polishing, site specific focused ion beam (FIB) milling, drop casting of dispersed particles, cleaving of semiconductors and many more as described in [154]. Within this thesis only techniques applicable to the investigated materials are mentioned and possible ways how to overcome difficulties are described.

7.1 Specimen preparation of nanocrystals

The fabrication of appropriate TEM specimens to investigate cubic nanocrystals was rather straightforward. The particles have been in vials dispersed within toluene as depicted in Figure 21a).

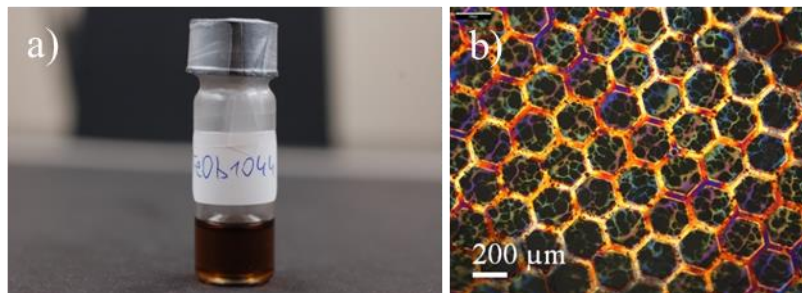


Figure 21: a) As-received vial containing particles (here Fe_xO_y) dispersed in toluene; b) light microscope image of a particle covered Formvar-film after particle deposition.

However, suitable TEM specimens of these nanocubes could not be prepared by simply drop-casting the solution on a holey Formvar-covered TEM copper grid due to the dissolution of the Formvar film through toluene. To obtain a usable TEM specimen the solvent had to be removed faster from the Formvar film. This was done by placing the TEM copper grid on a filter paper, which was lying on a hotplate at 50 – 60°C. 1 – 2 μl of solution were then drop-cast onto the TEM copper grid. Thereby the solvent is drawn away quickly by the filter paper and the remnants on the TEM copper grid evaporate, faster than the complete dissolution of the Formvar film. Some amount of Formvar film was dissolved but as depicted in Figure 21b) a sufficient part of the film was still intact. Also this type of TEM

² Note: Within this work “sample” means a certain example material that is investigated. The term “TEM specimen” denotes a processed fraction of this example material which can be used for electron microscopical investigations.

specimen preparation ensures that all elusive remnants of solvent or other hydrocarbons were evaporated. This was beneficial for lowering the carbon contamination during TEM investigations.

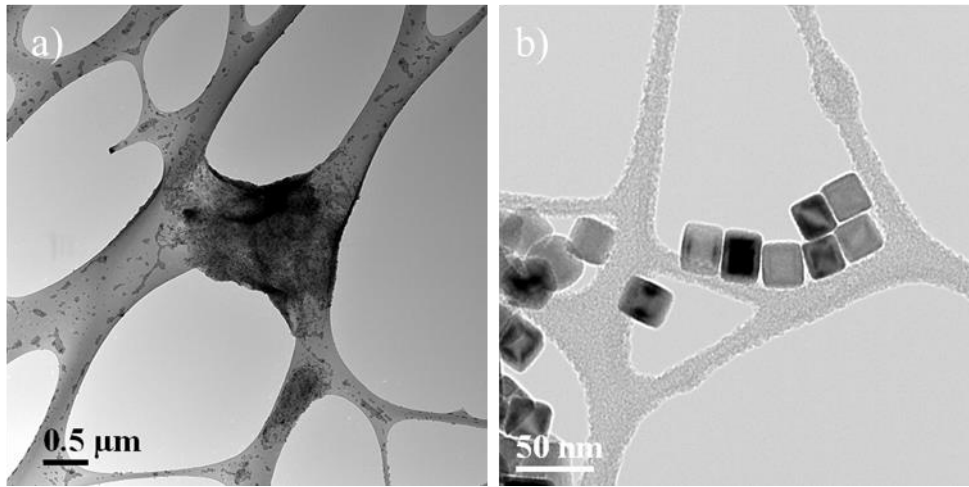


Figure 22: a) BF overview image of sufficient particle coverage on a Formvar-film covered TEM copper grid; b) BF image showing particles, in this case core-shell particles, in more detail with a few of them being attached to the Formvar film only on one side.

The TEM copper grids with the Formvar film exhibited sufficient coverage with particles as shown in Figure 22a). Figure 22b) depicts that a few particles were only attached with one side to the thin Formvar net making them ideal candidates for analytical investigations.

7.2 Specimen preparation of GaN

GaN grown on (0001)-sapphire is a challenging material combination. Sapphire constitutes a hard and brittle substrate, on which a delicate GaN layer has been grown. The lattice mismatch between sapphire and GaN creates internal strain [155]. A thin section of this material combination can fracture easily due to this strain.

7.2.1 Standardized TEM specimen preparation

As a starting point a standardized cross section preparation technique was applied. Two sample pieces with the GaN layers facing each other were glued together using G1 resist (© Gatan Inc.). The sandwich was then cured for 10 min at 130°C on a hotplate and subsequently cut with a diamond wire saw to appropriate dimensions in order to fit the stack into a sapphire tube (inner diameter: 1.8 mm; outer diameter: 3 mm). The sapphire/GaN stack was then embedded with semi-circular sapphire spacers inside the sapphire tube using G1 resist. Figure 23a) shows a schematic cross section of the setup. A ~0.5 mm thick slice was then cut from this tube and attached to a disc grinder (model 623, © Gatan Inc.) using a thermal resist.

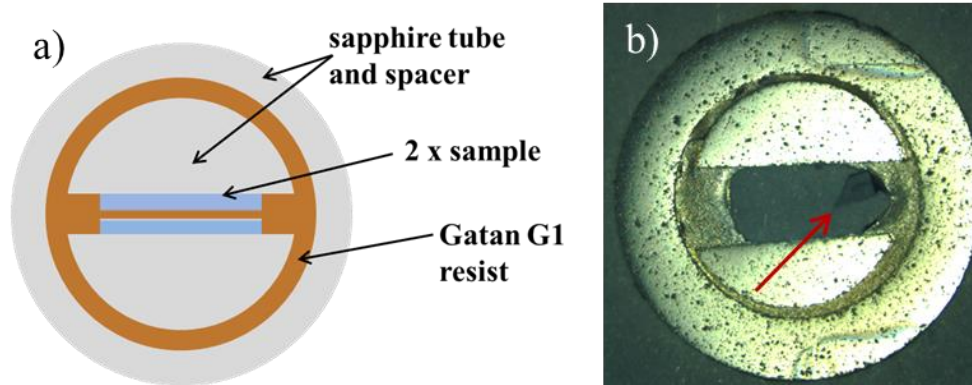


Figure 23: a) Schematic setup of the standardized cross-section preparation technique; b) broken out sample-layers during Ar-ion thinning (red arrow indicates sample-debris).

The first side was flattened with diamond covered abrasive discs with diamond sizes of 30 μm and 15 μm . During the procedure both discs were rinsed with water to wash away milling debris. In-between the polishing steps, the polished surface of the sample was checked with a light microscope. Polishing of the sample surface was performed using a motorized grinder equipped with polishing clothes were 6 μm and 0.25 μm diamonds (“DP-Spray” from Struers GmbH) were deposited. The rotating speed was set to 250 rpm for the 6 μm diamonds and 500 rpm for the 0.25 μm diamonds. The water flow was adjusted such that a sufficient gliding of the manually held disc grinder was obtained. At roughly 1 min. intervals the result of the surface polishing was checked on a light microscope. After obtaining a mirroring surface the sample was dismantled from the grinder by dissolving the thermal resist in acetone. The second side of the sample was polished in the same way subsequently, as described above with the additional goal to reduce the overall thickness of the specimen to preferably 120 μm . The obtained sample thickness was checked with an optical InfiniteFocus microscope (© Alicona Imaging GmbH). In the next step, the sample was mounted onto a dimple grinder (Model 656 from Gatan Inc.) using a thermal resist. After adjusting the total TEM specimen height (TEM specimen together with thermal resist) and centering the sample rotation a 6 μm diamond paste (DP-Paste P from Struers GmbH) diluted with de-ionized water was applied to abrade a dimple into the specimen area containing the layers of interest. The setup of the dimple grinder was chosen such that the abrasion stops automatically at a final ROI thickness of preferably 15 μm . Due to the coarse nature of the machine a more precise thickness control was not possible. After finishing the process TEM specimen and dimple grinder were rinsed off with de-ionized water to remove the whole abrading medium and sample remnants. A final polishing step using a 0.25 μm diamond past (DP-Paste P from Struers GmbH) was performed to remove coarse scratches. After 5 min the polishing was stopped and the sample was dismantled. A final rinsing step using de-ionized water, acetone and toluene was carried out to ensure cleanliness of the sample. Thinning down to electron transparency was performed using a precision ion polishing system (PIPS, © Gatan Inc.) at an ion accelerating voltage of 4 keV and 6° incident angle. This yielded no usable TEM specimens due to the break out of both sample-layers during the thinning process. An example is shown in Figure 23b) as indicated by

the red arrow. The reason therefore was found to be a too large amount of G1 resist filling up gaps between actual sample layer and sapphire spacers as visible in Figure 23b). The resist cannot withstand the ion-bombardment long enough to provide support until the sapphire/GaN layers become thinned. Due to the large dimensions of the ion beam produced by a PIPS (~1 mm in diameter on the sample) compared to the total diameter of a TEM specimen (3 mm) an un-intentional thinning of the resist cannot be avoided. To obtain usable TEM specimens a modification of the geometry was necessary. The amount of G1 resist filling up spaces between sample-layers, spacers and confining ring was reduced. Furthermore, an improved heat and current conductivity (for subsequent TEM investigations) was required. In the resulting setup only one sapphire/GaN sample layer was mounted between four 0.7 mm thick Si/SiO_x-spacers. The Si/SiO_x spacers (dimensions: 4 x 5 mm) were cut from a standard wafer used in device production. The polished sides of the Si/SiO_x spacers face towards the actual sample. G1 resist was again used for bonding and the stack was compressed with a specimen clamp vise from the Gatan Cross Section Kit (Modell 601.07000) as shown in Figure 24a). After curing the resist for 10 min at 130°C on a hotplate a cylinder was cut out from the stack as depicted in Figure 24b) using an ultrasonic disc cutter (Model 601 from Gatan Inc.). SiC (Part No. 601-06-030; Gatan Inc.) dissolved in de-ionized water was used as cutting medium.

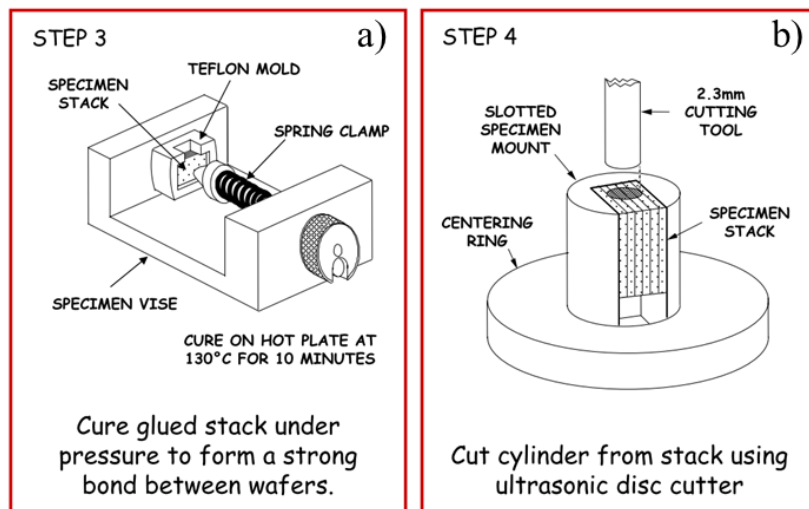


Figure 24: a) Schematic drawing of the stack being glued together; b) cutting out of a cylinder from the glued sample-stack; both drawings taken from the manual for the Model 601.07000 Cross Section Kit from Gatan Inc. and modified.

The obtained cylindrically shaped stack (~2.3 mm diameter) as shown in Figure 25a) was then glued with G1 resist into a brass cylinder (3 mm outside diameter). The inner hole of the brass cylinder was ~2.5 mm to have enough space for insertion of the cylindrically shaped stack.

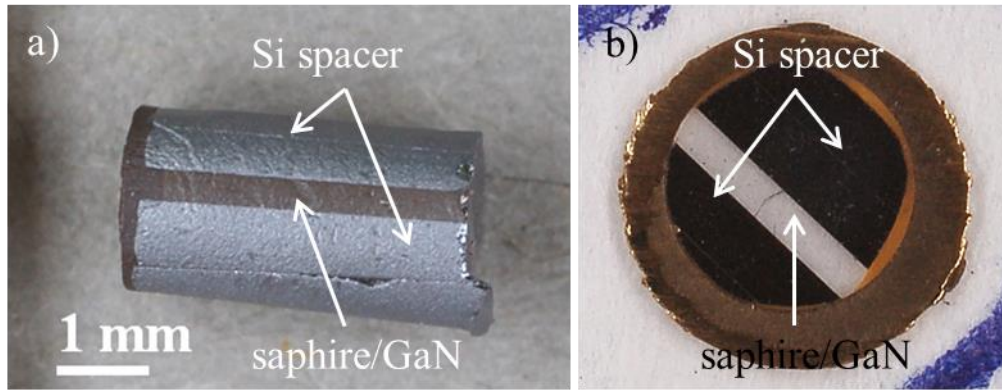


Figure 25: a) Cut out cylinder with Si spacers and sapphire/GaN layer; b) sample after finishing the polishing steps (before dimpling step) with indication of the various layers.

Further processing, flattening and polishing of first and second side, was performed according to the standardized recipe described above. TEM investigations revealed that the obtained electron transparent areas were rather thick with a t/λ value between 1.5 and 2 as shown in Figure 26.

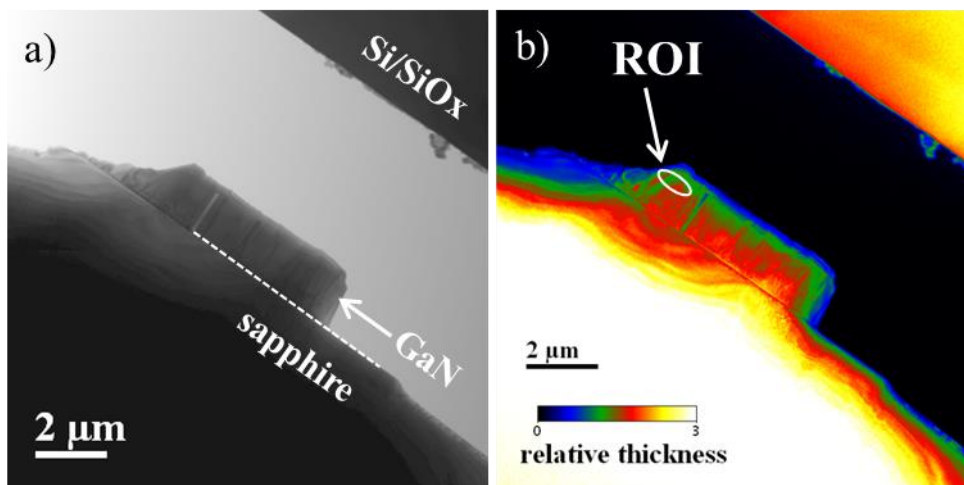


Figure 26: a) BF image of an electron transparent region of GaN; b) corresponding thickness map (t/λ map) showing a rather high thickness-value of 1.5 – 2 in the RIO.

Ultimately it was possible to pin down two reasons for this non-satisfying result. First the rather large distance between the Si spacer and the GaN layer of roughly 5 μm, as shown in Figure 26a), resulted in an insufficient protection of the GaN by the Si counterpart. During PIPS thinning the ions hit the GaN edge-on thereby sputtering away thin areas. A second reason was remaining scratches on the sample surface. Due to the coarse steps during the dimpling process (from 6 μm to 0.25 μm) remnant scratches were not polished away. Figure 27a) shows an AFM height image of the sample surface after the dimpling process was finished. Long scratches across the image can be seen in Figure 27a) which originates probably from the grinding using 0.25 μm diamonds. The scratches arranged in circular manner were caused by the dimpling process. Figure 27b) depicts the situation in more detail. The white arrows indicate remnant GaN debris adhered to the TEM specimen surface. This debris could

not be removed by rinsing the TEM specimen with de-ionized water, acetone and isopropanol. Figure 27c) contains a local contrast image which visualizes more clearly the enormous amount of surface-damage. Figure 27d) is a height measurement across the dimpling crater indicated by white a dashed line in Figure 27a). This graph shows that the deepest scratches exhibit a depth of ~ 30 nm but due to the enormous number such a surface was not ideal for further processing.

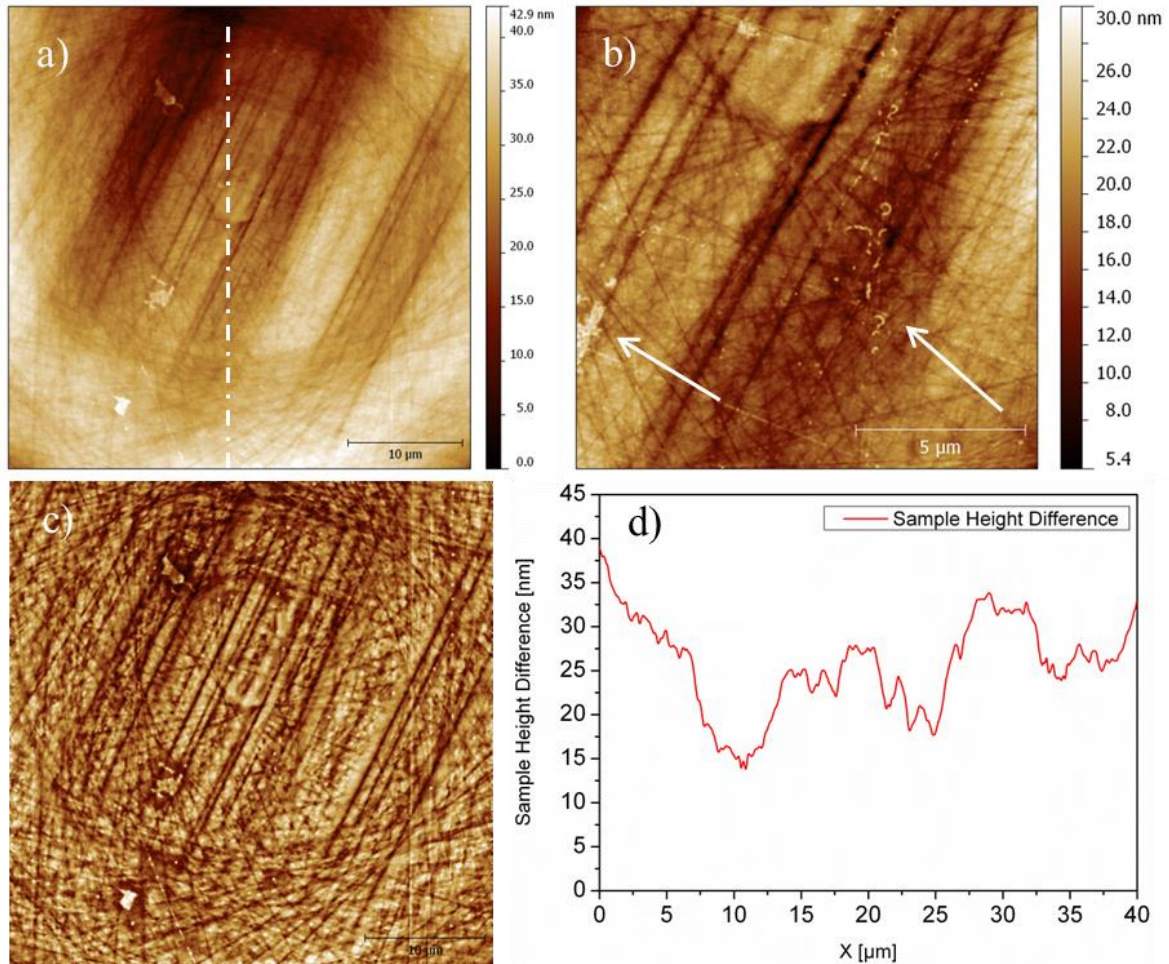


Figure 27: a) AFM height image of a GaN TEM specimen after finishing the dimpling process; it exhibits long, straight scratches originating from the polishing and circular-formed scratches from the dimpling process; b) detailed view of a) with white arrows indicating GaN remnants on the surface; c) local contrast image for better visualization of the amount of surface-modification; d) height-measurement from a) (indicated by white dashed line in a) to determine the depth of the scratches.

Such scratches lead to preferential etching within the dimpled region. The ions hit the surface not in a low angle but rather head-on due to the indent of the scratch. As a result material within the vicinity of the scratch will be milled away faster than flat, less scratchy areas making even thinning impossible [156].

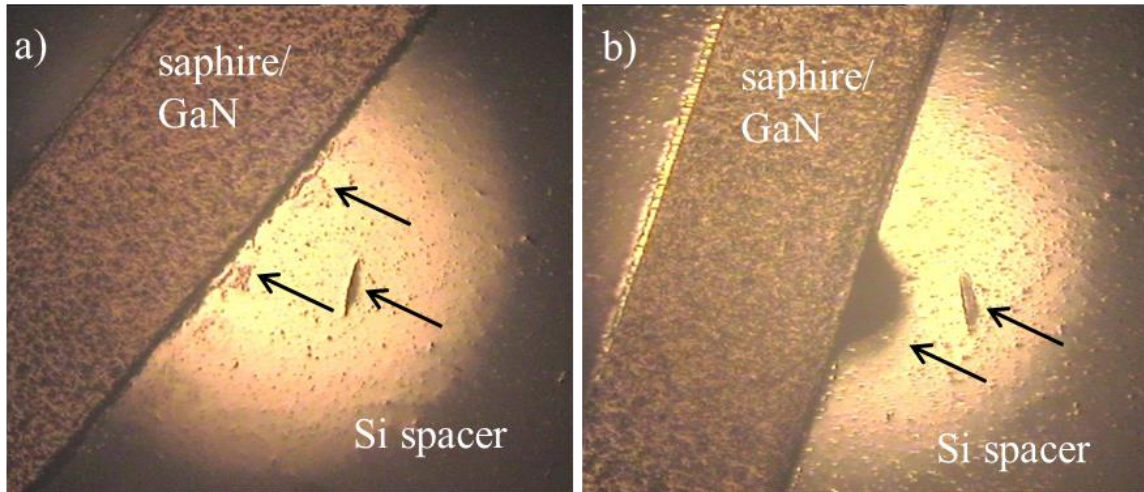


Figure 28: a) Light microscopy image of a sample before PIPS ion milling at 4 kV, the arrows indicate large scratches which are surrounded by smaller indentations; b) after 150 min PIPS milling at 4 kV became the scratches enlarged or a hole (indicated by arrows).

Figure 28a) shows a light microscopy image of a test TEM specimen before PIPS ion thinning at 4 kV. The arrows indicate larger scratches which are surrounded by smaller indentations. Figure 28b) shows that the scratches and indentations have been preferentially etched leading to a faster appearance of a hole (indicated by arrow).

7.2.2 Focused ion beam processing of GaN

Focused ion beam (FIB) processing is a very popular and frequently used technique to obtain electron transparent TEM specimens [157]. Its advantages are to be very site selective and fast in combination with the ability to visualize the area of TEM specimen extraction beforehand by using the electron source [157]. FIB processing of GaN samples has been performed using a Nova 200 from FEI Company at FELMI. In this it is possible to deposit protective Pt, mill with Ga-ions and visualize the processing with ions or electrons. Before cutting out the lamella by the lift out technique, the surface is covered by a 2 μm thick Pt protection layer. Unfortunately the FIB technique has some disadvantages for the TEM specimen preparation of GaN. As mentioned in section 7.2.1 surface amorphization during thinning is one of the major problems especially for HR-TEM investigation and accuracy of analytical investigations [158–160]. The FIB thinning process at FELMI is stopped at 5 kV accelerating voltage of the Ga ions with incident angle of 4° at a current of 70 pA. This leaves the surface on both sides of the lamella modified, with the depth of damage being material dependent [158,161]. If such TEM specimens are intended to be used for HR-TEM or STEM measurements and investigations the amorphized material at the surface has to be removed. Another disadvantage of this type of processing is that during milling the lamella is often bend. This bending is unavoidable and further processing of such a lamella leads to regions with slightly different orientations and thicknesses in the fully processed lamella as shown in Figure 29a).

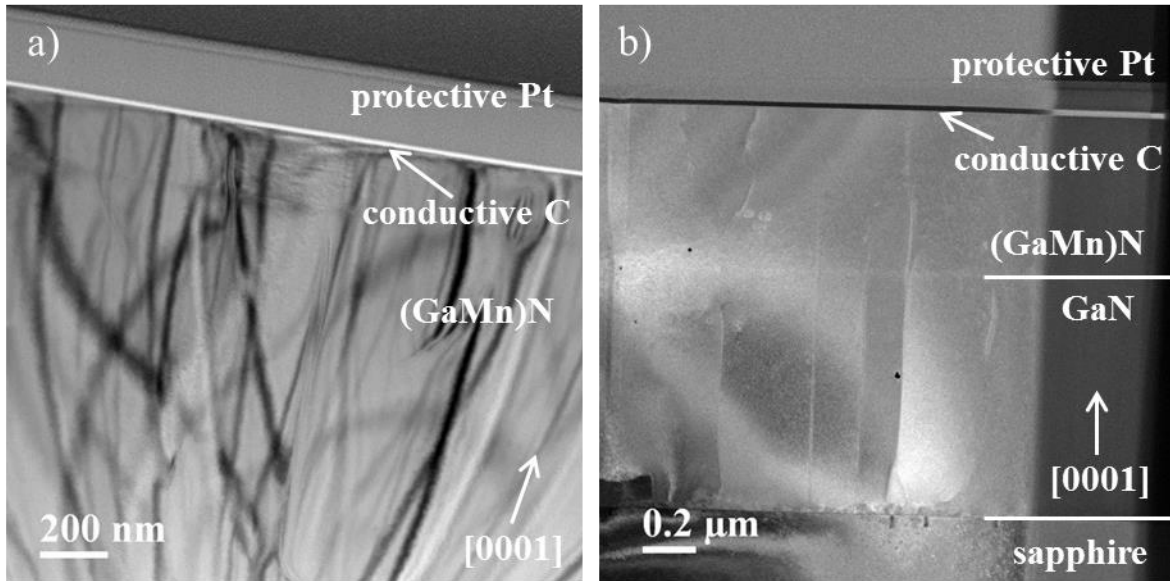


Figure 29: a) BF image of a GaN/(GaMn)N layer exhibiting bend contours; b) ADF image of the same lamella exhibiting different contrast due to different orientations and surface amorphization. Dislocations, which are visible as bright vertical lines, pass through both GaN layers.

This situation provides challenging conditions for HR-TEM and HR-STEM imaging which often requires precise orientation into a zone axis of the lamella. As a result only very small areas can be properly oriented towards the electron beam and re-orientation needs to be carried out if the investigated area is changed. Figure 29b) shows a ADF image where slight deviations from the zone axis are observable. This can be seen as varying contrast between adjacent areas caused by diffraction changes. Furthermore, surface amorphization is observable as a diffuse, cloud-like layer across the whole TEM specimen. Surface amorphization is usually removed by low energy polishing with Ar ions. At the time of this thesis this has not been possible with FIB lamellas at FELMI. During a measurement visit at the Ernst Ruska-Centre in Jülich, Germany it was possible to fabricate FIB lamellas of iron-doped GaN with a Helios NanoLab 400s from FEI using the lift-out technique. Processing of the lamella was stopped at 5 kV accelerating voltage of Ga-ions. Next a low energy ion system NanoMill from Fischione Instruments was utilized to remove remaining surface amorphization. The term “low energy” in this context is very material dependent and means for GaN on sapphire that one cleaning step at 900 eV for 10 min and one final polishing step at 500 eV for 15 min were performed. Both steps were carried out between 10° – 15° incident angle with a beam current of roughly 100 μA. After each polishing step a TEM investigation in a Tecnai 200 kV FEG instrument was undertaken to visualize the amount of amorphous material left. Based on the result it was decided about further cleaning. The significant improvement of the TEM specimen quality can be seen within BF images, shown in Figure 30. The top row shows an overview of the FIB lamella where a damaged surface is clearly visible in Figure 30a) as a cloud-like deposit. The white arrows indicate the ROI containing iron-rich nanocrystals. After 4 cleaning steps the BF image shows the strong reduction of amorphous material on the surface (Figure 30b). Figure 30c) and d) show the reduction of

the surface amorphization in more detail with insets displaying FFTs of GaN where more reflections with greater distance from the center and less diffuse background can be observed.

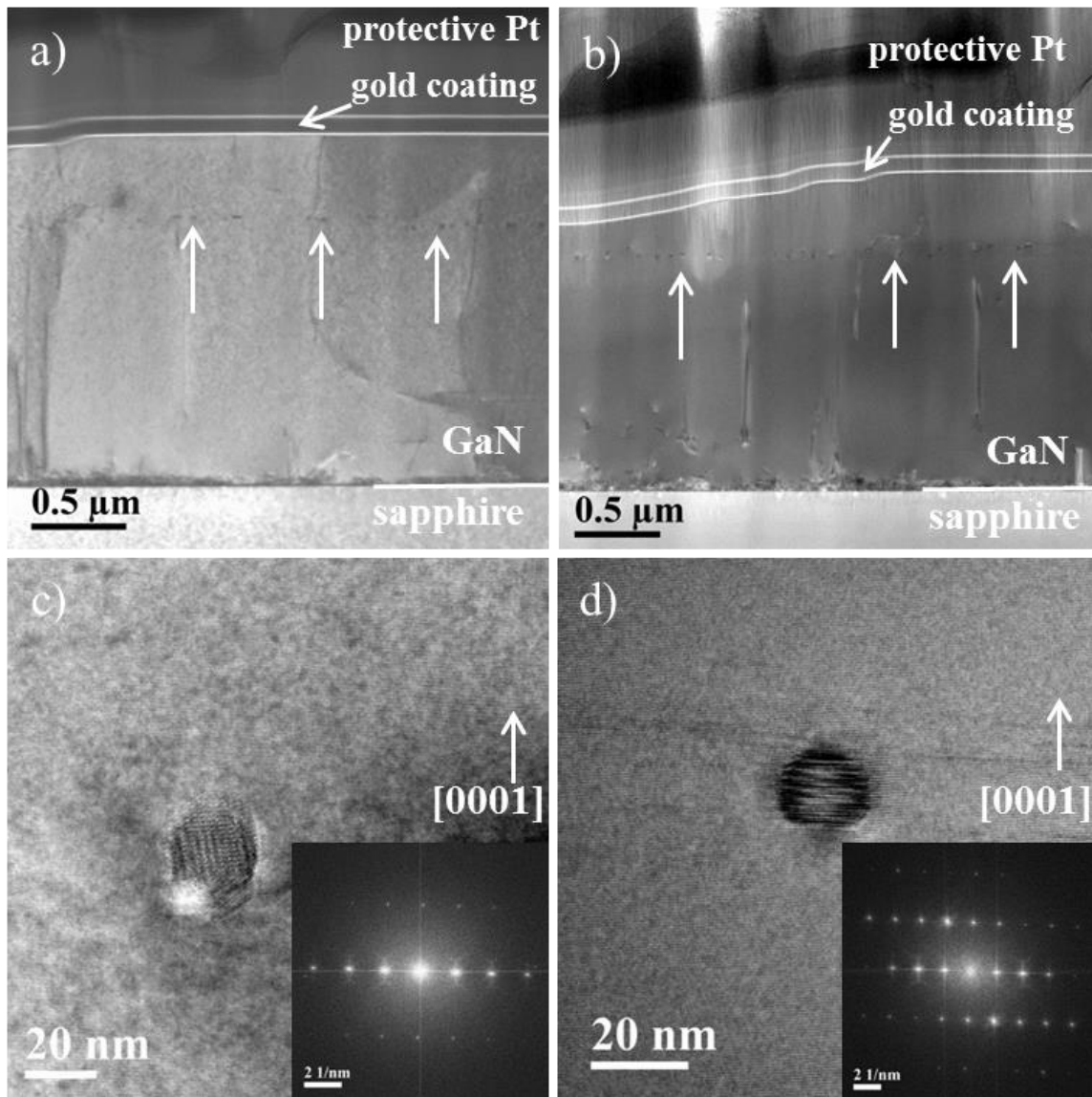


Figure 30: BF overview images of: a) FIB lamella before and b) after 4 polishing steps using a NanoMill; white arrows indicate ROI containing iron-rich nanocrystals; c) nanocrystal embedded in GaN exhibiting a considerable amount of surface amorphization; inset: FFT of GaN with diffuse background through amorphization; d) nanocrystal after cleaning the TEM specimen where considerably less surface amorphization is observable; inset: FFT of GaN with extended information limit. The figures c) and d) were composed by the author of this thesis and taken from [42].

It could not be excluded that an implantation of Ga ions took place during FIB processing thereby modifying the Ga content within the TEM specimen [162]. To avoid difficulties, TEM specimens produced by means of FIB, were only used for imaging purposes but not for quantitative measurements.

7.2.3 Wedge polishing of GaN grown on sapphire

A semi-automated wedge polishing machine (MultiPrep Polishing System; Allied High Tech Products Inc.) with an 8" platen was used to prepare TEM specimens by mechanical wedge polishing. This method provided a fast and simple procedure for the specimen preparation for TEM. A detailed method description for the specimen preparation of GaN and other materials are described in the diploma thesis by Sabine Neumayer [163]. This includes the following steps:

- Initial cutting using a diamond wire saw (dimensions roughly 3 x 2 x 0.5 mm).
- Attachment sample holder.
- Flattening and polishing of the first side.
- Turning of sample to process the second side.
- Polishing of the wedge with $\sim 3^\circ$ angle.
- Dismounting from sample holder and attaching to a TEM grid.

Figure 31a) shows a BF image of a fully processed wedge of (GaMn)N grown on sapphire. In Figure 31c) a more detailed image is presented with white arrows indicating debris material residing on the TEM specimen surface. This is one of the major limitations of wedge polishing of GaN grown on sapphire. Due to the strain within the material the thinnest parts tend to break off, typically in the thickness range suitable for analytical investigations using EELS (i.e. t/λ value < 1). Attempts to remove this debris by bathing the specimen in acetone and isopropanol have been without success.

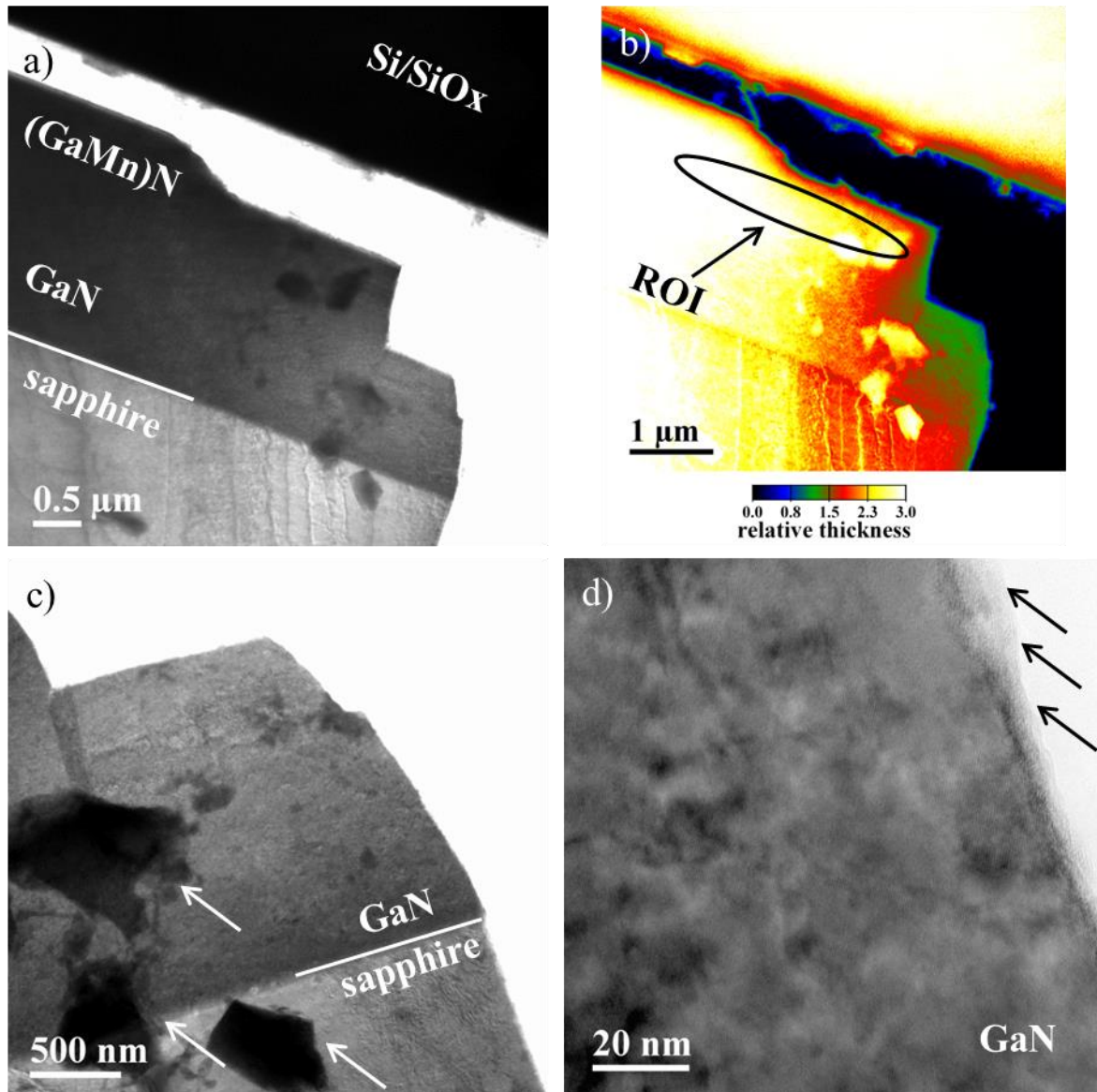


Figure 31: a) BF image of a wedge polished (GaMn)N; b) corresponding t/λ map showing rather high values in the ROI; c) more detailed image of a) with white arrows indicating debris material residing on the TEM specimen surface; d) HR-TEM image showing surface amorphization (indicated by black arrows) and surface modification.

Figure 31b) shows a thickness map (corresponding to Figure 31a) where only very small areas (less than 50 nm) were suitable for analytical investigations. Figure 31d) shows a HR-TEM image of GaN with severe surface modification (black arrows) at the specimen edge. All in all Figure 31 shows that wedge polished TEM specimens of GaN grown on sapphire exhibit two major limitations:

- Breaking-out of TEM specimen pieces during fabrication leading to a non-ideal TEM specimen thickness.
- Surface amorphization and modification.

In the future, with the help of low-energy polishing equipment utilizing a focused Ar-ion beam, for example as in a NanoMill (© Fischione) or a Gentle Mill 3 (© Technoorg Linda) it will be possible to remove the surface modification and amorphization.

7.2.4 Advanced cross-section preparation of GaN

To improve the quality of TEM specimens the buildup of the TEM specimen was changed such that 3 Si-spacers (2 on the GaN-side and one on the sapphire side) were glued together (using G1 resist) with as much pressure as possible to obtain a stack with roughly 3 mm side measures and 3 mm height. The pressure is generated using a small vise with Teflon-covered jaws as shown in Figure 32a). The Teflon coverage of the jaws helps to distribute the pressure evenly across the stack.

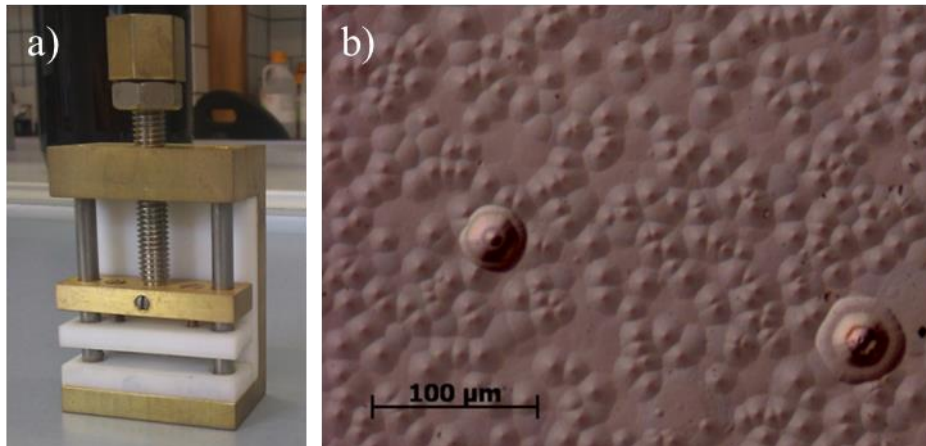


Figure 32: a) Vise with Teflon-covered jaws used for applying pressure; b) light-microscopy image of the overgrown (GaMn)N surface.

For an overgrown GaN sample surface, meaning that the surface exhibits an inhomogeneous height, special care has to be taken to the adhesion of the protective Si to the layers of interest. Figure 32b) depicts exemplarily observable height differences obtained during the growth of a (GaMn)N layer. Several cone-shaped pillars stick out of the (GaMn)N layer. These pillars cause an enlargement of the distance between the (resist filled) protective Si and the GaN-layer during TEM specimen preparation as described in section 7.2.1. During sandwiching of the protective Si with the actual sample sufficient pressure had to be applied on the whole stack (depicted in Figure 33a) to reduce the glue-filled gaps between the individual layers. If this distance was larger than 1 μm the Si could no protect the GaN layers during ion thinning. In this case, the GaN layers have been only protected by the resist which is eroded fastest by ions. Subsequently the sandwich got cut apart to obtain a roughly 1 mm thick cross-section. This 1 mm thick cross-section was then polished on one side using 15 μm , 3 μm , 1 μm , 0.5 μm and 0.25 μm lapping films until optical inspection of the polished surface showed no remaining scratches and a mirror-like surface. It was important that a high precision polishing system such as the MultiPrep System was used to ensure stability regarding amount of applied pressure, uniformity of pressure, uniformity of sample movement perpendicular to plate rotation to avoid preferential thinning and rotational flatness of the plate system. When changing from one lapping film to another material of at least twice of the grain size of the lapping film used before was removed with the subsequent lapping film (e.g. remove 6 μm material with 1 μm lapping film if 3 μm lapping film has been used before). This ensured the removal of all scratches and indentations caused by the prior

lapping film. The lapping direction was along the direction of the glue line between the sandwiched layers. This reduced the amount of hard material (sapphire or Si) which got removed during lapping to cause indentations within the delicate GaN layer. The polished side was then glued onto a molybdenum TEM slot grid to ensure mechanical stability using a Gatan G1 resist. Curing of the resist was performed on a hotplate at 150°C for 3 min. Subsequently, the slot grid/GaN setup was attached with epoxy-resin on a Pyrex stub of a MultiPrep system such that it was possible to polish the second, unprocessed side. The molybdenum slot grid acted as a spacer between the already polished side and the Pyrex-stub. Lapping and polishing was done in the same way as stated above. This time the thinning started with 30 μm to efficiently abrade material. This coarse first step intended to thin the sample down to a thickness of $\sim 50 \mu\text{m}$. With the thinning steps of 15 μm and 3 μm lapping films the sample layer thickness was reduced to $\sim 20 \mu\text{m}$ thickness.

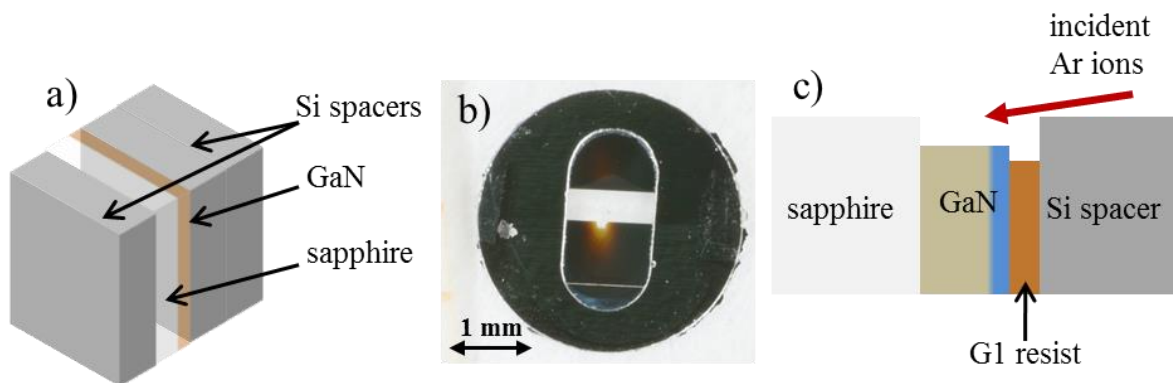


Figure 33: a) Schematic view of a glued stack; b) TEM slot grid with attached TEM specimen (after PIPS thinning); the Si spacers exhibit the brown-reddish color indicating a thickness of $\sim 10 \mu\text{m}$; c) schematic cross-section of Si protecting the GaN layer during ion-tinning.

The lapping was continued with 1 μm , 0.5 μm and 0.25 μm films until the Si became translucent in a brown-reddish color in daylight as depicted in Figure 33b) which indicated a total thickness of $\sim 10 \mu\text{m}$ [164]. Subsequent thinning was performed using a PIPS system and it had to be ensured that the ions hit the GaN layer frontal such that the Si protected the soft GaN from getting thinned too fast as shown in Figure 33c). On the other hand, Ar ions hit the sapphire not in a small angle but rather head-on (i.e. close to 90°). Through this setup it was possible to thin sapphire in combination with GaN. Thinning was performed at acceleration voltage energy of 4 kV, a beam current of 20 μA , 3 rpm and an incident angle of 5° . As soon as the first hole in the Si spacer was visible the procedure was stopped. The TEM specimen was transferred into a low energy ion cleaning systems such as the Gentle Mill 3. The incident direction of the ions was changed by 180° to polish the thinned areas (i.e. the ions came from the sapphire side). The ion acceleration voltage was reduced to 500 V, the incident angle was elevated to 12° and a beam current of 1 μA was set. Each side of the TEM specimen was polished for 30 min to remove surface amorphization. Through this procedure electron transparent areas of a high quality were obtained. Figure 34a) depicts a light microscopy image of a fully

processed TEM specimen with a zoom-in b) showing a light interference pattern caused by an area with a smooth thickness gradient towards the edge of the TEM specimen. In Figure 34a) also a wave-shaped structure can be observed within sapphire showing that this material has experienced a certain amount of thinning.

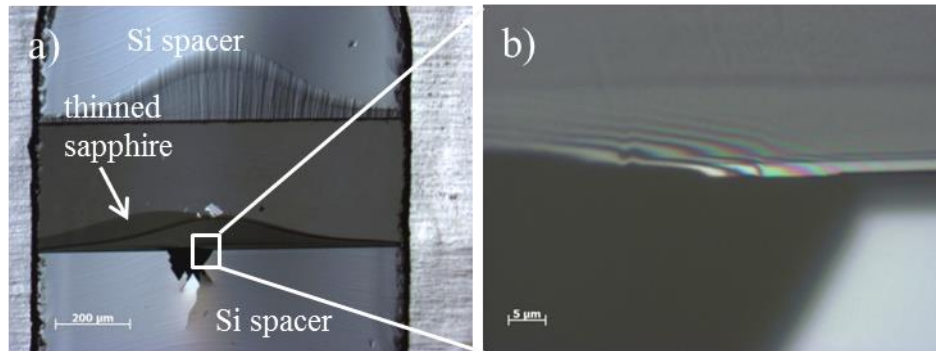


Figure 34: a) Light optical microscopy image of a finished TEM specimen; b) zoom-in into the GaN ROI showing a light-interference pattern due to the smooth thickness-gradient of the TEM specimen.

Through this process it was possible to obtain TEM specimens exhibiting only a very thin amorphous layer (about 2 – 3 nm as seen in Figure 34) making the TEM specimen useful for aberration corrected HR-TEM imaging. Figure 35 shows an aberration corrected HR-TEM image of homogeneously doped (GaMn)N in [11-20] orientation.

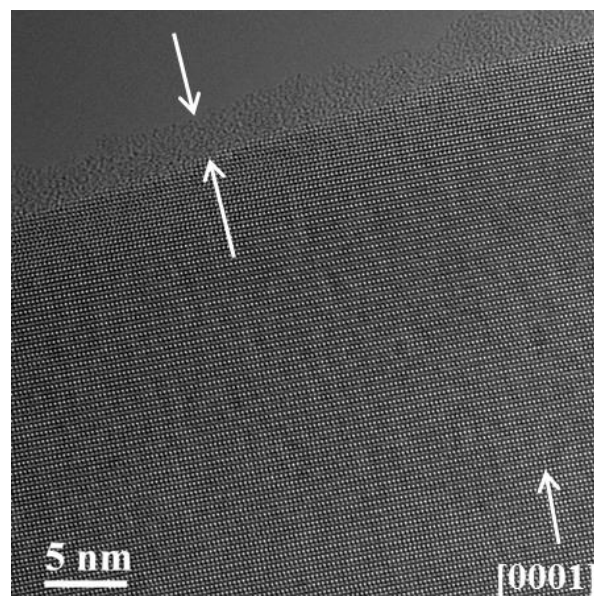


Figure 35: Aberration corrected HR-TEM image of homogeneously doped (GaMn)N in [11-20] orientation with an amorphous layer at the edge of roughly 2 - 3 nm (indicated by white arrows); image recorded at the DTU Copenhagen.

The lattice is visualized with a barely noticeable distortion caused by the amorphous layer. The contrast within a line of Ga atoms varies with less than 5 %. By looking at the edge of the TEM

specimen it was possible to estimate this layer to 2 – 3 nm, indicated by the two white arrows. This might not be the absolute thickness of amorphization but was useful as a first guess.

7.3 Conclusion of TEM specimen preparation

A multitude of sample preparation techniques (conventional cross-sectioning, FIB lift-out technique, wedge polishing) and combinatorial routes (conventional cross-sectioning vs. advanced processing) were attempted to obtain suitable TEM specimens of the following GaN samples:

- a) Homogeneously Mn-doped: during GaN growth Mn has been continuously co-evaporated with a concentration of 1.55 at% of Mn atoms within the 700 nm doped GaN which has been determined by SQUID measurement.
- b) δ -doped Mn: manganese has been co-evaporated during GaN growth in a pulsed process; during each of the 160 pulses first undoped GaN has been grown for 15 sec, then Mn has been added to GaN flow for another 2 min; this has led to a total, relative concentration of 1.3 at% of Mn which has been determined by SQUID; the doped layer has a total width of 150 nm.
- c) Fe-doped: iron co-doping with a nominal concentration of 0.25 at% and 0.5 at% (measured by secondary ion mass spectrometry) has been performed leading to embedded Fe-rich nanocrystals; the nanocrystal density has been measured to be $(9 \pm 2) \cdot 10^9$ nanocrystals/cm² with the possibility to adjust the density during growth [38]; the Fe_xN nanocrystals have a narrow size distribution, which is independent of the phase and growth conditions; it has furthermore been shown that (GaFe)N is stable in the as-grown phase under post-growth annealing up to 900°C [38].

The process of improving TEM specimen preparation was continuously performed during the work and is therefore a significant and substantial part of the results achieved in this thesis. With increasing image resolution and analytical detail in the investigated samples it became obvious, that improvements in TEM specimen preparation were required.

8. Analytical results and discussion

8.1 Phase determination of Fe_xO_y reference nanocrystals

During the initial phase of investigations chemical phase identification of cubic nanocrystals was carried out. Scope of this subchapter is to determine the oxidation state of iron, i.e. whether they are composed of Fe_3O_4 , Fe_2O_3 , or FeO (or a stoichiometry close to it) [5]. Figure 36a) shows the nanocrystals dispersed on Formvar film, b) a HR-TEM image of a single particle displaying the crystalline nature. The side measure of this type of cube is typically around 15 nm with a rather few structural deviations and a small size variation of <6% as depicted in Figure 36c) [5].

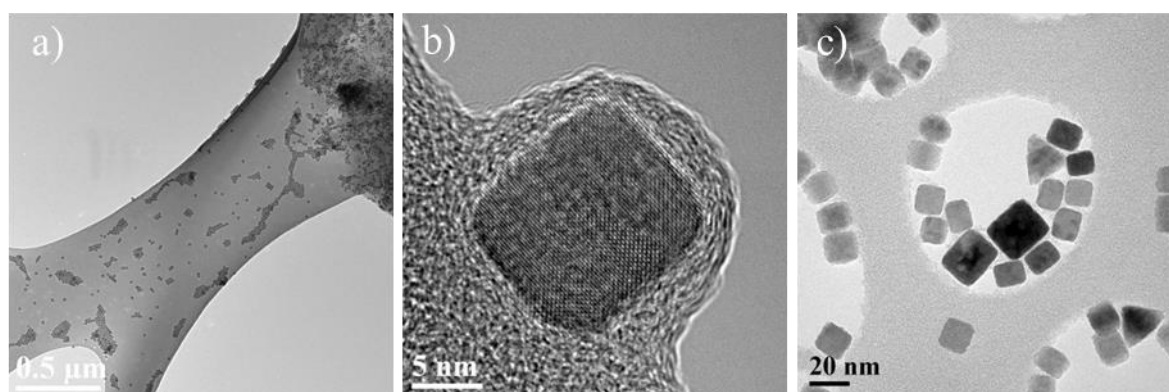


Figure 36: a) BF image of Fe_xO_y reference particles deposited on Formvar film; b) HR-TEM image of a single nanocrystal showing its crystalline structure; c) relatively few nanocrystals exhibit different side measures or some have triangular shape with varying size.

With conventional XRD and SAED it could be excluded that the nanocrystals are composed of FeO since the corresponding XRD reflexes and rings in SAED patterns are missing in the respective datasets. Furthermore, FeO is known to be unstable under ambient conditions [165].

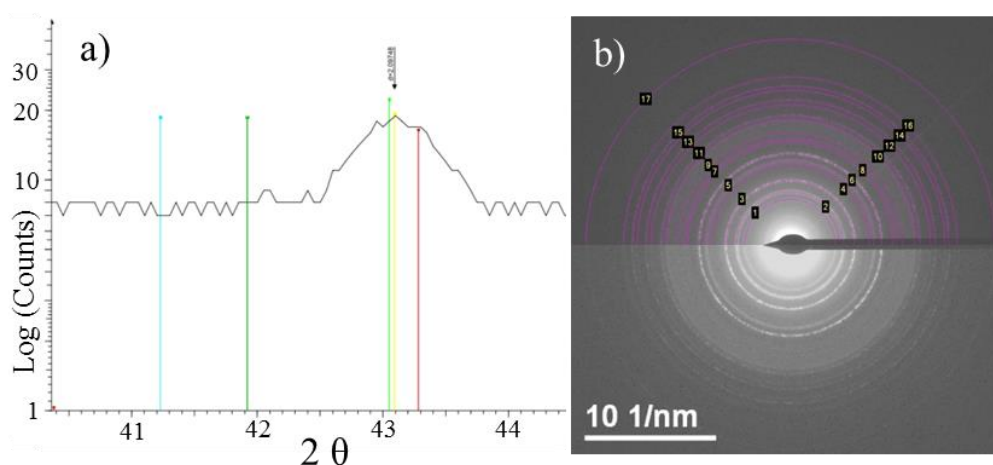


Figure 37: a) Zoom-in of the XRD 2θ -scan showing that Fe_2O_3 (red), Fe_3O_4 (green) and FeO (yellow) have similar reflections; b) experimental (lower half) and analyzed (upper half) SAED-pattern showing rings only for Fe_3O_4 and Fe_2O_3 .

Fe_2O_3 or Fe_3O_4 cannot reliably be distinguished by XRD reflexes or ring distances in SAED (see Figure 37). Diffraction ring analysis was done using the “CHD Diffraction analysis” plugin of DigitalMicrograph (© Gatan Inc.) created by Mitchell [166].

Table 4: Identified rings by the “CHD Diffraction analysis” plugin as shown in Figure 37b).

Ring number	Radius [1/nm]	1/Radius [nm]
1	3.450	0.290
2	4.061	0.246
3	4.885	0.205
4	5.985	0.167
5	6.343	0.158
6	6.924	0.144
7	7.798	0.128
8	8.002	0.125
9	8.501	0.118
10	9.383	0.107
11	9.800	0.102
12	10.602	0.094
13	10.959	0.091
14	11.679	0.086
15	12.012	0.083
16	12.657	0.079
17	15.533	0.064

Table 5 lists the diffraction files which are taken from the “The International Centre for Diffraction Data”³ used for comparison of the XRD and SAED measurements.

Table 5: Reference data used for comparison of the XRD and SAED measurements.

Material	file # used of XRD comparison	file # used of SAED comparison
Fe_2O_3	021-0920	033-0664
	039-1346	039-1346
Fe_3O_4	019-0629	019-0629
	079-0416	089-3854
FeO (or close stoichiometry)	006-0615	079-1972
	079-1967	079-1973
	089-2468	
	085-0625	
	089-0689	

A standard low-energy-resolution EEL spectrum was recorded using the Tecnai TF20 with the electron beam not monochromated. Spectra from randomly chosen TEM specimen positions were recorded in TEM imaging mode. A dispersion of 0.05 eV/channel to record the oxygen K edge (measurement window from 490 eV to 592.4 eV) and the iron L_{23} edge (measurement window from

³ see: <http://www.icdd.com/index.htm>

670 eV to 772.4 eV) was used. The recorded data were processed in DigitalMicrograph applying the regular EELS background subtraction scheme modeled as a power law. Background subtracted reference files were obtained from “The EELS Data Base”⁴ using the Fe_3O_4 reference from [167] and the Fe_2O_3 reference from the database entry of Qiang Xu. By comparing the measured oxygen and iron spectra with the reference data from both compounds it is not possible to rule out one of the two compositions. The two phases, however, could be resolved by re-measuring the TEM specimen at a FWHM of the ZLP of 0.3 eV by looking at the fine-structure of oxygen and iron with more detail. The dispersion was set to 0.02 eV/channel and the 2.5 mm entrance aperture of the GIF Quantum was selected. Oxygen was measured from 680 eV to 782.35 eV and iron was measured from 696 eV to 736.96 eV. Again, the data were evaluated with a power law background removal.

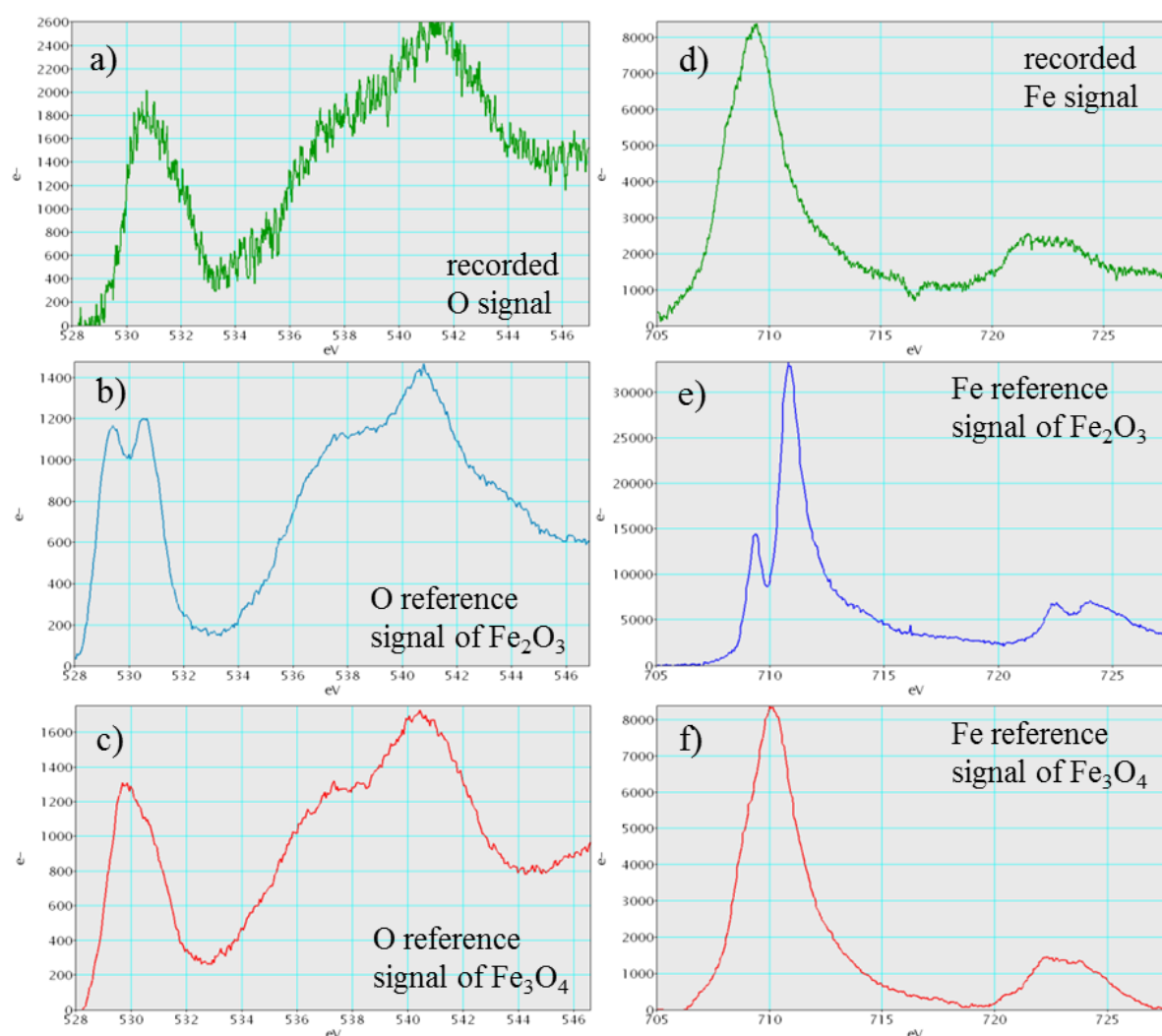


Figure 38: a) and d): Background subtracted EEL spectra and their corresponding reference signals for oxygen depicted in b) and c) and for iron depicted in e) and f). Note: a dip in the spectrum d) around 716 eV is an artifact from an intense ZLP.

⁴ see: <http://pc-web.cemes.fr/eelsdb/index.php?page=home.php>

Figure 38a) and d) show the recorded EEL spectra of iron and oxygen and their respective references in b), c), e) and f). At 0.3 eV resolution it is possible to resolve the double-peak around 530 eV (separation: 1.1 eV) of oxygen and the shoulder peak around 710 eV of iron (distance between peak and shoulder: 1.5 eV) within the Fe_2O_3 spectrum. The measured spectra were compared with the reference spectra to prove Fe_3O_4 stoichiometry.

8.2 Composition analysis of core-shell nanocrystals

After determining the oxidation state of references, core-shell nanocrystals were investigated. These investigations should deliver more information about the elemental distribution within the core and shell and – if necessary – a determination of the chemical composition of both. The investigated nanocrystals exhibited a side measure of ~ 26 nm. To ensure reliability of analytical measurements the nanocrystals were properly oriented towards the electron beam. Attention was paid to avoid nanocrystals stacked on top of each other, aggravating analytical measurements. For this, tilt series in α and β direction were performed.

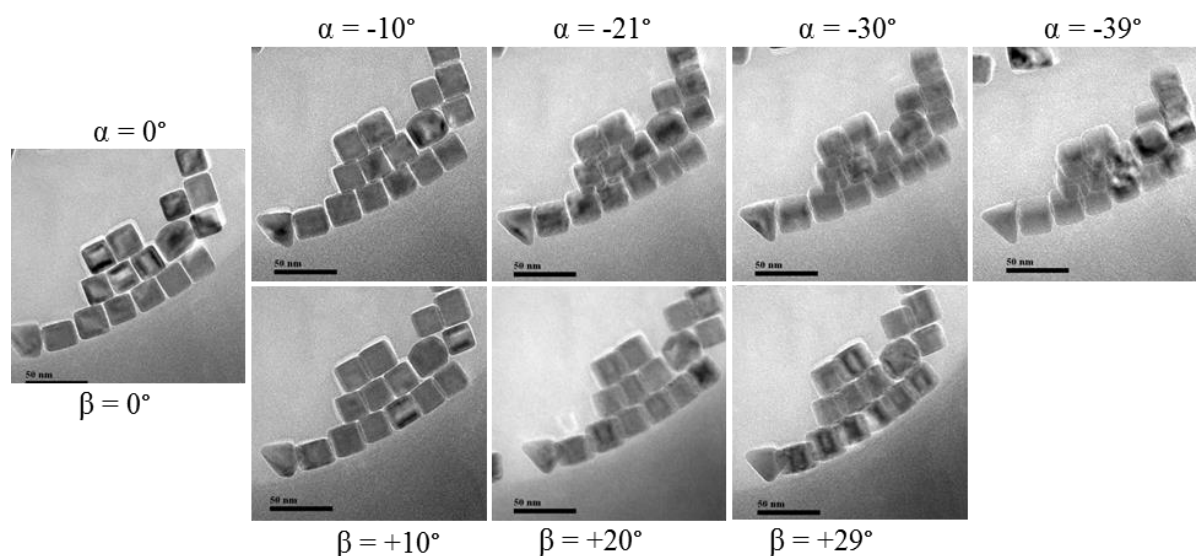


Figure 39: Tilt-series of nanocrystals in α and β direction to assure proper orientation and no stacking of particles above each other.

Figure 39 shows the tilt series for several nanocrystals. Through tilting either in α or β direction it becomes obvious that the top surface of most of the nanocrystals within this image is oriented around 90° towards the incident beam. With increasing tilt an overlap between individual particles becomes apparent and they even seem to reveal the 3-dimensionality at higher tilt angles (see $\alpha = -39^\circ$ image). Furthermore, during the tilt series nanocrystals possibly stacked above each other could easily be identified.

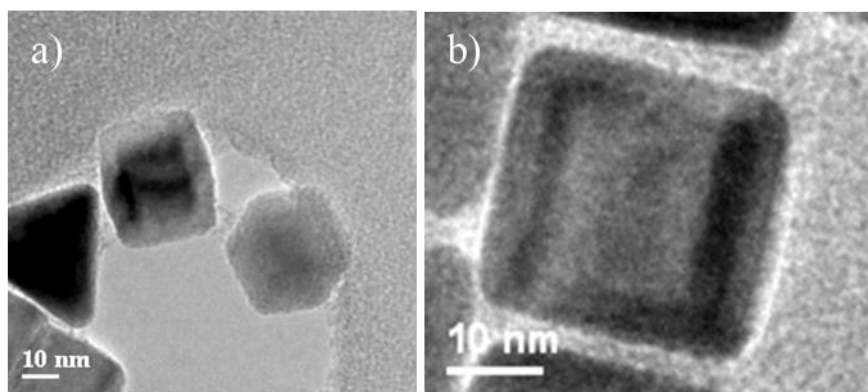


Figure 40: Two BF images showing diffraction contrast between core and shell of randomly oriented nanocrystals in a) and when oriented normal to the incident electron beam in b).

Figure 40a) shows nanocrystals with a 3-dimensional appearance due to diffraction contrast between the core and the shell, especially strong contrast is visible in the particle on the left. Figure 40b) displays strong diffraction contrast of a crystal when oriented normal to the incident electron beam, allowing to determine the dimension of the core and the shell. The shell is measured to have a width of 3–4 nm on each side and the core measures of 19–20 nm. It was attempted to directly image a distinct interface between core and shell through HR-TEM imaging. Figure 41 shows three HR-TEM images of a nanocrystal with a continuous arrangement of atoms within the crystal. A distinct interface is not visible between the core and the shell providing evidence for a coherent transition from core to shell.

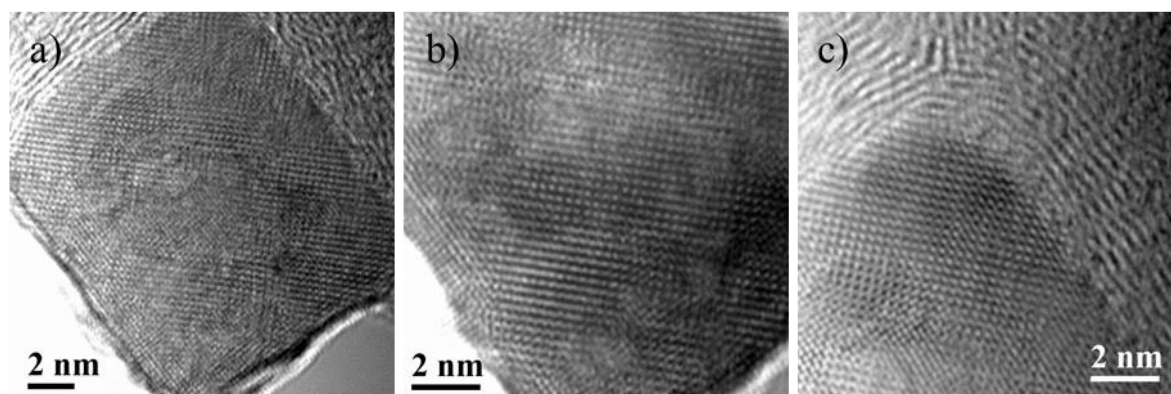


Figure 41: HR-TEM images of a single particle showing no distinct interface between core and shell.

In order to evaluate possibilities for detecting differences of the elemental composition between core and shell theoretical considerations were necessary. Therefore, the measured size of the core and the shell were used in combination with the assumed chemical composition [3] to estimate the number of atoms of Co, Fe and O when the electron beam passes through the shell or through the shell and the core. The crystal structure and composition of the core was assumed to be rock-salt Fe_xO matching the bulk $\text{Fe}_{0.95}\text{O}$ PDF-2 file. The shell was assumed to be stoichiometric CoFe_2O_4 crystallized in the spinel

structure. The beam diameter is assumed to be 1 nm corresponding to a reasonable spot size regarding resolution and beam current for analytical measurements performed on the Tecnai TF20.

Table 6: Estimated number of irradiated atoms of a single nanocrystal with an electron beam diameter of 1 nm. Assumptions for the core were bulk $\text{Fe}_{0.95}\text{O}$ in rock-salt structure and stoichiometric CoFe_2O_4 in the spinel structure.

Number of	core and shell	shell
# of O atoms	1225	1353
# of Fe atoms	1042	676
# of Co atoms	67	338

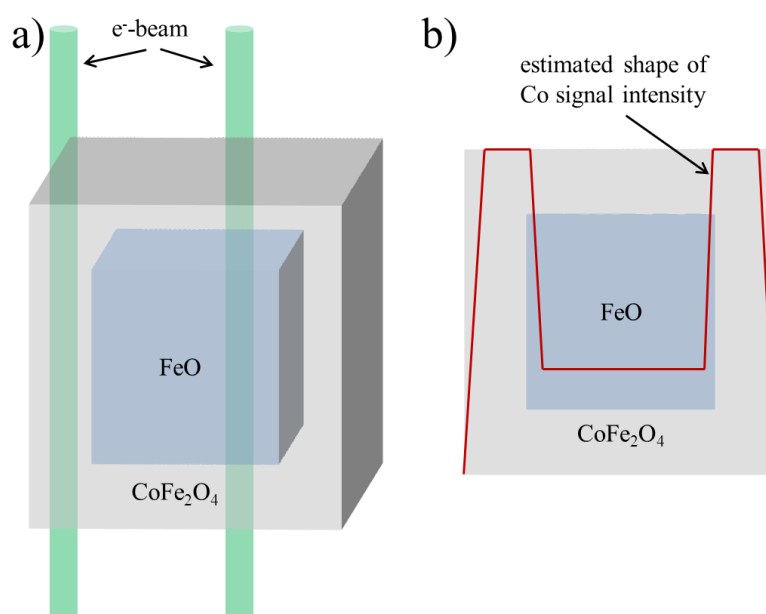


Figure 42: a) Schematic drawing of the STEM electron beam passing through the nanocrystal at different positions (shell only or core and shell); b) schematic Co signal intensity of a line scan through a particle.

Table 6 lists the number of atoms when the electron beam passes through the shell only or the core and the shell together (i.e. through the central part) as depicted in Figure 42a). When performing a line scan across the nanocrystal the cobalt signal should yield a significant change in intensity. A schematic of the expected Co signal intensity variation along a line scan across a nanocrystal is depicted in Figure 42b). The Co signal should show a higher intensity if the beam is positioned on the shell only and should significantly decrease but not go to zero if the beam is positioned in the center of the nanocrystal. Monochromatic EELS measurements to determine the composition of the core (as used for the analysis of the single phase particles in section 8.1) are strongly aggravated since the surrounding shell is predicted to be composed of oxygen and iron as well. This results in an intermixing of signals originating from core and shell. Figure 43a) shows the HAADF image of a single nanocrystal with a visible contrast difference between core and shell. Additionally, the image confirms a thickness for the shell of roughly 3 nm. The subtle difference in contrast of about 15 % indicates that there is a certain difference in average atomic number between core and shell. Several STEM-EELS line scans were performed to confirm the above assumption of the elemental

distribution. The line scans were performed on the Tecnai 200 kV microscope in STEM mode with a convergence angle of 7.40 mrad and a step size of ~ 1 nm. The line scan direction is indicated by the white arrow in Figure 43a). For EELS acquisition the collection angle was 35.34 mrad with a dispersion of 0.2 eV/channel, a spectrum offset of 490 eV and an exposure time of 3 sec/pixel. The background was modeled as a power law and the signal was integrated for the oxygen K edge from 540 eV – 590 eV and for the iron L_{23} edge from 720 eV – 770 eV.

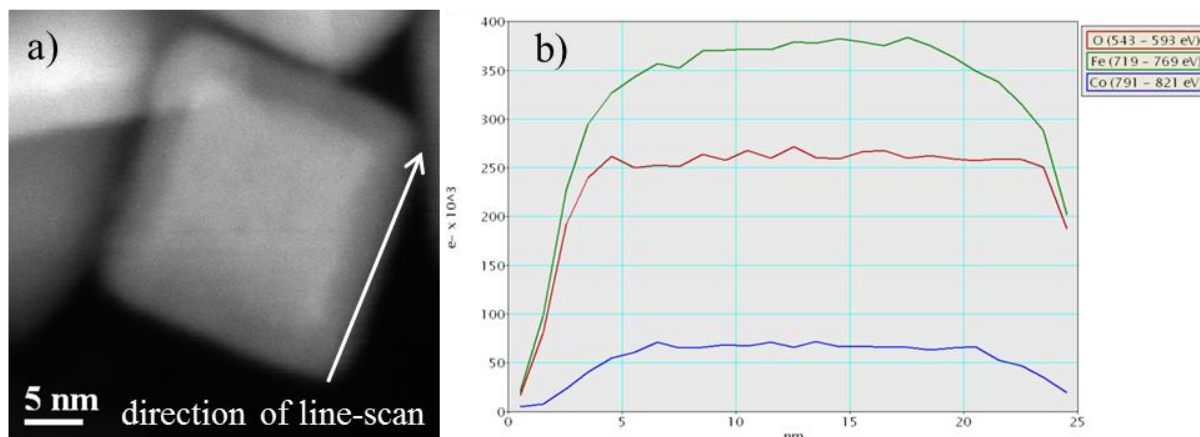


Figure 43: a) HAADF image of a nanocrystal exhibiting a clear contrast difference between the core and the shell; the direction of the EELS line scan is indicated by a white arrow; b) background subtracted and integrated EELS signal profiles of O, Fe and Co along the line-scan.

Surprisingly, the integrated and background subtracted signal of a STEM-EELS line scan from the Co L_{23} edge as depicted in Figure 43b) did not reveal the expected intensity variations of Co as schematically shown in Figure 42b). However, by aligning the signal intensities of all three elements according to their maximum it is possible to extract further information.

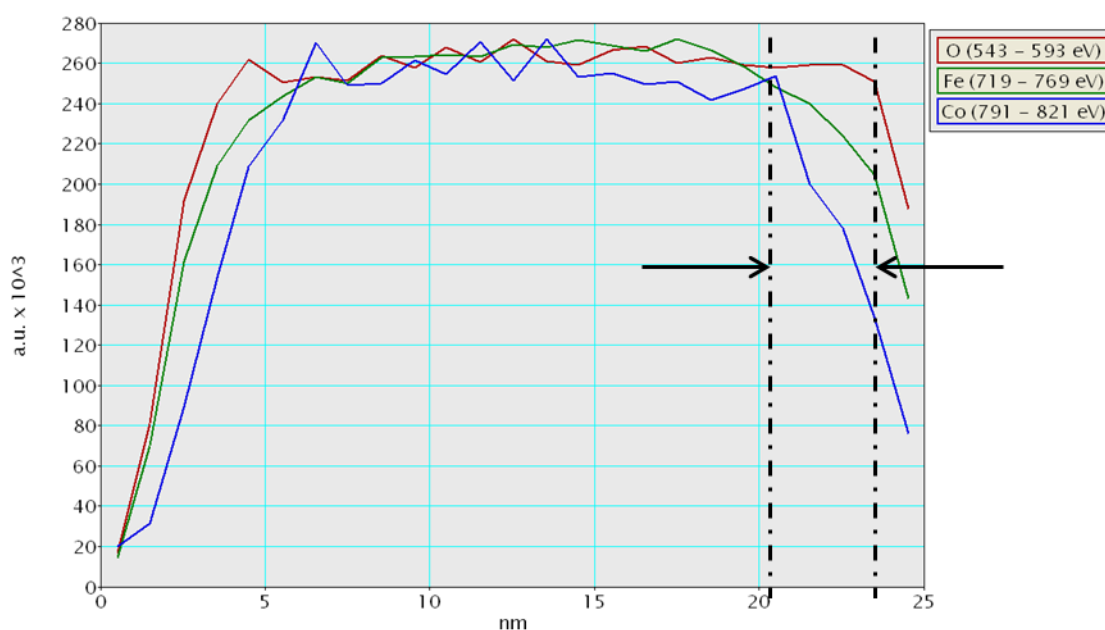


Figure 44: Signal intensities of O, Fe and Co aligned to the maximum values; dashed lines indicate delay of maximum between oxygen and cobalt.

Figure 44 shows that Co is present across the whole particle and has a particular intensity maximum in the particle core. The first maximum of the Co signal is positioned about 3 nm after the onset of iron. This corresponds to the width of the shell and is not in agreement with the assumptions made above. The distance between the maximum of the Co and the Fe signal intensity is indicated by black dashed lines in Figure 44. The oxygen signal shows a rather steep onset followed by a fairly constant amount across the whole cube. The signal of iron shows a slightly flatter increase from the edge towards the center of the particle. These two findings are in good agreement with theoretical considerations. The observed contrast increase of the core in the STEM image of Figure 43a) is explicable through the enrichment of Co within the core. This leads to the idea that a layer of mainly iron oxide is encapsulating a cobalt-iron oxide core, increasing the average Z. Thickness effects due to a fairly constant overall thickness of the nanocrystal can be excluded. Unfortunately, a relatively long exposure time per pixel was needed, leaving a trace of beam damage after the line scan as depicted in Figure 45. It has to be mentioned that an alteration of the composition caused by energetic electron beam during the line scan measurement could not be completely excluded.

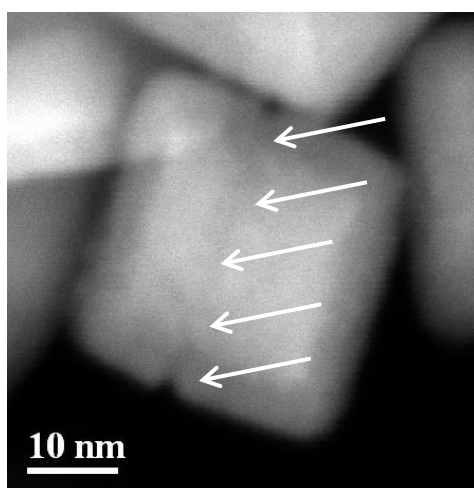


Figure 45: HAADF image of an observable trace of beam damage after a STEM-EELS line-scan indicated by white arrows.

To further assure the observed findings, several EFTEM image series have been recorded at reduced acquisition time and electron dose from the low loss regime using the Fe M_{23} at 54 eV and the Co M_{23} at 60 eV. EFTEM images were recorded with 5 sec per image, a slit width of 4 eV and a step size of 2 eV over a range from 30 eV to 84 eV.

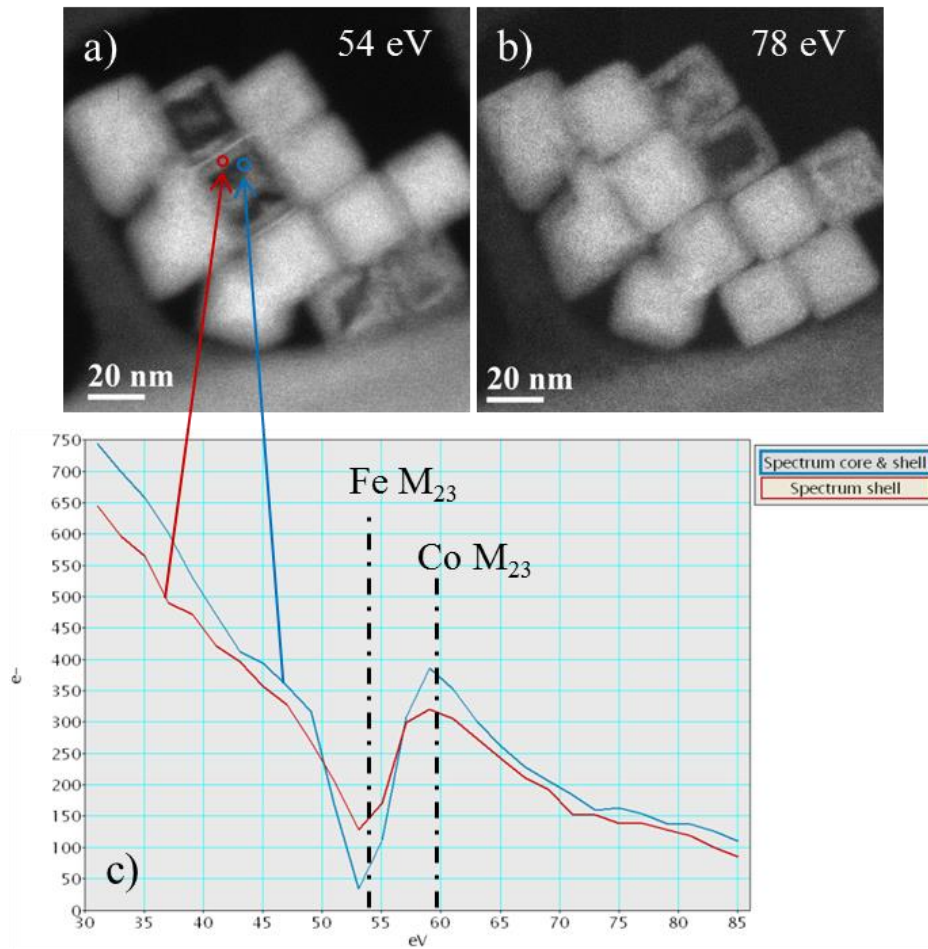


Figure 46: a) & b) EFTEM images acquired at different energies show some nanocrystals having a core-shell structure visible as diffraction contrast; c) shows extracted EEL spectra with marked regions of extraction and denotation of edges.

Figure 46a) and b) are EFTEM images at two different energies showing again the core-shell structure. Residual diffraction contrast is very prominent since different particles show the same core-shell structure at different energies. By aligning the whole image stack to correct for TEM specimen drift during acquisition it is possible to extract EEL spectra. Figure 46c) shows an overlay of 2 unprocessed spectra extracted from the marked regions in Figure 46a). The edge intensity at the Co M_{23} energy within the spectrum of the core and the shell is slightly higher. Contrary shows the shell spectrum more electrons at the Fe M_{23} energy. This finding supports that Co is mainly present within the core. To improve the spectral quality STEM-EELS spectrum images across entire particles in the low loss region were performed. STEM images were acquired with a convergence angle of 7.40 mrad and an acquisition time of 0.84 nm per step. For the EELS acquisition a dispersion of 0.25 eV/channel, an acquisition time of 0.5 sec/pixel, a collection angle of 32.22 mrad and a spectrum offset of 70 eV were chosen. Figure 47a) shows a BF image of the investigated particle marked with a rectangle. Both particles show traces of a core shell structure visible as dark line roughly 3 nm inside from the particle edge.

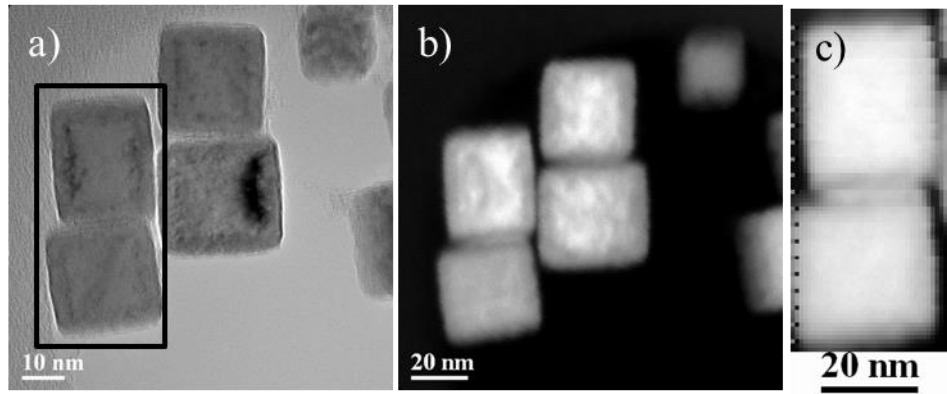


Figure 47: a) BF image of the nanocrystals with the investigated particles indicated by a black rectangle; b) the corresponding HAADF image; c) the obtained SI with drift correction artifacts (regular arranged pixels on the left side of the image).

Figure 47b) shows the corresponding HAADF-STEM image and c) the obtained SI within the low loss region. Unprocessed spectra of the Fe M_{23} and Co M_{23} edges of the core and shell and the shell only were extracted. Figure 48a) shows the overlaid spectra for the shell only and the core and shell aligned to their respective maximum of the iron-peak at 58 eV. Figure 48b) shows the regions of spectrum extraction marked in red and blue.

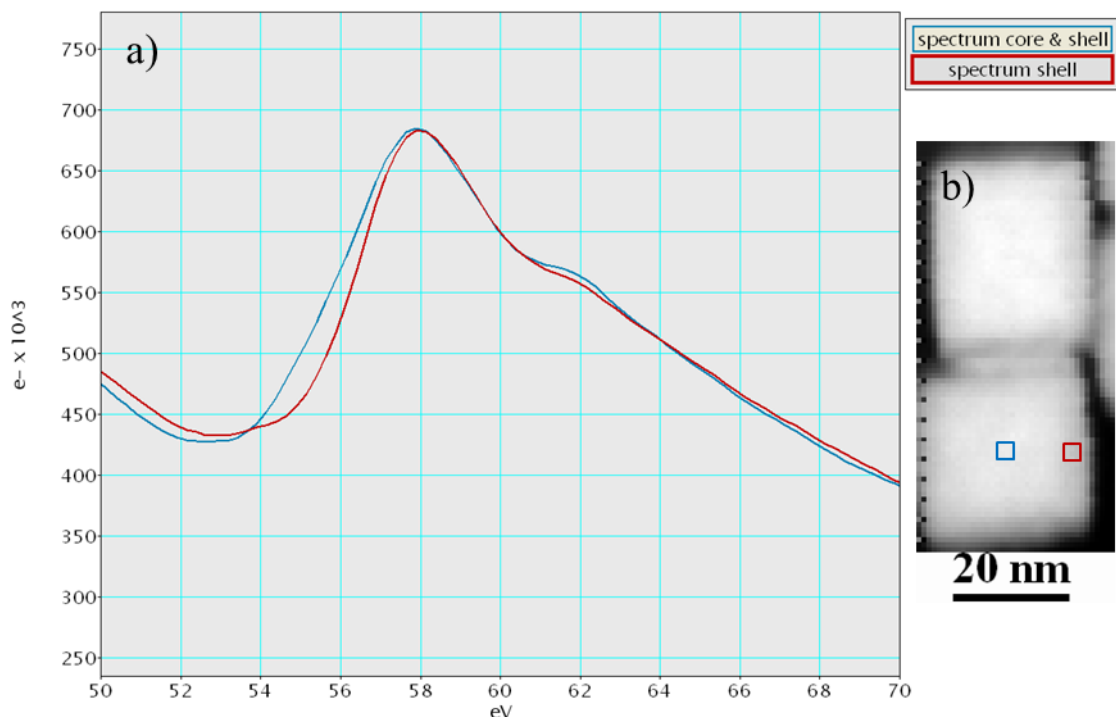


Figure 48: a) Spectra of the core and shell and the shell only aligned to the maximum at 58 eV extracted from the SI shown in Figure 47; b) marked regions (blue = core and shell, red = shell only) for the extraction of the spectra.

Two differences between both spectra can be observed. First the onset of the Fe edge within the spectrum of the shell starts at slightly higher energy loss of ~ 1.5 eV compared to the one of core and shell. This can be interpreted as a different chemical surrounding for Fe. Secondly a subtle increase in

intensity of the shoulder starting at 60 eV and ranging until 63 eV is visible in the spectrum of core and shell corresponding to the onset of the Co M_{23} edge at 60 eV. Again both findings hint for an enhanced aggregation of cobalt in the core of the particle.

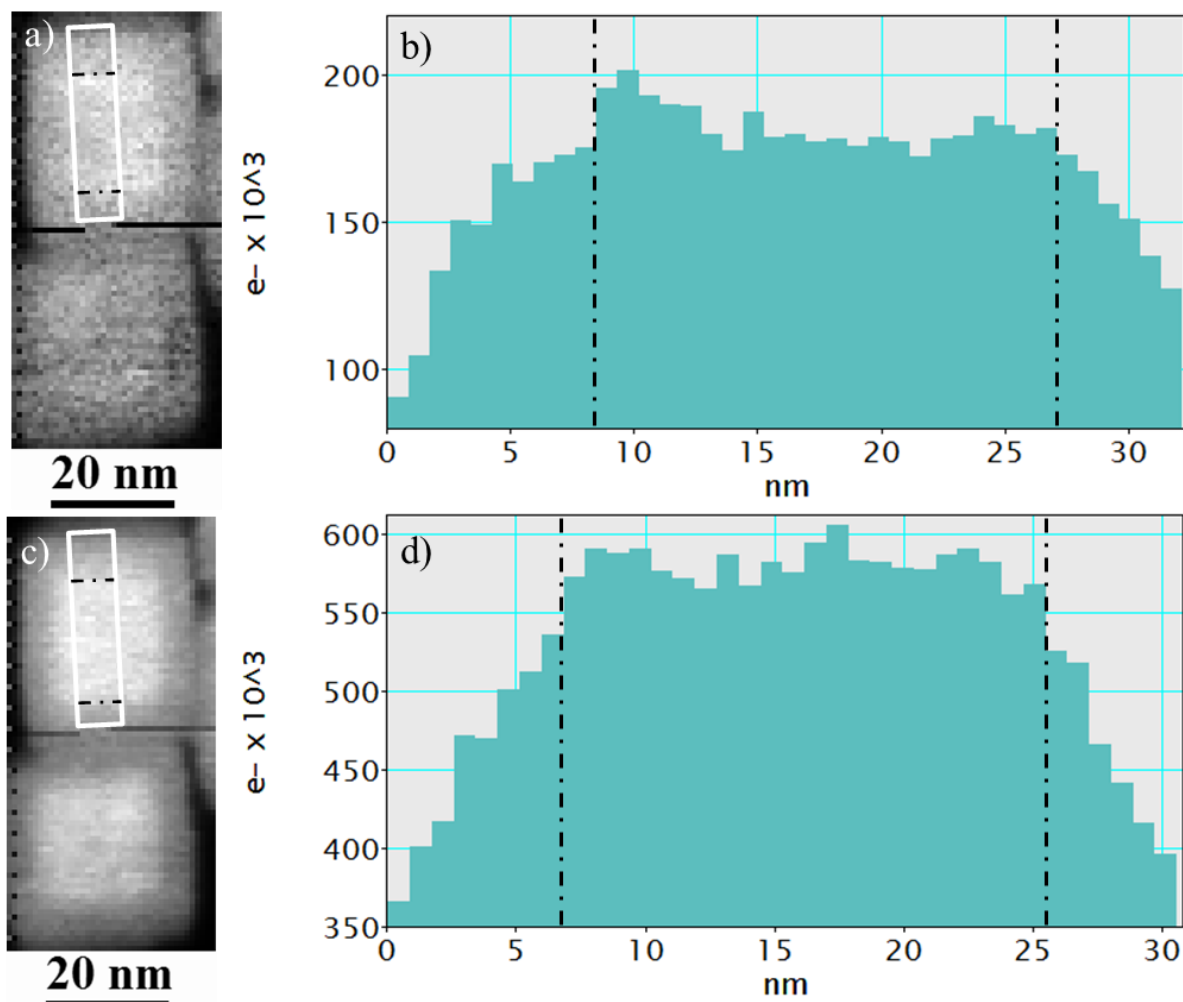


Figure 49: a) Background subtracted SI of Co (61 eV – 64 eV) with an increased signal in the core; white rectangle: region of line profile; dashed black line: indication of core; b) line profile of a) showing an increased signal in the core (black vertical lines); c) background subtracted SI of Fe (54 eV – 57 eV) with a clearly visible signal increase in the core; white rectangle: region of line profile; dashed black line: indication of core; d) line profile of c) showing clearly an increased signal in the core (black dashed lines). The black lines in the center of the SIs (a and c) originate from an environmental disturbance during the acquisition.

By power law background subtraction and extracting signal integrated SIs of Co (from 61 eV – 64 eV) and Fe (54 eV – 57 eV) as depicted in Figure 49a) and c), it is possible to visualize an enhanced signal of Fe and Co within the core. The increase is faint for the Co signal image and visible in the line profile (Figure 49c) with black dashed lines indicating the core. The signal enhancement is clearly visible in the line profile of Fe (Figure 49d) with black dashed lines indicating the core. The enhanced signal in the core supports the findings shown in Figure 43b). The black lines in the center of the SIs are caused by an environmental disturbance during data acquisition.

The obtained results allow the following conclusions: All performed measurements indicate a difference in composition in the core compared to the shell as seen in BF and HAADF images. Due to the increased intensity of the core, the average atomic number compared to the shell seems higher. Therefore, Co, which has an atomic number of +1 compared to iron, is assumed to be enriched in the core of the nanocrystal. The nature of the fabrication process as a one-pot reaction [3] supports that a Co-rich core forms first. After the preferred Co-precursor consumption (i.e. the core of the particle is formed) the growth of the shell takes place. The remaining constituents form the shell of the nanocrystal. This assumption allows explaining the findings of the EELS measurements of iron and cobalt in the plasmon region and in the high loss region. Combination of these results leads to a rather clear picture of the cobalt distribution within the nanocrystal. The EFTEM images are affected by elastic contrast as well which allows only a qualitative observation of the core-shell structure of the particles.

8.3 Compound semiconductor gallium nitride

As a first step, appropriate sample preparation methods for GaN needed to be developed to reach the required TEM specimen quality for the following TEM investigations, including minimization of carbon contamination and TEM specimen surface amorphization. Secondly, appropriate beam current and applicable dwell times for image acquisition had to be determined. This was done to minimize material alteration due to beam damage or sputtering of nitrogen. In contrast to the investigations on the nanoparticles the challenge here was that atomic resolution for the characterization of the material is necessary.

If not explicitly mentioned all images of GaN are oriented along the GaN [11-20] zone axis.

8.3.1 STEM resolution improvement in GaN

For the study of GaN, C_s -correction has brought numerous advantages therefore a study of GaN in [10-10] orientation is given. Undoped GaN was utilized firsthand to explore HR-STEM possibilities enabled by the commissioning of the newly installed TITAN microscope. In addition, it was used to find the applicable microscope settings for the investigation of transition metal doped GaN. Figure 50a) and b) show HAADF images of GaN in [10-10] orientation with the rectangular arrangement of Ga columns corresponding to the structure model shown in the inset in b). Figure 50c) shows a line profile of the marked region in b) where a distance of 157 pm between the Ga columns was measured. This is in good agreement with values obtained from the structure model. According to the structure model (Figure 51a) nitrogen is placed 69 pm away from Ga.

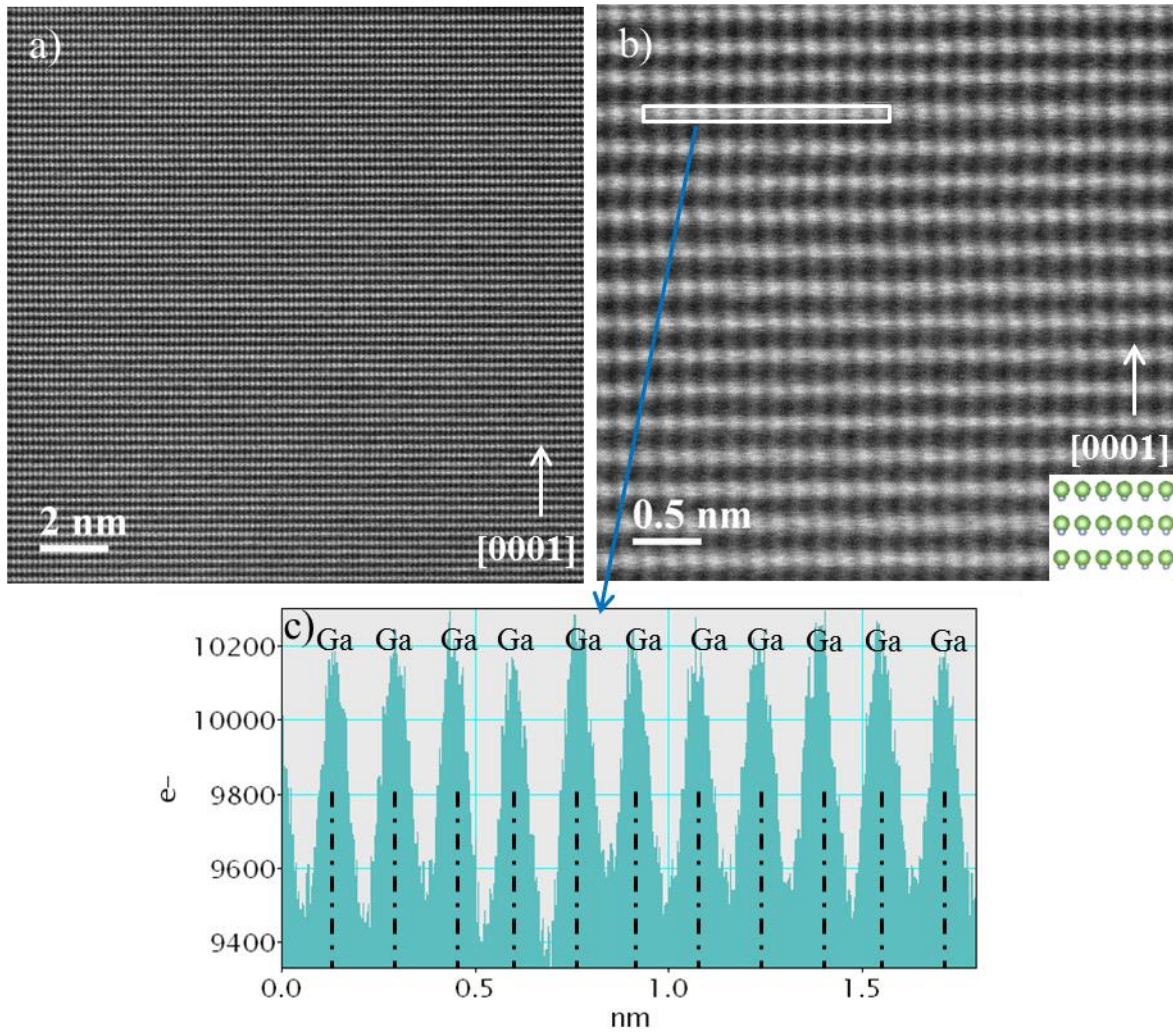


Figure 50: a) and b) STEM HAADF images of GaN in [10-10] orientation; c) shows a line profile of the marked region in b) where a distance of 157 pm was measured.

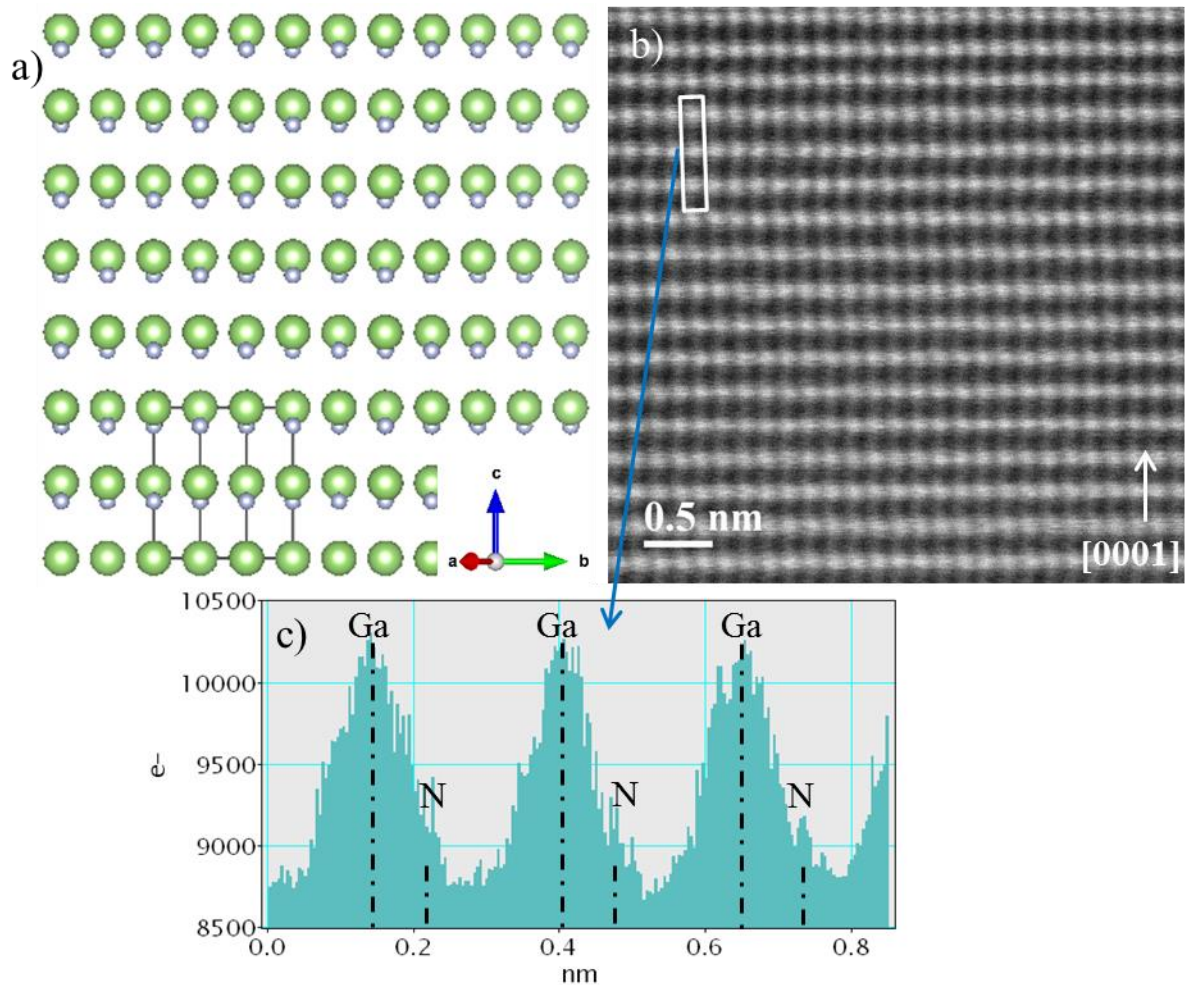


Figure 51: a) Structure model of GaN in [10-10] orientation showing an alternating arrangement of Ga and N at a distance of ~69 pm; b) corresponding STEM HAADF image to a) showing the region of the extracted line profile; c) line profile of b) showing a slight shoulder on the right hand side of each Ga column corresponding to the nitrogen position of the structure model shown in a).

A line profile along the c-axis of the HAADF image (Figure 51b) depicted in Figure 51c) reveals a slight shoulder on the right side of each Ga column. The distance of ~75 pm is in line with the theoretical distance demonstrating an aberration-corrected resolution equal or better than 75 pm.

8.3.2 GaN – image simulations

Z-contrast STEM imaging usually provides contrast for the heavy Ga atoms leaving the lighter N “invisible”. In contrast, ABF imaging allows for the acquisition of both types of species at the same time [168]. Here, this technique is ideal for GaN with its potential to image the heavy Ga and the light N simultaneously [90], since the atomic columns of Ga and N are well separated in [11-20] orientation. To obtain ABF images it is important to correct for slight misorientations of the TEM specimen, to minimize surface amorphization and to avoid carbon surface contamination during image acquisition. Due to its relative insensitivity to TEM specimen thickness ABF can be carried out on a wide range of TEM specimen positions HR-STEM [90]. The Fischione HAADF detector of the

TITAN microscope was used to generate the wide-angle Z-contrast image. This was utilized to select an appropriate TEM specimen position, to focus and to correct for remaining astigmatism. Using a camera length of 185 mm for ABF imaging this detector would cover an angular range from 26 mrad to 95 mrad. Instead, the GIF Quantum STEM detector was used as the actual ABF detector giving an appropriate angular range between 10 mrad and 20 mrad. The images were recorded with 20 μsec per pixel at a beam current of ~ 80 pA.

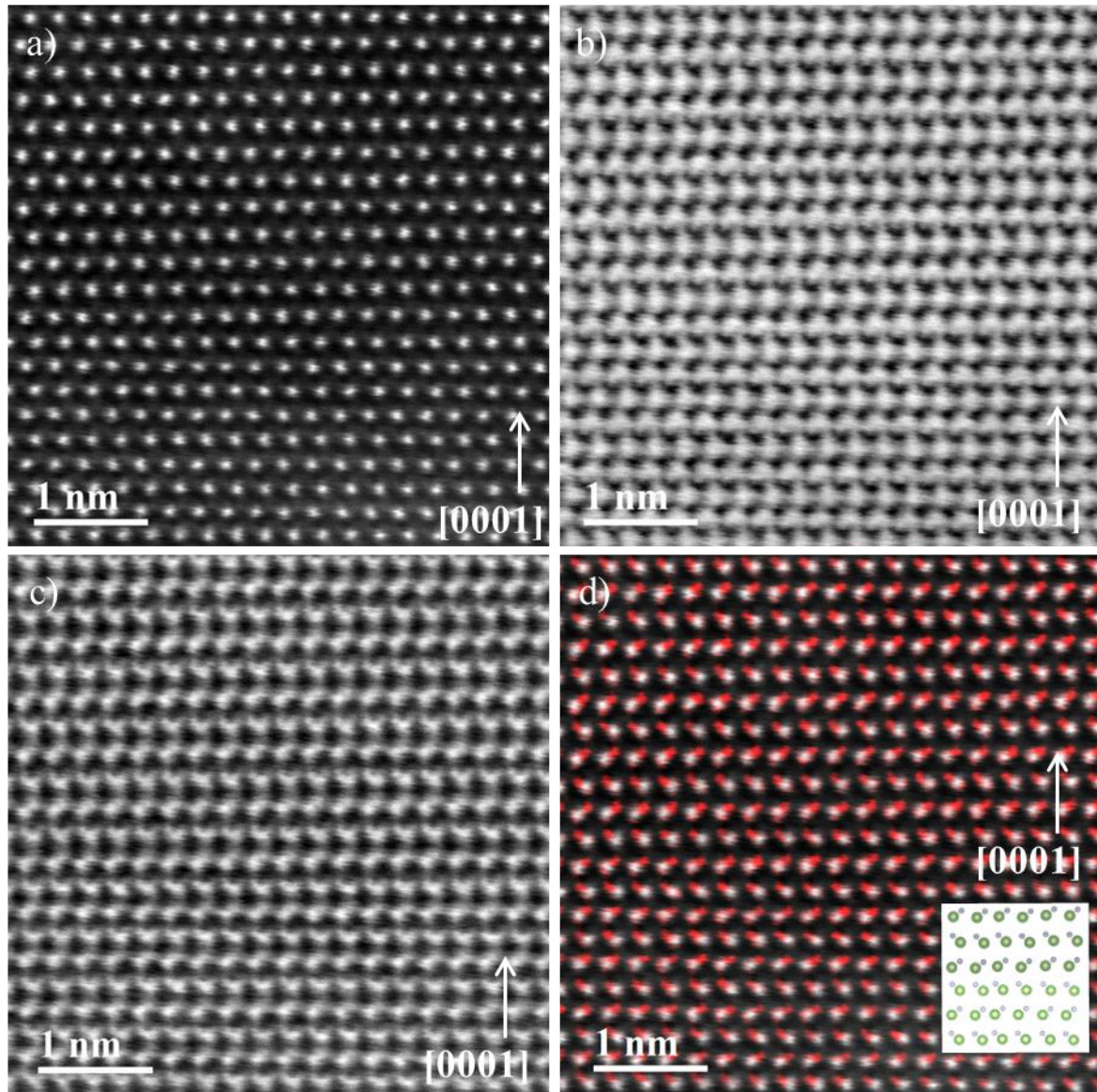


Figure 52: a) HAADF image of undoped GaN; b) corresponding ABF image; c) contrast-inverted image of b) showing Ga and N columns; d) colored overlay of a) and c) showing the matching of the individual signals (N in red; Ga in white) (inset: structure model of GaN in [11-20] orientation with Ga in green and N in blue visualized by the software package VESTA 3.1.3).

Figure 52a) shows the HAADF image of GaN and b) the simultaneously recorded ABF image. The ABF image reveals the periodic structure as dark spots, corresponding to the atomic position of Ga. Next to the dark spots on either side, alternating and in diameter smaller, features matching the atomic

position of N are visible. Figure 52c) shows a contrast inverted image used for superposition in d). Additional bright contrast in Figure 52c) originates from channeling effects. The position of Ga and N are in accordance with the structure model shown in the inset of Figure 52d) with the ICSD number 005-4698. The model was visualized using the VESTA software package (version 3.1.3) [169].

To confirm the experimental ABF images, theoretical simulations were performed by Stefan Löffler from the Universitäre Service-Einrichtung für Transmissionselektronenmikroskopie at the Vienna University of Technology. A reference image was calculated by using the software package “ixchel” [170] based on a multislice algorithm of Kirkland [148]. The parameters used for the simulation are listed in Table 7 and Table 8.

Table 7: Image and crystal parameters used for the ABF image simulation performed with the software package ixchel.

Image:

Space	Real Space	Reciprocal Space
Size	512 x 512 pixel (44.201939 x 41.440002 Å)	512 x 512 pixel (11.583202 x 12.355212 Å ⁻¹ ; 228.044234 x 243.243162 mrad)
Calibration	0.086332 x 0.080938 Å/pixel	0.022623 x 0.024131 (Å/pixel) ⁻¹ (0.445399 x 0.475084 mrad/pixel)
Pixel Aspect Ratio:	1.066649	0.937515

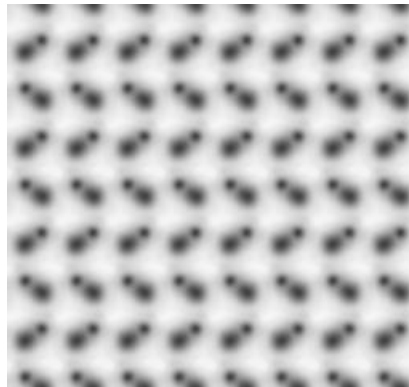
Crystal structure:

Unit cell	64 x 64 pixel (5.525242 x 5.180000 Å)
Replication	8 x 8
Layers	376
Size	512 x 512 x 376 pixel (44.201939 x 41.440002 x 599.718750 Å)

Table 8: Applied microscope parameters for the ABF image simulation using the ixchel code.

Acceleration Voltage	300 kV
λ	0.019687 Å
Topological Charge	0
Convergence Semi-Angle	19.6 mrad
qmax:	6.255262 / Ang (2 Pi/d)
C_s:	0.000 mm
df:	-0.00000Å
Width:	512 pixel (44.201939 Å)
Height:	512 pixel (41.440002 Å)
FWHM:	0.611653 Å

The x- and y-calibrations are different which has been taken into account. Figure 53 shows the simulated ABF image with well separated Ga and N columns. This is ascribed to the fact that a model about the effective source size ($\sim 0.8\text{Å}$) was not considered.

**Figure 53:** Simulated ABF image of GaN in [11-20] orientation showing well separated Ga and N columns.

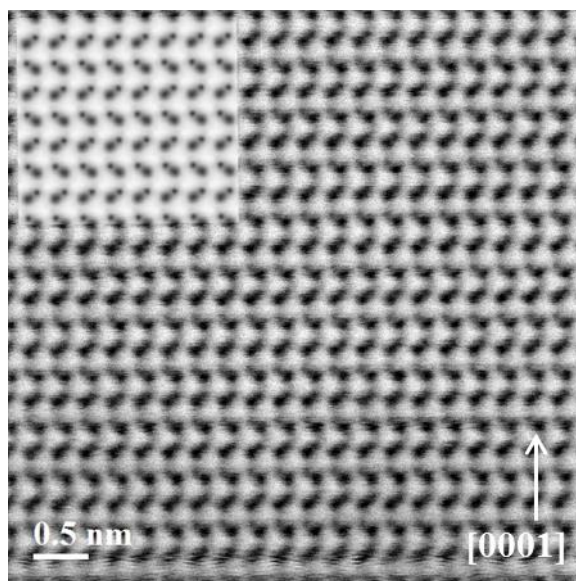


Figure 54: Overlay of the experimental and simulated ABF image.

Figure 54 shows a comparison between the simulated and the recorded ABF image. Both images correspond well in terms of periodicity and contrast. The higher resolution in the simulation shows better separation between the Ga and N columns which can be ascribed to the absence of a spherical aberration in the electron beam, the perfect crystal and an ideal TEM specimen.

8.3.3 GaN – analytical investigations

Qualitative STEM-EDXS analysis was carried out using the new ChemiSTEM technology (© FEI Company) installed on the TITAN microscope in Graz. This allows mapping the Ga-lattice atomically (Figure 55) by using the Ga $K\alpha$ radiation. For the 512x512 pixels STEM image acquisition a dwell time of 40 μsec per pixel was used. The 128x128 pixels STEM-EDXS map was recorded with 25 μsec per pixel at a beam current of ~ 150 pA by continuously integrating frames for 5 min. Beginning beam-damage in the center of the image was visible under these conditions. Nonetheless the unprocessed Ga $K\alpha$ map shows well-separated atomic columns as depicted in Figure 55b).

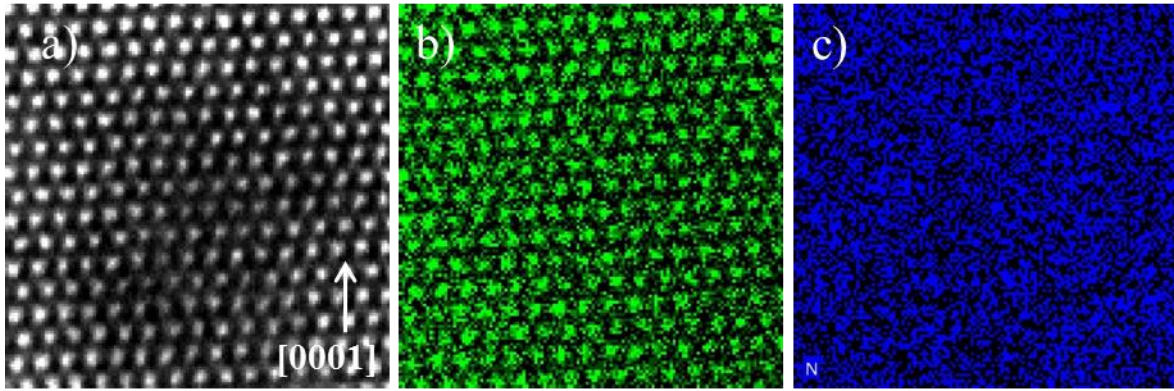


Figure 55: a) HAADF image of GaN with beginning beam damage visible in the center of the image; b) corresponding signal map of Ga $K\alpha$ radiation showing atomic columns of Ga; c) diffuse signal map of N $K\alpha$ radiation.

Light elements such as nitrogen suffer from poor X-ray generation and have a high cross section for knock-on damage and displacement at commonly used accelerating voltages of 200 kV – 300 kV [62,171–173]. This led to a diffuse map for N $K\alpha$ intensities (Figure 55c) lacking atomic resolution information. To get time resolved information about reduction of the nitrogen signal due to displacement and knock-on, EELS measurements were carried out. This was done by placing the STEM beam of the TITAN microscope operated at 300 kV on a spot within un-doped GaN using a beam current of ~ 3.4 nA and a convergence angle of 19.6 mrad. The EEL spectra were recorded every 0.05 sec for 300 seconds. The collection angle was 16.3 mrad and a dispersion of 0.25 eV/pixel was used.

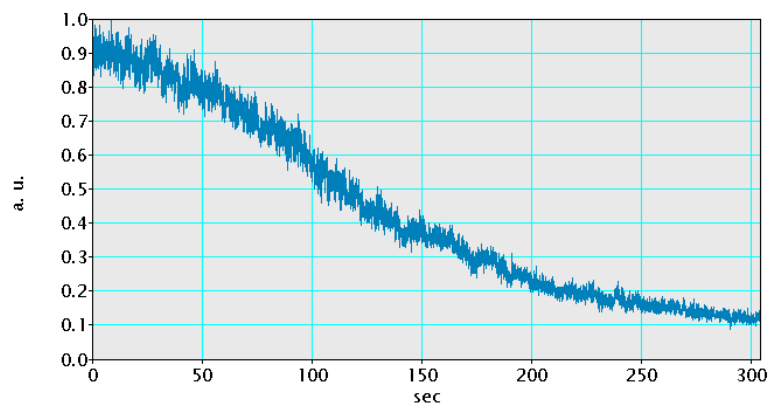


Figure 56: Normalized nitrogen concentration of GaN showing a time-dependent signal decrease due to the electron beam irradiation with a beam current of 3.4 nA at 300 kV accelerating voltage.

Figure 56 depicts the normalized decrease of the N signal over time for a dose of 1.7×10^{11} e/nm² corresponding to 3.4 nA electron beam current within 2 Å probe diameter. This shows that at 300 kV accelerating voltage and at a high dose the nitrogen signal drops to a tenth of the initial intensity within 300 sec. If the dose is significantly reduced to 3.5×10^{10} e/nm² corresponding to 0.177 nA beam current within 1 Å probe diameter the effects of specimen heating and radiolysis are reduced [171]. Furthermore, through decreasing the acquisition time and continuously scanning over a

50x50 nm large region reliable results concerning quantification can be obtained [171]. Table 9 shows the results of 3 randomly picked sample positions leading to an average value of 51 at% of Ga (L_{23} edge) and 48 at% of N (K edge) with a slight oxidation of 1 at% (K edge). Oxygen was included into the data analysis because it has been detected in noticeable amounts in all TEM specimens. An explanation for the origin of the oxygen signal will be given later. A slight under-estimation of nitrogen visible in Table 9 is ascribed to the already mentioned difficulties for nitrogen, e.g. sputtering, displacement and knock-on damage [62,172]. Microscope settings for the TITAN microscope were the following: 300 kV acceleration voltage, 19.6 mrad convergence angle and ~ 0.173 nA beam current. The spectrometer settings were: 0.3 sec exposure time per frame, 100 frames summarized, 25.88 mrad collection angle, 0.5 eV/channel and 400 V energy offset.

Table 9: Quantification results of EELS for GaN (Ga L_{23} and N K edge) with a slightly oxidized surface (O K edge).

	Ga [at%]	N [at%]	O [at%]
GaN	50.5	47.6	1.9
GaN	53.0	47.0	0.0
GaN	49.5	49.4	1.1
average	51 ± 1.6	48 ± 1.0	1 ± 1.0

Quantitative EELS calculations were done using the following settings and considerations:

- All data were evaluated in DigitalMicrograph applying regular EELS quantification schemes with account for multiple scattering by low-loss deconvolution.
- Background was modeled as a power law and a Hartree-Slater model was used for the cross-section calculation.
- Background and signal windows were kept constant for quantification of all relevant elements (Ga, N, O, Fe and Mn); detailed values are listed in Table 10.
- Signal windows used for N, O and Mn were positioned slightly after the edge-onset to account for small energy offsets.
- An uncertainty of the cross-section for Ga of about 10 – 20 % was assumed [134].

Table 10: Background and signal windows used for quantification in comparison with tabulated values taken from [134].

Element	edge onset-energy [eV]	background window [eV]	background window width [eV]	start of signal window [eV]	signal window width [eV]
Ga	1115	900	200	1170	100
N	401	340	50	450	50
O	532	495	30	545	40
Mn	640	590	40	635	40
Fe	708	645	50	750	50

8.3.4 Determination of the origin of the oxygen

To study the origin of the oxygen a cross-section from an existing TEM specimen was fabricated. This was done using a Focused Ion Beam system (Nova 200 Nanolab from FEI Company). The TEM specimen has been investigated beforehand and an oxygen signal was detected with EELS. Figure 57a) shows a SEM image recorded during the TEM lamella preparation process with protective Pt already deposited on the region of interest. Surface roughness across the whole TEM specimen and especially in electron transparent areas (around the protective Pt) can be observed. Figure 57b) shows a HAADF overview image of the fully processed TEM-lamella with a labeling of the various features and the investigated region of interest.

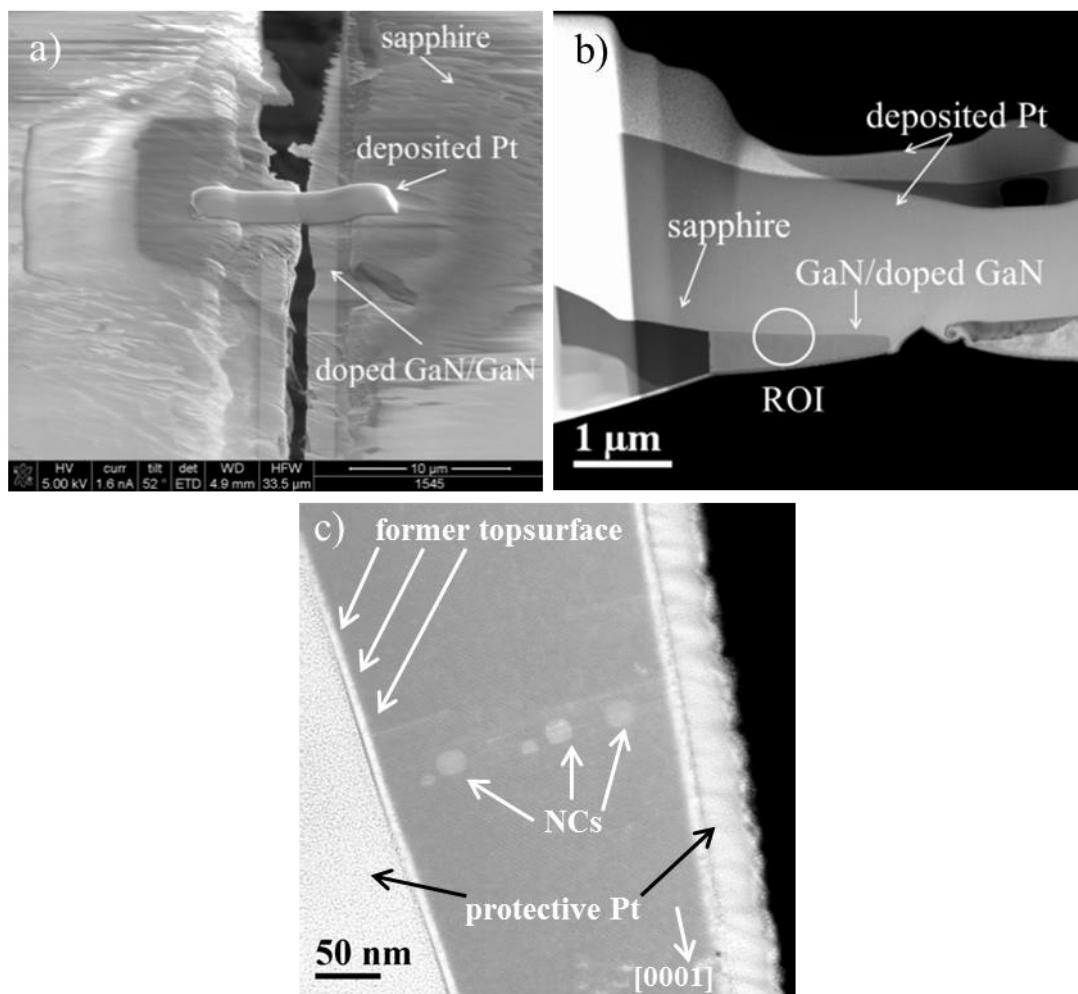


Figure 57: a) SEM image of the extraction region with protective Pt deposited for the TEM lamella extraction; b) HAADF overview image of the fully processed lamella with indicated ROI; c) HAADF image showing the ROI in detail (labelled as former topsurface) with iron-rich nanocrystals in the field of view.

Figure 57c) indicates the area of investigation in more detail marked as “former topsurface”, being from a TEM specimen containing iron-rich nanocrystals. Combined STEM-EELS and -EDXS line scans (within undoped GaN towards the protective platinum as depicted in the STEM image of Figure 58a) across the former top-surface) revealed a strongly oxidized layer of roughly 3 nm width. For the

analysis of the spectrum image the background subtracted EELS signals of the oxygen K edge (signal from 532 eV to 632 eV) and Ga L₂₃ edge (signal from 1142 eV to 1242 eV) were utilized. The unprocessed EDXS signal of the Pt M line (signal from 1.999 keV to 2.199 keV) was used to image the Pt side of the interface. The TITAN microscope was operated at 300 kV with a convergence angle of 19.6 mrad and ~150 pA beam current to record the STEM images shown in Figure 56. The collection angle for EELS was 20.5 mrad with a dispersion of 0.5 eV/channel. The exposure time was 0.05 sec/pixel with a binning of 130. The dispersion of the EDX detector was set to 10 eV/channel with a conversion time of 1 µsec.

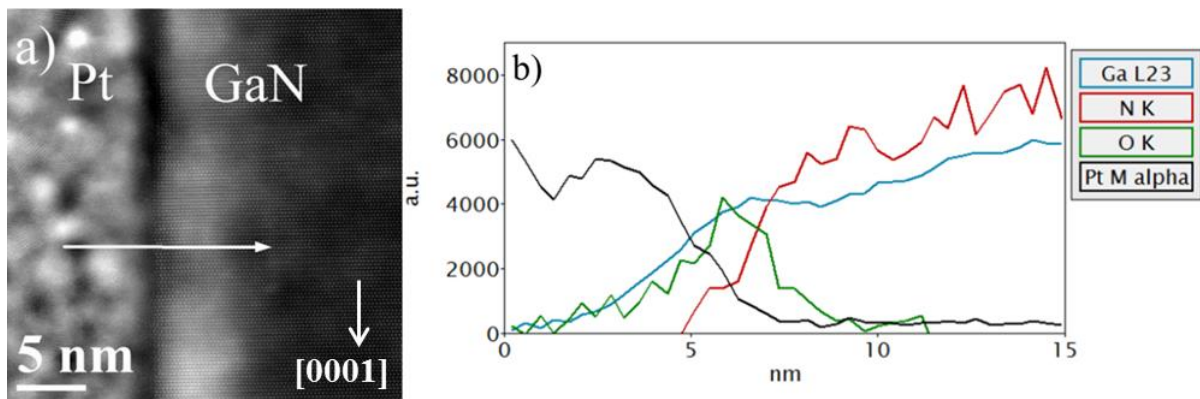


Figure 58: 7 a) HAADF image and STEM-EELS-EDXS line scan with the scan direction indicated by a white arrow; b) extracted line profiles for Ga, N, O and Pt showing surface oxidation with a width of 3 nm. This figure was composed by the author of this thesis and taken from [42].

Figure 58b) is a line plot of the Ga L₂₃, N K and O K edge signals and the STEM-EDXS Pt M α peak signal, combining the relative strengths of both techniques for the detection of light and heavy elements. For the Pt (serving as a protection layer during FIB-cutting) and Ga, strong intermixing occurs, explainable on one hand by the surface roughness and on the other hand by the implantation of FIB-Ga ions into the protection layer, which gets slightly oxidized as well. The surface oxidation of the sample might be introduced by handling the sample on air after the TEM lamella preparation. In parts this is also attributable to the subsequent plasma cleaning step (75 % Ar, 25 % O₂) which is necessary for a contamination-free analysis. The chemistry of the oxidized layer is hardly controllable and consists of varying amounts of oxidized GaN on top of un-modified material.

A possible way to overcome this surface oxidation might be a TEM specimen preparation and subsequent transfer into the TEM under oxygen free conditions. However, this requires rather costly and highly specialized equipment which was not present during the time of this thesis.

8.4 Manganese-doped GaN semiconductors

Two kinds of Mn-doped GaN were investigated as already depicted in Figure 3. Investigations should make clear whether Mn is coherently embedded within the matrix or if any sort of precipitation can be observed. A quantification of the Mn content with EELS and EDXS should furthermore deliver nominal concentrations of the dopant within the matrix. A comparison with other indirect techniques as published in [23,36,37,174] can then be performed.

8.4.1 Homogeneously Mn-doped GaN

To probe the homogeneity of the Mn-doped GaN, aberration-corrected HR-TEM was carried out at the Center for Electron Nanoscopy with a TITAN transmission electron microscope operated at 300 kV acceleration voltage. No distinct phase separation can be observed within the homogeneously Mn-doped region of GaN (Figure 59a). The image was recorded with an aberration free zone of better than 19 mrad leading to a resolution of $> 1 \text{ \AA}$. A similar observation was found for HR-STEM HAADF investigations carried out with the TITAN microscope at FELMI-ZFE in Graz which was operated at 300 kV acceleration voltage. The beam convergence angle was 19.6 mrad and corrector tuning was performed until an aberration free zone of 20 mrad was reached leading to a resolution of 1 \AA or better. Figure 59b) shows a HAADF image with the Ga columns of GaN within the Mn-doped part. Again no distinct phase separation can be observed within the doped part.

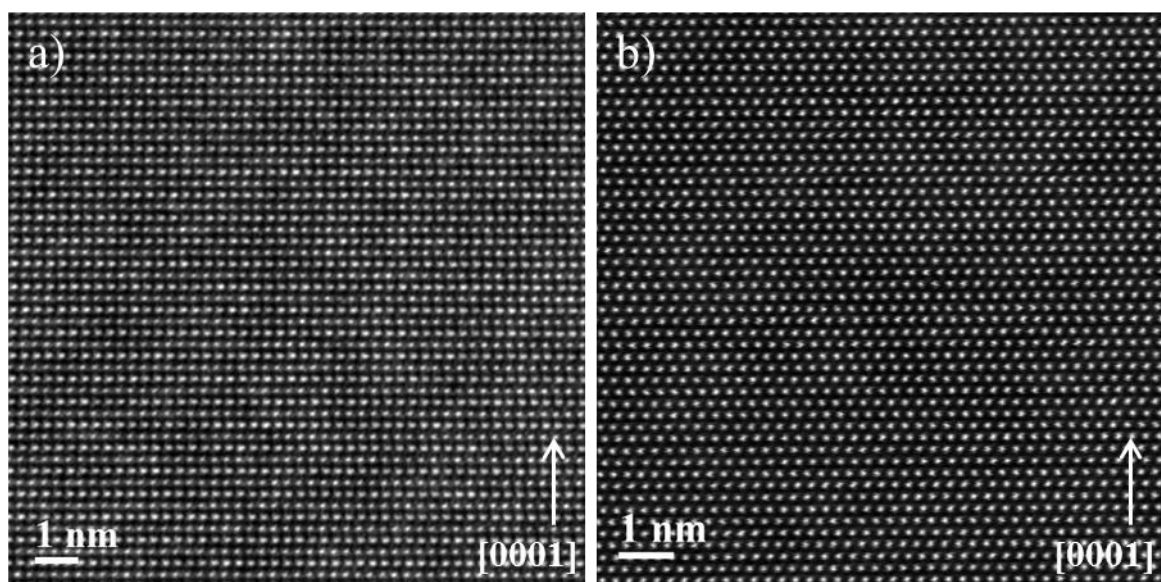


Figure 59: a) Aberration-corrected HR-TEM image of (GaMn)N (recorded at the DTU Copenhagen); b) probe-corrected HAADF image; in both images no distinct phase separation in the homogeneously Mn-doped GaN can be observed.

At the intersection of the GaN buffer and the Mn-doped region a contrast difference at medium magnifications within the HAADF image became visible as shown in Figure 61a). In this image a few

dislocations reach from the buffer layer into the doped GaN layer identifiable as bright vertical lines. High-resolution imaging and analytical measurements were always carried out at least 100 nm away from these dislocations to exclude possible influence. At the interface GaN/(GaMn)N no significant lattice mismatch or crystallographic phase separation despite the rather high doping level was found (Figure 61b). Geometrical phase analysis (GPA) of the GaN/(GaMn)N interface (Figure 60) revealed strain at the interface being in the order of $< 1\%$ for the normal strain components ϵ_{xx} and ϵ_{yy} [175]. The maps were calculated based on Figure 61b).

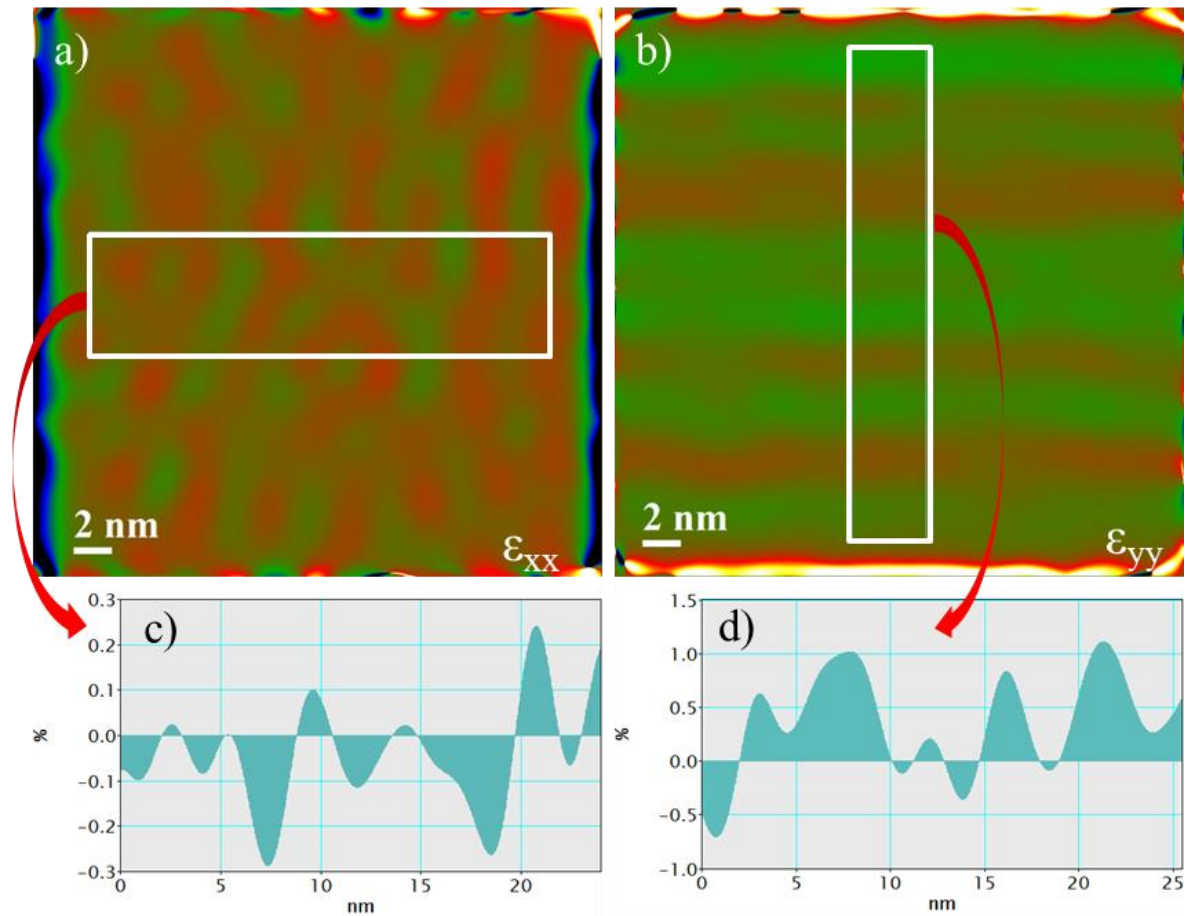


Figure 60: Geometric phase analysis based on the HAADF image of Figure 61b). The results of the normal strain components ϵ_{xx} and ϵ_{yy} are presented in a) and b). The corresponding line profiles are shown in c) and d) displaying a value $< 1\%$.

A faint contrast difference between the GaN/(GaMn)N interface can be identified due to changes in average Z , because of Mn having been mixed homogeneously into the pure GaN solid solution. Figure 61c) displays the profile of the marked region in b) where an increased level of the diffuse background in the order of 2% (indicated by black vertical line) can be identified. The signal of the atomic columns scales accordingly to the background, which can be interpreted as an indication that Mn replaces substitutionally and randomly N or might occupy interstitial sites [34]. This was not expected since Mn is thought to occupy Ga sites. In this case, the average Z should decrease resulting in a reversed contrast compared to the one observed in Figure 61a).

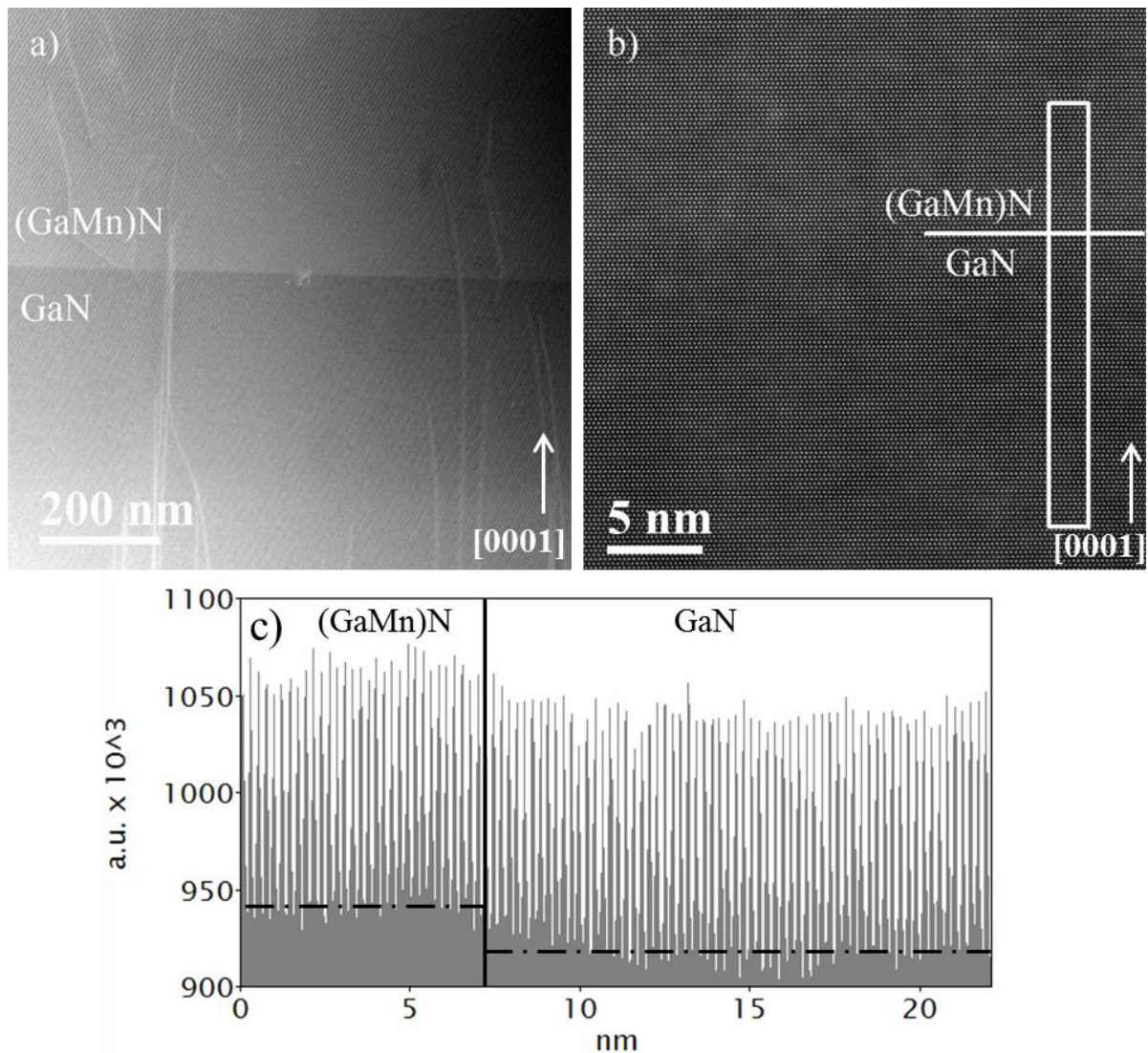


Figure 61: HAADF images of: a) interface between GaN buffer and (GaMn)N, an increased signal intensity for (GaMn)N doped area compared to un-doped GaN detectable; b) no crystallographic phase separation at the interface of (GaMn)N and GaN observable, white rectangle area for line profile; c) extracted line profile of b) showing a stepped contrast increase of the background of ~2% when going from GaN into (GaMn)N (black vertical line). This figure was composed by the author of this thesis and taken from [42].

Spectroscopy was carried out at several randomly picked sample positions within the homogeneously Mn-doped region of GaN, and the EELS Ga L₂₃, N K, O K and Mn L₂₃ edges were quantified. Un-doped GaN was used to orient the TEM specimen to the [11-20] zone axis. Cross-checks for the un-doped GaN showed no presence of Mn and are therefore omitted. Quantification yields a rather uniform Mn concentration of 1.6 ± 0.1 at% averaged over several locations as listed in Table 11 being in good agreement with SQUID data [34]. Concentration values of the other elements are: Ga: 45.4 ± 0.6 at%; N: 48.8 ± 0.8 at% and O: 4.2 ± 1.1 at%.

Table 11: EELS composition taken from randomly picked sample positions within homogeneously Mn-doped GaN (using the Ga L₂₃, N K, O K and Mn L₂₃ edges).

(GaMn)N	Ga [at%]	N [at%]	Mn [at%]	O [at%]
spot 1	45.4	48.6	1.5	4.5
spot 2	45.7	50.4	1.4	2.5
spot 3	45.2	49.0	1.6	4.2
spot 4	46.3	48.1	1.6	4.0
spot 5	44.4	48.1	1.7	5.9
average	45.4 ± 0.6	48.8 ± 0.8	1.6 ± 0.1	4.2 ± 1.1

This TEM specimen exhibited a higher surface oxidation compared to un-doped GaN. The influence of surface oxidation of Mn is negligible since by far most of the co-doped Mn was contained in the bulk GaN matrix.

8.4.2 δ -doped (GaMn)N

Manganese was co-doped in a digital way (δ -doping) as schematically shown in Figure 3b). δ -doped (GaMn)N (Figure 62a) exhibited no apparent precipitation in the Mn-doped area, only slight amorphization occurring as a dark cloud-like overlay originating from the ion thinning process. Nonetheless a quasi-layered structure can be observed, especially, on the left side of Figure 62a) within the δ -doped layer. This is assigned to a mass-contrast rather to a thickness variation since the t/λ map (inset of Figure 62a) displays a rather constant, towards the top part of the TEM specimen decreasing value. Hereby, the value for t/λ varies only by 0.2, increasing from 0.4 to 0.6. The occurrence of a pronounced layer at the beginning of the δ -doped region is not totally clear, but might be attributable to a slight segregation towards the surface in the onset of the doping process.

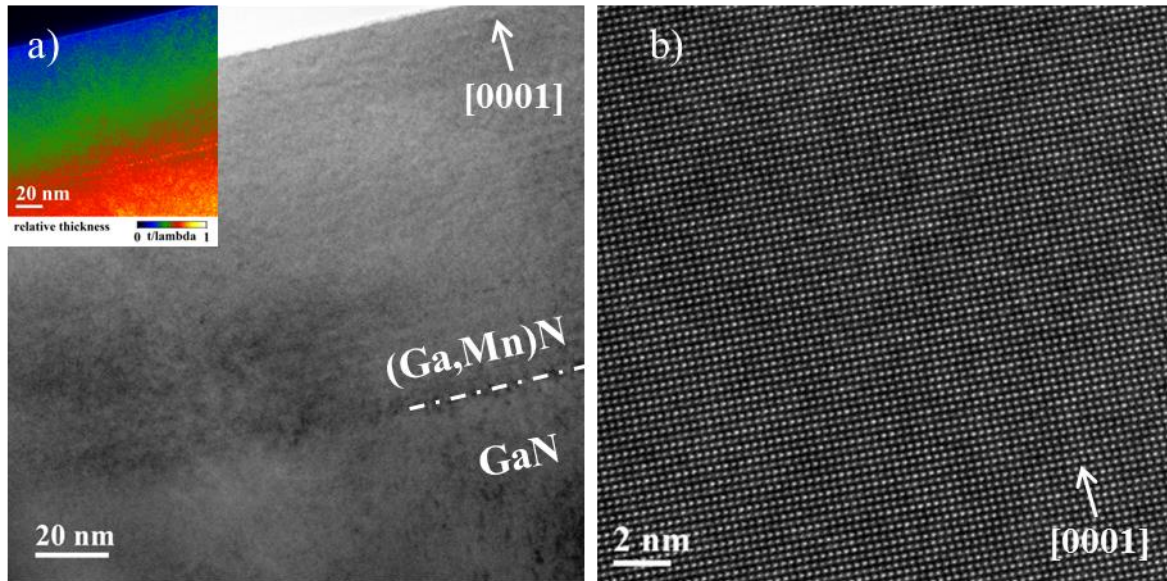


Figure 62: a) BF image of δ -doped GaN exhibiting a layered structure due to mass contrast; inset: corresponding t/λ map with a rather homogeneous, towards the TEM specimen surface decreasing value; b) aberration corrected HR-TEM image showing no traces of precipitation at the atomic level (image recorded at the DTU Copenhagen).

Figure 62b) is an aberration corrected HR-TEM image recorded at the DTU Copenhagen. The TITAN microscope was operated at 300 kV acceleration voltage and the aberration free zone was better than 19 mrad leading to a resolution of $> 1 \text{ \AA}$. The image was acquired in the doped part of the TEM specimen. The electron micrograph shows that Mn is coherently embedded in the GaN matrix.

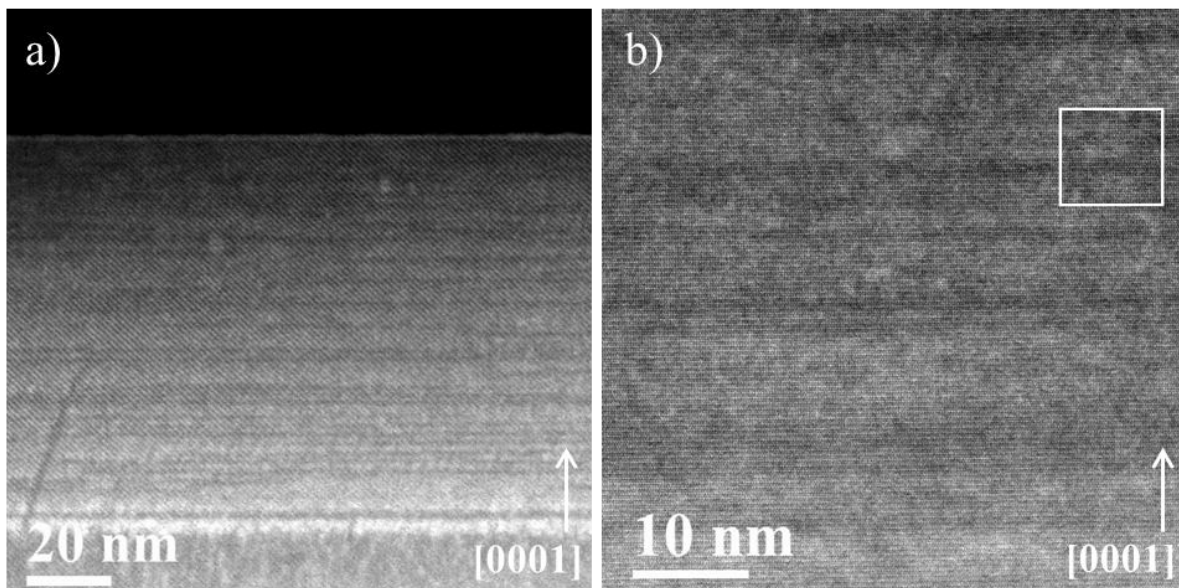


Figure 63: a) HAADF image of the layered structure of the Mn δ -doped GaN; b) higher magnification reveals the irregular appearance of the doping; bright rectangle is the zoom region of Figure 64a). Figures b) was composed by the author of this thesis and taken from [42].

The contrast variation observed in BF imaging becomes even more pronounced by looking at the HAADF image of Figure 63a). A quasi-layered structure can be observed, assigned to the fluctuating

doping level. Figure 63b) shows the disorder in more detail. The layers exhibit irregular periodicity, are irregular in width and often do not continue through the field of view. The white rectangle indicates the region for imaging of Figure 64a).

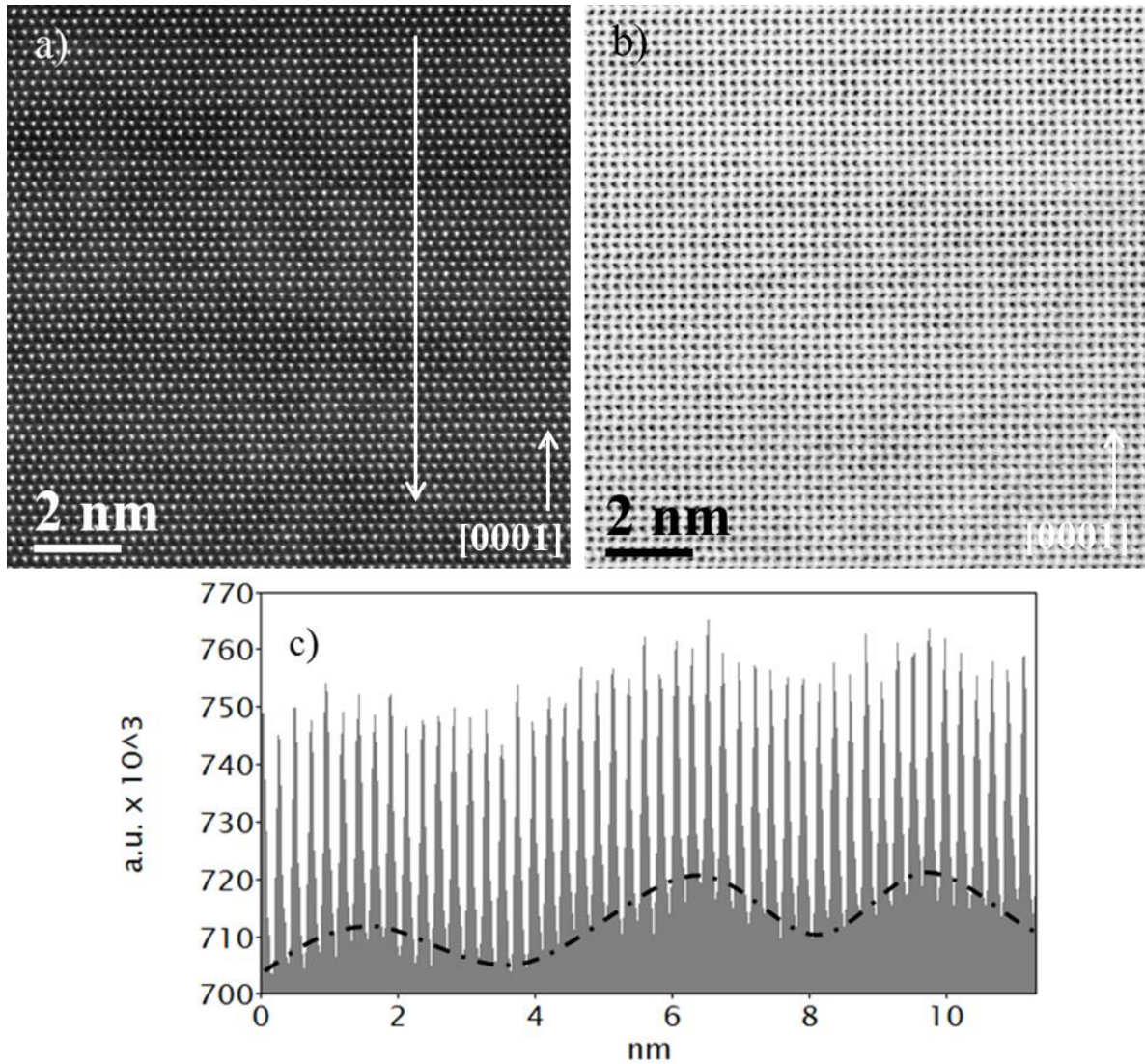


Figure 64: a) High resolution HAADF image of Mn δ -doped GaN exhibiting contrast variation, white arrow: indication of line profile area; b) corresponding ABF image revealing only information about Ga and N; c) extracted line profile of a) showing a sinus-like contrast variation of the background in the order of $\sim 2\%$ as indicated by a dashed line. This figure was composed by the author of this thesis and taken from [42].

GPA analysis was performed based on the high resolution HAADF image of Figure 64a) and the resulting images are shown in Figure 65.

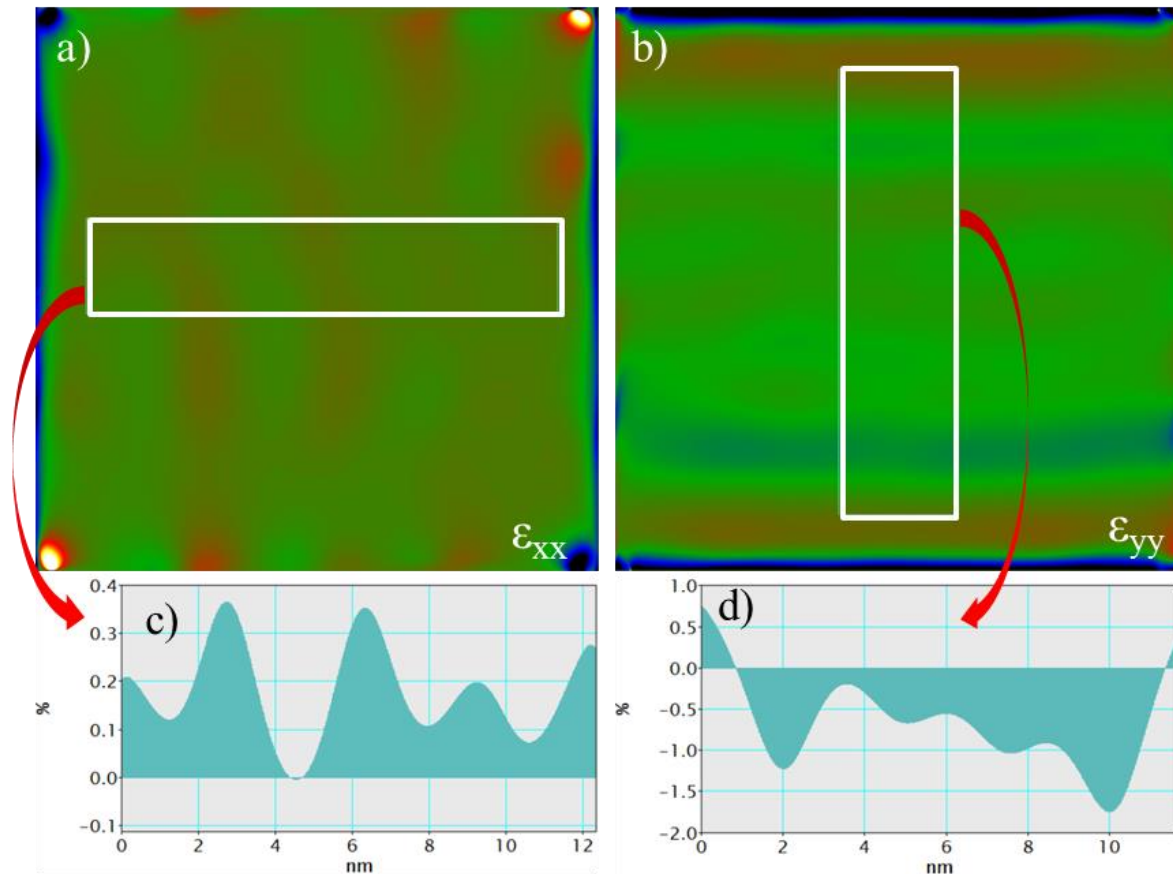


Figure 65: Geometric phase analysis based on the HAADF image of Figure 64a). The results of the normal strain components ϵ_{xx} and ϵ_{yy} are presented in a) and b). The corresponding line profiles are shown in c) and d) displaying a value $> 1\%$.

ϵ_{xx} reveals a positive strain value well below 1% , whereas ϵ_{yy} exhibits a negative maximum of -1.7% . However, both strain components are not significant and indicate the coherent embedment of Mn within the δ -doped region. Figure 64c) depicts an extracted line profile of Figure 64a) showing a sinus-like contrast variation between the bright and dark lines as indicated by a dashed line. To gain more insight to the cause of this contrast variation, EFTEM jump ratio imaging of the Mn L_{23} edge was carried out as displayed in Figure 66a). A slit width of 30 eV for images recorded at 620 eV and 655 eV and an exposure time of 70 sec was used. This was performed on the Tecnai 200kV FEG microscope located in Graz equipped with a GIF Tridiem. The onset of the δ -doping and the subsequent layering is clearly visible. The occurrence of an increased Mn signal at the beginning of the δ -doped region was also resolved as already observed in Figure 62a). From the extracted profile of the Mn distribution image in Figure 66b) two aspects become obvious. Approximately after every 3 nm a Mn doped layer was introduced by the pulsing. The widths of the Mn doped layers range from 2 to 5 nm , depending somewhat on the quality of the deposition within the profiled area. For the integration a relatively undisturbed area was chosen. In addition, an intensity ramp is observed. Since this was a jump ratio experiment, known to be subject to mass-thickness variations, this ramp reflects an altered signal-to-background ratio rather than a concentration change. This is due to the fact that the

total variation in the indicated area (relative to the inelastic mean free path) was only been 0.2, going from 0.4 to 0.6 as shown in the inset of Figure 62a).

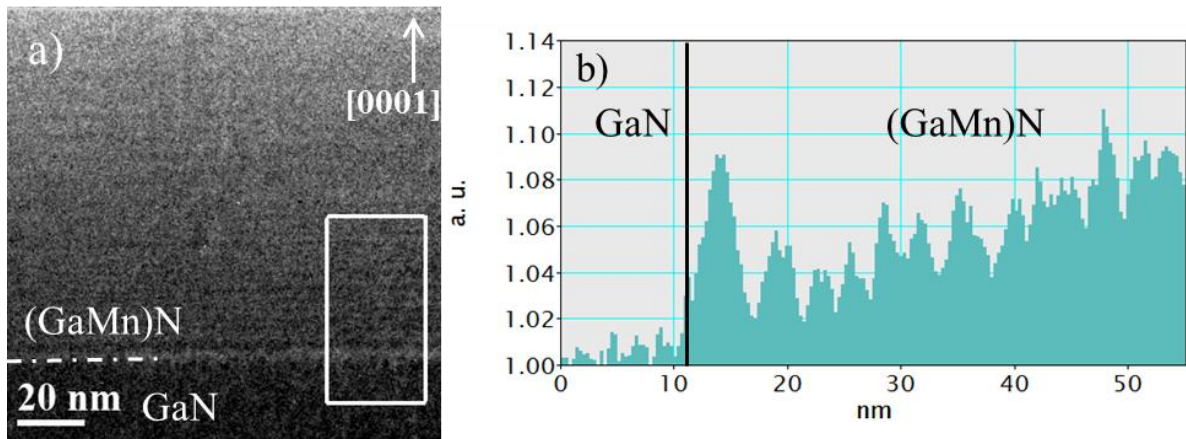


Figure 66: a) Obtained jump ratio map using the Mn L_{23} edge; b) profile of the marked region in a) showing the quasi-layered structure. This figure was composed by the author of this thesis and taken from [42].

Qualitative EDX spectroscopy was carried out at the FEI NanoPort in Eindhoven using a probe-corrected TITAN microscope operated at 200 kV and equipped with the ChemiSTEM technology, (Figure 67a). With this technology it was possible to qualitatively map the doping using Mn $K\alpha$ radiation. Again the irregular layered structure can be observed. Furthermore, Figure 67b) shows that the Mn signal is only varying in intensity but not completely going to zero in the intentionally undoped regions.

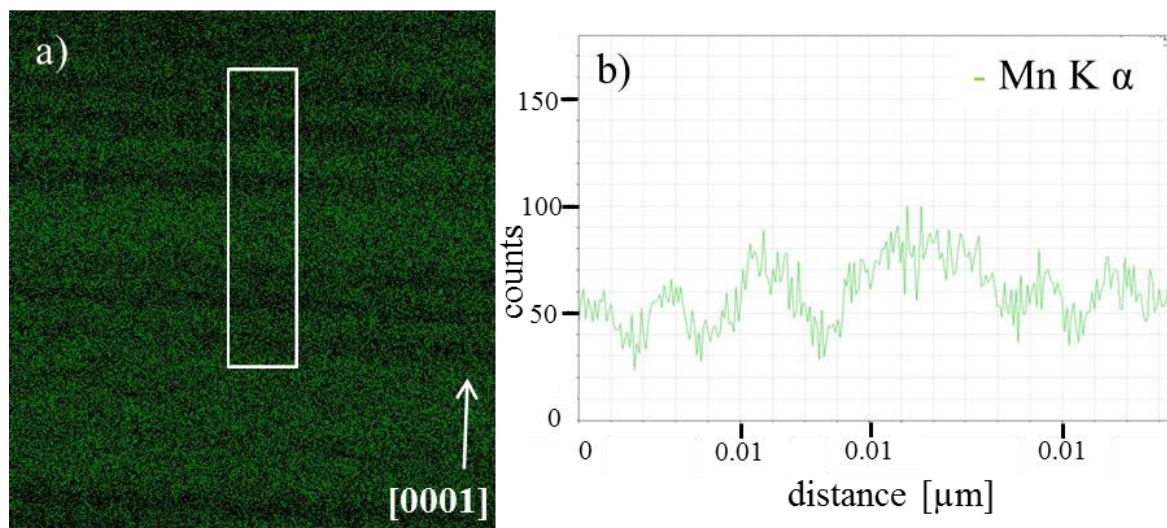


Figure 67: a) Layered structure of Mn δ -doped GaN using Mn $K\alpha$ radiation for imaging (image not calibrated therefore the scalebar is omitted); b) extracted line profile with varying signal, note that the signal does not decrease to zero (labeling edited for better visibility).

No X-ray sensitivity factors and beam current measurements were available to perform any quantification. For quantification EEL spectroscopy at randomly picked sample positions within Mn-

doped GaN [11-20] zone axis was performed on the TITAN microscope in Graz. It was crucial to place the probe on or between one of the lines and assure that the TEM specimen drift was negligible during spectrum acquisition. The measurements were performed at 300 kV accelerating voltage with a convergence angle of 19.6 mrad. A dispersion of 0.5 eV/channel with a collection angle of 40.3 mrad and an energy offset of 400 eV were used for the EELS measurements. Table 12 shows the obtained results for dark and bright layers by utilizing the Ga L₂₃, N K, O K and Mn L₂₃ edges.

Table 12: Quantitative EELS results obtained from randomly picked sample position within Mn δ -doped GaN utilizing the Ga L₂₃, N K, O K and Mn L₂₃ edges.

Position number	quasi-layer type	Ga [at%]	N [at%]	Mn [at%]	O [at%]
spot 1	dark	47.2	43.4	1.1	8.4
spot 2	dark	46.7	40.9	1.7	10.7
spot 3	dark	45.0	44.3	0.3	10.4
spot 4	dark	49.7	48.8	1.9	0.0
spot 5	dark	47.6	45.1	1.7	5.6
spot 6	dark	49.2	45.3	0.0	4.2
spot A	bright	47.9	45.9	3.5	2.6
spot B	bright	47.3	44.1	3.5	5.1
spot C	bright	47.9	47.7	2.4	2.1
spot D	bright	48.7	48.8	3.1	0.0
spot E	bright	47.4	49.9	2.8	0.0
spot F	bright	44.4	44.1	2.3	9.2

The average Mn concentration in bright layers is found as 2.9 ± 0.5 at%, with Ga to be 47.3 ± 4 at%, N to be 46.8 ± 2.2 at% and O to be 3.2 ± 3.2 at%. The average value of Mn in between dark layers is 1.3 ± 0.5 at%, with Ga: 47.6 ± 1.6 at%; N: 44.6 ± 2.4 at% and O: 6.5 ± 3.7 at%. This is about 50 % less compared to the doped layers but not reaching the nominal zero. The high concentration variation of both layer-types reflects the heterogeneous deposition of Mn contrasting the homogeneously doped sample. Due to this strong local inhomogeneity between the lines and within a line itself, it is not feasible to give a meaningful average dopant concentration as it was done for the homogeneous sample. An absolute quantification was obtained using the “StripeSTEM” technique [176]. This technique has been developed at the Ernst Ruska-Centre for Microscopy and Spectroscopy with Electrons (Forschungszentrum Jülich) and is installed at the “FEI TITAN STEM” electron microscope which was operated at 300 kV acceleration voltage. A HAADF image utilizing a probe with a convergence angle of 19.6 mrad and an aberration-free zone of 19 mrad leading to a resolution of ~ 1 Å was recorded with a rather long dwell time of 91 μ sec per pixel. At the same time a GIF Tridien was recording the resulting EEL spectrum with a collection angle of 9 mrad, a dispersion of 0.5 eV/channel, a 2 sec per spectrum dwell time and vertical binning of 8. In this way one EEL

spectrum corresponds to roughly one atomic line of the HAADF image. The relative thickness t/λ measured in the ROI was 0.44. The used conditions were such that 20 lines of the STEM image contribute to 1 EEL spectrum. Figure 68a) is a HAADF image overlaid with the background-subtracted EEL spectrum of Mn L₂₃ using a signal width from 638 eV to 678 eV.

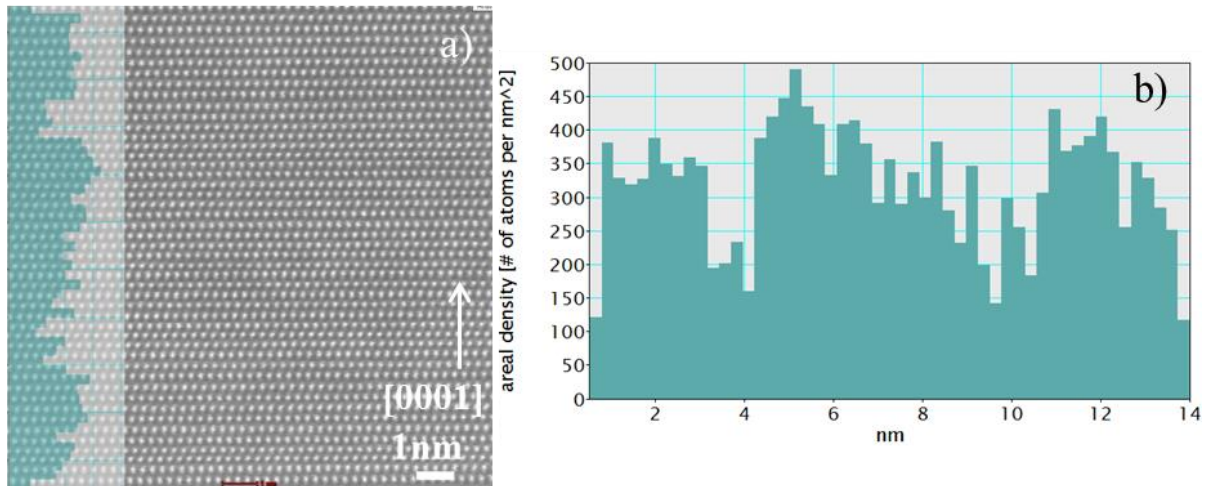


Figure 68: a) “StripeSTEM”-technique: EEL spectra of the background-subtracted Mn L₂₃ signal overlaid with the recorded STEM image; b) number of atoms per unit area [nm²].

Figure 68a) and b) show that the Mn content is fluctuating but never vanishing. The absolute number of Mn atoms is varying between 100 and 500 per nm². This confirms the previous result that the intentionally un-doped layers are rather small with 2 to 3 nm.

8.5 Iron-doped GaN semiconductors

This class of material was studied by the collaborators in Linz beforehand with respect to their magnetic and optical properties via both conventional and synchrotron radiation-based techniques [31,35,38,177,178]. The scientific questions related to AEM were specifically formulated based on these pre-studies:

- Is it possible to image the nanocrystals and determine whether a coherent embedment of nanocrystals is present?
- Is iron only present in the nanocrystal or also in the GaN matrix?
- Can a direct quantification of individual nanocrystals for two different nominal concentrations be performed?
- Is it possible to link the obtained nanocrystal composition to XRD and magnetization results?

XRD and magnetization measurements indicate a preferred composition of the nanocrystals leading to the assumption that the nanocrystals are preferably composed of Fe₃N for the sample with nominally 0.25 at% Fe doping. A mixture of Fe₃N and Fe₄N for the sample with nominally 0.5 at% Fe doping was indicated [38]. Structural investigations confirmed that the nanocrystals are in a planar

arrangement as depicted in Figure 69a) [38]. The nanocrystals grow in a certain depth which is triggered by the detailed growing conditions [37]. They grow with a rather narrow size distribution at a defined depth within the sample [177]. Figure 69b) depicts exemplarily a size variation of the individual nanocrystals. The diameters of the nanocrystals range from 5 nm (smallest observed) to 50 nm (biggest observed). It is found (Figure 70) that many of the nanocrystals exhibit an elongated shape perpendicular to the growth direction. A plane-view TEM investigation shown in [38] confirms a spheroidal shape of the nanocrystals.

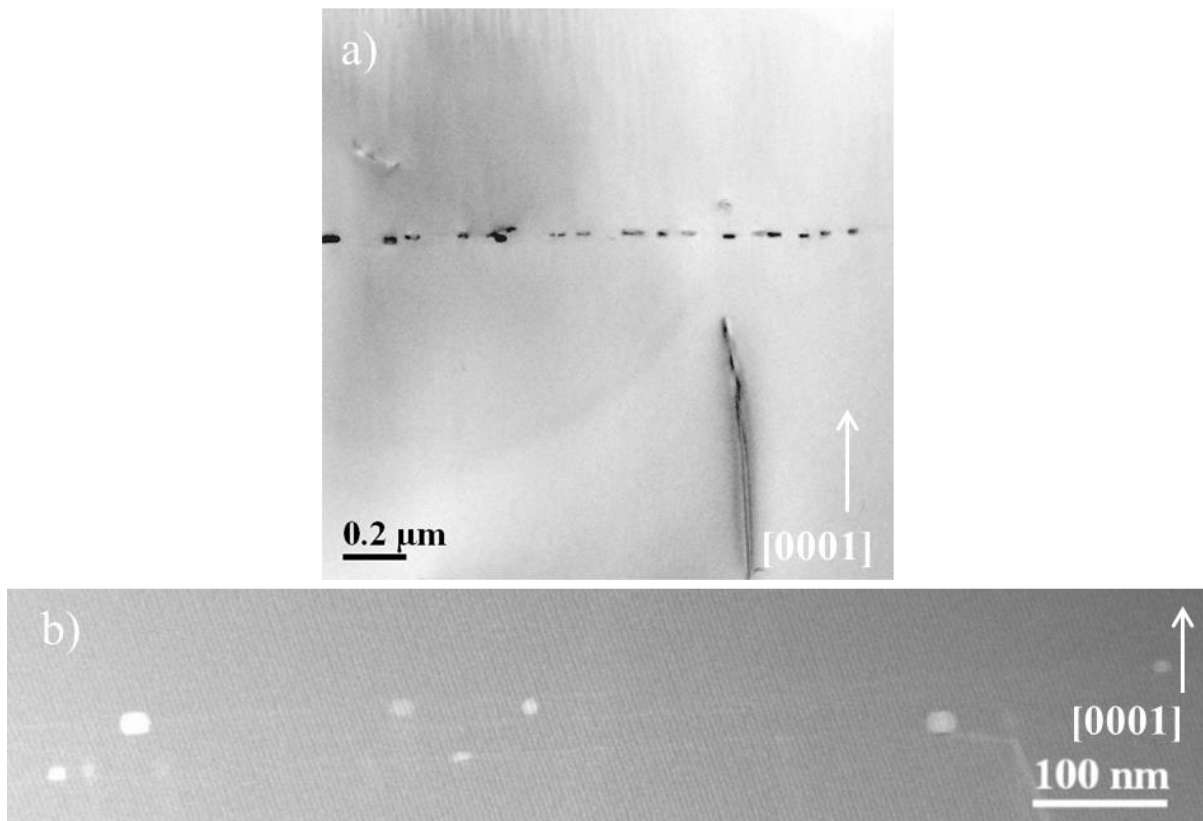


Figure 69: a) BF TEM image showing a planar arrangement of the nanocrystals; b) HAADF overview image of nanocrystals aligned within the ROI.

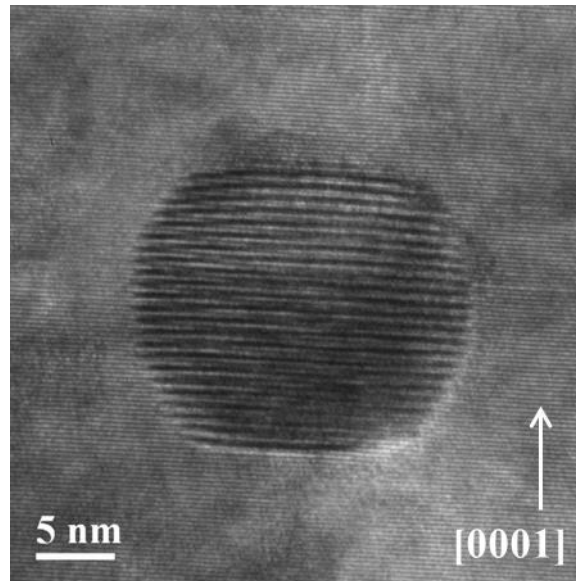


Figure 70: HR-TEM image of a typically sized nanocrystal with Moiré fringes originating from the different lattices of the GaN and the nanocrystal.

A difference in contrast between the individual nanocrystals can be observed in Figure 69b). This is ascribed to two possibilities schematically depicted in Figure 71:

1. The individual nanocrystals have a different composition leading to a variation in contrast based on the epitaxial nature of the growth process.
2. A number of nanocrystals were sliced during the ion thinning process and thereby altered their composition (e.g.: through oxidation).

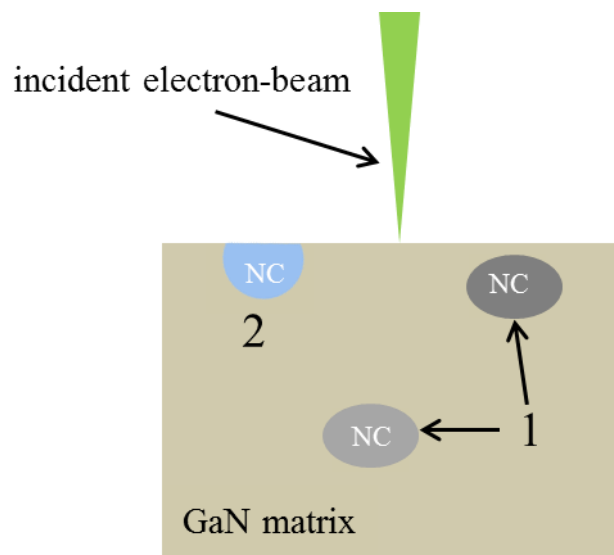


Figure 71: Two possibilities for the observed contrast differences between individual nanocrystals: 1: individual chemical composition; 2: slicing during ion-tinning.

Figure 72a) displays an atomically resolved HAADF image of a typical nanocrystal. Figure 72b) are Fourier transforms of the regions marked in a) indicating an epitaxial relationship between the

nanocrystal and the matrix. This strengthens the assumption that the nanocrystals grow epitaxial into the matrix [38].

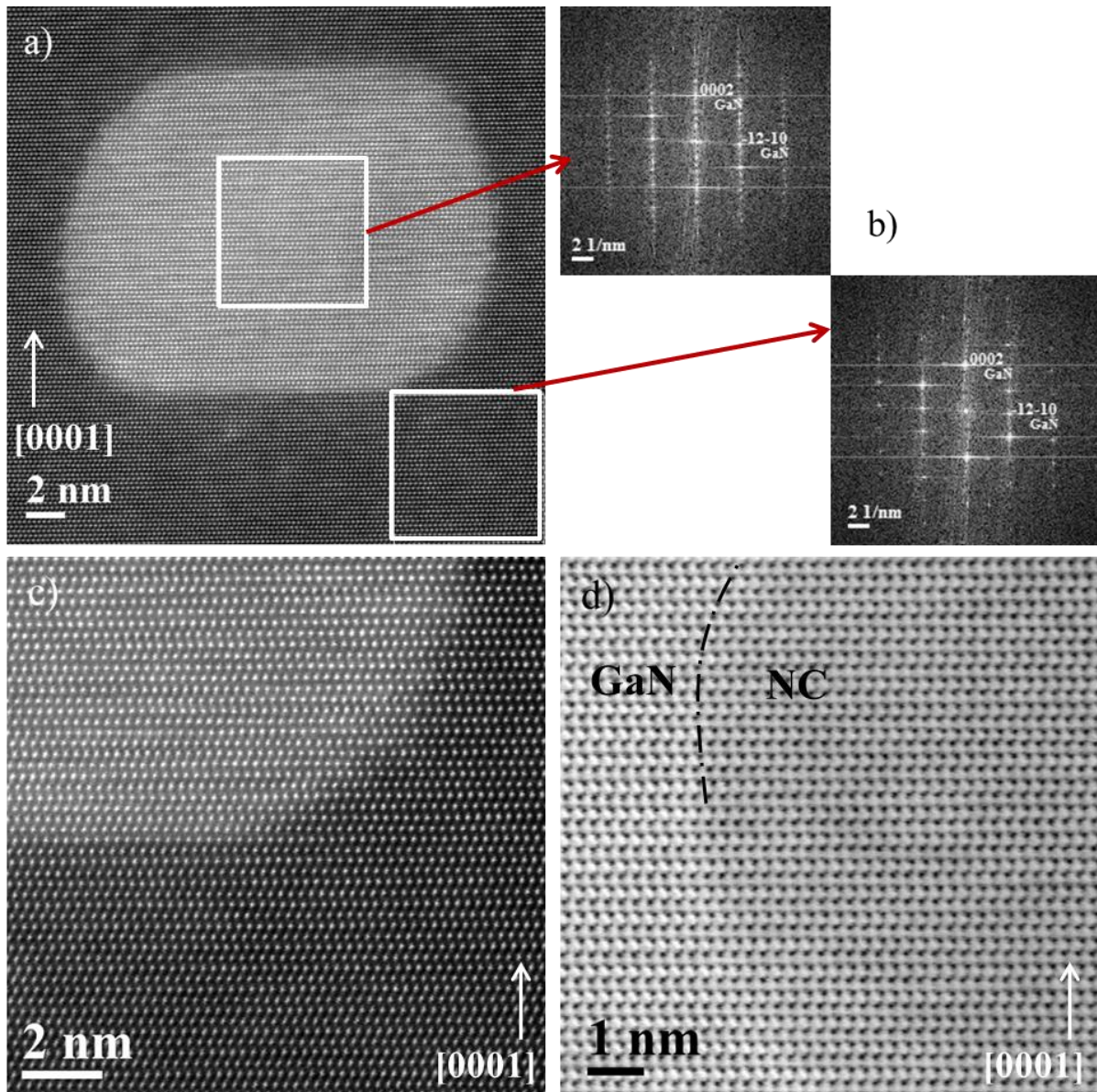


Figure 72: a) HAADF image of a typical nanocrystal; b) Fourier transforms of the marked regions a) showing an aligned superposition of frequencies, being a fingerprint for an epitaxial relationship between nanocrystal and matrix; c) coherent embedding of the nanocrystal in the matrix; d) ABF image of a GaN/NC transition revealing no observable lattice distortion of the surrounding matrix. The figures a), c) and d) were composed by the author of this thesis and taken from [42].

The HAADF and ABF images in Figure 72c) and d) display the interface between a typical nanocrystal and the GaN matrix. Both reveal no apparent structural changes or lattice distortions across the interface. Only a variation of the background can be observed in both images caused by the nanocrystal. By overlaying both images in color as shown in Figure 73 no distinct structural change of the GaN matrix can be observed.

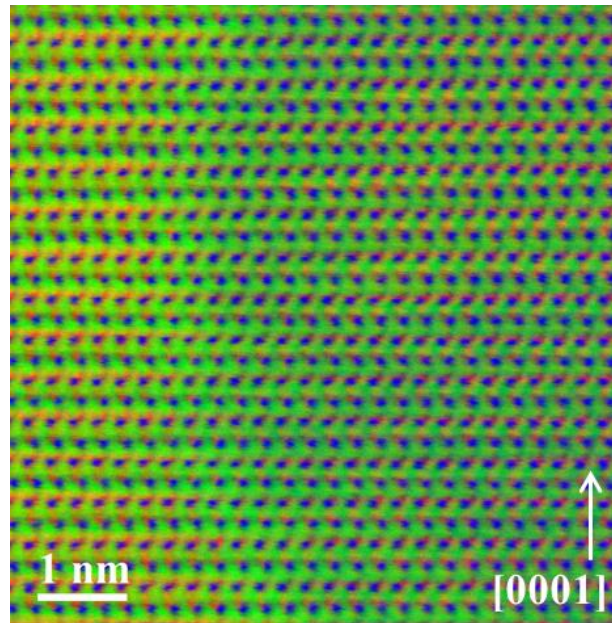


Figure 73: Colored overlay of the ABF image taken from Figure 72d) and the corresponding HAADF image; the overlay reveals no distinct structural change of the GaN matrix; Ga = blue; N = red; background = green.

Figure 74 shows a background subtracted STEM-EELS elemental map of iron for a nanocrystal using the Fe L_{23} edge.

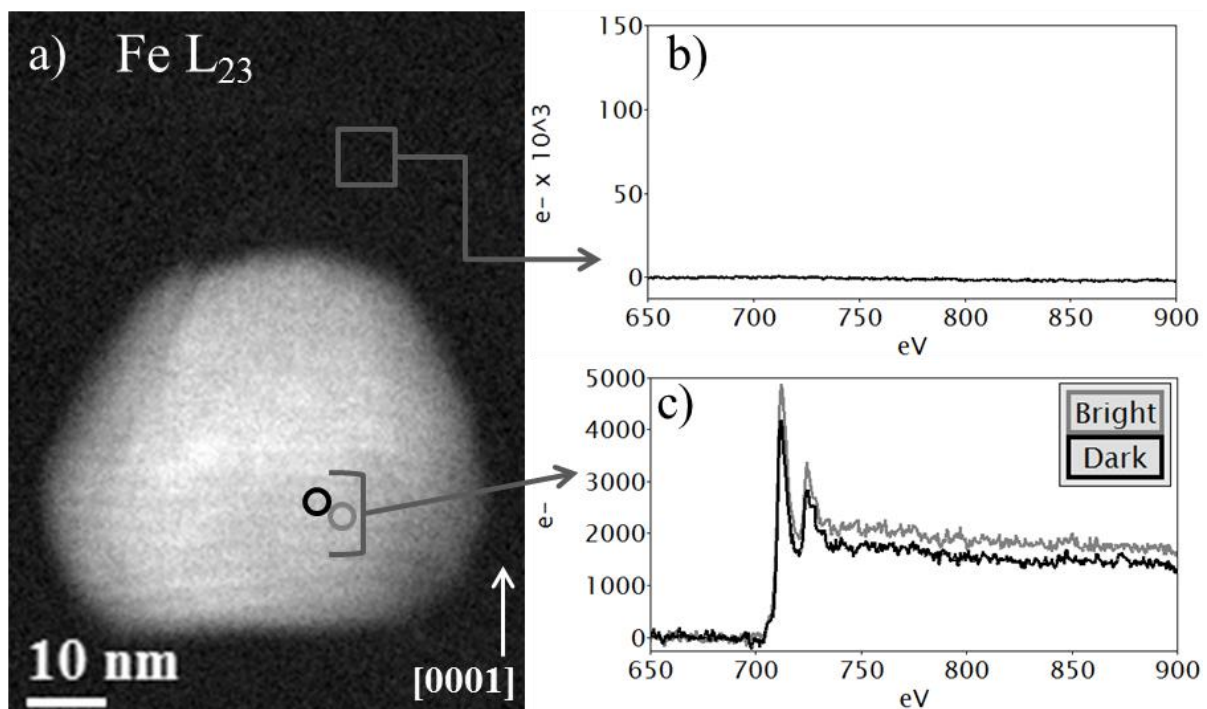


Figure 74: a) Background subtracted Fe L_{23} EELS map of a nanocrystal surrounded by the GaN matrix; extracted and summed EEL spectra from the marked regions in a) for: b) displaying the presence of Fe only within the nanocrystal; c) intensity differences within an Fe-rich nanocrystal. This figure was composed by the author of this thesis and taken from [42].

Figure 74b) contains the summed spectra of the region marked in Figure 74a) depicting that iron is only present within the nanocrystal and not diffused into the matrix during growth or post-growth

treatment. In a few rare cases the precipitates display an elemental variation as observable in the elemental map of Figure 74. The corresponding spectra of Figure 74c) indicate intensity differences within the nanocrystal of approximately 20 % change of Fe concentration. This modulation is compensated by an equal amount of Ga where Fe is depleted. Although these effects might be present in all particles the overall variation in Fe content from nanocrystal to nanocrystal is by far larger. To obtain a statistical result several nanocrystals of both doping amounts were analytically investigated. Quantitative measurements were performed by recording EELS signals (Ga L_{23} , N K, O K and Fe L_{23} edges) and EDXS signals (N $K\alpha$, O $K\alpha$, Ga $K\alpha$ and Fe $K\alpha$). Actual measurements were carried out in the form of ROI scans across the central part of the nanocrystal with the 200 kV FEG Tecnai microscope in STEM mode. A beam current ranging from 150 pA to 250 pA was used. The acquisition time for EELS was set to 200 sec with a collection angle of 15.9 mrad and a dispersion of 0.5 eV/channel. The TEM specimen was tilted 15° towards the EDXS detector to avoid channeling effects and to maximize signal collection during the 400 sec acquisition time. The EDXS data were evaluated with the ζ -factor method being described in detail in section 6.8. Table 13 lists background windows and the signal window used for EDXS quantification. Background subtraction from the signal window was performed by summing up and averaging the counts of both windows left and right of each respective line. The signal window was chosen to be 1.2 times the FWHM of each respective line [62].

Table 13: Signal window and background windows used for quantification by the ζ -factor method.

Element	Background window 1 [keV]	Background window 2 [keV]	Signal window [keV]
N	0.171 - 0.191	0.801 - 0.841	0.321 - 0.451
O	0.171 - 0.191	0.801 - 0.841	0.461 - 0.561
Fe	5.601 - 5.751	7.251 - 7.401	6.331 - 6.481
Ga	8.311 - 8.521	10.791 - 11.001	9.141 - 9.351

Actual quantifications were performed using a software package written by Watanabe [140]. After insertion of the background subtracted counts of each respective element, the detector properties, the experimentally determined ζ -factors and the used beam current the software returns an element composition given in at%.

A ROI scan was chosen to reduce beam induced damage to the nanocrystal as a result of the long acquisition time for EDXS and to reduce preferential sputtering of nitrogen. Each nanocrystal was measured only once due to the fact that re-measurements of the same nanocrystal, even if the nanocrystal appeared unaltered in a STEM image, showed a noticeable decrease of the nitrogen signal. Initially, oxygen was not included into the quantification of the nanocrystals. It was attempted to “synthesize” nanocrystals with a composition of Fe_3N or Fe_4N embedded within the GaN matrix. For this, the obtained amount of Ga was subtracted from the obtained N amount to form the GaN matrix.

In a next step the remaining amount of N was used to calculate a nanocrystal composition with the obtained Fe content. By looking at the data in Table 14 it was obvious that the ratio of Fe/N was strongly fluctuating and not close to the expected ones (3 for Fe₃N or 4 for Fe₄N).

Table 14: Quantification results (EELS) of several nanocrystals with the ratio of Fe/N after Ga subtraction.

Nanocrystal	Ga [at%]	N [at%]	Fe [at%]	Fe/N ratio after Ga subtraction
#1	27.6	43.9	28.5	1.7
#2	31.7	48.0	20.3	1.2
#3	40.4	54.7	4.9	0.3
#4	39.9	54.8	5.3	0.4
#5	25.2	43.1	31.7	1.8

The inclusion of oxygen to the data analysis led to the following picture: On average, the amount of Ga content is increased and the amount of Fe and N are decreased. Several further attempts of an elaborate data-processing (with the inclusion of the oxygen signal) were performed:

- GaN matrix measurements, usually at a distance of 30 – 50 nm from a nanocrystal, were used as a “reference”. At this distance the composition of the matrix should be stoichiometric, i.e. 50 at% Ga and 50 at% N. Due to the deviation of the analytical results from this composition correction factors for Ga and N were calculated based on the GaN matrix measurement. These correction factors were used either to increase the nitrogen content or alternatively decrease the gallium content of nanocrystal measurements and thereby adjusting the Fe content accordingly by re-normalizing all constituents to 100 at%. Results of this procedure are exemplarily shown in Table 15. It can be seen that the values obtained in both correction procedures still differ for each element. The obtained concentration values of the modification via increase of nitrogen and decrease of gallium for each nanocrystal were then averaged separately for each quantification technique (EDXS and EELS). This was done in order to further even out uncertainties caused by limitations of the used quantification procedure.

Table 15: Results of corrected at% values in the case for EELS for several nanocrystals (identical nanocrystals as listed in Table 14).

Nanocrystal	increase	modified	modified	modified	decrease	modified
	Ga [at%]	N [at%]	Fe [at%]	Ga [at%]	N [at%]	Fe [at%]
#1	32.8	40.7	26.5	30.5	37.9	31.6
#2	37.4	44.0	18.6	35.5	41.9	22.6
#3	46.6	49.0	4.4	45.0	48.5	5.5
#4	45.0	49.2	4.8	45.4	48.6	6.0
#5	30.2	40.2	29.6	27.9	37.1	35.0

- It was tried to identify classes of nanocrystals belonging to certain chemical phases within a ternary diagram. Both, the original and the corrected compositional values were used. However, it was not feasible due to the large scatter of the data.
- In an attempt to extract surface oxygen, in order to get an approximate value of the nanocrystal composition, a gallium oxide (Ga_2O_3) layer was assumed being the only source for oxygen in the sample. A stoichiometric fractional intensity of Ga being scaled to oxygen was subtracted from the nanocrystal. Subtraction of the remaining amount of gallium to form the matrix was performed as a next step. With the remaining amount of nitrogen a comparison with Fe_3N and Fe_4N was done but no reasonable match could be achieved for a statistically significant number of nanocrystals.

It became obvious that absolute concentration measurements had limitations mostly due to uncertainties related to tackle the embedding of the nanocrystals properly. Therefore, further data analysis was performed in a relative way for each measurement technique separately. The two phases were compared among themselves as shown in Table 16. Systematic errors associated with low detection sensitivities and absorption for light elements (e.g. N, O) in EDXS, and the uncertainties in the inner-shell ionization cross sections for heavier elements (e.g. Ga) in the case for EELS could be reduced.

Table 16: Concentration ratio of samples with 0.25 at% and 0.5 at% for EELS and EDXS; the ratio is given separately for Ga, N, Fe and O; both measurement techniques reflect similar trends for the individual ratios.

EELS	Ga	N	Fe	O
0.5 at%/0.25 at%	0.8 ± 0.1	0.9 ± 0.1	2.6 ± 1.9	1.7 ± 1.9
EDX	Ga	N	Fe	O
0.5 at%/0.25 at%	0.8 ± 0.1	0.9 ± 0.2	2.3 ± 1.5	2.3 ± 1.9

In general, the two techniques show similar trends. The Ga and N concentrations decrease to accommodate the large amounts of dopant and the additional oxygen. The Fe concentrations are on average about 2.5 times larger in the 0.5 at% doped sample compared to the 0.25 at% one. This yields a ratio of ~25 % higher than the nominal one, with slight differences in Fe signal between the techniques. The situation on a per nanocrystal basis, showing the fluctuations in O and Fe content, is depicted in Figure 75. The dashed lines indicate the calculated average value for each technique within each graph. The values are:

- 0.25 at% Fe doping:
 - EELS: Fe: 7 ± 4 at%; O: 4 ± 2 at%
 - EDXS: 9 ± 4 at%; O: 3 ± 2 at%
- 0.5 at% Fe doping:
 - EELS: Fe: 17 ± 9 at%; O: 7 ± 2 at%
 - EDXS: 21 ± 10 at%; O: 7 ± 2 at%

The amounts of oxygen in the 0.25 at% doped sample are as low as 0 at% and go up to 7 at%, whereas in the 0.5 at% counterpart, the oxygen level has a minimum of 2 at% and almost reaches 9 at%.

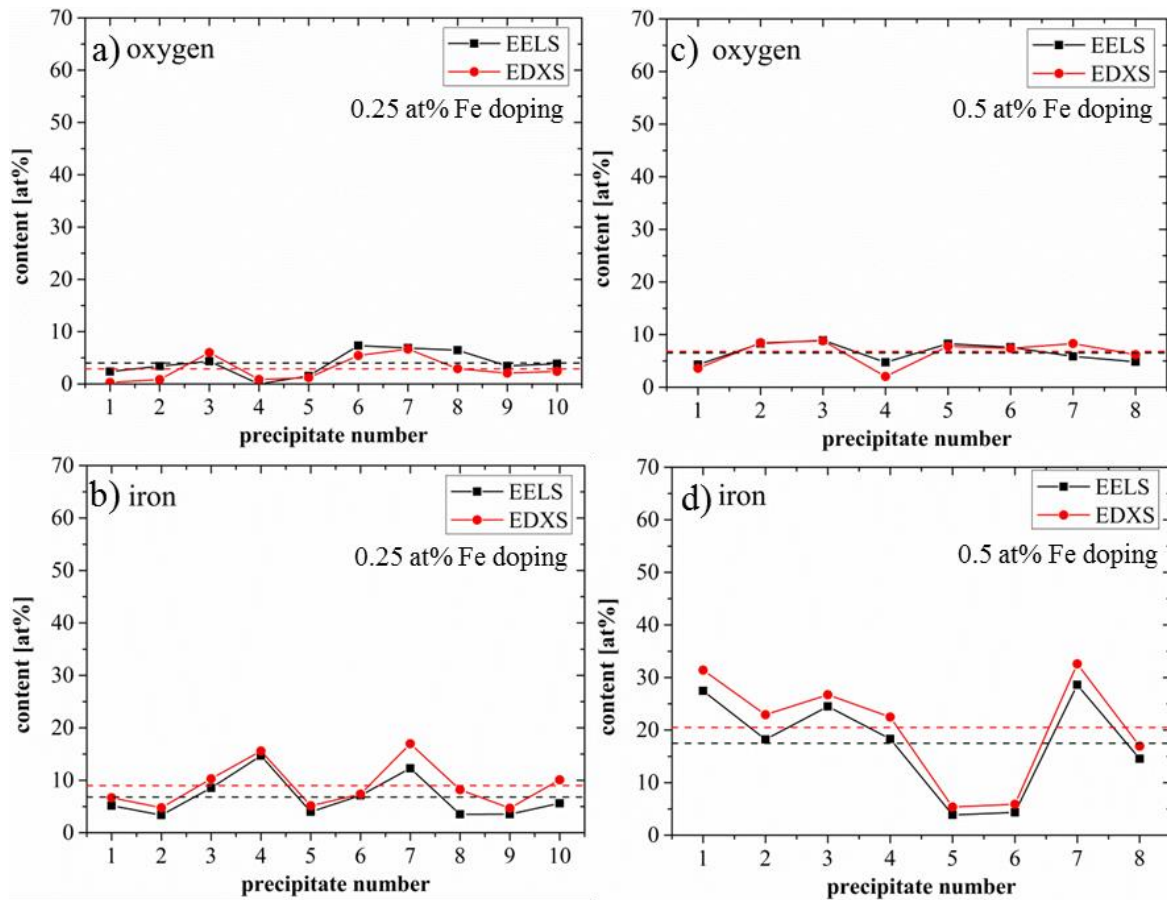


Figure 75: Variation of O and Fe content from nanocrystal to nanocrystal for 0.25 at% Fe doping (a and c) and 0.5 at% Fe doping (b and d); dashed lines indicate the average value of Fe and O for each doping level. This figure was composed by the author of this thesis and taken from [42].

The amounts of the remaining constituents are depicted in Figure 76. The obtained values are as follows:

- 0.25 at% Fe doping:
 - EELS: Ga: 35 ± 2 at%; N: 54 ± 2 at%
 - EDXS: Ga: 55 ± 5 at%; N: 33 ± 8 at%
- 0.5 at% Fe doping:
 - EELS: Ga: 29 ± 5 at%; N: 47 ± 4 at%
 - EDXS: Ga: 43 ± 6 at%; N: 30 ± 4 at%

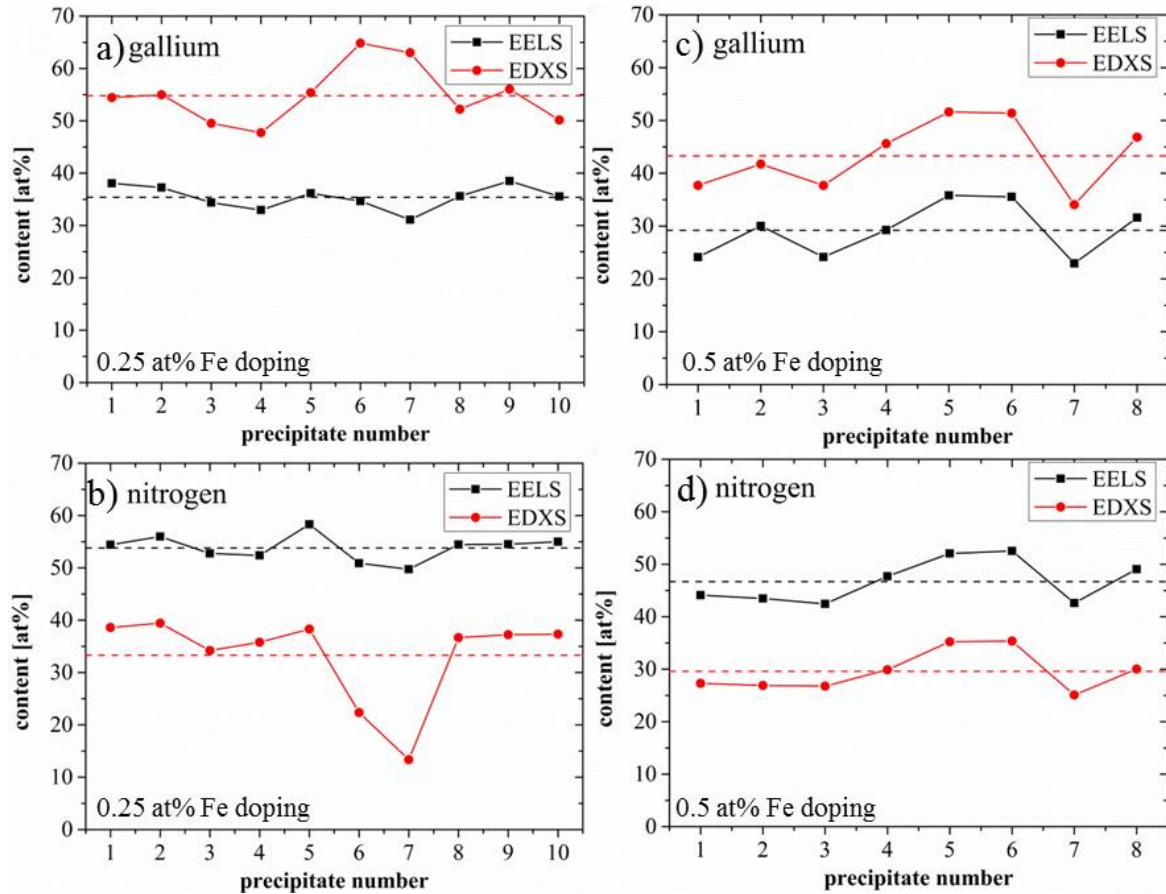


Figure 76: Variation of Ga and N content from nanocrystal to nanocrystal for 0.25 % Fe doping (a and c) and 0.5 % Fe doping (b and d); dashed lines indicate the average value of Ga and N for each doping level.

On average, the O concentrations are about twice as high in the 0.5 at% doped case, including and assuming equal amounts of surface oxygen in both samples. The discrepancy between EELS and EDXS measurements might be due to the uncertainty in the peak extraction at low energies for EDXS. The general picture of having more oxygen with increasing dopant concentrations falls short when looking at the individual nanocrystals. Both in the 0.25 at% and in the 0.5 at% case Fe and O levels vary largely, indicating the formation of complex phases. A possible reason might be the location of the nanocrystal closer to the TEM specimen surface. To better account for the embedding of the nanocrystals in the matrix in a quantitative analysis, one either has to make assumptions about the volumes of the crystal and correlate it with an absolute volumetric evaluation, perhaps by means of tomography. Alternatively, a particle extraction preparation process might be considered, taking into account that in this case etching, consequent reduction of the nanocrystal size, modification of their stoichiometry and surface oxidation can occur.

8.6 Diffusion characterizations of Heusler-alloys on GaAs

The technological aspects of Heusler alloys are outlined in section 4.3 and the composition of the layers is presented. Interdiffusion has been identified by Auger depth profiling and for a quantitative characterization of the diffusion (GaAs substrate and ferromagnetic FeSi Heusler alloy) two FIB lamellas were fabricated.

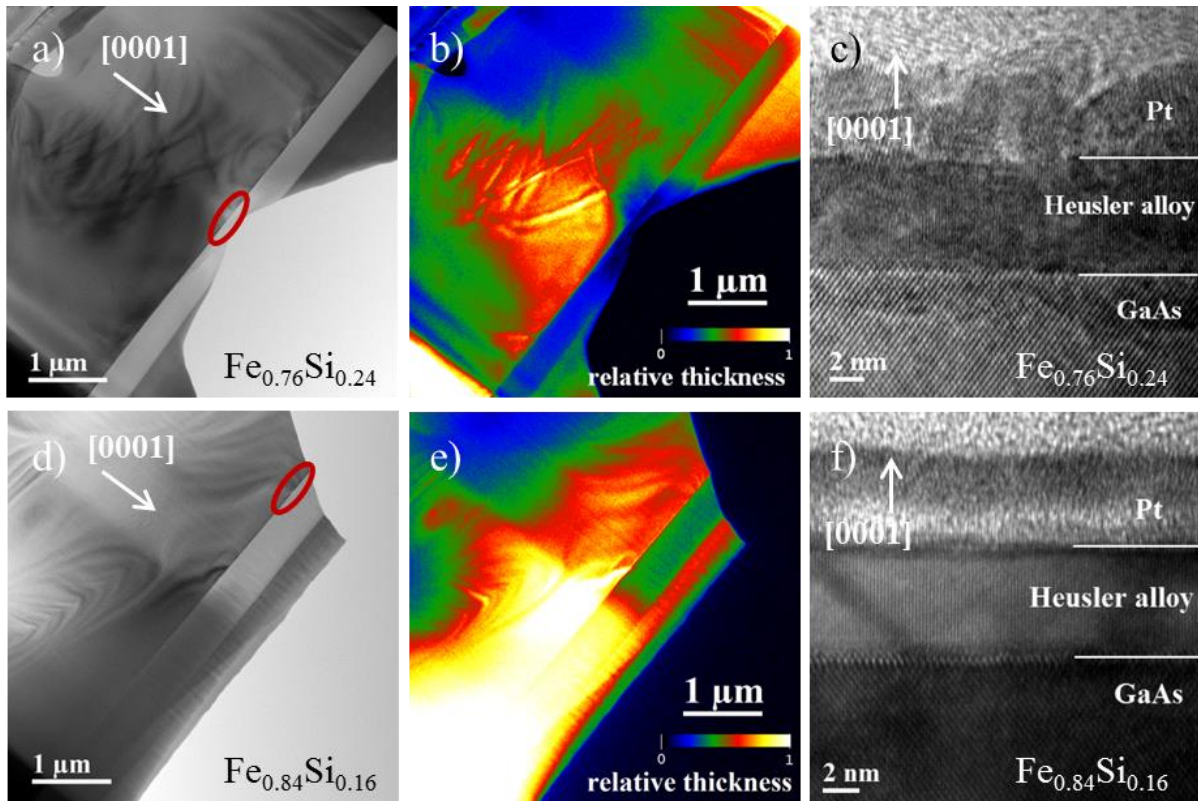


Figure 77: BF image with indication of region of interest for analytical investigations (red oval) for: a) $\text{Fe}_{0.76}\text{Si}_{0.24}$, d) $\text{Fe}_{0.84}\text{Si}_{0.16}$; corresponding t/λ maps showing a value of ~ 0.5 in the ROI for: b) $\text{Fe}_{0.76}\text{Si}_{0.24}$, e) $\text{Fe}_{0.84}\text{Si}_{0.16}$; HR-TEM images depicting the individual layers (TEM specimens oriented in $[11-20]$ zone axis of GaAs) for: c) $\text{Fe}_{0.76}\text{Si}_{0.24}$, f) $\text{Fe}_{0.84}\text{Si}_{0.16}$.

Before starting analytical investigations it had to be ensured that both lamellas exhibit appropriate characteristics for analytical investigations. The lamellas shown in Figure 77 were oriented into the GaAs $[11-20]$ zone axis during investigations. Figure 77a) shows a BF overview image with a red ellipse indicating the area of analytical investigations for the $\text{Fe}_{0.76}\text{Si}_{0.24}$ case and Figure 77d) for the $\text{Fe}_{0.84}\text{Si}_{0.16}$ case. The corresponding t/λ maps are displayed in Figure 77b) and e) and show a value of the t/λ in the range of 0.4 – 0.6 within the area of interest being suitable for analytical investigations. Figure 77c) and f) show a HR-TEM image of the various layers for each layer type. It can be seen that for both cases the Heusler alloy exhibits a thickness of roughly 7 nm with protective Pt on top. In order to gain a more detailed insight into the diffusion profiles of all 4 participating elements within the two TEM specimens, STEM-EDXS linescans were performed. A compromise between an appropriate resolution and sufficient beam current was made. Therefore, the FWHM of the STEM

beam of the Tecnai 200 kV FEG microscope was chosen to be 0.36 nm. The distance between the individual measurement spots along the linescan was 0.4 nm. Prior to all analytical measurements the TEM specimens were oriented into the GaAs [11-20] zone axis in the vicinity of the measurement region. Each spectrum was recorded with 100 sec per pixel.

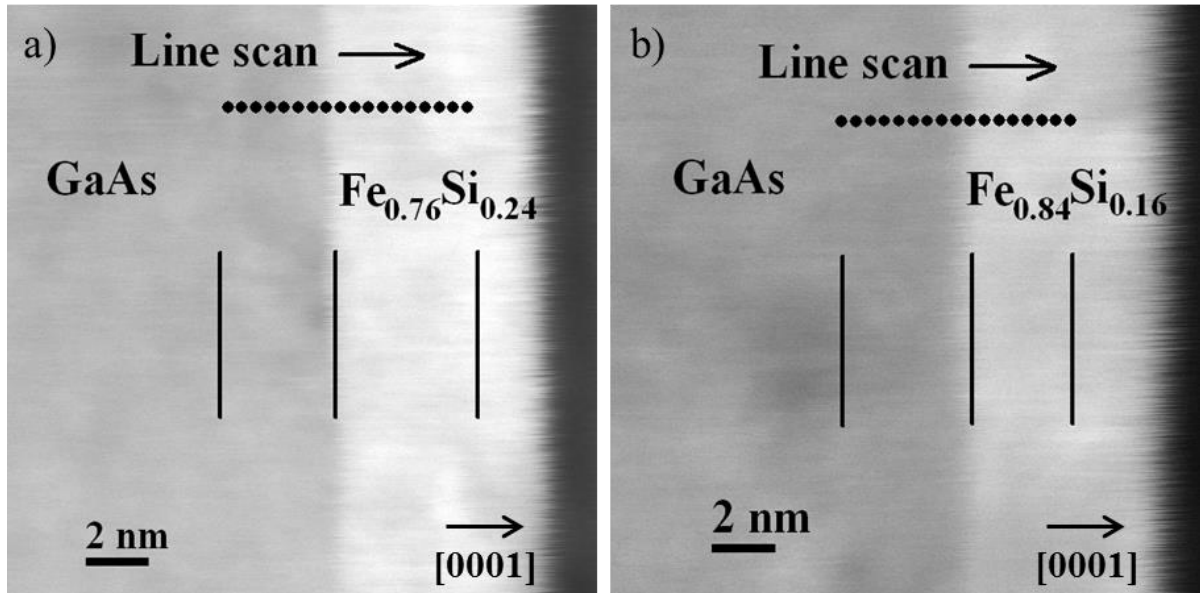


Figure 78: HAADF images of both TEM specimens with indications of measurement points (black dots) for the EDXS linescans; black vertical lines indicate the start and end position of the linescan and the position of the actual interface.

In Figure 78 both HAADF images with the positions of the recorded spectra on both TEM specimens are shown. The image quality, especially in the vicinity of the Heusler-layer, is deteriorated due to its magnetic properties. The true interface position was marked based on EDXS signals. In order to account for the possibility of an electron beam broadening simulations were carried as mentioned in section 6.10. The outcome of the simulation is depicted Figure 79. The simulations were performed using the software package “CASINO” version 2.0. The displayed simulation contains tracking of 10.000 electrons within a 0.4 nm broad electron beam passing through a 50 nm thick GaAs layer. This is suitable for both TEM specimens. The simulation shows that the electron beam spread affects only 1% of the electrons thereby being outside of the nominal beam diameter. This assures that beam broadening due to the TEM specimen thickness was negligible during data acquisition.

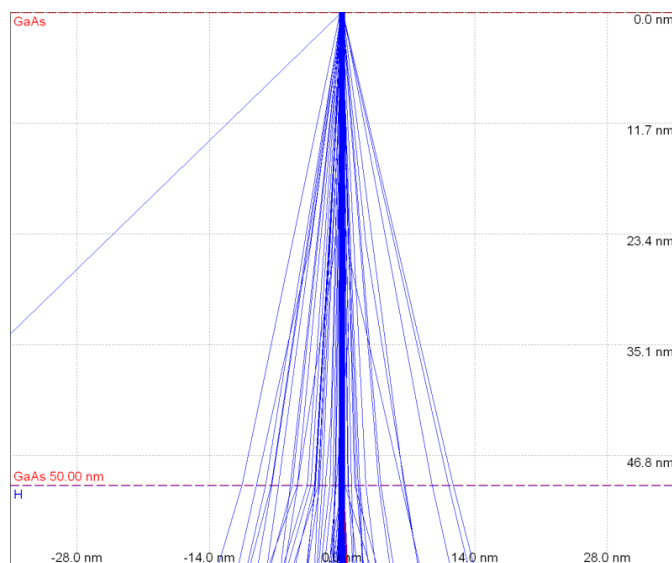


Figure 79: Simulation of 10,000 electrons going through 50 nm GaAs showing that only 1 % of the incident electrons are outside the nominal beam diameter (0.4 nm); simulation done with the software-package Casino v 2.0.

EDXS data of both TEM specimens were quantified with the k-factor method [62,137] as presented in Table 17. The table lists further the background windows and the signal window used for quantification of the K-lines of Fe, Si, Ga and As. Background subtraction from the signal window was performed by summing up and averaging the counts of both windows left and right of each respective line. The signal window was chosen to be 1.2 times the FWHM of each respective line [62].

Table 17: Background windows, signal window and k-factors used for EDXS quantification.

Element	Background window 1 [keV]	Background window 2 [keV]	Signal window [keV]	k-factors
Si	1.44 – 1.64	1.95 – 2.15	1.64 – 1.84	1
Fe	5.75 – 6.00	7.40 – 7.65	6.27 – 6.52	1.418
Ga	8.40 – 8.70	9.6 – 9.90	9.10 – 9.40	1.949
As	9.7 – 10.00	10.9 – 11.20	10.37 – 10.67	2.248

To quantify the amount of stray radiation EDX spectra with no TEM specimen in the electron beam path were recorded. The obtained co-counts originate from the pole piece material of the microscope (Fe) and the EDXS detector material (Si) [62]. These counts were used as a reference in both situations i.e. TEM specimen in the electron beam path and no specimen in the electron beam path. Since no strong deviations in co-counts were observed in both cases, the Fe counts and Si counts of the situation without TEM specimen in the electron beam path were averaged and subtracted from the actual measured data. In this way, it is ensured that no pole piece or EDXS detector signal were quantified. The quantified STEM-EDXS linescans shown in Figure 80a) and b) reveal that both, the GaAs and the FeSi layers are not affected by interdiffusion at a distance further away than 3 nm from

each side of the interface. At this distance from the interface the quantified values are close to the specified composition.

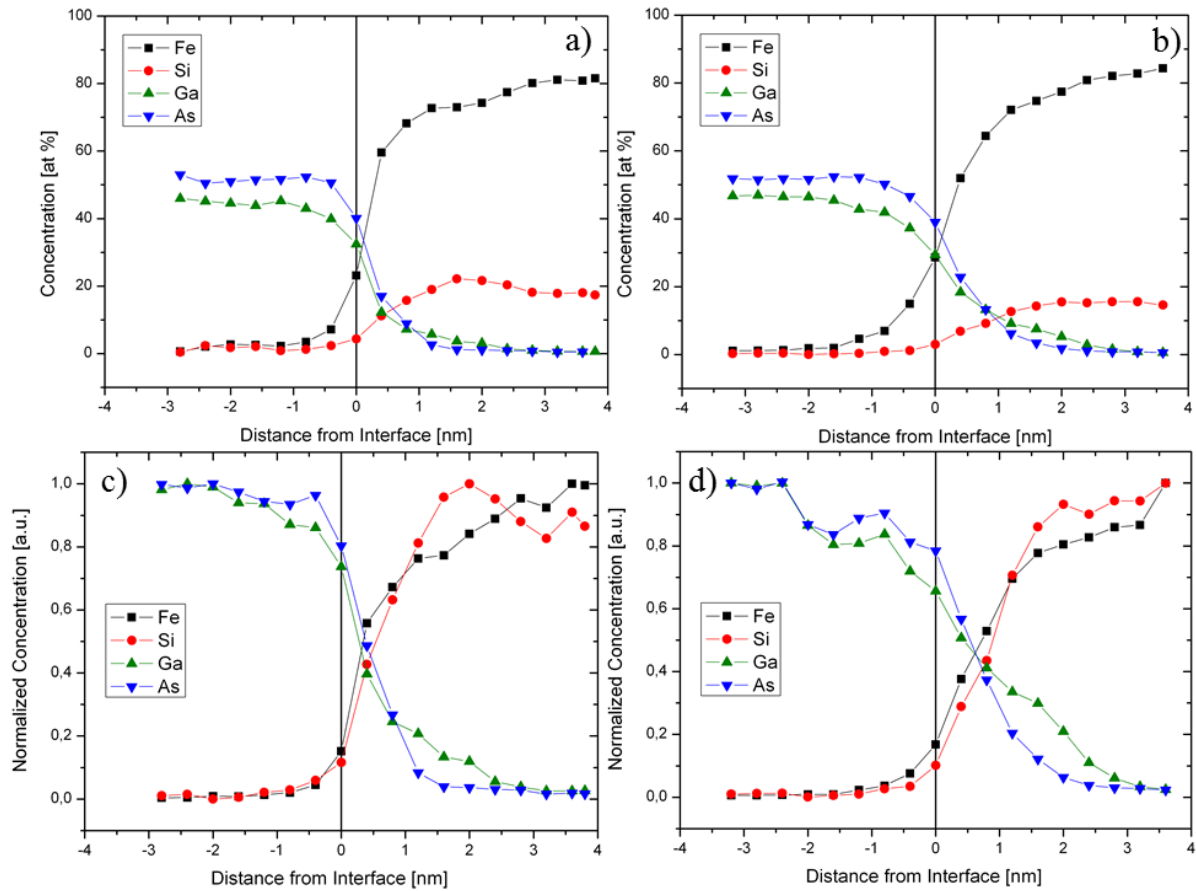


Figure 80: Quantified STEM-EDXS linescan of TEM specimen with a composition of: a) $\text{Fe}_{0.76}\text{Si}_{0.24}$; b) $\text{Fe}_{0.84}\text{Si}_{0.16}$; c) normalized concentration to a); d) normalized concentration to b).

The graphs of Figure 80c) and d) were normalized to the maximum value of each analyzed element. They depict that there is an excess of Ga and As within the FeSi layer for both TEM specimens. On the other side of the interface within the GaAs it appears that Fe is the stronger diffusing component compared to Si. Overall one can see that the zone of interdiffusion has a length of roughly 5 nm in both TEM specimens being slightly shifted towards the Heusler-alloy side. The finding of having a broad intermixed region at the interface between $\text{Fe}_{1-x}\text{Si}_x$ films and GaAs(001) substrate that forms already at temperatures necessary for the crystallographic ordering of Heusler films is crucially for a further development of spintronic devices [54]. For production of such devices a way to limit this interdiffusion has to be found. One possible approach might be the insertion of an appropriate thin barrier layer. This barrier layer has to fulfill two purposes: (i) it has to suppress the interdiffusion to a minimum and (ii) it should not significantly reduce spin-polarized injection of electrons into the semiconductor.

9. Summary

The possibility of investigating materials with an analytical aberration-corrected TEM microscope allows one to gain relevant information about the micro and nanostructure of a material. Such an instrument provides spatially resolved images at high resolution in various modes (TEM and STEM) and recently has opened access to image even light elements by a technique called annular bright-field (ABF) imaging. Moreover, analytical investigations can be carried out at increased performance with the latest generation of EELS spectrometers and EDXS detectors. This is supported by increased beam currents, high speed acquisition possibilities in EELS, the possibility to acquire different EELS spectral regions into a single pixel and by the much improved collection efficiency in X-ray detection. All this is combined in the ASTEM microscope at the ZFE / FELMI TU-Graz and enables material science investigations with unprecedented detail, greater detection efficiency and speed, and hence reduced specimen damage in beam sensitive materials.

An aberration corrected instrument mercilessly shows the shortcomings of TEM specimen preparation and a big part of this work was focusing on implementing the right preparation techniques to obtain pristine TEM specimens. The removal of amorphous layers from TEM specimen surface by ion polishing at low acceleration voltages was intensively applied. For GaN it was shown that this amorphous layer not only deteriorates the TEM and STEM image quality but it also prevents meaningful analytical investigations by adding extra complexity due to unknown surface compositions and layer thicknesses. The polishing had to be carried out iteratively, usually cross-checking with TEM several times. For FIB TEM specimens the dedicated low energy ion polishing machines Nanomill (© Fischione Instruments) has proven to be beneficial in addition to being fast and site-selective, essential for the investigation of GaN specimens. The alternative approach of wedge polishing was unsatisfying since the stress between sapphire substrate and GaN deposit led to break-outs of thin specimen pieces. Also the stronger surface modification introduced by abrasion of material was not favorable.

Pre-characterizations of the materials investigated in this work were carried out by the project partners beforehand. Specific questions regarding structural homogeneity, elemental distribution and composition information were tackled in this thesis by working on state-of-the-art electron microscope facilities across Europe and mostly in Graz.

Analytical investigations were started on cubic Fe(Co)oxide nanocrystals, and FeO_x references were used to derive chemical phase information. It was found by monochromated EELS measurements and an analysis of the edge fine-structures that the oxidation state of the reference crystals correspond to Fe₃O₄. Further measurements of the elemental distribution revealed the nanocrystal setup. It was expected to observe an iron oxide core surrounded by a cobalt iron oxide shell. Measurements proved that a cobalt iron oxide compound is present in the core being surrounded by an iron oxide shell. This

information was of great value for understanding the mechanism of exchange interaction and therefore necessary for the further development of these crystals.

The most prominent part of this thesis entailed studies of transition-metal doped GaN layers. GaN is one of the favorable materials in industry and academic research for applications such as lighting and integrated circuits with high speeds. Based on the idea of fabricating a magnetic semiconductor, leading to spintronic devices, information at the atomic level was required and different types of doped GaN have been investigated. For the first time in Graz, atomic resolution TEM and STEM images of undoped GaN were recorded, necessitating the generation of a set of acquisition parameters to be used further on. Annular bright-field imaging was used to visualize the GaN structure by its ability to image low (nitrogen) and high Z (gallium) materials at the same time. These measurements were furthermore backed up by image simulations. ChemiSTEM technology (© FEI Company), using Ga $K\alpha$ radiation, for the first time allowed the mapping of the Ga lattice in an atomically resolved manner. Such maps show impressive possibilities for qualitative imaging, yet for quantifiable results the applied electron dose needs to be controlled and minimized. EELS on the other hand, still favorable in many cases grace to its higher detection sensitivity, has shown that it is possible to obtain quantitative results for Ga and N, which are in good agreement with the expectable stoichiometry. This was a necessary basis for subsequent analytical investigations of doped GaN samples.

For the homogeneously Mn doped GaN sample it could be shown that Mn was coherently embedded and no precipitation took place. The doped layer could furthermore be directly visualized by means of STEM imaging. Quantitative measurements of the dopant were in good agreement with nominal concentrations. For the pulsed Mn GaN sample, where the Mn flow periodically was turned on and off during layer growth, no structural precipitation was observed and a coherent embedment of the dopant within the GaN lattice took place. HAADF imaging and EDXS maps of Ga $K\alpha$ as well as EFTEM confirmed the presence of layers with non-uniform width. Presence of Mn within intentionally undoped layers was found and it was possible to determine the amount of doping for high and low doped layers. Due to the non-uniform width of the layers and the large fluctuation of dopant between the layers, an average value turned out to be rather meaningless, preventing a comparison with the nominal concentration.

For GaN doped with iron at two nominal concentrations, nanocrystals embedded in the GaN matrix were observed. The specific growth conditions have led to nanocrystal formation at a defined depth, coherently embedded in the sample, as shown by ABF and HAADF imaging. Spectrum imaging revealed iron to be only present in the nanocrystals and not in the matrix. Attempts were taken to extract detailed information of the individual nanocrystal composition, however, having been severely hampered by an oxide layer with unknown stoichiometry on the TEM specimen surface. With a FIB cross-section of the existing TEM lamella, the oxide layer thickness could be determined and more sophisticated data processing was possible, trying to eliminate the influence of the oxide layer on the

quantification. Measuring undoped GaN in the vicinity of the nanocrystal and assuming a certain oxygen concentration on the surface did not lead to uniform composition values. However, it was possible to observe trends regarding the iron content of these nanocrystals. In general, a higher nominal Fe doping concentration has led to an increased average Fe level in the nanocrystals, yet fluctuating strongly from one precipitate to the other. In rare cases a modulation of the nanocrystal structure could be observed, where the crystal is periodically changing between iron to gallium dominating zones.

Heusler-alloys deposited on GaAs substrates have been investigated for potential applications in spintronic devices. The magnetic layers shall act as spin injectors and to obtain high spin injection, an abrupt interface between semiconductor and spin injector is necessary. For a technological exploitation, knowledge of the amount of intermixing is important to optimize device fabrication. In practice abrupt interfaces are difficult to achieve and intermixing is likely to happen. STEM-EDXS linescans helped to reveal and chemically analyze such zones. It was observed that gallium and iron tend to diffuse more compared to arsenide and silicon and a quantitative analysis allowed to determine individual concentration gradients for the different constituents, reaching the nominal compositions away from this zone. These findings have helped optimizing growth conditions and suggested the adding of barrier layers, which inhibit interdiffusion.

Obviously, many ideas for improvements came up during the work on this thesis, on one hand related to material design, which are expertedly handled by the project partners, but also with respect to microscopic techniques and experimental approaches. Perhaps one of the most important aspects is sample preparation, which aims at structurally and chemically unaltered material. The possibility to handle all specimen manipulations under vacuum, including sample taking, preparation, microscope transfer and analysis (ideally under cryo conditions to minimize damage), would be of tremendous benefit for getting less ambiguous results. Investigations carried out in all three dimensions, i.e. electron tomography, could help alleviate the TEM projection problem, and reveal compositions and gradients without surface or matrix effects. Finally, adding high energy-resolution EELS measurements to tomography, could provide extra information on the electronic structure of materials and help correlating electronic and structural properties.

10. Abbreviations

ABF	annular bright field
ADF	annular dark field
AF	anti-ferromagnetic
AFM	atomic force microscopy
BF	bright-field
CBM	cantilever beam magnetometry
CCD	charge coupled device
DMS	dilute magnetic semiconductor
EDXS	energy dispersive X-ray spectroscopy
EELS	electron energy loss spectroscopy
EFTEM	energy filtering transmission electron microscopy
ELNES	energy loss near edge fine structure
EXAFS	extended energy loss fine structure
FEG	field emission gun
FIB	focused ion beam
FM	ferromagnetic
GaN	gallium nitride
GIF	Gatan imaging filter
LEED	low energy electron diffraction
MOVPE	metal-organic vapor phase epitaxy
NC	nano crystal
PIPS	precision ion polishing system
RHEED	reflection high energy electron diffraction
ROI	region of interest
RPM	rotation per minute
RT	room-temperature
SAED	selected area electron diffraction
SEM	scanning electron microscope
SI	spectrum image
Si(Li)	silicon crystal doped with lithium
STEM	scanning transmission electron microscopy
TC	Curie temperature
TEM	transmission electron microscopy
TM	transition metal
XRD	X-ray diffraction
ZL	zero loss

11. References

- [1] H. Zeng, J. Li, J. P. Liu, Z. L. Wang and S. Sun, *Nature* **420**, 395 (2002).
- [2] V. Skumryev, S. Stoyanov, Y. Zhang, G. Hadjipanayis, D. Givord, J. Nogués, T. Ic and S. T. Ic, *Nature* **423**, 19 (2003).
- [3] M. I. Bodnarchuk, M. V Kovalenko, H. Groiss, R. Resel, G. Hesser, T. Lechner, F. Schäffler, W. Heiss, M. Reissner, R. T. Lechner and W. Steiner, *Small* **5**, 2247 (2009).
- [4] A. Goldman, *Modern Ferrite Technology*, 2nd edition (Springer, 2006).
- [5] M. V Kovalenko, M. I. Bodnarchuk, R. T. Lechner, G. Hesser, F. Schäffler and W. Heiss, *J. Am. Chem. Soc.* **129**, 6352 (2007).
- [6] D. W. Palmer, <http://www.semiconductors.co.uk/nitrides.htm#GaN> (n.d.).
- [7] D. W. Runton and B. Trabert, *IEEE Microw. Mag.* **14**, 82 (2013).
- [8] C. Jia, T. Yu, H. Lu, C. Zhong, Y. Sun, Y. Tong, G. Zhang and G. Leds, *Opt. Express* **21**, 8444 (2013).
- [9] A. Pantellini, C. Lanzieri, A. Nanni, A. Bentini, W. Ciccognani, S. Colangeli and E. Limiti, *Mater. Sci. Forum* **711**, 223 (2012).
- [10] J. Würfl, O. Hilt, E. Bahat-Treidel, R. Zhytnytska, K. Klein, P. Kotara, F. Brunner, A. Knauer, O. Krüger, M. Weyers and G. Tränkle, *ECS Trans.*, 979–989 (2013).
- [11] M. J. Scott, J. Li and J. Wang, 2013 IEEE Power Energy Conf. Illinois 1 (2013).
- [12] I. M. Watson, *Coord. Chem. Rev.* **257**, 2120 (2013).
- [13] F. Scholz, *Semicond. Sci. Technol.* **27**, 024002 (2012).
- [14] S.-R. Jian, W.-C. Ke and J.-Y. Juang, *Nanosci. Nanotechnol. Lett.* **4**, 598–603 (2012).
- [15] M. A. Moram, M. J. Kappers, F. Massabuau, R. A. Oliver and C. J. Humphreys, *J. Appl. Phys.* **109**, 073509 (2011).
- [16] K. Sato, L. Bergqvist, J. Kudrnovský, P. H. Dederichs, O. Eriksson, I. Turek, B. Sanyal, G. Bouzerar, H. Katayama-Yoshida, V. A. Dinh, T. Fukushima, H. Kizaki and R. Zeller, *Rev. Mod. Phys.* **82**, 1633 (2010).
- [17] A. Bonanni and T. Dietl, *Chem. Soc. Rev.* **39**, 528 (2010).
- [18] M. Jamet, A. Barski, T. Devillers, V. Poydenot, R. Dujardin, P. Bayle-Guillemaud, J. Rothman, E. Bellet-Amalric, A. Marty, J. Cibert, R. Mattana and S. Tatarenko, *Nat Mater* **5**, 653 (2006).
- [19] M. Yokoyama, H. Yamaguchi, T. Ogawa and M. Tanaka, *J. Appl. Phys.* **97**, 10D317 (2005).
- [20] T. Dietl, D. D. Awschalom, M. Kaminska and H. Ohno, *Spintronics*, 1st edition (Academic Press, 2008).

-
- [21] Y. Hao, J. Zhang, B. Shen and X. Liu, *J. Semicond.* **33**, 081001 (2012).
- [22] I. Žutić, J. Fabian and S. Das Sarma, *Rev. Mod. Phys.* **76**, 323 (2004).
- [23] A. Bonanni, *Semicond. Sci. Technol.* **22**, R41 (2007).
- [24] N. Kondo, *Chem. Vap. Depos.* **2**, 24 (1996).
- [25] D. Ferrand, J. Cibert, A. Wasiela, C. Bourgoignon, S. Tatarenko, G. Fishman, T. Andrearczyk, J. Jaroszyński, S. Koleśnik, T. Dietl, B. Barbara and D. Dufeu, *Phys. Rev. B* **63**, 85201 (2001).
- [26] H. Ohno, *Science* **281**, 951 (1998).
- [27] K. H. J. Buschow, *Handbook of Magnetic Materials*, 21st edition (Elsevier, 2013).
- [28] S. Ohya, K. Ohno and M. Tanaka, *Appl. Phys. Lett.* **90**, 112503 (2007).
- [29] D. Chiba, Y. Nishitani, F. Matsukura and H. Ohno, *Appl. Phys. Lett.* **90**, 122503 (2007).
- [30] T. Dietl, *Science* **287**, 1019 (2000).
- [31] A. Navarro-Quezada, N. Gonzalez Szwacki, W. Stefanowicz, T. Li, A. Grois, T. Devillers, M. Rovezzi, R. Jakiela, B. Faina, J. A. Majewski, M. Sawicki, T. Dietl and A. Bonanni, *Phys. Rev. B* **84**, 155321 (2011).
- [32] A. Bonanni, A. Navarro-Quezada, T. Li, M. Wegscheider, Z. Matěj, V. Holý, R. T. Lechner, G. Bauer, M. Rovezzi, F. D'Acapito, M. Kiecana, M. Sawicki, T. Dietl and Z. Mate, *Phys. Rev. Lett.* **101**, 1 (2008).
- [33] W. Pacuski, P. Kossacki, D. Ferrand, A. Golnik, J. Cibert, M. Wegscheider, A. Navarro-Quezada, A. Bonanni, M. Kiecana, M. Sawicki and T. Dietl, *Phys. Rev. Lett.* **100**, 25 (2008).
- [34] A. Bonanni, M. Sawicki, T. Devillers, W. Stefanowicz, B. Faina, T. Li, T. Winkler, D. Sztenkiel, A. Navarro-Quezada, M. Rovezzi, R. Jakiela, A. Grois, M. Wegscheider, W. Jantsch, J. Suffczyński, F. D'Acapito, A. Meingast, G. Kothleitner and T. Dietl, *Phys. Rev. B* **84**, 1 (2011).
- [35] A. Navarro-Quezada, W. Stefanowicz, T. Li, B. Faina, M. Rovezzi, R. T. Lechner, T. Devillers, F. d'Acapito, G. Bauer, M. Sawicki, T. Dietl and A. Bonanni, *Phys. Rev. B* **81**, 205206 (2010).
- [36] T. Devillers, M. Rovezzi, N. G. Szwacki, S. Dobkowska, W. Stefanowicz, D. Sztenkiel, A. Grois, J. Suffczyński, A. Navarro-Quezada, B. Faina, T. Li, P. Glatzel, F. d'Acapito, R. Jakiela, M. Sawicki, J. A. Majewski, T. Dietl and A. Bonanni, *Sci. Rep.* **2**, 722 (2012).
- [37] A. Bonanni, C. Simbrunner, M. Wegscheider, H. Przybylinska, A. Wolos, H. Sitter and W. Jantsch, *Phys. Status Solidi* **243**, 1701 (2006).
- [38] A. Navarro-Quezada, T. Devillers, T. Li and A. Bonanni, *Appl. Phys. Lett.* **101**, 081911 (2012).
- [39] A. Núñez, R. Duine, P. Haney and A. MacDonald, *Phys. Rev. B* **73**, 214426 (2006).

-
- [40] A. Shick, S. Khmelevskiy, O. Mryasov, J. Wunderlich and T. Jungwirth, *Phys. Rev. B* **81**, 212409 (2010).
- [41] A. Bonanni, D. Stifter, A. Montaigne-Ramil, K. Schmidegg, K. Hingerl and H. Sitter, *J. Cryst. Growth* **248**, 211 (2003).
- [42] A. Meingast, A. Navarro Quezada, T. Devillers, A. Kovács, M. Albu, S. Fladischer, A. Bonanni and G. Kothleitner, *Semicond. Sci. Technol.* **30**, 035002 (2015).
- [43] H. Zhu, M. Ramsteiner, H. Kostial, M. Wassermeier, H.-P. Schönherr and K. Ploog, *Phys. Rev. Lett.* **87**, 016601 (2001).
- [44] S. Datta and B. Das, *Appl. Phys. Lett.* **56**, 665 (1990).
- [45] A. Ney, C. Pampuch, R. Koch and K. H. Ploog, *Nature* **425**, 485 (2003).
- [46] B. D. Schultz, H. H. Farrell, M. M. R. Evans, K. Lüdge, and C. J. Palmstrøm, *J. Vac. Sci. Technol. B Microelectron. Nanom. Struct.* **20**, 1600 (2002).
- [47] G. Kioseoglou, T. J. Zega, A. T. Hanbicki, S. C. Erwin, Z. Igor, C. H. Li, B. T. Jonker, R. M. Stroud and I. Žutić, *Phys. Rev. Lett.* **96**, 196101 (2006).
- [48] S. Députier, R. Guérin and A. Guivarc'h, *Eur. Phys. J. - Appl. Phys.* **2**, 127 (1998).
- [49] D. Orgassa, H. Fujiwara, T. C. Schulthess and W. H. Butler, *Phys. B Condens. Matter* **60**, 237 (1999).
- [50] A. Ionescu, C. Vaz, T. Trypiniotis, C. Gürtler, H. García-Miquel, J. Bland, M. Vickers, R. Dalglish, S. Langridge, Y. Bugoslavsky, Y. Miyoshi, L. Cohen and K. Ziebeck, *Phys. Rev. B* **71**, 094401 (2005).
- [51] B. Hülsen, M. Scheffler and P. Kratzer, *Phys. Rev. Lett.* **103**, 046802 (2009).
- [52] M. Ramsteiner, O. Brandt, T. Flissikowski, H. T. Grahn, M. Hashimoto, J. Herfort and H. Kostial, *Phys. Rev. B* **78**, 121303 (2008).
- [53] M. Hashimoto, J. Herfort, A. Trampert, H.-P. Schönherr and K. H. Ploog, *J. Vac. Sci. Technol. B Microelectron. Nanom. Struct.* **24**, 2004 (2006).
- [54] C. Gusenbauer, T. Ashraf, J. Stangl, G. Hesser, T. Plach, A. Meingast, G. Kothleitner and R. Koch, *Phys. Rev. B* **83**, 1 (2011).
- [55] B. Schaffer, W. Grogger and G. Kothleitner, *Ultramicroscopy* **102**, 27 (2004).
- [56] K. Riegler and G. Kothleitner, *Ultramicroscopy* **110**, 1004 (2010).
- [57] W. Grogger, B. Schaffer, K. M. Krishnan and F. Hofer, *Ultramicroscopy* **96**, 481 (2003).
- [58] B. Schaffer, G. Kothleitner and W. Grogger, *Ultramicroscopy* **106**, 1129 (2006).
- [59] M. Haider, H. Rose, S. Uhlemann, E. Schwan, B. Kabius and K. Urban, **75**, 53 (1998).
- [60] S. Uhlemann and M. Haider, *Ultramicroscopy* **72**, 109 (1998).

-
- [61] D. B. Williams, A. J. Papworth and M. Watanabe, *J. Electron Microsc.* **51**, S113 (2002).
- [62] D. B. Williams and C. B. Carter, *Transmission Electron Microscopy: A Textbook for Materials Science* (Springer, 2009).
- [63] M. Baram and W. D. Kaplan, *J. Microsc.* **232**, 395 (2008).
- [64] V. J. Keast, M. J. Gladys, T. C. Petersen, C. Dwyer, C. T. Koch, T. Haber and G. Kothleitner, *Appl. Phys. Lett.* **99**, 221905 (2011).
- [65] M. A O'Keefe, *Ultramicroscopy* **108**, 196 (2008).
- [66] H. H. Rose, *Sci. Technol. Adv. Mater.* **9**, 014107 (2008).
- [67] P. C. Tiemeijer, M. Bischoff, B. Freitag and C. Kisielowski, *Ultramicroscopy* **114**, 72 (2012).
- [68] M. Haider, P. Hartel, H. Müller, S. Uhlemann and J. Zach, *Microsc. Microanal.* **16**, 393 (2010).
- [69] C. Gspan, W. Grogger, B. Bitschnau, E. Bucher, W. Sitte and F. Hofer, *J. Solid State Chem.* **181**, 2976 (2008).
- [70] S. Cho, K. Kikuchi, T. Miyazaki, A. Kawasaki, Y. Arami and J. F. Silvain, *Acta Mater.* **61**, 708 (2013).
- [71] R. Erni, H. Heinrich and G. Kostorz, *Ultramicroscopy* **94**, 125 (2003).
- [72] G. Servanton, R. Pantel, M. Juhel and F. Bertin, *Micron* **40**, 543 (2009).
- [73] N. Dellby, O. L. Krivanek, P. D. Nellist, P. E. Batson, and A R. Lupini, *J. Electron Microsc.* **50**, 177 (2001).
- [74] O. L. Krivanek, T. C. Lovejoy, N. Dellby and R. W. Carpenter, *Microscopy* **62**, 3 (2013).
- [75] O. L. Krivanek, G. J. Corbin, N. Dellby, B. F. Elston, R. J. Keyse, M. F. Murfitt, C. S. Own, Z. S. Szilagy and J. W. Woodruff, *Ultramicroscopy* **108**, 179 (2008).
- [76] P. Tiemeijer, *Monochromator Manual Titan VI.2* (FEI Electron Optics, 2011).
- [77] A. V Crewe, *Reports Prog. Phys.* **43**, 621 (1980).
- [78] S. J. Pennycook, B. Rafferty and P. D. Nellist, *Microsc. Microanal.* **6**, 343 (2000).
- [79] P. D. Nellist, *The Principles and Interpretation of Annular Dark-Field Z-Contrast Imaging* *Adv. in Imag. and Elec. Phys.* **113**, 148-200 (2000).
- [80] S. J. Pennycook and P. D. Nellist, *Scanning Transmission Electron Microscopy: Imaging and Analysis* (Springer, 2011).
- [81] L. J. Allen, S. D. Findlay, M. P. Oxley and C. J. Rossouw, *Ultramicroscopy* **96**, 47 (2003).
- [82] L. J. Allen, S. D. Findlay, M. P. Oxley and C. J. Rossouw, *Ultramicroscopy* **96**, 65 (2003).
- [83] A. M. Donald and A. J. Craven, *Philos. Mag. A* **39**, 1 (1979).

- [84] S. J. Pennycook, A. R. Lupini, A. Kadavanich, J. R. McBride, S. J. Rosenthal, R. C. Puetter, A. Yahil, O. L. Krivanek, N. Dellby, P. D. L. Nellist, G. Duscher, L. G. Wang and S. T. Pantelides, *Zeitschrift Für Met.* **94**, 350 (2003).
- [85] P. D. Nellist and S. J. Pennycook, *Ultramicroscopy* **78**, 111 (1999).
- [86] G. Almer, K. Wernig, M. Saba-Lepek, S. Haj-Yahya, J. Rattenberger, J. Wagner, K. Gradauer, D. Frascione, G. Pabst, G. Leitinger, H. Mange, A. Zimmer and R. Prassl, *Int. J. Nanomedicine* **6**, 1279 (2011).
- [87] J. Angseryd, M. Albu, H.-O. Andrén and G. Kothleitner, *Micron* **42**, 608 (2011).
- [88] P. D. Nellist, M. F. Chisholm, N. Dellby, O. L. Krivanek, M. F. Murfitt, Z. S. Szilagyi, A. R. Lupini, A. Borisevich, W. H. Sides and S. J. Pennycook, *Science* **305**, 1741 (2004).
- [89] K. Hirahara, J. Yamasaki, K. Saitoh and N. Tanaka, *Microsc. Microanal.* **13**, 890 (2007).
- [90] S. D. Findlay, N. Shibata, H. Sawada, E. Okunishi, Y. Kondo and Y. Ikuhara, *Ultramicroscopy* **110**, 903 (2010).
- [91] S. D. Findlay, N. Shibata, H. Sawada, E. Okunishi, Y. Kondo, T. Yamamoto and Y. Ikuhara, *Appl. Phys. Lett.* **95**, 191913 (2009).
- [92] R. Ishikawa, E. Okunishi, H. Sawada, Y. Kondo, F. Hosokawa and E. Abe, *Nat. Mater.* **10**, 278 (2011).
- [93] M. de la Mata, C. Magen, J. Gazquez, M. I. B. Utama, M. Heiss, S. Lopatin, F. Furtmayr, C. J. Fernández-Rojas, B. Peng, J. R. Morante, R. Rurali, M. Eickhoff, A. Fontcuberta i Morral, Q. Xiong, J. Arbiol, M. De Mata, M. Iqbal, B. Utama, C. J. Ferna, M. Eickho and A. Fontcuberta, *Nano Lett.* **12**, 2579 (2012).
- [94] E. Okunishi, I. Ishikawa, H. Sawada, F. Hosokawa, M. Hori and Y. Kondo, *Microsc. Microanal.* **15**, 164 (2009).
- [95] J. R. McBride, A. Lupini, S. J. Pennycook and S. J. Rosenthal, *Aberration-Corrected Z-Contrast STEM: Semiconducting Nanocrystals*, Dekker Encyclopedia of Nanoscience and Nanotechnology 2nd edition (2009).
- [96] J. M. Cowley, *Appl. Phys. Lett.* **15**, (1969).
- [97] H. Rose, *Ultramicroscopy* **2**, 251 (1977).
- [98] H. Rose and J. Fertig, *Ultramicroscopy* **2**, 77 (1976).
- [99] J. M. Cowley, M. S. Hansen and S.-Y. Wang, *Ultramicroscopy* **58**, 18 (1995).
- [100] R. F. Egerton, *Ultramicroscopy* **145**, 85 (2014).
- [101] U. Kaiser, J. Biskupek, J. C. Meyer, J. Leschner, L. Lechner, H. Rose, M. Stöger-Pollach, A. N. Khlobystov, P. Hartel, H. Müller, M. Haider, S. Eyhusen and G. Benner, *Ultramicroscopy* **111**, 1239 (2011).
- [102] D. C. Bell, C. J. Russo and D. V. Kolmykov, *Ultramicroscopy* **114**, 31 (2012).

-
- [103] P. Tiemeijer, *Inst. Phys. Conf. Series* **161**, 191 (1999).
- [104] P. C. Tiemeijer, *Ultramicroscopy* **78**, 53 (1999).
- [105] P. C. Tiemeijer, M. Bischoff, B. Freitag and C. Kisielowski, *Ultramicroscopy* **118**, 35 (2012).
- [106] M. Haider, S. Uhlemann and J. Zach, *Ultramicroscopy* **81**, 163 (2000).
- [107] R. F. Egerton, *Micron* **34**, 127 (2003).
- [108] C. Mitterbauer, G. Kothleitner, W. Grogger, H. Zandbergen, B. Freitag, P. Tiemeijer and F. Hofer, *Ultramicroscopy* **96**, 469 (2003).
- [109] R. Erni and N. D. Browning, *Ultramicroscopy* **104**, 176 (2005).
- [110] D. Su, H. Zandbergen, P. C. Tiemeijer, G. Kothleitner, M. Hävecker, C. Hébert, A. Knop-Gericke, B. Freitag, F. Hofer, R. Schlögl, C. He, M. Ha and R. Schlo, *Microchim. Acta* **34**, 235 (2003).
- [111] S. Turner, S. Lazar, B. Freitag, R. Egoavil, J. Verbeeck, S. Put, Y. Strauven and G. Van Tendeloo, *Nanoscale* **3**, 3385 (2011).
- [112] A. L. Koh, K. Bao, I. Khan, W. E. Smith, G. Kothleitner, K. P. Nordlander, S. A. Maier and D. W. McComb, *ACS Nano* **3**, 3015 (2009).
- [113] O. Scherzer, *Zeitschrift Für Phys.* **101**, 593 (1936).
- [114] O. Scherzer, *Opt.* **2**, 114 (1947).
- [115] R. Seeliger, *Opt.* **8**, 311 (1951).
- [116] P. W. Hawkes, *Philos. Trans. R. Soc. A* **257**, 479 (1965).
- [117] J. Orloff, *Handbook of Charged Particle Optics*, 2nd edition (CRC Press, 2008).
- [118] A. Bleloch and A. Lupini, *Mater. Today* **7**, 42 (2004).
- [119] O. L. Krivanek, N. Dellby, A. J. Spence, R. A. Camps and L. M. Brown, *Electron Microsc. Anal. Gr. Conf.* **153**, 35 (1997).
- [120] H. Rose, *Optik* **85**, 19 (1990).
- [121] M. Haider, G. Braunshausen and E. Schwan, *Opt.* **99**, 167 (1995).
- [122] V. D. Beck, *Opt.* **53**, 241 (1979).
- [123] H. Rose, *Nucl. Inst. Methods Phys. Res.* **187**, 187 (1981).
- [124] A. V Crewe, *Opt.* **60**, 271 (1982).
- [125] M. Haider, S. Uhlemann, E. Schwan, H. Rose, B. Kabius and K. Urban, *Nature* **392**, 768 (1998).

-
- [126] M. Haider, H. Müller and S. Uhlemann, *Adv. Imaging Electron Phys.* **153**, 43–119 (2008).
- [127] R. Brydson, *Aberration-Corrected Analytical Transmission Electron Microscopy* (Wiley, 2011).
- [128] O. L. Krivanek, N. Dellby and A. R. Lupini, *Ultramicroscopy* **78**, 1 (1999).
- [129] G. Kothleitner, J. Neish, R. Lugg, D. Findlay, W. Grogger, F. Hofer and J. Allen, *Phys. Rev. Lett.* **112**, 85501 (2014).
- [130] R. F. Egerton, *Electron Energy-Loss Spectroscopy in the Electron Microscope*, 3rd edition (Springer, 2011).
- [131] R. Brydson, *Electron Energy Loss Spectroscopy* (Bios Scientific Publ, 2001).
- [132] A. Gubbens, M. Barfels, C. Trevor, R. Twesten, P. Mooney, P. Thomas, N. Menon, B. Kraus, C. Mao and B. McGinn, *Ultramicroscopy* **110**, 962 (2010).
- [133] J. K. N. Lindner, M. Häberlen, F. Schwarz, G. Thorwarth, B. Stritzker, C. Hammerl and W. Assmann, *Nucl. Instruments Methods Phys. Res. Sect. B Beam Interact. with Mater. Atoms* **249**, 833 (2006).
- [134] C. C. Ahn and O. L. Krivanek, *EELS ATLAS - A Reference Collection of Electron Energy Loss Spectra Covering All Stable Elements* (Arizona State University and Gatan Inc., 1983).
- [135] G. Bertoni and J. Verbeeck, *Ultramicroscopy* **108**, 782 (2008).
- [136] D. C. B. A. J. Garratt-Reed, *Energy Dispersive X-Ray Analysis in the Electron Microscope* (Bios Scientific Publ, 2003).
- [137] S. Fladischer, *Application of New EDXS Quantification Schemes in TEM on Organic Semiconducting Devices*, Graz University of Technology, 2009.
- [138] FEI Company, <http://investor.fei.com/releasedetail.cfm?ReleaseID=574000> (2011).
- [139] M. Watanabe, Z. Horita and M. Nemoto, *Ultramicroscopy* **65**, 187 (1996).
- [140] D. B. Watanabe, M. Williams, *J. Microsc.* **221**, 89 (2006).
- [141] S. Fladischer, *New Methods of Quantitative X-Ray Analysis in a Transmission Electron Microscope*, Graz University of Technology, 2009.
- [142] S. Fladischer and W. Grogger, *Ultramicroscopy* **136**, 26 (2014).
- [143] V. Grillo and E. Rotunno, *Ultramicroscopy* **125**, 97 (2013).
- [144] E. J. Kirkland, *Image Simulation in Transmission Electron Microscopy* (2006).
- [145] M. P. Oxley and S. J. Pennycook, *Micron* **39**, 676 (2008).
- [146] K. Ishizuka, *Ultramicroscopy* **90**, 71 (2001).
- [147] J. Verbeeck, P. Schattschneider and A. Rosenauer, *Ultramicroscopy* **109**, 350 (2009).

-
- [148] E. J. Kirkland, *Advanced Computing in Electron Microscopy*, 2nd edition (Springer, 2010).
- [149] J. M. Cowley and A. F. Moodie, *Acta Crystallogr.* **10**, 609 (1957).
- [150] K. Ishizuka, *Ultramicroscopy* **90**, 71 (2002).
- [151] D. Drouin, A. R. Couture, D. Joly, X. Tastet, V. Aimez and R. Gauvin, *Scanning* **29**, 92 (2007).
- [152] J. Goldstein, D. E. Newbury, D. C. Joy, C. E. Lyman, P. Echlin, E. Lifshin, L. Sawyer and J. R. Michael, *Scanning Electron Microscopy and X-Ray Microanalysis*, 3rd edition (Springer, 2003).
- [153] D. C. Joy, *Scanning Microsc.* **5**, 329 (1991).
- [154] J. Ayache, L. Beaunier, J. Boumendil, G. Ehret and D. Laub, *Sample Preparation Handbook for Transmission Electron Microscopy: Techniques* (Springer, 2010).
- [155] S. Das Bhattacharyya, P. Mukhopadhyay, P. Das and D. Biswas, *J. Nano- Electron. Phys.* **3**, 67 (2011).
- [156] D. V. S. Rao, K. Muraleedharan and C. J. Humphreys, *Microsc. Sci. Technol.* 1232 (2010).
- [157] N. Yao, *Focused Ion Beam Systems: Basics and Applications* (Cambridge University Press, 2011).
- [158] L. Pastewka, R. Salzer, A. Graff, F. Altmann and M. Moseler, *Nucl. Instruments Methods Phys. Res. Sect. B Beam Interact. with Mater. Atoms* **267**, 3072 (2009).
- [159] N. I. Kato, *J. Electron Microsc.* (Tokyo). **53**, 451 (2004).
- [160] M. Schaffer, B. Schaffer and Q. Ramasse, *Ultramicroscopy* **114**, 62 (2012).
- [161] J. El-Awady, C. Woodward, D. Dimiduk and N. Ghoniem, *Phys. Rev. B* **80**, 1 (2009).
- [162] P. Roediger, H. D. Wanzenboeck, S. Waid, G. Hochleitner and E. Bertagnolli, *Nanotechnology* **22**, 235302 (2011).
- [163] S. Neumayer, *Wedge Polishing as Sample Preparation Method for Transmission Electron Microscopy : A Systematic Study*, Graz University of Technology, 2011.
- [164] J. P. Mccaffrey and J. Hulse, *Micron* **29**, 139 (1998).
- [165] P. Patnaik, *Handbook of Inorganic Chemical Compounds* (Mcgraw-Hill Professional, 2002).
- [166] D. R. G. Mitchell, *Microsc. Res. Tech.* **71**, 588 (2008).
- [167] A. Gloter, A. Douiri, M. Tencé, C. Colliex and M. Tenc, *Ultramicroscopy* **96**, 385 (2003).
- [168] S. D. Findlay, N. Shibata, H. Sawada, E. Okunishi and Y. Kondo, *Appl. Phys. Lett.* **95**, 10 (2009).
- [169] K. Momma and F. Izumi, *J. Appl. Crystallogr.* **44**, 1272 (2011).

-
- [170] M. Zauner, Multislice Approach for High Resolution Energy Filtered Inelastic Image Simulation, University of Vienna, 2010.
- [171] R. F. Egerton, P. Li and M. Malac, *Micron* **35**, 399 (2004).
- [172] R. F. Egerton, *Ultramicroscopy* **127**, 100 (2013).
- [173] R. F. Egerton, R. McLeod, F. Wang and M. Malac, *Ultramicroscopy* **110**, 991 (2010).
- [174] T. Ā. Li, C. Simbrunner, M. Wegscheider, A. Navarro-Quezada, M. Quast, K. Schmidegg and A. Bonanni, *J. Cryst. Growth* **310**, 13 (2008).
- [175] M. J. Hýtch, E. Snoeck and R. Kilaas, *Ultramicroscopy* **74**, 131 (1998).
- [176] M. Heidelmann, J. Barthel and L. Houben, *Ultramicroscopy* **109**, 1447 (2009).
- [177] A. Navarro-Quezada, T. Li, C. Simbrunner, M. Kiecana, G. Hernandez-Sosa, M. Quast, M. Wegscheider, M. Sawicki, T. Dietl and A. Bonanni, *J. Cryst. Growth* **310**, 1772 (2008).
- [178] I. A. Kowalik, A. Persson, M. Á. Niño, A. Navarro-Quezada, B. Faina, A. Bonanni, T. Dietl, D. Arvanitis and A. Samples, *Phys. Rev. B* **85**, 184411 (2012).

12. Peer reviewed papers

This section lists the peer reviewed works that were published benefiting from this thesis in full length. The necessary permission was granted by the respective publisher in a written form.

12.1 Highly defined nanocrystals

NANO LETTERS

Letter

pubs.acs.org/NanoLett

Tuning the Magnetic Properties of Metal Oxide Nanocrystal Heterostructures by Cation Exchange

Mykhailo Sytnyk,[†] Raimund Kirchschlager,[†] Maryna I. Bodnarchuk,^{‡,§} Daniel Primetzhofer,[‡] Dominik Kriegner,[†] Herbert Enser,[†] Julian Stangl,[†] Peter Bauer,^{||} Michael Voith,[○] Achim Walter Hassel,[○] Frank Krumeich,[‡] Frank Ludwig,[#] Arno Meingast,[▽] Gerald Kothleitner,[▽] Maksym V. Kovalenko,^{‡,§} and Wolfgang Heiss^{†,*}

[†]Institute of Semiconductor and Solid State Physics, University Linz, Altenbergerstraße 69, 4040 Linz, Austria

[‡]Institute of Inorganic Chemistry, Department of Chemistry and Applied Biosciences, ETH Zurich, CH-8093, Switzerland

[§]Laboratory for Thin Films and Photovoltaics, EMPA-Swiss Federal Laboratories for Materials Science and Technology, CH-8060, Switzerland

[‡]Ion physics, Department of Physics and Astronomy, Uppsala University, 75120 Uppsala, Sweden

^{||}Institute of Experimental Physics, University Linz, 4040 Linz, Austria

[○]Institute for Chemical Technology of Inorganic Materials, University Linz, 4040 Linz, Austria

[#]Institut für Elektrische Messtechnik und Grundlagen der Elektrotechnik, TU Braunschweig, 38106 Braunschweig, Germany

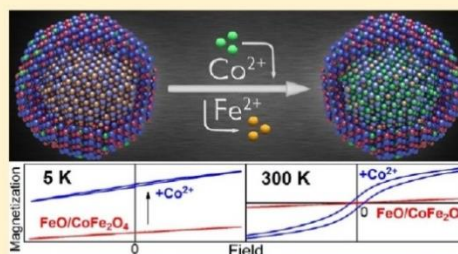
[▽]Austrian Centre for Electron Microscopy and Nanoanalysis, Institute for Electron Microscopy, Graz University of Technology, 8010 Graz, Austria

Supporting Information

ABSTRACT: For three types of colloidal magnetic nanocrystals, we demonstrate that postsynthetic cation exchange enables tuning of the nanocrystal's magnetic properties and achieving characteristics not obtainable by conventional synthetic routes. While the cation exchange procedure, performed in solution phase approach, was restricted so far to chalcogenide based semiconductor nanocrystals, here ferrite-based nanocrystals were subjected to a Fe²⁺ to Co²⁺ cation exchange procedure. This allows tracing of the compositional modifications by systematic and detailed magnetic characterization. In homogeneous magnetite nanocrystals and in gold/magnetite core shell nanocrystals the cation exchange increases the coercivity field, the remanence magnetization, as well as the superparamagnetic blocking temperature.

For core/shell nanoheterostructures a selective doping of either the shell or predominantly of the core with Co²⁺ is demonstrated. By applying the cation exchange to FeO/CoFe₂O₄ core/shell nanocrystals the Néel temperature of the core material is increased and exchange-bias effects are enhanced so that vertical shifts of the hysteresis loops are obtained which are superior to those in any other system.

KEYWORDS: magnetic nanocrystals, cation exchange, exchange bias, nanoheterostructures, ferrites



Postsynthetic substitution reactions, including galvanic replacement and cation exchange, applied to colloidal nanocrystals,^{1–14} represent a simple and versatile tool to achieve nanoarchitectures not readily accomplishable by other methods. The galvanic replacement is predominantly applied to form noble metal nanocrystals, such as Au nanocages and nanoboxes, by reacting solutions of appropriate salts with nanocrystals as “nanotemplates”.^{1–7} The cation exchange is a similar process, however, usually applied to compound semiconductors.^{8–14} By cation exchange procedures, e.g., nanorod superlattices of regularly spaced Ag₂S quantum dots in CdS colloidal quantum rods,⁹ nonepitaxial hybrid nanostructures with gold nanoparticle cores and CdS shells,¹⁵ or branched nanocrystals with either CdSe or Cu_{2-x}Se central

cores and Cu₂S pods,¹⁶ have been demonstrated. In contrast to the galvanic replacement where often substantial morphology changes are observed (e.g., hollow structures are obtained from solid nanoparticles)^{3,4} during cation exchange the nanocrystal shape is nearly preserved.^{12,14,16} The latter is caused by an anionic framework conservation, which might result from the larger ionic size of the anions in the lattice, causing their lower diffusion velocity as compared to that of the cations.¹⁷ As will be discussed below, also the coordinating solvent applied

Received: November 7, 2012

Revised: January 26, 2013

Published: January 30, 2013

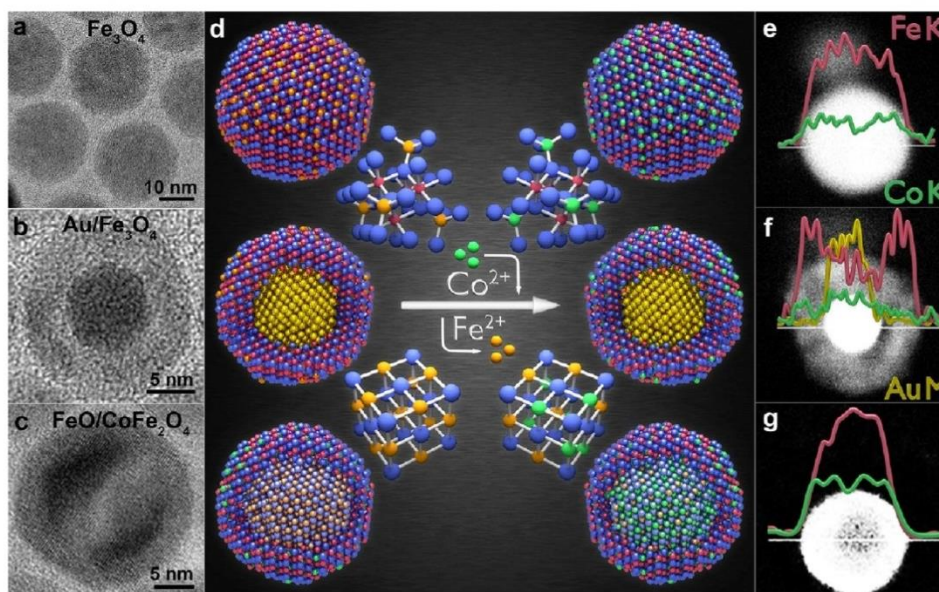


Figure 1. Three classes of magnetic nanocrystals are investigated: (a, e) homogeneous spherical magnetite (Fe_3O_4) nanocrystals, (b, f) gold/magnetite core/shell nanocrystals, and (c, g) wüstite (FeO)/magnetite core/shell nanocrystals. (a–c) TEM images of the starting materials. (d) Scheme of the cation exchange procedure in the three different nanocrystal types with inverse spinel or rock-salt crystal structure, (blue balls represent oxygen atoms; red balls, Fe^{3+} ; orange, Fe^{2+} ; green, Co^{2+} ; gold, Au atoms). (e, f) are high-angle annular dark field STEM images of nanocrystals after the Fe^{2+} to Co^{2+} cation exchange procedure is performed. The ion concentration distributions for Fe (red) and Co (green), and Au (golden) across the nanocrystals, shown by the EDX line scans (obtained for transitions from the K or M shell respectively), evidence the Co doping after the cation exchange treatment.

during cation exchange might contribute to the anionic framework conservation. Cation exchange reactions have been applied also to improve the properties of semiconductor nanocrystals. Treating PbX ($X = \text{S}, \text{Se}, \text{Te}$) with Cd^{2+} ions results, e.g., in the formation of protective CdX shells, causing a significant increase of the photoluminescence quantum yield of these materials.^{18,19}

While the high potential for tailoring of material properties by the cation exchange treatment has been demonstrated for ionic semiconductors (primarily chalcogenides),^{8–20} here it is applied to ionic magnetic oxide materials. In particular, ferrite-based single component nanocrystals and multicomponent core/shell nanocrystal heterostructures were chosen as starting materials for the cation exchange treatments (Figure 1), because of their high potential in biomedical sciences^{21–31} and their highly reproducible synthesis by facile solution-phase thermolysis routes.^{32–35} Synthesizing them as nanoheterostructures allows obtaining physical properties which are unreachable in bulk materials.³⁶ Two examples for such nanoheterostructures with properties not reachable in bulk are presented in the following to demonstrate the cation exchange procedure. The first example are nanoheterostructures combining ferrites with coinage metals (Figure 1b) exhibiting combined plasmonic and magnetic properties.^{37–39} The second example are core/shell nanocrystals combining magnetic materials of different magnetic phases (Figure 1c), showing pronounced exchange bias effects.^{40–43} The latter can be used to overcome some fundamental limitations of nanomaterials such as the superparamagnetic limit for a given nanocrystal size⁴¹ and are essential for the operation of magneto-electronic devices such as spin valves and magnetic tunnel junctions.⁴⁴

The structural similarity between Fe_3O_4 , more precisely written as $\text{Fe}^{\text{II}}\text{Fe}^{\text{III}}_2\text{O}_4$, to metal-doped spinel-type ferrites, $\text{M}^{\text{II}}\text{Fe}^{\text{III}}_2\text{O}_4$ (M abbreviates the transition metals Co, Ni, or Mn), allows the magnetic engineering of iron oxide nanocrystals by replacing the Fe^{2+} by M^{2+} .^{26,32,45} While uniform $\text{M}^{\text{II}}\text{Fe}^{\text{III}}_2\text{O}_4$ nanocrystals are usually synthesized from mixtures of appropriate precursors,^{26,32,45} synthesizing core/shell structures with $\text{M}^{\text{II}}\text{Fe}^{\text{III}}_2\text{O}_4$ shells covering either noble metal seeds or cores of other magnetic metal oxides is hardly achievable by conventional seeded-growth methods. For such cases the cation exchange procedure offers an elegant way to obtain the desired morphologies and magnetic doping levels by a simple post synthetic treatment, as is shown below. Applied to Fe_3O_4 , the cation exchange is especially attractive when it is performed with Co^{2+} , because even though the mass magnetization of CoFe_2O_4 is almost identical to that of pure magnetite, several other important parameters such as the coercivity and the magnetic blocking temperature are significantly increased, due to the higher spin–orbit coupling.⁴⁶ Thus, even small compositional modifications due to the cation exchange can be sensitively traced by inspecting the magnetic properties of the nanocrystals. While here the Fe^{2+} is replaced by Co^{2+} the same procedure can be easily expanded to further transition metals, in order to fine-tune the nanocrystals magnetic properties, and optimize them for different requirements of potential applications, including magnetic hyperthermia,²⁷ or spin-electronic device developments,⁴⁴ or for the rapidly increasing research field of magnonics.⁴⁷

To perform the Fe^{2+} to Co^{2+} cation exchange the nanocrystals, stabilized by oleic acid (OA), are treated by the following procedure: 1.2 g of CoCl_2 are dispersed in 28 mL of oleylamine. This mixture is degassed under vacuum and heated

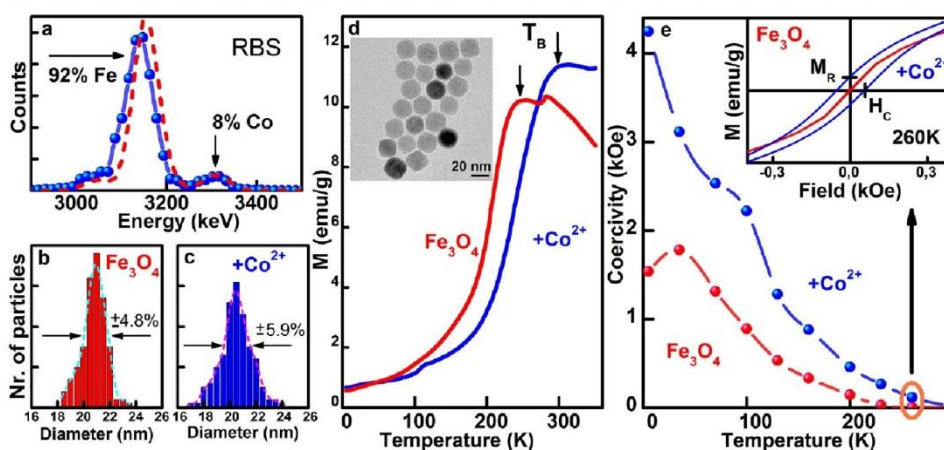


Figure 2. Co^{2+} -treated magnetite (Fe_3O_4) nanocrystals. (a) Rutherford backscattering provides a Co/Fe ratio of 8% to 92% after the Co^{2+} treatment is performed at 220 °C for 30 min. The dashed line is a model calculation. The mean sizes and size distribution, extracted from TEM images (Figure S2, Supporting Information), before (b) and after Co treatment (c), are almost identical. (d) Zero field cooled magnetization data, measured at an applied field of 100 Oe, evidence an increase of the blocking temperature T_B upon Co^{2+} treatment, as is indicated by the arrows. Inset: TEM image of the nanocrystals after Co^{2+} treatment. (e) Temperature dependent coercivity field, extracted from the data shown in Figure S5, Supporting Information. The inset shows exemplarily the 260 K hysteresis loops, exhibiting an opening after Co^{2+} treatment while being absent before the treatment. M_R and H_C are indicated for the hysteresis loop obtained after Co treatment.

to 120 °C for 20 min to completely dissolve the CoCl_2 . After cooling the solution down to room temperature in an argon atmosphere, 20 mg of nanocrystals dispersed in 0.5 mL of chloroform are added to the mixture, which is then degassed under vacuum again and heated for 20 min to 100 °C to remove the chloroform, before 1.5 mL trioctylphosphine (TOP) is injected under Ar atmosphere. The reaction is taking place at temperatures between 200 and 220 °C, and the Co content in the final nanocrystals can be controlled by both, reaction temperature and time, which was varied between 5 and 80 min. This procedure results in a cation exchange reaction which greatly preserves the nanocrystals core/shell structures, sizes and shapes (Figure S1–S3, Supporting Information show examples of Fe_3O_4 nanocrystals after the cation exchange process). Significant morphological changes are observed, however, when the reaction temperature increases above 220 °C, because the nanocrystals start to dissolve and to form aggregates of much smaller nanocrystals, or when the treatment time exceeds 80 min (Figures S3, Supporting Information). Also the addition of TOP was found to be of crucial importance, because in its absence at the reaction temperature the nanocrystals undergo fast digestive ripening leading to amorphous and small polydisperse nanoparticles (Figure S4, Supporting Information). Because of the high affinity of Co^{2+} and Fe^{2+} to oleylamine⁴⁸ not only the soluble salts are nicely dissolved but also insoluble compounds like iron oxide can be etched by solvation of Fe^{2+} with oleylamine at high temperature. In contrast, TOP has a significantly lower affinity to Fe^{2+} and Co^{2+} .⁴⁸ Thus, addition of TOP ligands to the oleylamine dispersion influences the equilibrium between solvated Fe^{2+} or Co^{2+} ions and cobalt/iron in the lattice. As was shown before for the case of cation exchange in CdSe nanocrystals treated by Pd^{2+} , and Pt^{4+} also in the present case by changing the solvent environment the thermodynamics of cation solvation is modified.⁴⁹ Another plausible effect of TOP may be related to its strongly reductive power and the ability to scavenge the traces of oxygen, thus protecting the Fe^{2+} ions in the lattice. It should be noted that in contrast to the cations Co^{2+} and Fe^{2+}

the anion O^{2-} does not react with oleylamine, because both, the O^{2-} and the oleylamine represent bases according to the theory of Pearson.⁵⁰ This might be another important reason why the anion framework is preserved during the cation exchange process.

The cation exchange is stopped by cooling down the nanocrystal solution. Chloroform is added to the solution and the nanocrystals are aggregated by ethanol together with acetone for the washing procedure. Few drops of OA are added to improve the colloidal stability in the chloroform solvent. The whole washing procedure is repeated 6 times and finished by filtration. This procedure removes the CoCl_2 and aggregates of other byproducts from the nanocrystal solution, to allow accurate determination of the Co content in the nanocrystals, probed by (i) EDX on relatively thick nanocrystal films, (ii) by Rutherford backscattering spectrometry (RBS) performed on nanocrystal (sub)monolayers, and (iii) by atomic absorption spectroscopy (AAS) performed from nanocrystals which are completely dissolved in acidic solutions. The Co concentrations are deduced from all three methods, and for the presented samples the scatter between the data is less than $\pm 1\%$.

To facilitate a comparison between the results of the three nanocrystal systems under investigation (Figures 1 and S1 (Supporting Information)), we have chosen in all cases spherically shaped nanocrystals with mean diameters close to 20 nm. The first system represents homogeneous magnetite nanocrystals with a mean diameter of 21 nm (Figures 1a, S1a, S2, and S3 (Supporting Information)), synthesized by thermal decomposition of iron-oleate in the presence of oleic acid.³³ In this case the cation exchange results in a rather homogeneous Co alloying of the nanocrystals, by replacing a part of the Fe^{2+} , residing on the octahedral sites of the inverse spinel structure of magnetite, by Co^{2+} (sketched in Figure 1d). This scenario is confirmed by the energy dispersive X-ray (EDX) analysis, performed after cation exchange by scanning transmission electron microscopy (STEM). The EDX line profile in Figure 1e shows an almost as smooth Co distribution across the nanocrystal as is also found for Fe. After 30 min of reaction

with CoCl_2 at 220 °C in this sample a Co content of 8% is detected, e.g., in the RBS spectrum in Figure 2a by the appearance of a distinct Co peak on the right-hand side of the Fe peak. TEM images confirm that the size and shape of the nanocrystals is almost preserved (Figure 2b,c; the inset in Figure 2d shows the nanocrystals after Co exchange and a direct comparison of the nanocrystals before and after treatment is given in Figure S2, Supporting Information). While the Co alloying causes only subtle effects with respect to nanocrystal morphology, it is greatly affecting their magnetic properties. The magnetic response changes because of strong spin–orbit couplings at the Co^{2+} sites and the concomitant increase of the magnetic anisotropy. The latter has a direct effect on the temperature dependence of the zero-field-cooling magnetization, showing the typical behavior of magnetic nanocrystals (Figure 2d). At low temperature the magnetic moments of the individual nanocrystals, resulting from the ferromagnetically coupled M^{2+} ion spins (the magnetic moments of the Fe^{3+} ions are antiferromagnetically coupled in ferrites and thus do not contribute to the magnetization), are blocked and are pointing randomly into all directions, so that the total magnetization of the sample is zero. With increasing temperature the sample magnetization, given here per weight of the magnetic ions (Fe and Co), increases and at high temperatures the thermal energy of the nanocrystals overcomes the magnetic anisotropic energy barrier between different magnetic easy axes and between the spin up and spin down direction within the same easy axis, respectively. As a consequence the magnetization typically shows a superparamagnetic behavior with a $1/T$ dependence of the sample magnetization (for the present sample the $1/T$ dependence can be expected to occur well above 300 K, whereas for the nanocrystals described in the next paragraph it is clearly displayed in Figure 3a). Thus, the magnetization as a function of temperature exhibits a maximum at the so defined blocking temperature T_B . For the Fe_3O_4 nanocrystals with a size of 21 nm this blocking temperature is found at 250 K, whereas the Co treatment increases T_B by 60 to 310 K. This causes also an opening of the hysteresis loop close to room temperature, which is observed after cation exchange but is completely absent for the initial Fe_3O_4 nanocrystals (inset in Figure 2e). From the opening of the hysteresis loops the values of the coercivity field, H_C , and remanent magnetization, M_R , are measured at zero magnetization and zero external field, respectively (indicated in the inset of Figure 2e). Both values are strongly temperature dependent, and at all temperatures, H_C is at least twice as high after the Co treatment (Figure 2e, the corresponding hysteresis data before and after Co^{2+} treatment are shown in Figure S5, Supporting Information). Thus, the Co treatment results in an overall increase of coercivity, remanence and blocking temperature, due to an increased magneto-crystalline anisotropy. The latter is directly probed by measuring the relaxation of the nanocrystals magnetic moment, after aligning them by an external magnetic field.⁵¹ If the nanoparticles are immobilized, magnetorelaxometry experiments provide a purely Néel relaxation time τ_N due to flipping of the magnetic moments within the nanocrystals caused by thermal activation. The flipping time is exponentially proportional to the magnetocrystalline anisotropy energy.⁵¹ After Co^{2+} treatment of the nanocrystals, room temperature flux gate magnetometry detects an increase in τ_N (Figure S6, Supporting Information). An even more significant increase of τ_N due to the Co^{2+} treatment of magnetite nanocrystals is

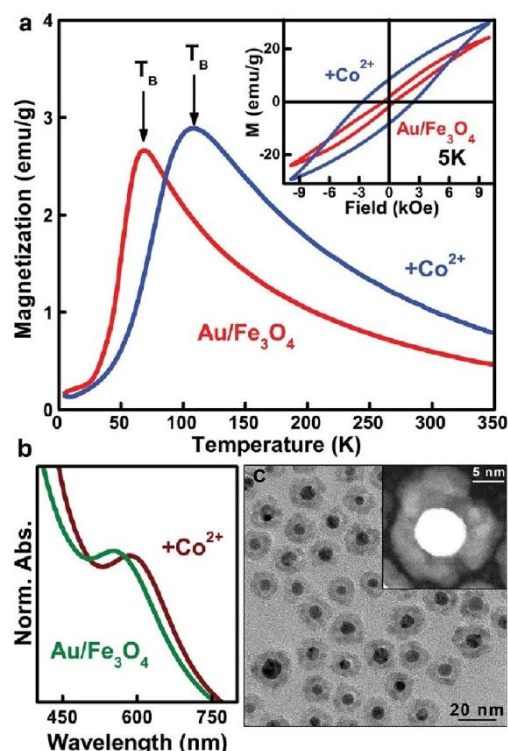


Figure 3. Co^{2+} treated gold/ Fe_3O_4 core/shell nanocrystals. (a) Zero-field cooled magnetization curves, measured at an applied field of 100 Oe, evidence an increased blocking temperature after Co^{2+} treatment. The inset shows the effect of the Co^{2+} treatment on low temperature hysteresis loops. (b) Normalized optical absorbance spectra exhibit plasmon peaks close to 600 nm wavelength. (c) TEM overview (bright field) of the nanocrystals after Co^{2+} treatment. The inset shows a dark field image of an individual nanocrystal, highlighting the defect structure (polycrystallinity) of the shell.

observed for smaller nanocrystal sizes (Figure S6b, Supporting Information). In Figure S7 (Supporting Information), the results for 9 nm large nanocrystals are summarized, showing also an increase of T_B from 150 to 206 K and an increase of the coercivity by a factor of 5.7. It should be noted that these observed modifications of the magnetic properties are solely due to the exchange of the Fe^{2+} to the Co^{2+} ions and not due to different states of nanocrystal aggregation. The latter is ruled out by concentration dependent magnetization measurements, showing almost no dependence of the normalized magnetization versus temperature, at least when the dilution of nanocrystals is performed in a good solvent (Figure S8, Supporting Information).

The second system investigated here represents a nano-heterostructure, formed by a gold core and a relatively uniform magnetite shell (Figures 1b, S1b, and S9 (Supporting Information)). Such magnetic–plasmonic core shell nanoparticles have attracted great interest because the localized surface plasmon of the gold cores provide an optical addressability for tracking or monitoring of the magnetic nanoparticles.³⁸ The gold/ Fe_3O_4 core/shell nanocrystals are grown by decomposition of iron pentacarbonyl on gold seed nanocrystals, and subsequent in situ oxidation of the iron shell into Fe_3O_4 .³⁹ The shortcoming of these core/shell nanocrystals

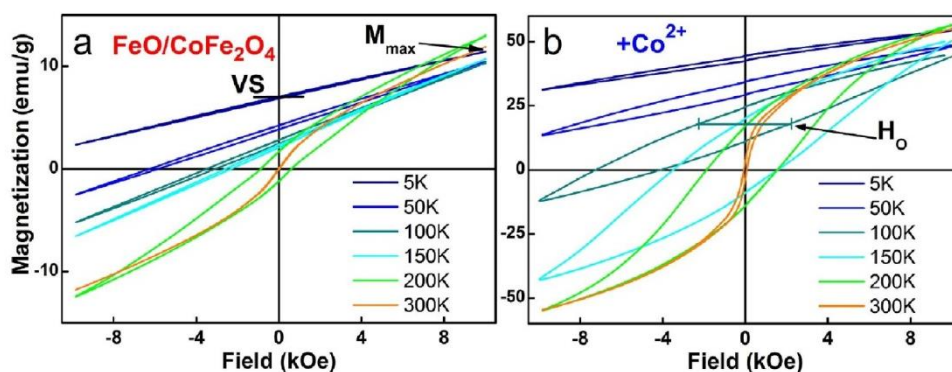


Figure 4. Hysteresis loops of FeO/CoFe₂O₄ core/shell nanocrystals before (a) and after (b) Co²⁺ treatment, measured after field cooling. The averaged Co content is 18% in part a and 27% in part b. The vertical loop shift VS, the maximum magnetization M_{max} and the opening of the hysteresis H_0 are exemplarily indicated.

is the relatively small magnetic moment observed at room temperature due to their limited shell thickness and their small magnetic blocking temperature.³⁹ Applying the Fe²⁺ to Co²⁺ cation exchange to these nanocrystals improves both of these parameters, T_B from 68 K to about 110 K and the room temperature magnetization from 0.62 emu/g to 1.08 emu/g (at a field of 100 Oe, Figure 3a). These improvements, together with an increase of the coercivity at low temperatures (inset in Figure 3a), is obtained here by doping of the nanocrystal shell by 11% of Co, as is deduced also by RBS (Figure S9, Supporting Information). Because of the high chemical stability of the gold core, it is not affected by any treatments with Co²⁺ precursors (Figure 1d,f). Thus, the optical properties of the nanoheterostructures, dominated by the plasmonic feature of the gold nanocrystal core, are almost preserved. As shown in Figure 3b, the plasmon resonance found at 553 nm before Co²⁺ treatment, shifts only 33 nm due to a change of the dielectric function of the nanocrystal shells. While the inert gold core is unaffected by the Co treatment, the shell becomes more polycrystalline during the cation exchange process (Figures 3c and S9 (Supporting Information)), which is important because defects in the lattice structure facilitate cation diffusion from the nanocrystals surfaces to their interior.^{20,52} That such a diffusion is indeed taking place is not only evidenced by the EDX line scans shown in Figure 1e,f but is confirmed also by the following experiments performed on FeO/CoFe₂O₄ core/shell nanocrystals.

The situation is completely different in the third system, which are magnetic heterostructure nanocrystals combining antiferromagnetic (AFM) and ferrimagnetic components. This combination is of special interest because it provides a set of unique magnetic properties by exchange coupling via the heterostructures interface,^{40–43} These exchange bias effects are important for giant magnetoresistance devices or spin valves,⁵³ which are applied e. g., in magnetic-random access memories (MRAMS) or in the read heads of hard discs. The present samples are spherical core/shell nanocrystals with FeO (Wüstite) in the center and CoFe₂O₄ shells (Figure 1c).⁴³ These nanocrystals exhibit a cubic NaCl crystal structure in the core, while the shell is formed by an inverse spinel structure. Interestingly, these nanocrystals are grown by thermolysis of a mixture of iron- and cobalt oleate, which initially was expected to result in homogeneously Co-doped magnetite nanocrystals as those shown above, obtained by the cation exchange

treatment of Fe₃O₄ nanocrystals. The hysteresis loops of these FeO/CoFe₂O₄ exhibit in particular very pronounced effects due to the exchange coupling, primarily anomalously large vertical shifts, VS, but dependent on temperature also increased coercivity (Figure 4a). These VSs are observed, when prior to the measurements all magnetic moments in the samples are aligned at high temperatures by an applied external field, which is maintained during cooling down. After cooling the samples, the hysteresis loops are measured by varying and reversing the external magnetic field. The vertical shifts of the hysteresis loops observed after field cooling indicate that a part of the ferromagnetic spins, which are present in our samples in the CoFe₂O₄ shell, are pinned by exchange interactions via the interface to the spins of the antiferromagnetic FeO core, which does not reverse under reversal of the external magnetic field.⁴³ VSs are observed when the *effective* Zeeman energy (difference between Zeeman energy and anisotropy energy) of the ferro- or ferrimagnetic material is smaller than the anisotropy energy of the antiferromagnetic material as well as smaller than the interface exchange energy.⁵⁴ In the present nanocrystals, this condition is fulfilled because of the large magnetic anisotropy present in CoFe₂O₄, which reduces the effective Zeeman energy in this material. In the present sample at 5 K, the VS is very pronounced and it amounts to 60% of the maximum magnetization, M_{max} , measured at an applied field of 1 T. This value is as high as the highest value reported for specially designed layered heterostructure systems.⁵⁵

While the exchange bias effects are very pronounced at low temperatures, they are unfortunately limited to temperatures below 200 K, which is the Néel temperature of the FeO core ($T_N(\text{FeO})$), at which the AF to paramagnetic phase transition occurs. To increase the maximum temperature where exchange bias effects can be found, which is mandatory because any application of these materials in devices such as spin valves requires this effect to be present at room temperature, the core material has to be modified. One possibility is given by changing the core from FeO toward Fe_{1-x}Co_xO, because CoO has a Néel temperature close to room temperature.⁵⁶ This modification of the core is again performed by the cation exchange procedure. In this case it hardly affects the CoFe₂O₄ shell, because it is already free of Fe²⁺ but predominantly affects the FeO core material. Indeed, after the cation-exchange treatment a rather uniform distribution of Co across the nanocrystal diameter is found (Figure 1g). This indicates that in

this case the Co^{2+} cation exchange converts the FeO to $\text{Co}_x\text{Fe}_{1-x}\text{O}$ (sketched in Figure 1d).

The Co doping of the Wüstite cores is confirmed by the magnetic properties of the nanocrystals after the Co^{2+} treatment. The hysteresis loops still show the characteristic features of exchange bias in the form of vertical loop shifts (Figure 4b). At 5 K, the VS even increased to 78% of M_{max} , which is the to the best of our knowledge the highest value ever reported for any system.⁵⁵ The value of the magnetization also increased, and the characteristic exchange bias effects are observed even above the Néel temperature of FeO ($T_N(\text{FeO})$). For the starting material, the latter can be clearly identified by an abrupt increase of the temperature dependent magnetization, measured after sample cooling in zero field and applying during the measurement a small field of 100 Oe (Figure 5a). This abrupt magnetization increase close to 190 K is caused by the AF to paramagnetic phase transition of the

core material, since in the AF phase all magnetic moments are canceling each other, whereas in the paramagnetic phase they contribute to the magnetization, because the small external field aligns them into field direction. The maximum of this curve, found close to 240 K corresponds to the superparamagnetic blocking temperature of the CoFe_2O_4 shell $T_B(\text{CoFe}_2\text{O}_4)$. While T_N of the core and T_B of the shell are well resolved in the magnetization data of the initial material, the Co^{2+} treatment results in a shift of both parameters to higher temperatures. While T_N cannot be clearly identified, (green and blue lines in Figure 5a) T_B still corresponds to the magnetization maximum. For the sample with the highest averaged Co^{2+} content of 27% it is found at 323 K, well above room temperature. Thus, the hysteresis loop of this sample shows a finite opening at 300 K, whereas initial nanocrystals show only a superparamagnetic behavior (inset in Figure 5b).

To obtain an estimate for the Néel temperature of the core after Co^{2+} treatment, a closer inspection of the exchange bias effects is required. In the present sample, the exchange bias across the interface affects two parameters, the opening of the hysteresis loop (H_o , indicated in Figure 4b) measured at the center of the loop, (which is eventually shifted in vertical direction), and the vertical shift of the loop (indicated in Figure 4a). Also the hysteresis opening H_o shows a characteristic feature close to the Néel temperature. For the initial material a peak is observed in H_o versus T close to T_N indicating an enhancement of the coercivity. This enhancement is again caused by the exchange interaction via the interface, because close to T_N the anisotropy energy of the antiferromagnet becomes strongly reduced. As soon as it is smaller than the exchange interaction across the interface, the antiferromagnetically aligned spins of the cores rotate coherently with the ferromagnetically aligned spins of the shells under field reversal,⁵⁴ thus enhancing the coercivity of the whole particles. Above T_N the core is in the paramagnetic state and the hysteresis opening is solely caused by the anisotropy energy of the ferromagnetic shell. After Co^{2+} treatment the opening of the hysteresis loop is increased at all temperatures, at the maximum of H_o versus temperature the opening amounts 5143 Oe, which is 18.8 times larger than for the initial material. Similarly, the VS of the hysteresis loop increased by the Co^{2+} treatment at all temperatures. At low temperature it increases from 6.97 to 43.51 emu/g (Figure 5c) and a finite vertical shift of the hysteresis loop is observed even up to room temperature (inset in Figure 5c). Since the VS is a results solely from the exchange interaction between core and shell of different magnetic phases, its observation at room temperature confirms the presence of an antiferromagnetic phase at least for a part of the nanocrystal batch. Thus, the Co^{2+} treatment shifted the AF phase transition temperature from 200 K, as observed for the initial material, to room temperature, which is only possible if the FeO cores of the nanocrystals have been changed to be rich of CoO. This fact evidence that the Fe^{2+} to Co^{2+} exchange can act quite efficiently even through an protective nanocrystal shell. This result is also of interest, because the observation of exchange bias effects is also the precondition for any application of these materials in spin valve based devices.⁵³

Overall, by the Co^{2+} treatment the Co content in the FeO/ CoFe_2O_4 nanocrystals increased from 18% to 27%, as is evidenced by AAS and RBS (Figure S10, Supporting Information). It changed, however, also the morphology of the nanocrystals. From inspections of TEM images (Figure S11, Supporting Information) the morphological changes are

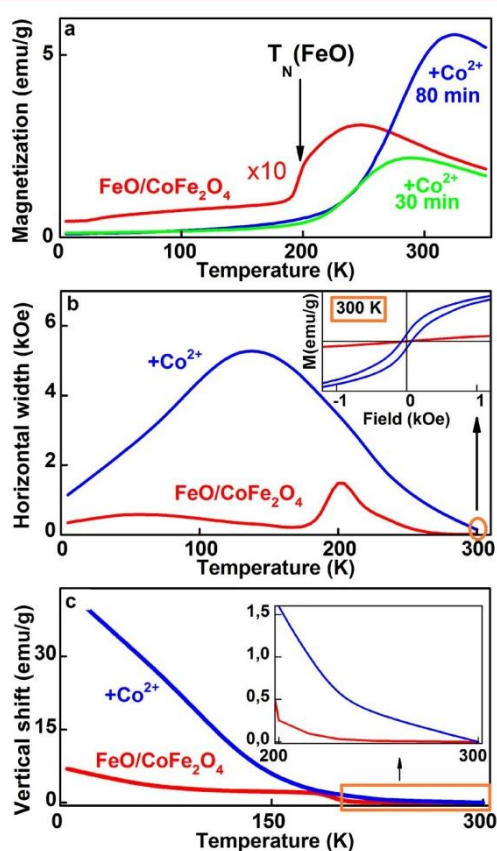


Figure 5. Effect of the Co^{2+} treatment on the exchange bias features of FeO/ CoFe_2O_4 nanocrystals. (a) Magnetization after zero field cooling, measured with an applied field of 100 Oe, shows a disappearance of the antiferromagnetic to paramagnetic phase transition upon Co^{2+} treatment (note that the data for the initial material is magnified by a factor of 10). (b) Opening of the hysteresis loop, measured at their vertically shifted center, is greatly enhanced. The inset shows an open hysteresis loop at 300 K for the Co treated nanocrystals (blue line) whereas the initial material (red line) exhibits a completely closed hysteresis. (c) Vertical loop shifts before (red line) and after (blue line) Co^{2+} treatment. The inset shows the high temperature region on magnified scale.

hardly seen, because of the polydispersity of the core/shell dimensions. However, the changes are clearly revealed by synchrotron X-ray diffraction, performed at beamline P02/HASYLAB Hamburg with 60 keV X-ray photons. The diffraction patterns shown in Figure 6a can be well fitted by assuming

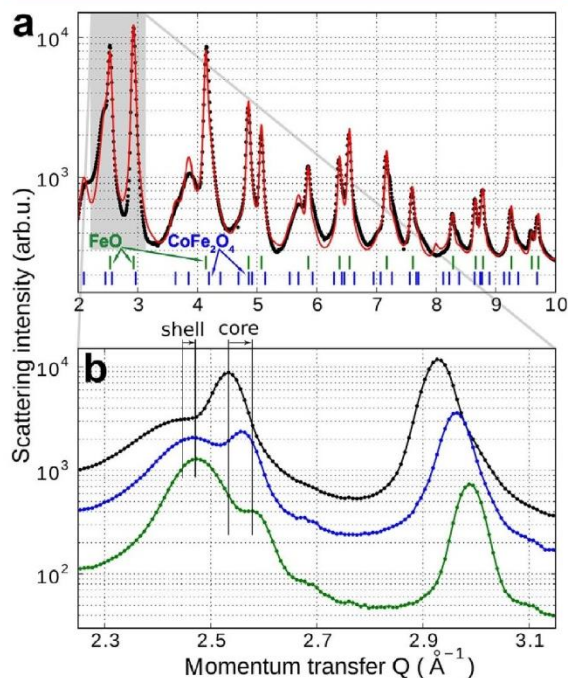


Figure 6. Change of the core and shell morphology during Co²⁺ treatment. (a) Synchrotron X-ray powder diffraction data from FeO/CoFe₂O₄ nanocrystals. The fit of the data (red line) is used to extract the ratio of core to shell volume. The green and blue dashes on the bottom indicate the peak positions of bulk CoFe₂O₄ and FeO, respectively. (b) Enlarged scale allows the observation of peak shifts and intensity changes upon Co²⁺ treatment.

separate phases of CoFe₂O₄ and of Fe_{1-x}Co_xO₄, by allowing the lattice parameters to vary with respect to that of bulk. By zooming out the region around a momentum transfer of 2.5 Å⁻¹ the effect of the Co²⁺ treatment can be monitored (Figure 6b). Here the narrow peak at 2.53 Å⁻¹ corresponds to the FeO core and that at 2.46 Å⁻¹ to the CoFe₂O₄ shell. For the core peak the Co²⁺ treatment results in a shift to larger diffraction angles, corresponding to a decrease of the lattice parameter, indicating the incorporation of Co into the cubic lattice of FeO (bulk FeO has a lattice parameter of 0.4332 nm while that of CoO is 0.4214 nm).^{57,58} The second peak shows a much smaller peak shift, but a rather pronounced narrowing of its width, and an increase of its intensity, both indicating an increase of the dimensions of the CoFe₂O₄ shell. From a fit of the data in Figure 6a the initial nanocrystals exhibit a core volume which is 41% of the nanocrystals total volume, whereas after the Co²⁺ treatment for 80 min the core volume shrinks to an average value of 8% (aliquots taken for shorter treatment times indicate that this shrink of the core and growth of shell is a continuous process). This increase of the CoFe₂O₄ phase during Co exchange explains also the observed increase of the magnetic moment of the nanocrystals (Figure 4 and 5) because the antiferromagnetic core does not contribute to the

magnetization. All these observations, however, confirm that the Co is able to diffuse into the nanocrystals sufficiently far to change the core composition from FeO toward Fe_{1-x}Co_xO, with increased Néel temperature. The growth of the CoFe₂O₄ shell in expense of the core we attribute to a partial oxidation of the Fe²⁺ present in the Fe_{1-x}Co_xO core after cation exchange. This process requires oxygen to diffuse through the shell to the core, which is facilitated by the cation exchange, producing defects in the shell acting as diffusion channels.^{20,52} Thus, the oxidation takes place after the samples are exposed to the ambient after the cation exchange is finished. Before the cation exchange process, these defect related diffusion channels were obviously absent, because the Fe₃O₄/FeO core/shell nanocrystals we found to have a stable morphology and composition for several years.

In conclusion, the cation exchange process is demonstrated here to be a valuable tool for tuning and improving the magnetic properties of different metal oxide based colloidal nanocrystals. Demonstrated is an increase of the superparamagnetic blocking temperature, of magnetic remanence and coercivity as well as of various exchange effects, by replacing Fe²⁺ by Co²⁺, due to an enhancement of the magnetocrystalline anisotropy. Outstanding are the demonstrated vertical shifts of the hysteresis loops in Co²⁺ treated core/shell nanocrystals, which amounts up to 78% of the saturation magnetization at low temperature, representing a substantially higher value than in any other system. The sizes and shapes of the nanocrystals are almost preserved. In homogeneous ferrite nanocrystals a rather homogeneous Co doping is achieved, whereas in nanocrystal heterostructures specific compounds of the nanocrystals can be selectively manipulated. In gold/iron-oxide core/shell nanocrystals exclusively the shell is modified by the cation exchange, whereas in FeO/CoFe₂O₄ nanocrystals the core undergoes severe changes. Thus, the cation exchange process enables to obtain novel nanoheterostructures with tunable magnetic properties, which are not achievable by direct synthesis. While nanocrystal materials with exchange bias effects at room temperature are of primary interest for applications in spin-valves and magnetoelectronic nanodevices based on them, the Fe²⁺ to Co²⁺ cation exchange process demonstrated here for metal-oxides can be easily expanded to further transition metal ions, for designing optimized materials for a large range of applications.

■ ASSOCIATED CONTENT

Supporting Information

Detailed experimental methods and Figures S1–S11 (STEM and TEM images, hysteresis loops, magnetization relaxation, solvent dependent magnetization, and Rutherford backscattering data). This material is available free of charge via the Internet at <http://pubs.acs.org>.

■ AUTHOR INFORMATION

Corresponding Author

* E-mail: Wolfgang.Heiss@jku.at.

Notes

The authors declare no competing financial interest.

■ ACKNOWLEDGMENTS

We thank Oleksandr Mykytiuk for his art work in Figure 1 and the abstract graphics. Financial support from the Austrian Science Fund FFG via the “Austrian Nano Initiative” (Project

NSI-NanoShape II) and from the FWF (project SFB IRON) is acknowledged. The work was also supported by two electron microscopy centers, at ETH Zurich (EMEZ) and at EMPA. M.I.B. acknowledges financial support from Swiss SNF (Marie-Heim Vögtlin grant). We thank the staff at beamline P02 at Petra III/HASYLAB Hamburg (P. Walter and A.-C. Dippel) for assistance with the synchrotron experiments. D.K. acknowledges financial support by the Austrian Academy of Science.

REFERENCES

- (1) Sun, Y.; Xia, Y. *Science* **2002**, *298*, 2176–2179.
- (2) González, E.; Arbiol, J.; Puntès, V. F. *Science* **2011**, *334*, 1377–1380.
- (3) Sun, Y.; Mayers, B. T.; Xia, Y. *Nano Lett.* **2002**, *2*, 481–485.
- (4) Sun, Y.; Xia, Y. *Nano Lett.* **2003**, *11*, 1569–1572.
- (5) Lu, X.; Tuan, H. Y.; Chen, J.; Li, Z. Y.; Korgel, B. A.; Xia, Y. *Nano Lett.* **2005**, *5*, 2058–2062.
- (6) Lu, X.; Tuan, H. Y.; Chen, J.; Li, Z. Y.; Korgel, B. Y.; Xia, Y. *J. Am. Chem. Soc.* **2007**, *129*, 1733–1742.
- (7) Au, L.; Lu, X.; Xia, Y. *Adv. Mater.* **2008**, *20*, 2517–2522.
- (8) Son, D. H.; Hughes, S. M.; Yin, Y.; Alivisatos, A. P. *Science* **2004**, *306*, 1009–1012.
- (9) Robinson, R. D.; Sadtler, B.; Demchenko, D. O.; Erdonmez, C. K.; Wang, L. W.; Alivisatos, A. P. *Science* **2007**, *317*, 355–358.
- (10) Luther, J. M.; Zheng, H.; Sadtler, B.; Alivisatos, A. P. *J. Am. Chem. Soc.* **2009**, *131*, 16851–16857.
- (11) Sadtler, B.; Demchenko, D. O.; Zheng, H.; Hughes, S. M.; Merkle, M. G.; Dahmen, U.; Wang, L. W.; Alivisatos, A. P. *J. Am. Chem. Soc.* **2009**, *131*, 5285–5293.
- (12) Jain, P. K.; Amirav, L.; Aloni, S.; Alivisatos, A. P. *J. Am. Chem. Soc.* **2010**, *132*, 9997–9999.
- (13) Rivest, J. B.; Swisher, S. L.; Fong, L. K.; Zheng, H.; Alivisatos, A. P. *ACS Nano* **2011**, *5*, 3811–3816.
- (14) Jain, P. K.; Beberwyck, B. J.; Fong, L. K.; Polking, M. J.; Alivisatos, A. P. *Angew. Chem., Int. Ed.* **2012**, *51*, 1–5.
- (15) Zhang, J.; Tang, Y.; Lee, K.; Ouyang, M. *Science* **2010**, *327*, 1634–1638.
- (16) Miszta, K.; Dorfs, D.; Genovese, A.; Kim, M. R.; Manna, L. *ACS Nano* **2011**, *5*, 7176–7183.
- (17) Rivesta, J. B.; Jain, P. K. *Chem. Soc. Rev.* **2013**, *42*, 89–96.
- (18) Pietryga, J. M.; Werder, D. J.; Williams, D. J.; Casson, J. L.; Schaller, R. D.; Klimov, V. I.; Hollingsworth, J. A. *J. Am. Chem. Soc.* **2008**, *130*, 4879–4885.
- (19) Lambert, K.; De Geyter, B.; Moreels, L.; Hens, Z. *Chem. Mater.* **2009**, *21*, 778–790.
- (20) Casavola, M.; Van Huis, M. A.; Bals, S.; Lambert, K.; Hens, Z.; Vanmaeckelbergh, D. *Chem. Mater.* **2011**, *24*, 294–302.
- (21) Gupta, A. K.; Gupta, M. *Biomaterials* **2005**, *26*, 3995–4021.
- (22) Bulte, J. W. M.; Douglas, T.; Witwer, B.; Zhang, S. C.; Strable, E.; Lewis, B. K.; Zywicke, H.; Miller, B.; van Gelderen, P.; Moskowitz, B. M.; Duncan, I. D.; Frank, J. A. *Nat. Biotechnol.* **2001**, *19*, 1141–1147.
- (23) Wang, D.; He, J.; Rosenzweig, N.; Rosenzweig, Z. *Nano Lett.* **2004**, *4*, 409–413.
- (24) Scherer, F.; Anton, M.; Schillinger, U.; Henke, J.; Bergemann, C.; Krüger, A.; Gänsbacher, B.; Plank, C. *Gene Ther.* **2002**, *9*, 102–109.
- (25) Gleich, B.; Weizenecker, J. *Nature* **2005**, *435*, 1214–1217.
- (26) Lee, J. H.; Huh, Y. M.; Jun, Y. W.; Seo, J. W.; Jang, J. T.; Song, H. T.; Kim, S.; Cho, E. J.; Yoon, H. G.; Suh, J. S.; Cheon, J. *Nat. Med.* **2007**, *13*, 95–99.
- (27) Lee, J. H.; Jang, J. T.; Choi, J. S.; Moon, S. H.; Noh, S. H.; Kim, J. W.; Kim, J. G.; Kim, I. S.; Park, K. I.; Cheon, J. *Nat. Nanotechnol.* **2011**, *6*, 418–422.
- (28) Medarova, Z.; Pham, W.; Farrar, C.; Petkova, V.; Moore, A. *Nat. Med.* **2007**, *13*, 372–377.
- (29) Liong, M.; Lu, J.; Kovochich, M.; Xia, T.; Ruehm, S. G.; Nel, A. E.; Tamanoi, F.; Zink, J. I. *ACS Nano* **2008**, *2*, 889–96.
- (30) Koh, I.; Josephson, L. *Sensors* **2009**, *9*, 8130–8145.
- (31) Laurent, S.; Forge, D.; Port, M.; Roch, A.; Robic, C.; Vander Elst, L.; Muller, R. N. *Chem. Rev.* **2008**, *108*, 2064–2110.
- (32) Jana, N. R.; Chen, Y.; Peng, X. *Chem. Mater.* **2004**, *16*, 3931–3935.
- (33) Kovalenko, M. V.; Bodnarchuk, M. I.; Lechner, R. T.; Hesser, G.; Schäffler, F.; Heiss, W. *J. Am. Chem. Soc.* **2007**, *129*, 6352–6353.
- (34) Jun, Y. W.; Choi, J. S.; Cheon, J. *Angew. Chem., Int. Ed.* **2006**, *45*, 3414–3439.
- (35) Park, J.; An, K.; Hwang, Y.; Park, J. G.; Noh, H. J.; Kim, J. Y.; Park, J. H.; Hwang, N. M.; Hyeon, T. *Nat. Mater.* **2004**, *3*, 891–895.
- (36) Ronny, C.; Saunders, A. E.; Banin, U. *Angew. Chem., Int. Ed.* **2010**, *49*, 4878–4897.
- (37) Xu, Z.; Hou, Y.; Sun, S. *J. Am. Chem. Soc.* **2007**, *129*, 8696–8699.
- (38) Levin, C. S.; Hofmann, C.; Ali, T. A.; Kelly, A. T.; Morosan, E.; Nordlander, P.; Whitmire, K. H.; Halas, N. J. *ACS Nano* **2009**, *3*, 1379–1388.
- (39) Shevchenko, E. V.; Bodnarchuk, M. I.; Kovalenko, M. V.; Talapin, D. V.; Smith, R. K.; Aloni, S.; Heiss, W.; Alivisatos, A. P. *Adv. Mater.* **2008**, *20*, 4323–4329.
- (40) Kavich, D. W.; Dickerson, J. H.; Mahajan, S. V.; Hasan, S. A.; Park, J. H. *Phys. Rev. B* **2008**, *78*, 174414.
- (41) Skumryev, V.; Stoyanov, S.; Zhang, Y.; Hadjipanayis, G.; Givord, D.; Nogués, J. *Nature* **2003**, *423*, 850–853.
- (42) Pichon, B. P.; Gerber, O.; Lefevre, C.; Florea, I.; Fleutot, S.; Baaziz, W.; Pauly, M.; Ohlmann, M.; Ulhaq, C.; Ersen, O.; Pierron-Bohnes, V.; Panissod, P.; Drillon, M.; Begin-Colin, S. *Chem. Mater.* **2011**, *23*, 2886–2900.
- (43) Bodnarchuk, M. I.; Kovalenko, M. V.; Groiss, H.; Resel, R.; Reissner, M.; Hesser, G.; Lechner, R. T.; Steiner, W.; Schäffler, F.; Heiss, W. *Small* **2009**, *5*, 2247–2252.
- (44) Wolf, S. A.; Awschalom, D. D.; Buhrman, R. A.; Daughton, J. M.; von Molnár, S.; Roukes, M. L.; Chtchelkanova, A. Y.; Treger, D. M. *Science* **2001**, *16*, 1488–1495.
- (45) Sun, S.; Zeng, H.; Robinson, D. B.; Raoux, S.; Rice, P. M.; Wang, S. X.; Li, G. *J. Am. Chem. Soc.* **2004**, *126*, 273–279.
- (46) Song, Q.; Zhang, Z. *J. Phys. Chem B* **2006**, *110*, 11205–11209.
- (47) Neusser, S.; Grundle, D. *Adv. Mater.* **2009**, *21*, 2927–2932.
- (48) Ahrland, S.; Chatt, J.; Davies, N. R., Q. *Rev. Chem. Soc.* **1958**, *12*, 265–276.
- (49) Wark, S. E.; Hsia, C. H.; Son, D. H. *J. Am. Chem. Soc.* **2008**, *130*, 9550–9555.
- (50) Pearson, R. G. *J. Am. Chem. Soc.* **1963**, *85*, 3533–3539.
- (51) Ludwig, F.; Heim, E.; Schilling, M. *J. Appl. Phys.* **2007**, *101*, 113909 (10 pages).
- (52) Dieckmann, R. *J. Phys. Chem. Solids* **1998**, *59*, 507–525.
- (53) Nogués, J.; Schuller, I. K. *J. Magn. Magn. Mater.* **1999**, *192*, 203–232.
- (54) Dobrynin, A. N.; Ievlev, D. N.; Temst, K.; Lievens, P.; Margueritat, J.; Gonzalo, J.; Afonso, C. N.; Zhou, S. Q.; Vantomme, A.; Piscopiello, E.; Van Tendeloo, G. *Appl. Phys. Lett.* **2005**, *87*, 012501.
- (55) de la Venta, J.; Erekhinsky, M.; Wang, S.; West, K. G.; Morales, R.; Schuller, I. K. *Phys. Rev. B* **2012**, *84*, 134447.
- (56) Ambrose, T.; Chien, C. L. *Phys. Rev. Lett.* **1996**, *76*, 1743–1746.
- (57) Kannan, R.; Seehra, M. S. *Phys. Rev. B* **1987**, *35*, 6847–6853.
- (58) Jette, E. R.; Foote, F. J. *Chem. Phys.* **1933**, *1*, 29–36.

12.2 Gallium nitride doped with transition metals

PHYSICAL REVIEW B **84**, 035206 (2011)

Experimental probing of exchange interactions between localized spins in the dilute magnetic insulator (Ga,Mn)N

A. Bonanni,^{1,*} M. Sawicki,^{2,†} T. Devillers,¹ W. Stefanowicz,^{2,3} B. Faina,¹ Tian Li,¹ T. E. Winkler,¹ D. Sztankiel,² A. Navarro-Quezada,¹ M. Rovezzi,¹ R. Jakiela,² A. Grois,¹ M. Wegscheider,¹ W. Jantsch,¹ J. Suffczyński,⁴ F. D'Acapito,⁵ A. Meingast,⁶ G. Kothleitner,⁶ and T. Dietl^{2,4,‡}

¹Institut für Halbleiter- und Festkörperphysik, Johannes Kepler University, Altenbergerstrasse 69, 4040 Linz, Austria

²Institute of Physics, Polish Academy of Sciences, al. Lotników 32/46, 02-668 Warszawa, Poland

³Laboratory of Magnetism, Białystok University, ul. Lipowa 41, 15-424 Białystok, Poland

⁴Faculty of Physics, University of Warsaw, 00-681 Warszawa, Poland

⁵CNR-INFN-OGG, Italian Collaborating Research Group, "GILDA" - ESRF, 38043 Grenoble, France

⁶Institute for Electron Microscopy-FELMI, Graz University of Technology, 8010 Graz, Austria

(Received 19 May 2011; published 28 July 2011)

The sign, magnitude, and range of the exchange couplings between pairs of Mn ions is determined for (Ga,Mn)N and (Ga,Mn)N:Si with $x \lesssim 3\%$. The samples have been grown by metalorganic vapor phase epitaxy and characterized by secondary-ion mass spectroscopy; high-resolution transmission electron microscopy with capabilities allowing for chemical analysis, including the annular dark-field mode and electron energy loss spectroscopy; high-resolution and synchrotron x-ray diffraction; synchrotron extended x-ray absorption fine-structure; synchrotron x-ray absorption near-edge structure; infrared optics; and electron spin resonance. The results of high-resolution magnetic measurements and their quantitative interpretation have allowed us to verify a series of *ab initio* predictions on the possibility of ferromagnetism in dilute magnetic insulators and to demonstrate that the interaction changes from ferromagnetic to antiferromagnetic when the charge state of the Mn ions is reduced from 3+ to 2+.

DOI: 10.1103/PhysRevB.84.035206

PACS number(s): 75.50.Pp, 75.10.Dg, 75.30.Gw, 75.70.Ak

I. INTRODUCTION

The decisive role of holes in ordering the localized spins in dilute magnetic semiconductors (DMS's) is not only well established,¹⁻³ but it represents also the basis of the functionalities demonstrated for these systems.⁴ In view of the fact that most magnetic insulators are either antiferromagnets or ferrimagnets, particularly intriguing is the question whether ferromagnetism is at all possible in dilute magnetic insulators, where carriers remain strongly localized on parent impurities or defects.^{3,5,6} Actually, a *ferromagnetic* coupling between localized spins was predicted in a series of *ab initio* works for the model system (Ga,Mn)N,⁷ where, as shown in Fig. 1, a large value of the ferromagnetic exchange energy J_{nn} was calculated for the nearest-neighbor (nn) Mn pairs. Due to the highly localized character of the orbitals in question, the magnitude of J is expected to decay fast with the interspin distance. Nevertheless, according to recent Monte Carlo simulations, the predicted Curie temperature T_C is as high as 35 and 65 K for the Mn cation concentration $x = 3\%$ and 6%, respectively.³

As reviewed elsewhere,⁸⁻¹⁰ this clear-cut theoretical prediction has not yet been verified experimentally. Instead, a diversity of magnetic properties has been reported. For instance, no indication of ferromagnetic interactions was detected up to $x = 36\%$ in polycrystalline films prepared by ion-assisted deposition,¹¹ whereas T_C values ranging from 8 K (Ref. 12) up to over 300 K (Ref. 8) were found for (Ga,Mn)N grown by molecular beam epitaxy (MBE). However, the detection of phase separations¹³⁻¹⁶ may suggest that the determined T_C corresponds to the blocking temperature of

magnetic nanoparticles. It is increasingly clear that further progress in the understanding of this challenging system requires a precise control of both the spatial distribution and the charge state of the Mn ions.⁹

The samples whose properties are discussed in this paper have been grown by metalorganic vapor phase epitaxy (MOVPE) according to a procedure described in Sec. II. As detailed in Sec. III, our films have been characterized by the following: secondary-ion mass spectroscopy (SIMS); high-resolution (scanning) transmission electron microscopy [HR-(S)TEM] with capabilities allowing for chemical analysis, including energy-dispersive x-ray spectroscopy (EDS), high-angle annular dark-field (HAADF) mode, and electron energy loss spectroscopy (EELS); high-resolution and synchrotron x-ray diffraction (SXRD); synchrotron extended x-ray absorption fine-structure (EXAFS); synchrotron x-ray absorption near-edge structure (XANES); infrared optics; and electron spin resonance (ESR). This set of probes demonstrates the absence of precipitation, reveals a nonuniform Mn distribution in the digitally Mn-doped films, and shows that the concentration of Mn²⁺ ions reaches $4 \times 10^{20} \text{ cm}^{-3}$ in (Ga,Mn)N:Si. From four probe conductance measurements, the sheet resistance is of the order of 10 G Ω at 300 K for the (Ga,Mn)N film with the highest Mn content $x = 3.1\%$, where x is the concentration of Mn cations.

By combining this extensive growth and nanocharacterization program with the results of high-precision magnetic measurements discussed in Sec. IV, we demonstrate that the dominant interactions between neighbor Mn pairs are ferromagnetic in (Ga,Mn)N. However, according to the data, the coupling is too short-ranged to lead to magnetic ordering

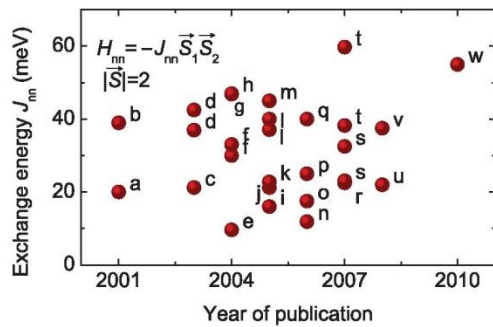


FIG. 1. (Color online) Exchange energy J_{nn} for the nearest-neighbor (nn) coupling from *ab initio* computations by various authors, as listed in Ref. 7. To obtain J_{nn} , the calculated energy differences for antiferromagnetic and ferromagnetic arrangements of spins within the nn Mn pair of the determined exchange energies have been mapped on the classical Heisenberg Hamiltonian.

above 1.85 K in the studied Mn concentration range up to $x = 3\%$. Employing a model of magnetic susceptibility suitable for wurtzite (Ga,Mn)N at high temperatures, and outlined in the Appendix, we evaluate from our experimental results the magnitude of the exchange energy for the nearest-neighbor ferromagnetic coupling. These findings allow us to verify the series of *ab initio* predictions summarized in Fig. 1 on the possibility of ferromagnetism in dilute magnetic insulators. At the same time, we show that the interactions become antiferromagnetic if the Mn charge state is altered by codoping with Si donors, clarifying in this way the array of magnetic properties reported for this system.

II. GROWTH METHOD AND STUDIED SAMPLES

In order to increase the Mn concentration in (Ga,Mn)N grown on GaN/c-sapphire by MOVPE at a substrate temperature of 850 °C,¹⁷ here the flow rate of the Ga precursor (TMGa) is reduced to one standard cubic centimeter per minute (sccm), maintaining the temperature of the Mn precursor source (MeCp₂Mn) at 22 °C and its flow rate up to 490 sccm. In addition to the uniformly doped Mn films, we also grow digitally (δ) Mn-doped structures, in which the Mn and Ga precursors are supplied alternately with a period ratio up to 8. Furthermore, a series of uniformly and digitally Mn-doped samples, respectively, is codoped with Si at a SiH₄ flow rate of either 1 or 2 sccm. The four types of considered samples are denoted by (Ga,Mn)N, (Ga, δ Mn)N, (Ga,Mn)N:Si, and (Ga, δ Mn)N:Si, respectively, where with δ Mn we refer to the Mn digitally doped layers.

In Table I, the list of the studied samples is presented, whose magnetic properties are reported in Figs. 11 and 12 (Sec. IV). An additional series of samples has been grown onto double-side epi-ready substrates for optical transmission studies. The Mn concentration x (x_{av} for the digital structures), as determined by the near-saturation value of the in-plane magnetization M at 50 kOe and 1.85 K, reaches over 3% in the samples with the highest Mn content.

TABLE I. Samples studied in this work with Mn cation concentrations x and x_{av} for the uniformly [(Ga,Mn)N] and digitally Mn-doped structures [(Ga, δ Mn)N], respectively, as determined by fitting the magnetic model to the data obtained by the superconducting quantum interference device (SQUID), as described in Sec. IV. The total thickness of the Mn-doped layer and precursor flow rates (in sccm) for the Ga-, Mn-, and Si-containing precursors are also given. The samples no. 1273 and 1274 have been grown on double-side epi-ready sapphire substrates suitable for optical transmission studies.

Sample no.	Label	Mn x_{av} (%)	Thickness (nm)	Thickness		
				Ga	Mn	Si
966	(Ga,Mn)N	0.5	470	5	490	0
1069	(Ga, δ Mn)N	1.8	140	5	δ -490	0
1071	(Ga, δ Mn)N	2.6	135	5	δ -490	0
1080	(Ga,Mn)N	1.1	740	5	490	0
1106	(Ga,Mn)N	1.8	750	1	490	0
1130	(Ga,Mn)N	1.8	200	1	490	0
1134	(Ga,Mn)N:Si	1.8	220	1	490	2
1142	(Ga,Mn)N	3.1	230	1	490	0
1152	(Ga,Mn)N:Si	3.3	200	1	490	2
1159	(Ga, δ Mn)N	1.5	140	1	δ -490	0
1160	(Ga, δ Mn)N:Si	2.4	135	1	δ -490	2
1161	(Ga,Mn)N:Si	2.9	200	1	490	1
1268	(Ga,Mn)N:Si	2.0	232	1	400	2
1269	(Ga,Mn)N:Si	1.9	232	1	300	2
1273	(Ga,Mn)N:Si	0.49	780	5	490	2
1274	(Ga,Mn)N	0.53	780	5	490	0

III. NANOCHARACTERIZATION

A. Crystallinity

The degree of crystallinity and possible precipitation of secondary crystallographic phases in uniformly and digitally Mn-doped films have been assessed by HR-TEM, HR-STEM, HR-XRD, SXRD, and EXAFS.

Our TEM studies have been carried out for all studied films on cross-sectional samples prepared by mechanical polishing followed by Ar⁺ ion milling, under a 4° angle at 4 kV for less than 2 h. The ion polishing has been performed in a Gatan 691 PIPS system.

The specimens have been investigated in Linz using a JEOL 2011 Fast TEM microscope operating at 200 kV and equipped with a Gatan CCD camera. The setup is capable of an ultimate point-to-point resolution of 0.19 nm, with the possibility to image lattice fringes with a 0.14 nm resolution.

As reported in Fig. 2, for both (Ga,Mn)N ($x = 3.1\%$) and (Ga, δ Mn)N ($x_{av} = 2.6\%$) samples, low-resolution TEM (left panels) shows no crystallographic phase separation and, in particular, no precipitates' segregation near the surface or interface. In fact, the HR-TEM images (right panels) clearly reveal the atomic positions in the lattice and, on the scale displayed, they show a homogeneous crystal ordering and no signs of precipitation within the Mn-doped layers.

To further verify the crystallographic homogeneity of the grown Mn-doped layers, HR-XRD measurements using a materials research diffractometer (MRD) and SXRD were performed. The HR-XRD experiments have been carried out with a Panalytical X'Pert PRO MRD in Linz at the photon energy of the Cu $K\alpha_1$ radiation (8 keV) using a hybrid

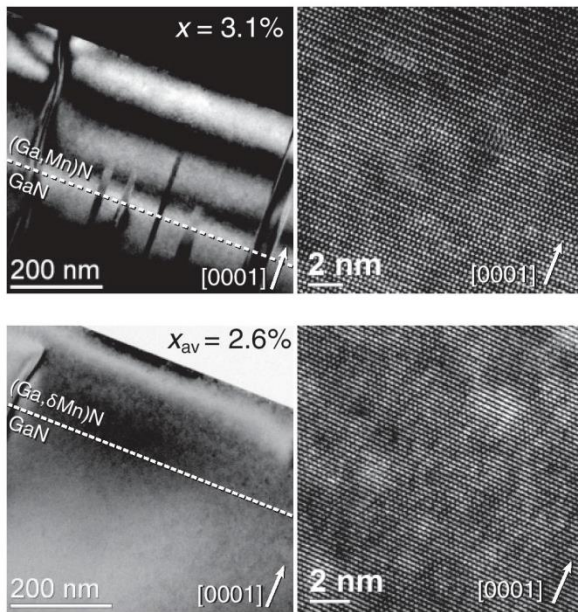


FIG. 2. Low-magnification TEM (left panel) and HR-TEM (right panel) for $(\text{Ga,Mn})\text{N}$ ($x = 3.1\%$, upper panels) and $(\text{Ga},\delta\text{Mn})\text{N}$ ($x_{\text{av}} = 2.6\%$, lower panels) without any evidence of crystallographic phase separation.

monochromator with a 0.25° slit for the incident optics and a pixel detector with an active length of 1 mm (19 channels) in the diffracted beam optics. The SXRD experiments have been performed at the beamline BM20 (Rossendorf Beam Line) of the European Synchrotron Radiation Facility (ESRF) in Grenoble using a point detector and 0.5 mm slits in front of the beam at an energy of 10 keV. Radial ω - 2θ scans of the GaN (002) to the GaN (004) diffraction peak do not show any trace of secondary phases. In Fig. 3, the radial scans acquired with both techniques for the same set of samples are shown for comparison, with the MRD scans in the upper panel and the SXRD in the lower one. The sharp (002) and (004) diffraction peaks of GaN and the (006) diffraction of the sapphire substrate are observed for all samples. The measurements carried out with the high-energy monochromatic beam at the synchrotron show a better signal-to-noise ratio and less diffuse scattering when compared to those performed with the MRD, but in both cases no trace of crystallographic precipitation can be observed.

The narrow full width at half-maxima (FWHM) of the GaN (002) and (004) peaks (with values between 240 and 290 arcsec) indicate the high crystallinity of the layers. From the GaN symmetric sharp diffraction peak from the Mn-doped samples—comparable to the one from the GaN reference—we have hints that Mn doping does not affect critically the dislocation density, as confirmed by the HR-TEM analysis on the same samples.

The XAFS measurements at the Mn K edge (6539 eV) have been carried out at the GILDA Italian collaborating research group beamline (BM08) of the ESRF in Grenoble, according to the experimental procedure detailed previously.^{17,18} Both

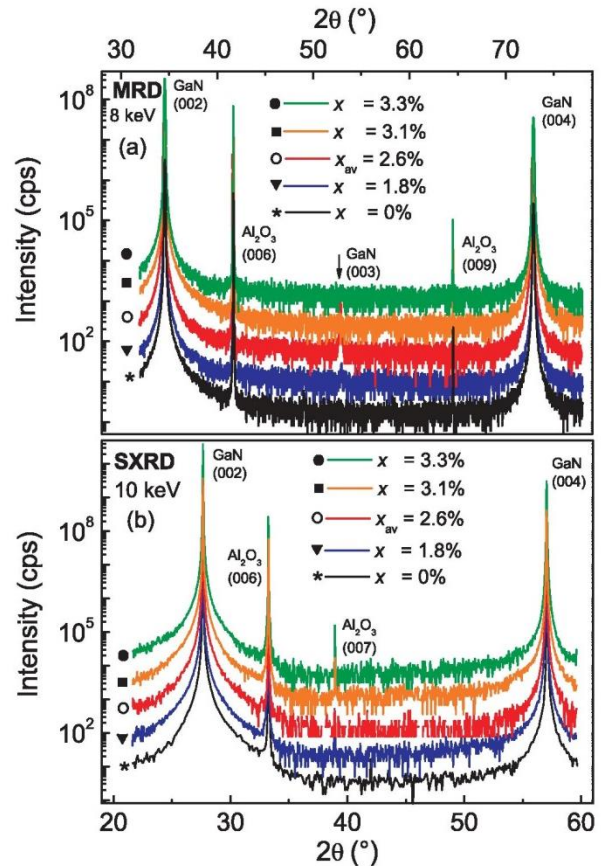


FIG. 3. (Color online) XRD radial scans of $(\text{Ga,Mn})\text{N}$ and $(\text{Ga},\delta\text{Mn})\text{N}$: (a) HR-XRD MRD, (b) SXRD collected at the BM20 of the ESRF.

EXAFS and XANES regions of the collected spectra have been analyzed.

Three representative samples have been studied: $(\text{Ga},\delta\text{Mn})\text{N}$ ($x_{\text{av}} = 2.6\%$), $(\text{Ga,Mn})\text{N}$ ($x = 3.1\%$), and $(\text{Ga,Mn})\text{N}:\text{Si}$ ($x = 3.3\%$). The collected data, with the polarization vector parallel to the c axis, and the relative fits resulting from the EXAFS analysis are shown in Fig. 4. The structural model employed consists of one Mn atom substituting Ga in a GaN wurtzite crystal plus a Mn-Mn contribution taken from the MnN crystal structure¹⁹ with a fitted coordination number ($N_{\text{Mn-Mn}}$) in order to account for possible Mn clusters. The quantitative results are reported in Table II and they are equivalent within the error bars for all the samples. The agreement with experimental data is good up to several coordination shells—as seen in Fig. 4—demonstrating the substitutional incorporation of Mn. The presence of an additional Mn-Mn coordination can be excluded within an uncertainty of 0.4 neighbors. Considering that the typical metal-metal coordination numbers are around 10 (12 Mn neighbors in MnN, 8 in Mn_3N_2), we can exclude the presence of secondary phases with a precision of about 5%. In addition, the possible Mn incorporation in interstitial sites (tetrahedral and octahedral) has been investigated, statistically

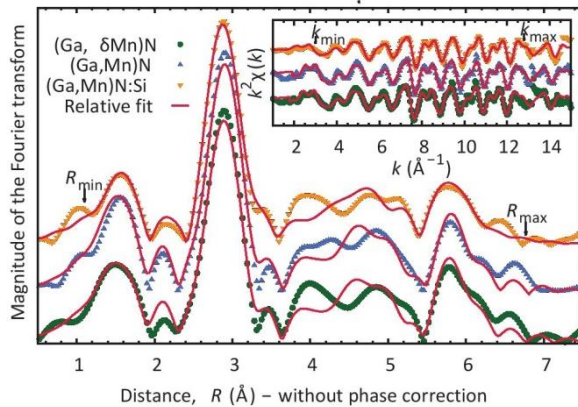


FIG. 4. (Color online) Magnitude of the Fourier-transformed k^2 -weighted EXAFS data (inset) in the range k_{\min} – k_{\max} with relative fits (described in the text) in the range R_{\min} – R_{\max} for representative samples: (Ga, δ Mn)N ($x_{\text{av}} = 2.6\%$), (Ga,Mn)N ($x = 3.1\%$), and (Ga,Mn)N:Si ($x = 3.3\%$)

not improving the fit quality. These results are equivalent to the XAFS structural analysis on our (Ga,Mn)N samples at lower concentrations.¹⁷

In conclusion, TEM, HR-(S)TEM, HR-XRD, SXRD, and EXAFS studies demonstrate a single-crystal character of the considered films with no traces, down to the atomic scale, of precipitations (crystallographic phase separation). This is in contrast with the case of some (Ga,Mn)N films grown by MBE (Refs. 14 and 21) as well as with (Ga,Fe)N layers obtained by MOVPE,^{18,22–24} for which crystallographic phase separations were detected by employing the same nanocharacterization tools.

B. Mn distribution

The Mn distribution along the growth direction and the Si distribution in the codoped films have been evaluated in Warsaw via SIMS, calibrated by Mn-implanted GaN, providing the absolute concentration of Mn atoms with an accuracy of about a factor 2. The SIMS depth profiles reported previously¹⁷ for the samples with $x \lesssim 1\%$ and the one shown

TABLE II. Quantitative results of the EXAFS analysis. For each sample, the fitted parameters are as follows: the common amplitude (S_0^2), the average bond distances from the central Mn to the 4 nearest neighbors ($R_{\text{Mn-N}}$) and 12 Ga next nearest neighbors ($R_{\text{Mn-Ga}}$) of the wurtzite structure plus a common expansion parameter for higher coordination shells (ΔR), and the coordination number ($N_{\text{Mn-Mn}}$) for the Mn-Mn bond distance at 2.98(2) Å. The Debye-Waller parameters attest all below $8(2) \times 10^{-3} \text{ \AA}^{-2}$ and a correlated Debye model²⁰ with a temperature of 500(50) K is used for the GaN multiple scattering contributions. Error bars are reported in the last digit.

Sample	$x_{(\text{av})}$	S_0^2 (%)	$R_{\text{Mn-N}}$ (Å)	$R_{\text{Mn-Ga}}$ (Å)	ΔR (%)	$N_{\text{Mn-Mn}}$
(Ga, δ Mn)N	2.6	0.90(5)	1.95(3)	3.20(2)	0.1(2)	0.4(4)
(Ga,Mn)N	3.1	0.94(5)	1.94(3)	3.19(2)	0.1(2)	0.2(4)
(Ga,Mn)N:Si	3.3	0.94(5)	1.96(3)	3.19(2)	0.1(2)	0.0(4)

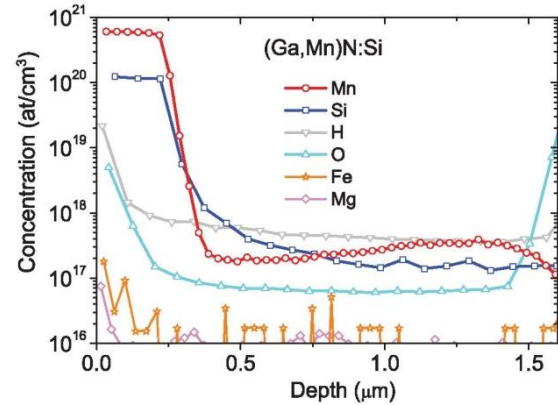


FIG. 5. (Color online) SIMS depth profiles of Mn and Si in the (Ga,Mn)N:Si film with $x = 1.9\%$. The residual contamination by H, O, Fe, and Mg is also shown.

in Fig. 5 for the present films indicate that the Mn distribution is uniform over the Mn-doped region and that the interface between the (Ga,Mn)N overlayer and the GaN buffer layer is sharp.

This is confirmed by chemical analysis performed in Linz with an Oxford Inca EDS system, which—with the sensitivity of 0.1% at.—does not provide any evidence for Mn diffusion into the nominally undoped GaN buffer.

For further characterization of the Mn doping, HAADF-STEM and EELS measurements have been performed—and are reported in Fig. 6—employing a FEI Tecnai F 20 200 kV transmission electron microscope in Graz. The STEM images and EELS spectra could be recorded with an upgraded spectrometer with an adapted STEM detection geometry, optimized for Z contrast and enhanced spectral collection EELS efficiency.^{25,26} In order to improve the signal-to-noise ratio at the high spatial resolution in question as well as to keep exposure times low for minimal sample drift, the EELS point spectra have been taken as an integral sum over the energy. Accordingly, a possible fine structure located within the first 20–30 eV around the ionization threshold energy of an edge has been averaged out.

The HAADF-STEM on (Ga,Mn)N ($x = 3.1\%$) and reported in Fig. 6(a) reveals a clear change in intensity when going from the substrate into the Mn-doped layer (from left to right), while within the doped layer no chemical contrast could be detected. The EELS spectra given in Fig. 6(b) evidence the presence of Mn only in the nominally Mn-doped layer.

In contrast, remarkably, as shown in Figs. 6(c) and 6(e), HAADF-STEM observations on the digital (Ga, δ Mn)N ($x_{\text{av}} = 2.6\%$) reveal intensity modulations. Additional EELS point spectra collected in Fig. 6(d) show the signal differences of the Mn L_{23} edge between the substrate and the intensity modulated lines.

In conclusion, the element-specific analysis demonstrates a spatially homogeneous Mn distribution over the volume of the uniformly Mn-doped (Ga,Mn)N films, with no segregation toward the surface, interface, or buffer regions. In contrast, in the case of the digitally Mn-doped films, nanoscale density modulation with a period imposed by the growth conditions

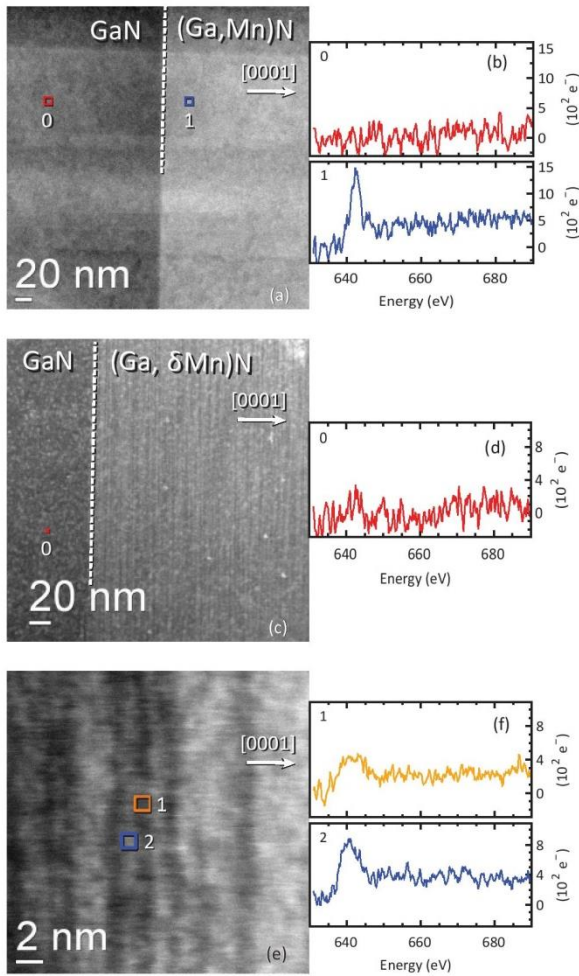


FIG. 6. (Color online) (a) HAADF-STEM image of $(\text{Ga,Mn})\text{N}$ ($x = 3.1\%$)—change in intensity (chemical contrast), when going from the substrate into the doped layer (from left to right). (b) EELS spectra for points 0 (GaN buffer layer) and 1 (nominally Mn-doped layer): evidence of the presence of Mn only in the Mn-doped layer (right side of the image). (c)–(f) Determination of the Mn distribution in the digitally Mn-doped sample $(\text{Ga},\delta\text{Mn})\text{N}$ ($x_{\text{av}} = 2.6\%$, 160 Mn periods, layer thickness 135 nm). (c,e) HAADF-STEM scans in the Mn-doped region giving modulated chemical contrast. (d,f) EELS spectra of points 0, 1, and 2, as marked in (c) and (e), respectively.

has been detected, meaning that in these δMn samples the local Mn concentration fluctuates between lower and higher x values around the x_{av} determined by SQUID magnetometry. As discussed in Sec. IV, such a nonrandom distribution of Mn ions increases the apparent Curie constant, particularly if the system is close to a ferromagnetic instability.

C. Concentrations of Si and Mn^{2+} ions

The incorporation and a uniform distribution of Si impurities in $(\text{Ga,Mn})\text{N}:\text{Si}$ layers is evidenced by the SIMS result displayed in Fig. 5. From the same measurements on all the

TABLE III. Values of parameters in Eq. (1) determined from reflectivity and transmission measurements for two series of samples (the upper and lower set of data, respectively). The concentration of Mn^{2+} ions is calculated according to $x^{(\text{Ga,Mn})\text{N}:\text{Si}} - x^{(\text{Ga,Mn})\text{N}}r$, where r is the ratio of the $fN_{\text{Mn}^{3+}}$ values within a given series of samples.

Label	x (%)	E_0 (meV)	$fN_{\text{Mn}^{3+}}$ (meV ²)	Γ (meV)	Mn^{2+} ($10^{20}/\text{cm}^3$)
$(\text{Ga,Mn})\text{N}$	1.8	1415	13000	6.1	
$(\text{Ga,Mn})\text{N}:\text{Si}$	1.8	1414	5300	3.6	4 ± 1
$(\text{Ga,Mn})\text{N}$	0.53	1413	950	2.57	
$(\text{Ga,Mn})\text{N}:\text{Si}$	0.49	1415	490	3.0	0.6 ± 0.1

considered samples, the Si concentration is found to be of the order of 10^{20} cm^{-3} for the Si and Ga precursor flow rates 1 or 2 and 1 sccm, respectively.

Following recent works on the Mn charge state in GaN,²⁷ the effect of codoping by Si donors on the Mn charge state has been quantitatively assessed by examining the magnitude of the intra-ion optical absorption, which occurs at $E_0 \approx 1.4 \text{ eV}$ for Mn^{3+} ions in GaN.^{28–31} Optical investigations have been performed in Warsaw and in Linz for two series of films, abridged in Table III, with the Mn concentrations $x \approx 1.8$ and 0.5% , respectively, and different Si content. The series with the lower Mn concentration has been designed for transmission and ESR measurements with the layers deposited on double-side epitaxially sapphire substrates.

As can be seen in Figs. 7 and 8, the Si doping quenches the intra-ion absorption, specific to Ga-substitutional Mn in the $3+$ charge state.

We determine the concentration ratio of the absorbing Mn^{3+} ions for samples without and with Si by fitting a model constructed within the transfer-matrix formalism of optical

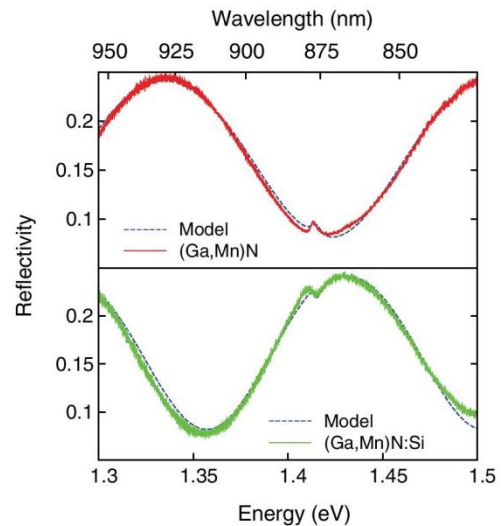


FIG. 7. (Color online) Optical reflectivity spectra for $(\text{Ga,Mn})\text{N}$ without and with Si codoping (upper and lower panel, respectively). The Mn concentration is 1.8% in both samples. The absorption feature at 1.41 eV is clearly resolved. The fitting results by the transfer-matrix multilayer model are given by the dashed lines.

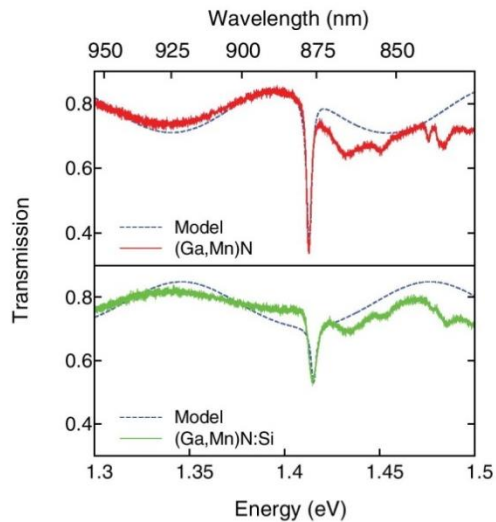


FIG. 8. (Color online) Optical transmission spectra for samples with a Mn concentration $x \approx 0.5\%$. Upper and lower graphs: data for samples without and with Si codoping, respectively. Next to the main absorption line at 1.41 eV, the phonon replicas of the line are observed. The fitting results by the multilayer model are given by the dashed lines.

transmission and reflectivity, taking into account the doped (Ga,Mn)N layer, the undoped GaN buffer, and the sapphire substrate.³²

The contribution of the Mn^{3+} ions to the dynamic dielectric function is modeled by damped Lorentzian oscillators of the form

$$\epsilon(\omega) = \epsilon_{\text{GaN}}(\omega) + \frac{f N_{\text{Mn}^{3+}}}{E_0^2 - (\hbar\omega)^2 - i\hbar\omega\Gamma}. \quad (1)$$

Here f is proportional to the oscillator strength and Γ is the damping energy. The refractive index of GaN is modeled using the Sellmeier equation³³ and the refractive index of the sapphire is set at 1.8. The thicknesses of the GaN buffer and (Ga,Mn)N layer are adjusted to reproduce the observed Fabry-Pérot interferences at a magnitude of thicknesses ratio as determined during the growth by *in situ* ellipsometry.

In Table III, the fitted values of the parameters in Eq. (1) are given. From the reduction of the Mn^{3+} absorption we can evaluate the concentration of Mn^{2+} ions assuming that electrons coming from Si shallow donors occupy the $\text{Mn}^{2+}/\text{Mn}^{3+}$ midgap level. Under this assumption, the concentration of Mn^{2+} ions reaches a level of 4×10^{20} per cm^3 for the highest employed flow of the Si precursor at the lowest Ga precursor flow.

Results of ESR studies carried out in Linz and reported in Fig. 9 for (Ga,Mn)N and (Ga,Mn)N:Si with the Mn concentration $x \approx 0.5\%$ demonstrate the emergence of a characteristic Mn^{2+} signal upon Si doping. In films with higher Mn concentrations, the line broadening, witnessing the presence of Mn^{2+} - Mn^{3+} coupling, as discussed in Sec. IV, has hampered the detection of a Mn^{2+} signal.

A nonzero value of the orbital momentum, and the associated spin-orbit interaction specific to Mn^{3+} ions, precludes

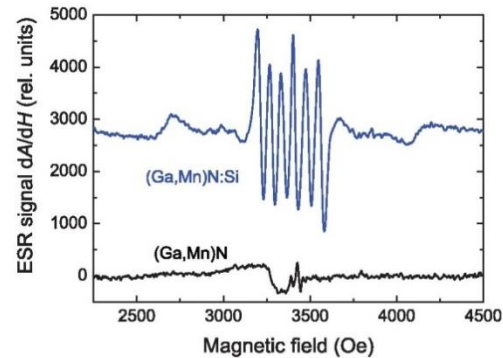


FIG. 9. (Color online) Results of ESR studies at 2 K for (Ga,Mn)N without and with Si codoping (lower and upper curve, respectively) showing the emergence of Mn^{2+} signal on Si doping. The Mn concentration is $x \approx 0.5\%$.

their observation by ESR (Ref. 27). At the same time, Mn^{2+} ions, corresponding to orbital singlets, give rise to a specific ESR response.^{27,34}

The results of the optical and ESR studies are confirmed also by XANES. In order to contribute to the determination of the Mn valence state, the position of the x-ray absorption edge and the pre-edge features have been considered as described in the XANES section of Ref. 17. In particular here the issue of reduction of the charge state is addressed. As can be appreciated in Fig. 10, a shift toward lower energies is visible for the Si codoped sample, while the position of the pre-edge peaks remains unchanged. This demonstrates the fine calibration of the incoming energy and suggests the presence of some Mn in a valence state lower than 3+, possibly 2+. Due to the lack of model compounds that would allow us to establish a precise relation between the edge shift and the valence state in nitrides, a quantitative statement cannot be given here. However, considering that in the case of sixfold-coordinated Mn ions (this example is taken as no data are reported for tetragonal Mn^{3+}) the ionic radius of Mn^{2+} is about 12% greater than the one of Mn^{3+} (Ref. 35) and that no visible evolution of the Mn-N distance is reported, we can expect a minority of Mn ions to be in the 2+ charge state.

In conclusion, our SIMS, optical, XANES, and ESR studies show consistently that co-doping with Si increases the concentration of Mn ions in the 2+ charge state, which for the highest employed flow of the Si precursor (2 sccm) and the lowest Ga precursor flow is up to 4×10^{20} cm^{-3} , about 30% of the total Mn concentration for $x = 3\%$. This evaluation substantiates the experimental data presented in the next section. It is worth noting that a coexistence of Mn^{3+} and Mn^{2+} ions was detected also in x-ray magnetic circular dichroism in (Ga,Mn)N samples undoped with Si,³⁶ pointing to the presence of residual or interfacial compensating donors.

IV. MAGNETIC PROPERTIES

According to our previous studies of (Ga,Mn)N with $x < 1\%$,¹⁷ the dependence of the magnetization M on temperature T , magnetic field H , and its orientation with respect to the wurtzite (wz) c axis can accurately be described in terms

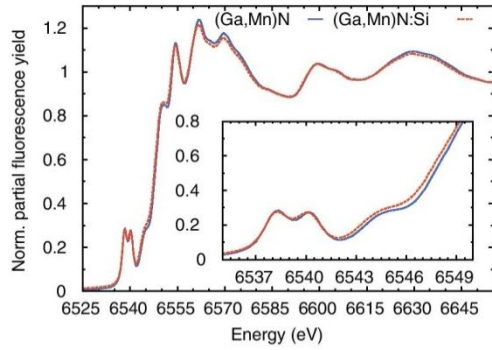


FIG. 10. (Color online) Partial fluorescence yield XANES spectra (integrated $K_{\alpha 1,2}$ fluorescence lines) for (Ga,Mn)N and (Ga,Mn)N:Si samples with the polarization vector parallel to the wurtzite c axis. Inset: focus on the shift of the main absorption edge between the two spectra. The position of the pre-edge peaks is constant.

of noninteracting Mn^{3+} ions substitutional of Ga. The good agreement between the experimental data and the model confirms a weak compensation by residual impurities, which, if present, would change the Mn charge state and thus the magnetic properties. The Mn^{3+} charge state is preserved in samples with higher Mn concentrations, where the persistence of a large anisotropy between the $M(H)$ values at 1.85 K for the two sample orientations $c \perp H$ and $c \parallel H$ is evidenced in Figs. 11(a) and 11(b). However, a gradual enhancement of $M(H)/M(50 \text{ kOe})$ over the magnitude expected for noninteracting spins is observed when increasing x up to 3% in both uniformly and digitally Mn-doped films, as seen in Figs. 11(a), 11(b), and 12(a). These results demonstrate univocally that, in spite of the absence of band carriers, the dominant exchange interaction between Mn^{3+} is *ferromagnetic* in (Ga,Mn)N.

Interestingly, a rather different behavior is observed in the case of (Ga,Mn)N:Si, where the trapping of donor electrons changes the Mn charge from $3+$ to $2+$ and the spin state S from 2 to $5/2$, for about 30% of the Mn ions at $x \approx 3\%$, as discussed in Sec. III C. According to the data collected in Figs. 11(c), 11(d), and 12(b), the increasing concentration of Mn^{2+} ions results in the foreseen decrease of the magnetization anisotropy. Furthermore, as shown in Fig. 12(b), $M(H)$ saturates *slower* than theoretically anticipated for noninteracting Mn ions. This finding points to an *antiferromagnetic* character of the exchange coupling between Mn^{2+} ions, and suggests that these ions may dominate in (Ga,Mn)N, when no ferromagnetic interactions are detected.^{11,37}

In the insets to Figs. 11(a)–11(d), the results of our search for the onset of a collective magnetic behavior in the samples with the highest Mn concentrations are given. A linear and a hysteretic $M(H)$ dependence in weak magnetic fields is observed for both configurations, $c \perp H$ and $c \parallel H$, pointing to the absence of spontaneous magnetization. These data imply that the ferromagnetic spin-spin couplings are too short-ranged to result in magnetic ordering and, hence, in spontaneous magnetization at $T \geq 1.85 \text{ K}$.

Quantitative information on J_{nn} is gained here by examining the dependence on the inverse temperature of the in-plane

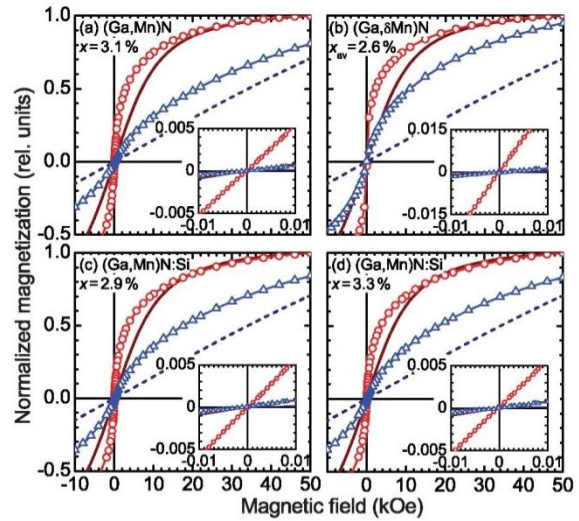


FIG. 11. (Color online) Magnetization at 1.85 K (normalized to its in-plane value at 50 kOe) as a function of the magnetic field applied perpendicular (circles) and parallel (triangles) to the wz c axis of (Ga,Mn)N (a,b) and (Ga,Mn)N:Si (c,d) films where Mn is introduced either uniformly (a,c,d) or digitally (b). Solid and dashed lines are calculated according to the group-theoretical model for noninteracting Mn^{3+} ions in wz -GaN for H perpendicular and parallel to the c axis, respectively.¹⁷ Insets: low-field magnetization loops.

magnetic moment $m(T)$ of Mn spins in GaN, as obtained by subtracting the value of $m(T)$ measured independently for a sapphire substrate (normalized by the corresponding sample weight). As reported in Fig. 13, $\chi(T) \equiv M/H \sim 1/T$ for $150 \lesssim T \lesssim 350 \text{ K}$. This behavior indicates that the contribution to the magnetic susceptibility from the (Ga,Mn)N films obeys the Curie law in this regime, $\chi(T) = C/T$. This dependence is expected if the spin pairs are either uncorrelated, $|J_{\text{nn}}|S^2 \ll k_B T$, or strongly bound, $|J_{\text{nn}}|S^2 \gg k_B T$.

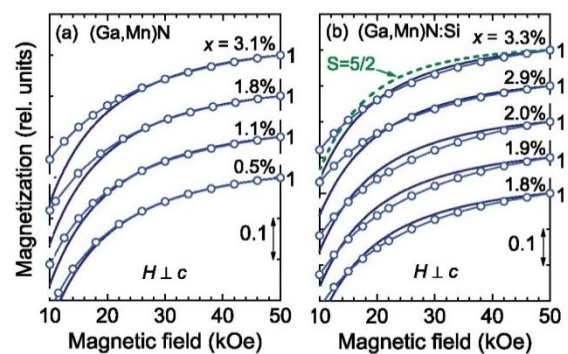


FIG. 12. (Color online) Comparison of magnetization saturation as a function of the magnetic field between (a) (Ga,Mn)N—no antiferromagnetic interactions and (b) (Ga,Mn)N:Si—with antiferromagnetic interactions. The relative experimental error is about one-half of the point size. Solid lines and the dashed line in (b) are calculated for noninteracting Mn^{3+} and Mn^{2+} ions, respectively.

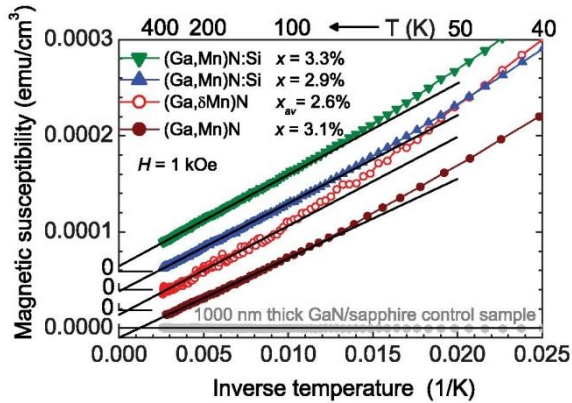


FIG. 13. (Color online) Magnetic susceptibility M/H for $c \perp H$ as a function of the inverse temperature for uniformly (solid symbols) and digitally (open symbols) doped (Ga,Mn)N (circles) and (Ga,Mn)N:Si (triangles) as well as GaN/sapphire control sample (light gray circles). Solid lines serve to determine the Curie constants at high temperatures. Deviations of their values from zero at $1/T = 0$ show the accuracy of the substrate subtraction.

In order to extract from these data the magnitude of J_{nn} , we extend the previous model of a single substitutional Mn^{3+} impurity in GaN (Ref. 17) by considering a pair of Mn^{3+} ions coupled by an exchange interaction $-J_{nn}\vec{S}_1\vec{S}_2$,^{38,39} the model discussed in detail in the Appendix. Assuming a random distribution of Mn over the cation hcp lattice, and allowing for the coupling between nn spins, we can evaluate $M(T, H)$ at a given J_{nn} and x . This approach implies, in particular, that for $x = 3\%$, $T < 350$ K, and $H = 1$ kOe, $\chi(T) = C/T$ if $J_{nn} > 10$ meV. However, in this case, due to the proportionality of $\chi(T)$ to the pair spin square, the magnitude of C is enhanced in comparison to the value C_0 corresponding to noninteracting spins. To evaluate experimentally $C_{\text{norm}} = C/C_0$, we consider that its magnitude can be determined from the magnetic moment $m(T, 1$ kOe) measured in-plane without knowing the exact value of the volume occupied by the Mn spins if the magnitude of the in-plane $m(1.85$ K, 50 kOe) is employed to obtain the Mn content x —and thus C_0 —for particular samples. Following the outcome of the experimental results for (Ga,Mn)N:Si (Sec. III C), demonstrating the presence of Mn^{2+} ions, their relative contribution to $M(T, H)$ is determined from the magnitude of the magnetic anisotropy.

As summarized in Fig. 14, $C_{\text{norm}} > 1$ for all studied samples, hinting to the presence of a considerable ferromagnetic spin-spin interaction. The theory presented in the Appendix describes quite well the magnitude of $C_{\text{norm}}(x)$ for the uniformly doped (Ga,Mn)N films, pointing to $J_{nn} > 10$ meV, in general agreement with the results of the *ab initio* studies outlined in Fig. 1. Furthermore, a low-temperature upturn of the experimental points over the C/T dependence, visible in Fig. 13 below ~ 100 K, suggests the existence of an additional weak ferromagnetic coupling between more distant neighbors. Moreover, the experimental values of $C_{\text{norm}}(x)$ in the case of digital δMn -doping are higher than theoretically expected.

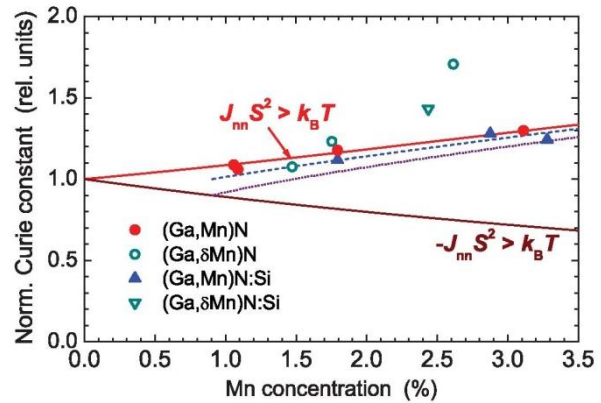


FIG. 14. (Color online) Normalized Curie constant C_{norm} as a function of the Mn content for uniformly (solid symbols) and digitally (open symbols) doped (Ga,Mn)N (circles) and (Ga,Mn)N:Si (triangles). The solid lines are computed assuming a random distribution of Mn^{3+} ions, and either ferromagnetic or antiferromagnetic strong coupling between the nearest-neighbor (nn) Mn spins, $|J_{nn}|S^2 \gg k_B T$. Dashed and dotted lines are calculated assuming that $4 \times 10^{20} \text{ cm}^{-3}$ Mn ions are in the 2+ charge state, and nn interactions are ferromagnetic except for nn Mn^{2+} pairs, for which $J_{nn} = 0$ or $-J_{nn}S^2 \gg k_B T$, respectively.

In order to clarify the different magnitude of C_{norm} in uniformly and digitally doped films, we refer to Sec. III B, where the detailed investigation of the Mn distribution for the two samples with the highest Mn concentration, namely (Ga,Mn)N ($x = 3.1\%$) and the digital (Ga, δMn)N ($x_{\text{av}} = 2.6\%$), respectively, have been shown. The data demonstrate the presence of a spatially modulated Mn concentration in the digitally Mn-doped films. Due to a nonlinear dependence of the Curie constant on the Mn concentration in the presence of ferromagnetic interactions, such a nonrandom distribution of Mn ions increases the apparent value of C_{norm} , particularly if the system is close to a ferromagnetic instability. This interpretation is supported by a much smaller effect in the films with lower values of x_{av} , and thus far from the ferromagnetic instability.

Finally, we comment on the magnitudes of $C_{\text{norm}}(x)$ in Si-doped samples. Here, we have ferromagnetically coupled $\text{Mn}^{3+}\text{-Mn}^{3+}$ and $\text{Mn}^{3+}\text{-Mn}^{2+}$ pairs as well as antiferromagnetically interacting $\text{Mn}^{2+}\text{-Mn}^{2+}$ pairs. As shown in Fig. 14, the theory developed for such a case and summarized in the Appendix is consistent with the data for Si-doped samples.

V. CONCLUSIONS

In this work, we have verified experimentally the presence of a strong ferromagnetic coupling between neighboring Mn spins in (Ga,Mn)N, supporting a very significant number of *ab initio* studies.^{3,5,7} Since the Mott-Hubbard localization precludes carrier hopping between magnetic ions, a ferromagnetic superexchange constitutes the relevant microscopic coupling mechanism.⁴⁰ However, according to our findings, the range of this interaction is too short to produce a long-range ferromagnetic ordering—at least above 1.85 K—in samples with 3% of randomly distributed substitutional Mn cations. Codoping

with Si may *a priori* result in a ferromagnetic double exchange, but apparently Anderson-Mott localization in the Mn impurity band renders this mechanism inefficient in the range of Mn contents explored so far by us. If, owing to a large density of donorlike defects or impurities, the concentration of Mn^{2+} prevails, antiferromagnetic superexchange becomes the dominant spin-spin coupling mechanism. This situation has presumably taken place in recently studied (Ga,Mn)N films with x up to 36% (Ref. 11) and some time ago in the case of $\text{In}_{1-x}\text{Mn}_x\text{As}$ layers with x up to 18%.⁴¹

ACKNOWLEDGMENTS

The work was supported by FunDMS Advanced Grant of ERC (Grant No. 227690) within the Ideas 7th Framework Programme of European Community, InTechFun (Grant No. POIG.01.03.01-00-159/08), SemiSpinNet (Grant No. PITNGA- 2008-215368), by the Austrian FWF (P20065, P22477, P20550) and FFG (N107-NAN), and by the NCBIr project LIDER.

APPENDIX: THEORETICAL EVALUATION OF THE CURIE CONSTANT

We evaluate the Curie constant C_{norm} for a random distribution of the Mn^{3+} and Mn^{2+} ions. While our model can be applied for a general situation, we discuss the case describing our data in the relevant temperature range $150 \lesssim T \leq 350$ K, i.e., we assume that the nearest-neighbor (nn) $\text{Mn}^{3+}\text{-Mn}^{3+}$ and $\text{Mn}^{3+}\text{-Mn}^{2+}$ pairs form ferromagnetically oriented dimers, whereas nn $\text{Mn}^{2+}\text{-Mn}^{2+}$ pairs are uncoupled.

In the paramagnetic region well above the ordering temperature (high-temperature limit), the magnetic susceptibility is expected to obey the Curie-Weiss law,

$$\chi = \frac{C_0}{T - \theta_C}, \quad (\text{A1})$$

$$C_0 = N \frac{(g\mu_B)^2 S(S+1)}{3k_B}, \quad (\text{A2})$$

where C and θ_C are the Curie constant and Curie-Weiss temperature, and N is the concentration of magnetic ions with spin S . However, in random magnetic alloys, where the interactions between spin pairs show a large dispersion owing to strong variations of the spin-spin distances, the magnitudes of C and θ_C may depend on the temperature.^{38,39,42}

We consider the case of dilute magnetic semiconductors (DMS's) and dilute magnetic oxides (DMO's). In the absence of band carriers that could mediate long-range spin-spin interactions, the strength of the exchange couplings decays rather fast with the spin-spin distance. In such a case, the exchange between magnetic ions occupying the nn cation positions dominates. Accordingly, below the percolation limit for the nn interaction ($x \lesssim 18\%$ for fcc and hcp lattices), the magnetic response can be evaluated as a sum of contributions coming from various types of clusters: isolated spins, nn pairs, nn triads, ..., whose relative importance depends on x .³⁹ The magnetic response of such small clusters can be easily calculated for given values of the exchange integral J_{nn} ,

temperature T , and magnetic field H . Possible interactions between more distant pairs of magnetic ions are neglected within this approach. Qualitatively, at low temperatures, $k_B T \ll |J_{\text{nn}}|$, at which the nn pairs are locked, the Curie constant is reduced ($C < C_0$) or enhanced ($C > C_0$) for antiferromagnetic interactions ($J_{\text{nn}} < 0$) and ferromagnetic interactions ($J_{\text{nn}} > 0$), respectively.

We are interested in the case of (Ga,Mn)N and (Ga,Mn)N:Si where, in general, both Mn^{2+} ($S = 5/2$) and Mn^{3+} ($S = 2$) ions are present with the concentrations $x_{\text{Mn}^{2+}}$ and $x_{\text{Mn}^{3+}}$, respectively ($x = x_{\text{Mn}^{2+}} + x_{\text{Mn}^{3+}}$). Here, we have ferromagnetically coupled $\text{Mn}^{3+}\text{-Mn}^{3+}$ and $\text{Mn}^{3+}\text{-Mn}^{2+}$ pairs as well as antiferromagnetically interacting $\text{Mn}^{2+}\text{-Mn}^{2+}$ pairs. To describe this case, we generalize the approach put forward previously for II-VI DMS's.³⁹ The probability that a given spin, e.g., a Mn^{3+} ion, is in a cluster belonging to the configuration r_{cl} is given by

$$P_{r_{\text{cl}}} = n_{r_{\text{cl}}} (x_{\text{Mn}^{2+}})^{n_{\text{Mn}^{2+}}} (x_{\text{Mn}^{3+}})^{n_{\text{Mn}^{3+}}-1} (1-x)^{\nu_{\text{cl}}}, \quad (\text{A3})$$

where $n_{\text{Mn}^{2+}}$ and $n_{\text{Mn}^{3+}}$ are the numbers of manganese ions in $2+$ and $3+$ charge states belonging to this cluster, and $n_{r_{\text{cl}}}$, ν_{cl} are parameters taken from Refs. 39 and 43. Then one should take into account all possible combinations of arrangements of Mn^{2+} ions within r_{cl} and calculate the total spin S_{cl} corresponding to the ground state (assuming that $|J_{\text{nn}}| \gg k_B T$). In the case of vanishing interactions between Mn^{2+} ions, we have to compute also the effective cluster size n_{cl} (some of the ions may be disconnected from the initial cluster because of $J_{\text{Mn}^{2+}\text{-Mn}^{2+}} = 0$). In this way, we obtain the probability matrix $P_{S_{\text{cl}}, n_{\text{cl}}}$ from which the Curie constant can be calculated,

$$C = x N_0 \frac{(g\mu_B)^2}{3k_B} \sum_{S_{\text{cl}}, n_{\text{cl}}} \frac{P_{S_{\text{cl}}, n_{\text{cl}}} S_{\text{cl}} (S_{\text{cl}} + 1)}{n_{\text{cl}}}, \quad (\text{A4})$$

where N_0 is the cation concentration.

In order to obtain the magnetization $M(T, H)$ of (Ga,Mn)N in the presence of interacting nn magnetic centers, we extend the previous model of a single substitutional Mn^{3+} impurity in GaN (Refs. 17, 29, and 44) by considering a pair of Mn^{3+} ions coupled by an exchange interaction $H(12) = -J_{\text{nn}} \vec{S}_1 \vec{S}_2$. Then, the energy structure of such a pair can be described by the Hamiltonian

$$H = H(1) + H(2) + H(12), \quad (\text{A5})$$

where $H(i)$ ($i = 1, 2$) accounts for the single Mn^{3+} ion ($L = 2$, $S = 2$) in GaN with the trigonal crystal field of the wurtzite structure and the Jahn-Teller distortion taken into account (for details, see Ref. 17). In the coupling scheme employed, the base states for the pair are characterized by the set of quantum numbers $|m_{L_1}, m_{S_1}, m_{L_2}, m_{S_2}\rangle$. The energy level scheme is calculated by a numerical diagonalization of the full 625×625 Hamiltonian (A5) matrix, which allows us to obtain an average magnetic moment of the Mn ion belonging to the pair ($\mathbf{m}_{\text{pairs}}$). Assuming a random distribution of Mn ions over the cation sites (the hcp lattice) and allowing for the coupling between the nn spins, we can then evaluate $M(T, H)$ at given J_{nn} and x ,

$$\mathbf{M} = \mu_B x N_0 [\langle \mathbf{m}_{\text{singlets}} \rangle P_{n_{\text{cl}}=1} + \langle \mathbf{m}_{\text{pairs}} \rangle (1 - P_{n_{\text{cl}}=1})]. \quad (\text{A6})$$

- *alberta.bonanni@jku.at
 †mikes@ifpan.edu.pl
 ‡dielt@ifpan.edu.pl
- ¹T. Dietl, H. Ohno, F. Matsukura, J. Cibert, and D. Ferrand, *Science* **287**, 1019 (2000).
²T. Jungwirth, J. Sinova, J. Mašek, J. Kučera, and A. H. MacDonald, *Rev. Mod. Phys.* **78**, 809 (2006).
³K. Sato *et al.*, *Rev. Mod. Phys.* **82**, 1633 (2010).
⁴*Spintronics*, Vol. 82 of *Semiconductors and Semimetals*, edited by T. Dietl, D. D. Awschalom, M. Kaminska, and H. Ohno (Elsevier, Amsterdam, 2008).
⁵A. Zunger, S. Lany, and H. Raebiger, *Physics* **3**, 53 (2010).
⁶T. Dietl, *Phys. Rev. B* **77**, 085208 (2008).
⁷K. Sato and H. Katayama-Yoshida, *Jpn. J. Appl. Phys.* **40**, L485 (2001); M. van Schilfgaarde and O. N. Mryasov, *Phys. Rev. B* **63**, 233205 (2001); Y. Uspenskii, E. Kulatov, H. Mariette, H. Nakayama, and H. Ohta, *J. Magn. Magn. Mater.* **258**, 248 (2003); B. Sanyal, O. Bengone, and S. Mirbt, *Phys. Rev. B* **68**, 205210 (2003); Q. Wang, Q. Sun, P. Jena, and Y. Kawazoe, *Phys. Rev. Lett.* **93**, 155501 (2004); M. Wierzbowska, D. Sanchez-Portal, and S. Sanvito, *Phys. Rev. B* **70**, 235209 (2004); P. Mahadevan and A. Zunger, *Appl. Phys. Lett.* **85**, 2860 (2004); Y.-J. Zhao, P. Mahadevan, and A. Zunger, *ibid.* **84**, 3753 (2004); L. Bergqvist, O. Eriksson, J. Kudrnovský, V. Drchal, A. Bergman, L. Nordström, and I. Turek, *Phys. Rev. B* **72**, 195210 (2005); P. Boguslawski and J. Bernholc, *ibid.* **72**, 115208 (2005); K. Sato, P. H. Dederichs, and H. Katayama-Yoshida, *Hyperfine Interact.* **160**, 57 (2005); J. Kang, K. J. Chang, and H. Katayama-Yoshida, *J. Supercond.* **18**, 55 (2005); X. Luo and R. M. Martin, *Phys. Rev. B* **72**, 035212 (2005); M. Marques, L. G. Ferreira, L. K. Teles, L. M. R. Scolfaro, J. Furthmüller, and F. Bechstedt, *Phys. Rev. B* **73**, 224409 (2006); N. Tandon, G. P. Das, and A. Kshirsagar, *J. Phys. Condens. Matter* **18**, 9245 (2006); T. Hynninen, H. Raebiger, and J. von Boehm, *ibid.* **18**, 1561 (2006); K. C. J. Kang, *Phys. B* **376**, 635 (2006); P. Larson and S. Satpathy, *Phys. Rev. B* **76**, 245205 (2007); X. Y. Cui, B. Delley, A. J. Freeman, and C. Stampfl, *ibid.* **76**, 045201 (2007); T. Hynninen, H. Raebiger, and J. von Boehm, *ibid.* **75**, 125208 (2007); P. Larson, Z. S. Popovic, and S. Satpathy, *ibid.* **78**, 113308 (2008); J. A. Chan, J. Z. Liu, H. Raebiger, S. Lany, and A. Zunger, *ibid.* **78**, 184109 (2008); N. Gonzalez Szwacki, J. A. Majewski, and T. Dietl, *ibid.* **83**, 184417 (2011).
⁸C. Liu, F. Yun, and H. Morkoç, *J. Mater. Sci.: Mater. Electron.* **16**, 555 (2005).
⁹A. Bonanni, *Semicond. Sci. Technol.* **22**, R41 (2007).
¹⁰T. Dietl, *Nat. Mater.* **9**, 965 (2010).
¹¹S. Granville, B. J. Ruck, F. Budde, H. J. Trodahl, and G. V. M. Williams, *Phys. Rev. B* **81**, 184425 (2010).
¹²E. Sarigiannidou, F. Wilhelm, E. Monroy, R. M. Galera, E. Bellet-Amalric, A. Rogalev, J. Goulon, J. Cibert, and H. Mariette, *Phys. Rev. B* **74**, 041306 (2006).
¹³M. Zajac, J. Gosk, E. Grzanka, M. Kamińska, A. Twardowski, B. Strojek, T. Szyszko, and S. Podsiadło, *J. Appl. Phys.* **93**, 4715 (2003).
¹⁴S. Dhar, O. Brandt, A. Trampert, L. Däweritz, K. J. Friedland, K. H. Ploog, J. Keller, B. Beschoten, and G. Güntherodt, *Appl. Phys. Lett.* **82**, 2077 (2003).
¹⁵G. Martinez-Criado, A. Somogyi, S. Ramos, J. Campo, R. Tucoulou, M. Salome, J. Susini, M. Hermann, M. Eickhoff, and M. Stutzmann, *Appl. Phys. Lett.* **86**, 131927 (2005).
¹⁶Y. Shon, S. Lee, H. Jeon, C. Park, T. Kang, J. Kim, E. Kim, C. S. Yoon, and Y. Kim, *Mater. Sci. Eng. B* **146**, 196 (2008).
¹⁷W. Stefanowicz *et al.*, *Phys. Rev. B* **81**, 235210 (2010).
¹⁸M. Rovezzi, F. D'Acapito, A. Navarro-Quezada, B. Faina, T. Li, A. Bonanni, F. Filippone, A. A. Bonapasta, and T. Dietl, *Phys. Rev. B* **79**, 195209 (2009).
¹⁹K. Suzuki, T. Kaneko, H. Yoshida, Y. Obi, H. Fujimori, and H. Morita, *J. Alloys Compd.* **306**, 66 (2000).
²⁰E. Sevillano, H. Meuth, and J. J. Rehr, *Phys. Rev. B* **20**, 4908 (1979).
²¹R. Giraud, S. Kuroda, S. Marcet, E. Bellet-Amalric, X. Biquard, B. Barbara, D. Fruchart, D. Ferrand, J. Cibert, and H. Mariette, *Europhys. Lett.* **65**, 553 (2004).
²²A. Bonanni *et al.*, *Phys. Rev. B* **75**, 125210 (2007).
²³A. Bonanni *et al.*, *Phys. Rev. Lett.* **101**, 135502 (2008).
²⁴A. Navarro-Quezada, W. Stefanowicz, T. Li, B. Faina, M. Rovezzi, R. T. Lechner, T. Devillers, F. d'Acapito, G. Bauer, M. Sawicki, T. Dietl, and A. Bonanni, *Phys. Rev. B* **81**, 205206 (2010).
²⁵A. Gubbens, M. Barfels, C. Trevor, R. Twesten, P. Mooney, P. Thomas, N. Menon, B. Kraus, C. Mao, and B. McGinn, *Ultramicroscopy* **110**, 962 (2010).
²⁶K. Riegler and G. Kothleitner, *Ultramicroscopy* **110**, 1004 (2010).
²⁷See, A. Wolos and M. Kaminska, in *Spintronics*, edited by T. Dietl, D. D. Awschalom, M. Kaminska, and H. Ohno, Vol. 82 of *Semiconductors and Semimetals* (Elsevier, Amsterdam, 2008), pp. 325–369, and references cited therein.
²⁸R. Y. Korotkov, J. M. Gregie, and B. W. Wessels, *Phys. B* **308–310**, 30 (2001).
²⁹A. Wolos, A. Wyszolek, M. Kaminska, A. Twardowski, M. Bockowski, I. Grzegory, S. Porowski, and M. Potemski, *Phys. Rev. B* **70**, 245202 (2004).
³⁰J. Zenneck, T. Niermann, D. Mai, M. Roeber, M. Kocan, J. Malindretos, M. Seibt, A. Rizzi, N. Kaluza, and H. Hardtdegen, *J. Appl. Phys.* **101**, 063504 (2007).
³¹E. Malguth, A. Hoffmann, W. Gehlhoff, M. H. Kane, and I. T. Ferguson, in *Materials Research Society Symposia Proceedings* (Materials Research Society, Pittsburgh, 2008), Vol. 1040 No. Q09-18.
³²C. C. Katsidis and D. I. Siapkas, *Appl. Opt.* **41**, 3978 (2002).
³³G. Yu, G. Wang, H. Ishikawa, M. Umeno, T. Soga, T. Egawa, J. Watanabe, and T. Jimbo, *Appl. Phys. Lett.* **70**, 3209 (1997).
³⁴T. Graf, M. Gjukic, M. Hermann, M. S. Brandt, M. Stutzmann, and O. Ambacher, *Phys. Rev. B* **67**, 165215 (2003).
³⁵R. D. Shannon, *Acta Crystallogr. Sect. A* **32**, 751 (1976).
³⁶A. A. Freeman, K. W. Edmonds, N. R. S. Farley, S. V. Novikov, R. P. Campion, C. T. Foxon, B. L. Gallagher, E. Sarigiannidou, and G. van der Laan, *Phys. Rev. B* **76**, 081201 (2007).
³⁷M. Zajac, J. Gosk, M. Kamińska, A. Twardowski, T. Szyszko, and S. Podsiadło, *Appl. Phys. Lett.* **79**, 2432 (2001).
³⁸J. Spalek, A. Lewicki, Z. Tarnawski, J. K. Furdyna, R. R. Gałgza, and Z. Obuszko, *Phys. Rev. B* **33**, 3407 (1986).
³⁹Y. Shapira and V. Bindilatti, *J. Appl. Phys.* **92**, 4155 (2002).
⁴⁰J. Blinowski, P. Kacman, and J. A. Majewski, *Phys. Rev. B* **53**, 9524 (1996).

EXPERIMENTAL PROBING OF EXCHANGE INTERACTIONS ...

PHYSICAL REVIEW B **84**, 035206 (2011)

⁴¹H. Munekata, H. Ohno, S. von Molnar, A. Segmüller, L. L. Chang, and L. Esaki, *Phys. Rev. Lett.* **63**, 1849 (1989).

⁴²R. N. Bhatt and P. A. Lee, *Phys. Rev. Lett.* **48**, 344 (1982).

⁴³See Supplemental Material at <http://netserver.aip.org/cgi-bin/epaps?ID=E-JAPIAU-92-110220> for the cluster tables for

nearest-neighbor models in the hcp lattices; these tables are from a previously unpublished work by V. Bindilatti and Y. Shapira.

⁴⁴J. Gosk, M. Zajac, A. Wolos, M. Kaminska, A. Twardowski, I. Grzegory, M. Bockowski, and S. Porowski, *Phys. Rev. B* **71**, 094432 (2005).

OPEN ACCESS

IOP Publishing

Semiconductor Science and Technology

Semicond. Sci. Technol. 30 (2015) 035002 (9pp)

doi:10.1088/0268-1242/30/3/035002

Analytical electron microscopy study on gallium nitride systems doped with manganese and iron

Arno Meingast^{1,2}, Andrea Navarro Quezada³, Thibaut Devillers³,
András Kovács⁴, Mihela Albu^{1,2}, Stefanie Fladischer^{1,2},
Alberta Bonanni³ and Gerald Kothleitner^{1,2}

¹ Institute for Electron Microscopy and Nanoanalysis, Graz University of Technology, Steyrergasse 17, 8010 Graz, Austria,

² Graz Centre for Electron Microscopy, Steyrergasse 17, 8010 Graz, Austria

³ Institut für Halbleiter- und Festkörperphysik, Johannes Kepler University, Altenbergerstrasse 69, 4040 Linz, Austria

⁴ Ernst Ruska-Centrum für Mikroskopie und Spektroskopie mit Elektronen, Forschungszentrum Jülich GmbH, 52425 Jülich, Germany

E-mail: arno.meingast@felmi-zfe.at

Received 30 July 2014, revised 26 November 2014

Accepted for publication 9 December 2014

Published 8 January 2015



Abstract

Modulated structures of gallium nitride (GaN) doped with transition metal ions (here Fe, Mn) are investigated by analytical (scanning) transmission electron microscopy to gain insight into the structural arrangement and chemical composition of the material, known to be critically correlated to the magnetic response and hence the functionality of these technologically relevant systems. Three classes of samples are considered: (i) homogeneous (dilute) (Ga, Mn)N; (ii) δ -Mn-doped (Ga, δ -Mn)N and phase separated (Ga, Fe)N, containing Fe-rich nanocrystals. The combination of various microscopic techniques employed, allows for a quantitative determination of the distribution of the magnetic ions in the samples, providing essential information on the structural and chemical asset of these systems.

Keywords: electron microscopy, gallium nitride, manganese, iron

(Some figures may appear in colour only in the online journal)

1. Introduction

Gallium nitride (GaN) based material systems are currently playing a key technological role, particularly in the field of optoelectronics and lighting for the future. It is expected that the addition of magnetic capabilities through doping with transition metals or rare earths, will extend the functionality of these materials systems to applications in spintronics, quantum information and magneto-optics [1–4]. A number of studies carried out over recent years, have highlighted how

the distribution of magnetic dopants in the semiconducting matrix substantially affects the structural, magnetic, electrical and optical properties of the resulting material. In particular, the recent advancements in the fabrication and characterization of magnetically doped nitrides, have made clear that depending on the growth conditions and eventually on the post-growth treatment, the introduction of magnetic ions can essentially result in: (i) a dilute (homogeneous) system [5]; (ii) a chemically inhomogeneous system (chemical phase separation) [6]; (iii) a crystallographically inhomogeneous system (crystallographic phase separation, secondary phases, embedded nanocrystals) [7]; (iv) a system containing functional magnetic complexes [8].

With these premises, the control over the formation, structure, arrangement and effect of inhomogeneity on the

 Content from this work may be used under the terms of the Creative Commons Attribution 3.0 licence. Any further distribution of this work must maintain attribution to the author(s) and the title of the work, journal citation and DOI.

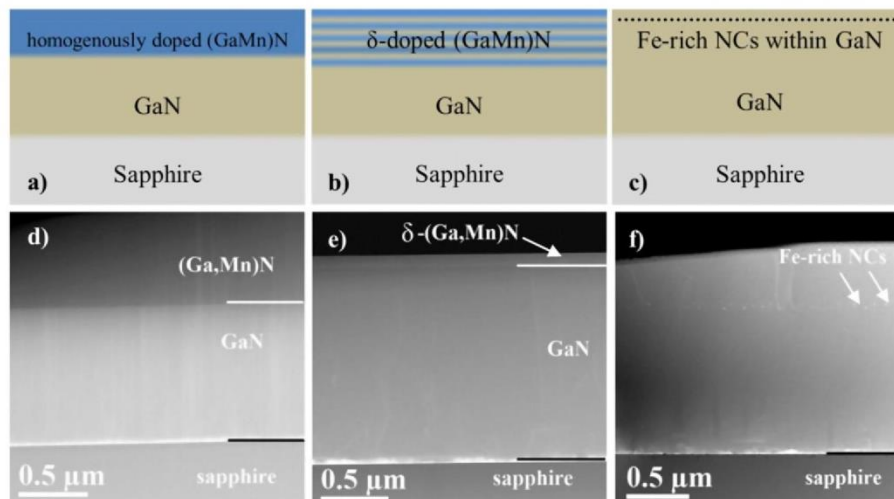


Figure 1. Schematic cross-sections not to scale of: (a) homogeneously Mn doped GaN; (b) Mn δ -doped GaN; (c) Fe-rich nanocrystals; (d)–(e) corresponding STEM HAADF images in GaN [11–20] orientation depicting the various layers and precipitates.

chemical and physical behavior of the host material is essential for the design and functionality of the next generation of devices.

Recently, it has been demonstrated that superexchange interactions account for ferromagnetism in (Ga, Mn)N in the absence of free carriers [5, 9]. In order to reliably exploit this material system in functional devices such as e.g. a new generation of spin filters, a control of the effective Mn incorporation in GaN and of the interfaces of (Ga, Mn)N in heterostructures is necessary [10].

Particularly in the case of embedded magnetic nanocrystals, it is essential to establish the correlation between the growth parameters and the local chemical composition and size of the nanostructures, considering that these figures have been shown to determine the magnetic properties of the whole system. For instance, in the case of Fe-rich nanocrystals embedded in GaN, it is found that by modifying the composition of the nanostructures, it is possible to tune the system from ferromagnetic to antiferromagnetic up to room temperature. Here the formation of magnetic Fe-rich nanocrystals paves the way to the realization of non-volatile flash-memories and tunable ferromagnetic/antiferromagnetic spintronic devices based on these hybrid systems [11].

In this work, electron microscopic techniques are applied to dilute (Ga, Mn)N systems, to two-dimensional (2D) layers of (Ga, Mn)N embedded in GaN, and to planar arrays of Fe-rich nanocrystals embedded in GaN.

2. Material and methods

All the samples considered are fabricated by metalorganic vapor phase epitaxy on *c*-sapphire, according to the procedures reported elsewhere and have been thoroughly characterized with respect to their magnetic and optical properties via both conventional and synchrotron radiation-based

techniques [5–7]. The microscopic and chemically-sensitive investigations of the structures are the focus of this work.

For the dilute (Ga, Mn), 2D (Ga, Mn)N layers and planar array of Fe-rich nanocrystals, schematic cross sections and their scanning transmission electron microscope (STEM) image counterparts (oriented along the GaN [11–20] zone-axis) are shown in figure 1. In the homogenous Mn co-doping process, a layer thickness of 700 nm is realized with a nominal concentration of 1.55 at% of Mn atoms within GaN. The 2D (Ga, Mn)N layers, having a total thickness of 150 nm, are obtained through δ -doping, a process realized by periodically providing Mn flow during GaN growth. Hereby, the starting point has been a sample with an averaged concentration of nominal 1.30 at% of Mn atoms within GaN. Samples of (Ga, Fe)N above the solubility limit of Fe, with crystallographic and chemically phase separated regions present, are investigated in addition. The growth conditions are given in [8]. The nominal Fe concentrations are 0.25% and 0.5%, respectively, found by secondary ion mass spectrometry (SIMS) in each case.

All cross-section specimens have been fabricated by mechanical polishing utilizing a semi-automated 8" Platen MultiPrep system from Allied High Tech. Ion-thinning has been performed by using a PIPS-system (Gatan Inc.) with Ar ions at 3, 4 kV voltage and 4° incident angle until perforation of the film. The final polishing step has then been performed on a Gentle Mill system (Technoorg Linda) at 500 eV with an incident angle of 14° for 30 min. This procedure has been repeated typically two to three times while observing the milling quality in the transmission electron microscope (TEM) until the specimen surface has exhibited a sufficient amorphous-free surface at the desired specimen position as visualized in figure 2, exemplified for the nanocrystal case.

The TEM and STEM investigations have been performed on different instruments depending on the equipment needed. Specimen orientations have been either along GaN [11–20] or

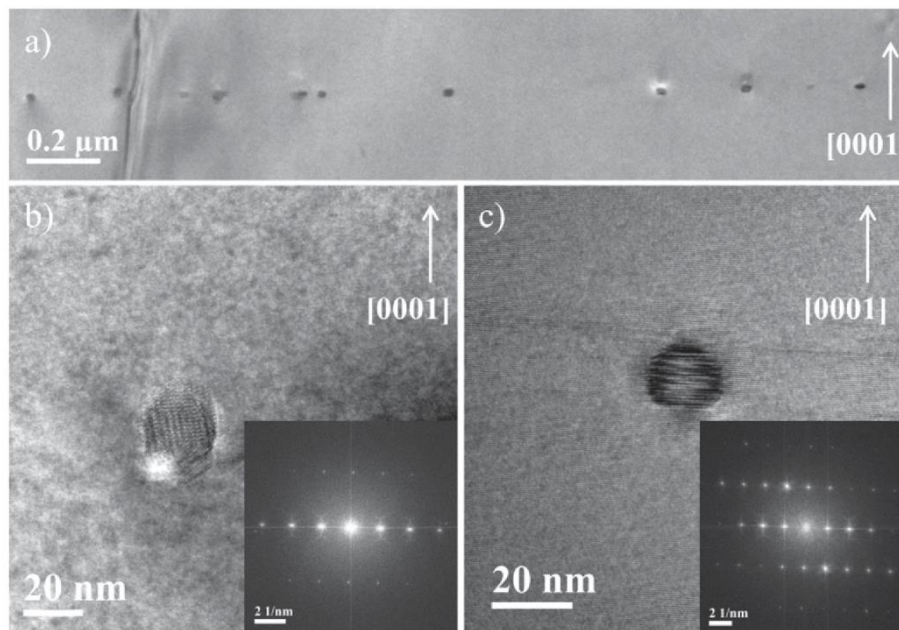


Figure 2. Bright field images of nanocrystals in GaN: (a) larger-scale image, depicting their density; (b) exhibiting considerable surface amorphization; inset: FFT with reduced information limit caused by amorphization; (c) sample area after low voltage milling.

close to this orientation, unless the sample has been tilted towards the energy dispersive x-ray spectroscopy (EDXS) detector, merely for maximum signal-collection. Conventional bright field TEM imaging investigations have been carried out on a Tecnai 200 kV FEG microscope from FEI, equipped with a Gatan GIF Tridiem electron energy loss spectroscopy (EELS) spectrometer [12] and an EDAX Phoenix Si(Li) x-ray detection system. This system has been used to record the energy filtered transmission electron microscopy (EFTEM) images as jump-ratio maps from the Mn L_{23} edge with a slit-width of 30 eV collected at 620 eV and 655 eV.

Furthermore, this system has been utilized for the quantitative analysis of the Fe-rich nanocrystals via EELS and EDXS reported later in this work. X-ray spectra have been subjected to a ζ -factor analysis, using the software-package written by Watanabe [13–15]. For the evaluation of concentrations, the peak intensities $K\alpha$ signals of N, O, Ga and Fe have been extracted by removing the background through bilinear interpolation, left and right of the respective line. Data acquisition has been performed by scanning a region of interest (50×50 pixels) across the central part of the individual nanocrystals. Hereby, a dwell-time of 15 μ s and a beam-current ranging from 150 pA to 250 pA have been used, accounting better for beam-induced modifications of the nanocrystal. Each nanocrystal has been measured only once to avoid erroneous measurements on possibly beam-modified material. In the case of visible heterogeneities in the crystal, individual, spatially resolved spectra have been recorded as spectrum images. The specimens investigated (with nominal Fe concentration of 0.25% and 0.5%) have been tilted 15°

towards the x-ray detector to avoid strong channeling effects and maximize signal collection efficiency.

The collection angles for EELS are 15.9 mrad for a GIF Tridiem installed at the Tecnai 200 kV FEG instrument (utilized for nanocrystal quantification) and 40.4 mrad for a DualEELS capable GIF Quantum [16] installed at the TITAN instrument operated at 300 kV (utilized for both Mn-doped GaN quantifications), respectively. Processing of the EELS data has been carried out with DigitalMicrograph (Gatan Inc.) applying regular EELS quantification schemes, however, accounting also for multiple scattering by low-loss deconvolution. For the quantification of the EELS signals the K edges of N (as well as O) and the L_{23} edges of Ga and Fe have been collected. The background is modeled by a power-law function and Hartree–Slater cross-sections are employed for conversion into concentrations.

High resolution STEM investigations have been carried out on a 60–300 kV probe- C_s -corrected TITAN microscope. Corrector tunings have always been performed until an aberration-free zone of 19 mrad or better has been reached, giving a spatial resolution better than 1 Å.

Annular bright field (ABF) imaging has been utilized as an alternative technique in order to harness its sensitivity for structural changes and its possibility to image lighter N atoms [17–21]. To obtain ABF images it has been paramount to avoid carbon surface contamination and to reduce surface-amorphization with the procedures described earlier. In our setup the ABF image has been registered with an annular detector as described in [20], collecting the direct beam diffraction disk within an angular range between 10 and 20 mrad for a beam convergence of 20 mrad. A beam current of of ~ 80 pA and a pixel time of 20 μ s have been used.

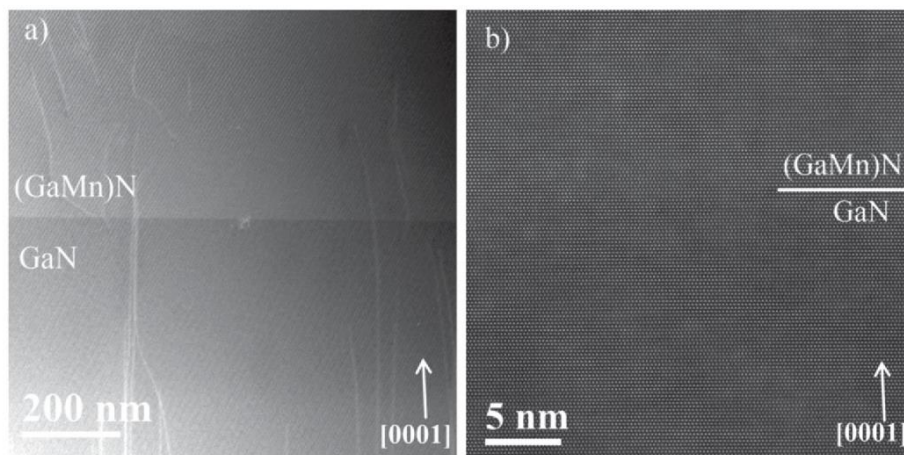


Figure 3. STEM HAADF images of: (a) GaN buffer and homogeneously doped (GaMn)N layer showing an increased signal intensity for (GaMn)N compared to un-doped GaN; (b) no structural modifications at the interface are observed.

Corresponding HAADF images have been recorded with an angular range from 26 mrad to 95 mrad.

3. Results and discussion

3.1. Mn-doped GaN

To examine the structural homogeneity of the Mn-doped GaN samples, aberration-corrected HR-STEM investigations have been carried out. In figure 3(a) the interface between the GaN buffer and the doped part of the homogeneously doped sample are shown. Dislocations originating at the interface substrate/GaN-buffer and propagating into the Mn-doped layer can be observed (in addition to a minor contamination spot in the field of view). All analytical measurements herein reported have been carried out at least 100 nm away from the dislocations. Structurally, at the interface GaN/(GaMn)N no significant lattice mismatch or crystallographic phase separation despite the rather high doping level (figure 3(b)) has been found. A geometrical phase analysis (GPA) [22] of the GaN/(GaMn)N interface has revealed strain at the interface being in the order of <1% (maps not shown). A faint brightness difference between the GaN/(GaMn)N interface can be identified due to changes in average Z, because of Mn having been mixed homogeneously into the otherwise nominally undoped GaN. An increase of ~2% in brightness can be identified when moving from GaN into (GaMn)N.

This intensity variation becomes more pronounced in figure 4, where the situation for the Mn δ -doped GaN is reported. A multi-layered structure is formed, leading δ -Mn regions. As evidenced in figure 4, the layers exhibit irregular periodicity and width.

High resolution HAADF and ABF images (figures 5(a) and (b)) have also been subject to a GPA analysis, and reveal no strain above 1%, indicating the coherent incorporation of Mn within the δ -doped region. A line-profile extracted from the HAADF signal (figure 5(c)) shows a sinusoidal-type

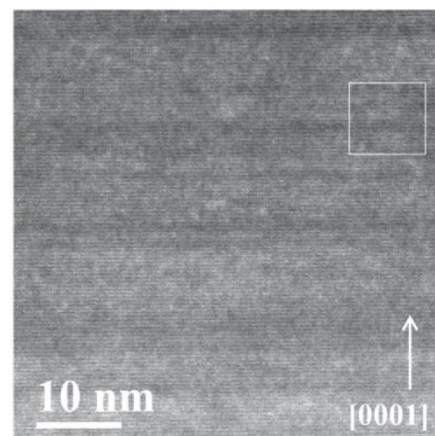


Figure 4. STEM-HAADF image depicting the irregular layering by Mn δ -doping; bright rectangle: region magnified in figure 5(a).

contrast variation between bright and dark lines as indicated by the dashed line. To shed more light onto the contrast variation, element specific EFTEM jump ratio imaging of the Mn L_{23} edge has been carried out, as displayed in figure 6(a).

Here the onset of the δ -doping (white dashed line) and the subsequent layering is clearly visible. The reason for the enhanced Mn signal at the onset of the δ -doped region (surface) is not yet completely clear but deemed to stem from segregation and/or initial nucleation of the doped layer.

From the extracted profile (figure 6(b)) of the Mn distribution image two aspects emerge: (i) approximately every 3 nm a layer has been introduced through the δ -process and its width is in the range 2–5 nm. (ii) Furthermore, when integrating perpendicular to the layers, an intensity ramp is detected. This is due to a thickness variation of the TEM foil, as determined by measuring the inelastic mean free path by means of EELS. The total relative thickness variation in the indicated area is going from 0.4 to 0.6.

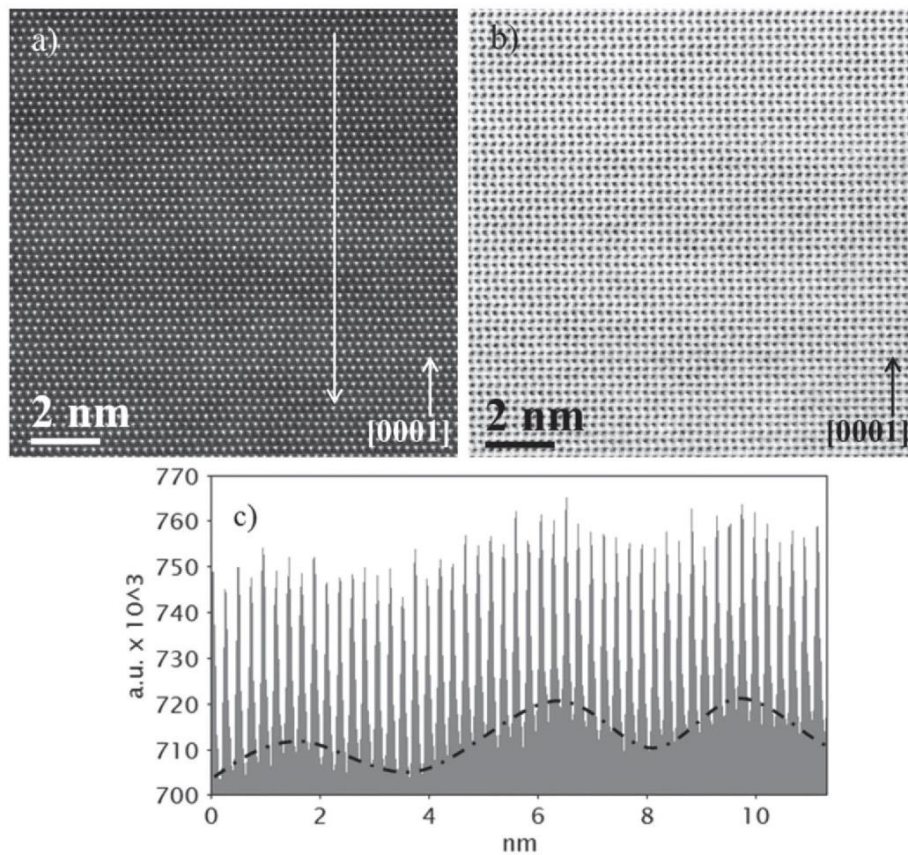


Figure 5. (a) High resolution HAADF image of Mn δ -doped GaN exhibiting contrast variation; white arrow: direction of profile extraction as depicted in (c); (b) corresponding ABF image providing information on the positions of Ga and N with a corresponding background variation as in (a); (c) extracted line-profile of (a) showing a sinusoidal contrast of the background of $\sim 2\%$ as indicated by the dashed line.

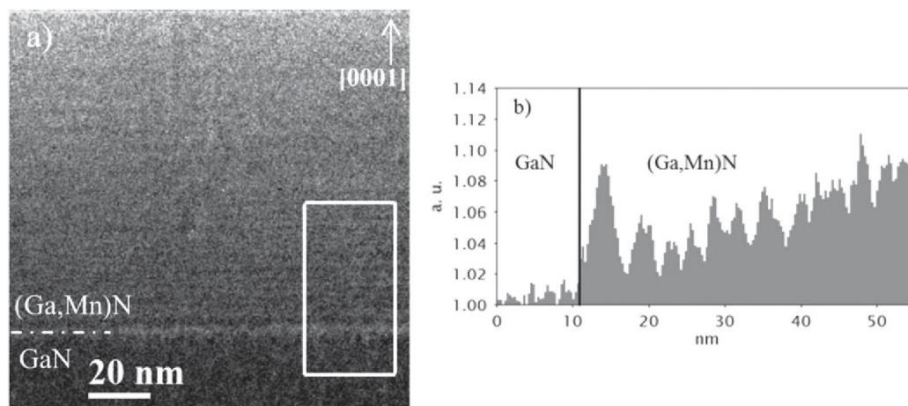


Figure 6. (a) EFTEM jump ratio map of the Mn L_{23} edge of Mn δ -doped GaN; white rectangle: region of profile extraction; (b) profile of the region marked in (a) showing a layering when moving from GaN into (Ga, Mn)N.

Spectroscopy has been carried out at several randomly chosen sample positions within the Mn-doped regions of GaN, and the EELS Ga L_{23} , N K, O K and Mn L_{23} edges have been quantified. Oxygen—detected in noticeable but similar amounts in all specimens—has been accounted for in the data analysis. To study the origin of the oxygen

signal and particularly its impact on the quantification, a cross-section extracted from an analyzed specimen has also been fabricated using a focused ion beam (FIB) system. Combined STEM EELS and EDXS line-scans from the protective platinum towards GaN (shown in the STEM image of figure 7(a)) across the former (specimen)

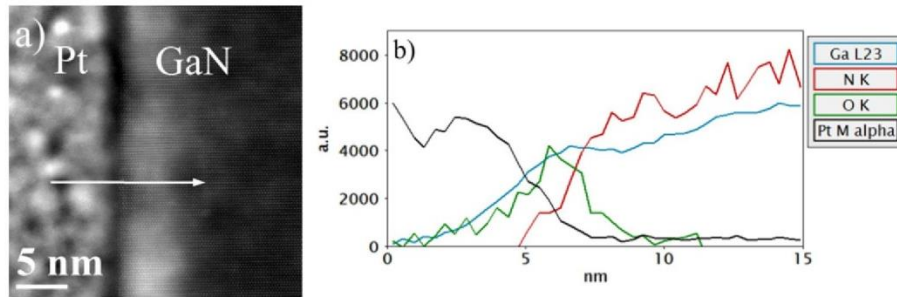


Figure 7. (a) HAADF image of the GaN-Pt interface with indication of the STEM-EELS-EDXS line-scan direction (white arrow); (b) extracted line-profiles for Ga, N, O and Pt confirming the presence of a 3 nm thick surface oxidation layer.

top-surface, have revealed an oxidized layer of 3 nm width.

In figure 7(b) a line-plot of the EELS Ga L_{23} , N K and O K edges and the EDXS Pt $M\alpha$ signal, harnessing the relative merits of both techniques for the efficient detection of light and heavy elements is shown. For Pt (serving as a protection layer during FIB-cutting) and Ga, strong intermixing occurs, and is explained on one hand by surface roughness but also by Ga ion implantation into the Pt-protection layer (getting slightly oxidized as well). The quantitative compositional analysis of the homogeneously Mn-doped region by EELS yields a rather uniform Mn concentration of 1.6 ± 0.1 at% averaged over several regions. The concentration values of the other elements are: Ga: 45.4 ± 0.6 at%; N: 48.8 ± 0.8 at% and O: 4.2 ± 1.1 at%, respectively.

For the analysis of the Mn delta-doped GaN, locations have been chosen such to assure that the beam has been placed either on or in between two bright lines. The average Mn concentration on bright layers is found to be 2.9 ± 0.5 at%, with Ga: 47.3 ± 1.4 at%; N: 46.8 ± 2.2 at% and O: 3.2 ± 3.2 at%. The average value of Mn in between the nominally doped layers is 1.3 ± 0.5 at% (with Ga: 47.6 ± 1.6 at%; N: 44.6 ± 2.4 at% and O: 6.5 ± 3.7 at%), being about 50% less compared to the doped layers but not vanishing. The high concentration variation of both layer-types reflects the heterogeneous deposition of Mn contrasting the homogeneously doped sample. Due to this strong local inhomogeneity between the lines and within a line itself it is not feasible to give a meaningful average dopant concentration as for the homogenous sample.

3.2. Fe-doped GaN

The perspective functionalities of transition metal doped nitrides are expected to be realized not only with the dilute/homogeneous systems analyzed in the previous section, but also in phase separated materials such as e.g. (Ga, Fe)N. Particular growth conditions (as detailed in [6]) have led to a very narrow size-distribution of the nanostructures at a defined depth in the sample, as shown in figure 2(a), aggregating in a planar arrangement perpendicular to the growth direction. A comprehensive analysis of the structures and of their magnetic properties is reported in reference [23]. The

HAADF imaging (figure 8(a)) reveals a typical 2-side faceted nanocrystal exhibiting a length of 25 nm and a height of approximately 17 nm. Figure 8(b) is a Fourier transform of figure 8(a) indicating an epitaxial relationship between the nanocrystal and the matrix. Higher resolution HAADF (figure 8(c)) and ABF (figure 8(d)) images do not show lattice distortions, supporting a coherent epitaxial growth mechanism.

To derive the composition of the nanocrystals, several of them (in samples with nominal doping concentrations of 0.25% and 0.5%) have been investigated and EELS as well as EDXS spectrum images have been recorded. Spectra collected from regions surrounding the nanocrystal (figure 9(b)) show no detectable presence of Fe confirming a confinement of the dopant within the nanocrystal. In a few non-typical cases, the nanocrystals display elemental inhomogeneity, as visible in figure 9. The Fe L_{23} map (figure 9(a)) and the respective spectra (figure 9(c)) indicate intensity differences within the nanocrystal, pointing to $\sim 20\%$ change in Fe concentration. This modulation is counterbalanced by an equal amount of Ga, where Fe is depleted (spectra not shown). Although these effects can be present, the overall variation in Fe content from crystal to crystal is by far larger.

Since absolute concentration measurements with each technique have shortcomings, we have performed data analysis in a relative manner with each technique comparing the two phases as shown in table 1. In this way systematic errors associated with low detection sensitivities and absorption for light elements in EDXS (N, O), and the uncertainties in the inner-shell ionization cross-sections for heavier elements (Ga, Fe) in the case for EELS can be avoided.

The general picture—averaging over all analyzed nanocrystals—is similar for the two techniques and shows similar trends. The Ga and N concentrations decrease to accommodate the large amounts of dopant and the extra oxygen. The Fe concentrations are on average about 2.5 times larger in the 0.5% Fe-doped sample than in the 0.25% Fe-doped one, yielding a ratio which is $\sim 25\%$ higher than the nominal one (with slight differences in Fe signal between the techniques). The situation on a per nanocrystal basis, showing the fluctuations in O and Fe content from nanocrystal to nanocrystal, is reported in figure 10. The dashed lines indicate the calculated average value for each technique within each graph. The

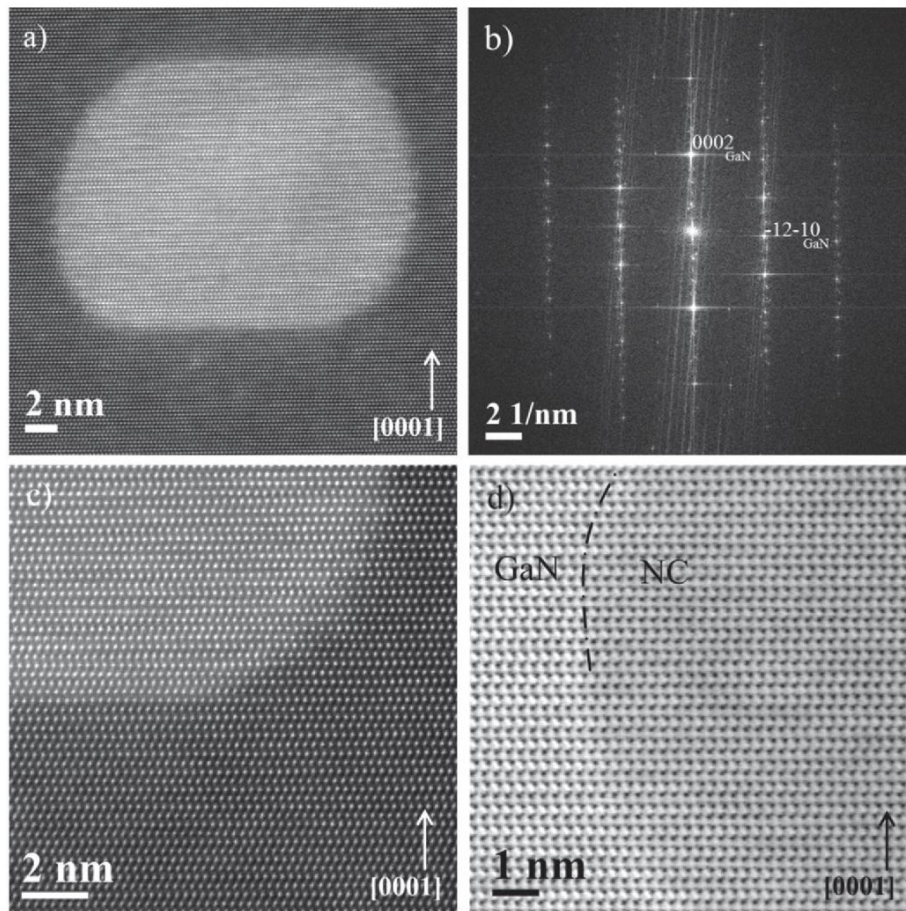


Figure 8. (a) High resolution STEM HAADF image of a typical nanocrystal; (b) Fourier transform, showing an aligned superposition of frequencies, fingerprint for an epitaxial relationship between nanocrystal and matrix; (c) coherent embedding of the nanocrystal in the matrix; (d) ABF image of a GaN/NC transition revealing no observable lattice distortion of the surrounding matrix.

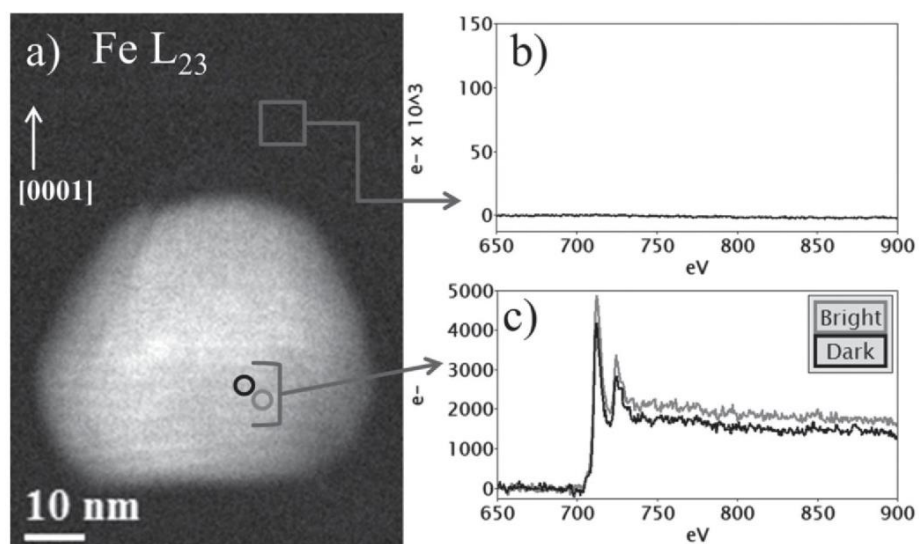


Figure 9. (a) Fe L_{23} EELS map from a nanocrystal; background-subtracted, integrated spectra from the spectrum image areas indicated in (a) for: (b) GaN matrix and (c) intensity differences within a Fe-rich nanocrystal.

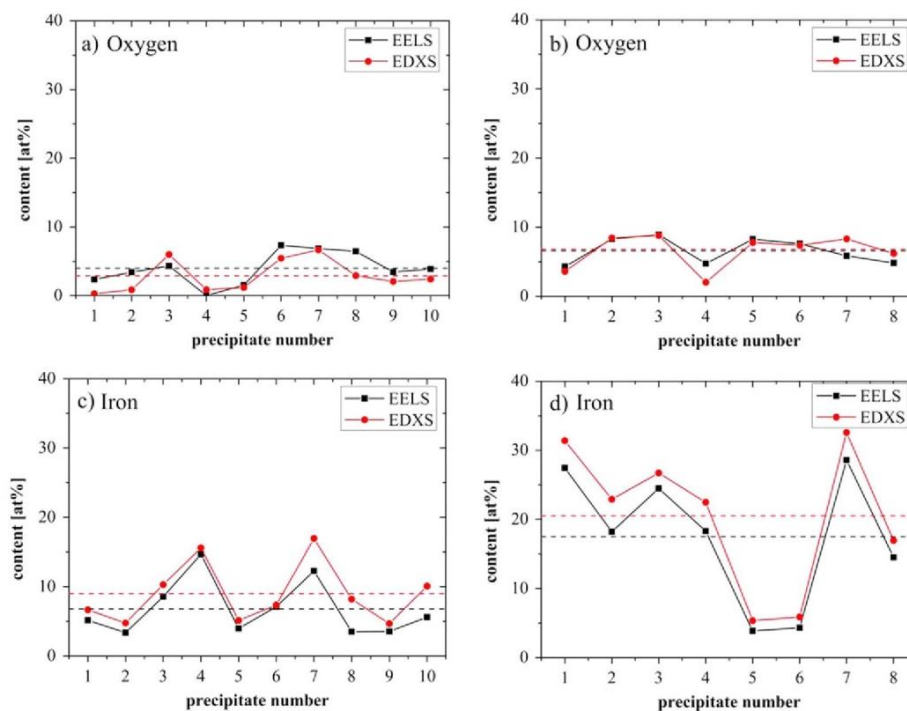


Figure 10. Variation of O and Fe content from nanocrystal to nanocrystal for: 0.25% Fe doping (a) and (c) and 0.5% Fe doping (b) and (d); dashed lines indicate the average value of Fe and O for each doping level.

Table 1. EELS and EDXS concentration ratio of Ga, N, Fe and O for two nominal doping concentrations (0.25% and 0.5%).

EELS	Ga	N	Fe	O
0.5%/0.25%	0.8 ± 0.1	0.9 ± 0.1	2.6 ± 1.9	1.7 ± 1.9
EDX	Ga	N	Fe	O
0.5%/0.25%	0.8 ± 0.1	0.9 ± 0.2	2.3 ± 1.5	2.3 ± 1.9

amount of oxygen in the 0.25% doped sample is as low as 0 at% and go up to 7 at%, whereas in the 0.5% specimen, the oxygen level reaches ~ 9 at% and is never less than 2 at%.

On average, the O concentration is about twice as high in the 0.5% doped case as in the 25% one, including and assuming equal amounts of surface oxygen in both samples. The deviation between EELS and EDXS measurements is likely due to uncertainties in peak extraction at low energies for EDXS. The correlation between having more oxygen and increasing dopant concentrations falls short when looking at the individual nanocrystals, both in the 0.25% and in the 0.5% case Fe and O levels vary largely, indicating the formation of complex phases. In an attempt to separate out surface oxygen, in order to get an approximate value of the nanocrystal composition, a Ga_2O_3 layer has been assumed (being the only source of oxygen) and a stoichiometric fractional intensity of Ga (scaled to oxygen) has been subtracted from the nanocrystal. By back-adding different amounts of GaN matrix to the result and upon comparison with assumed γ' - GaFe_3N and γ' - Fe_4N phases, no reasonable match has been achieved for a

statistically significant number of nanocrystals hinting at a complex formation of mixed nitride oxides. To better account for the embedding of the nanocrystals in the matrix in a quantitative analysis, one has to make assumptions about the volumes of the crystal and correlate it with an absolute volumetric evaluation, e.g. by means of tomography. Alternatively, a particle extraction preparation process might be considered, taking into account that in this case of etching, consequent reduction of the nanocrystal size and modification of their stoichiometry can occur.

4. Conclusions

Modulated semiconductor structures require microscopic characterization techniques to unravel the distribution and chemistry of magnetic dopants, which critically determine the magnetic properties that are decisive for the performance of perspective devices such as spin filters (homogenous and 2D layers) or antiferromagnetic spintronic elements (nanocrystal based).

In this study, we have investigated structure and chemistry of different transition metal doped GaN systems, relevant for new technologies. Depending on the formation process, homogenous doping or layering in the case of Mn, and coherent formation of ordered Fe-rich nanocrystals in the case of Fe have been obtained. High-angle annular dark-field STEM as well as annular bright field in combination with analytical techniques such as EFTEM and quantitative EDXS

and EELS spectrum imaging have been chosen to investigate structure and homogeneity. Whereas the continuously doped samples show an even level of dopant material and negligible lattice modifications, the δ -doped material reveals a largely fluctuating amount of dopant, forming modulated, linear structures. Even in untreated regions, doping material is found to be significantly present. The introduction of a barrier layer is likely to foster the confinement of dopant to the desired regions.

In systems containing planar arrays of Fe-enriched coherently embedded nanocrystals, the modulation of growth parameters (substrate temperature and flow ratio) allows producing embedded nanocrystals with composition—and consequently magnetic response—on demand and studies in this direction are currently being undertaken. A success in this direction will give access to a system that can be tailored to be either ferromagnetic or antiferromagnetic at up to room temperature—depending on the phase of the nanocrystals—opening remarkable functionalities for both ferromagnetic and antiferromagnetic spintronics.

Acknowledgments

This work has been supported by the Austrian NANO Initiative within the project number: 819702, by the European Research Council (ERC Advanced Grant 227690) and by the Austrian Science Foundation (FWF Projects 22477, and 24471). The authors thank M Dienstleder, Graz Centre for Electron Microscopy, for technical support.

References

- [1] Sato K *et al* 2010 First-principles theory of dilute magnetic semiconductors *Rev. Mod. Phys.* **82** 1633–90
- [2] Bonanni A and Dietl T 2010 A story of high-temperature ferromagnetism in semiconductors *Chem. Soc. Rev.* **39** 528–39
- [3] Jamet M *et al* 2006 High-Curie-temperature ferromagnetism in self-organized $\text{Ge}_{1-x}\text{Mn}_x$ nanocolumns *Nat. Mater.* **5** 653–9
- [4] Yokoyama M, Yamaguchi H, Ogawa T and Tanaka M 2005 Zinc-blende-type MnAs nanoclusters embedded in GaAs *J. Appl. Phys.* **97** 10D3171
- [5] Bonanni A *et al* 2011 Experimental probing of exchange interactions between localized spins in the dilute magnetic insulator $(\text{Ga}, \text{Mn})\text{N}$ *Phys. Rev. B* **84** 035206
- [6] Bonanni A *et al* 2008 Controlled aggregation of magnetic ions in a semiconductor: an experimental demonstration *Phys. Rev. Lett.* **101** 135502
- [7] Navarro-Quezada A *et al* 2010 Embedded magnetic phases in $(\text{Ga}, \text{Fe})\text{N}$: key role of growth temperature *Phys. Rev. B* **81** 205206
- [8] Devillers T *et al* 2012 Manipulating Mn-Mg_k cation complexes to control the charge- and spin-state of Mn in GaN *Sci. Rep.* **2** 7221–6
- [9] Stefanowicz W *et al* 2010 Structural and paramagnetic properties of dilute $\text{Ga}_{1-x}\text{Mn}_x\text{N}$ *Phys. Rev. B* **81** 235210
- [10] Bonanni A 2007 Ferromagnetic nitride-based semiconductors doped with transition metals *Semicond. Sci. Technol.* **22** R41–56
- [11] Navarro-Quezada A, Devillers T, Li T and Bonanni A 2012 Planar arrays of magnetic nanocrystals embedded in GaN *Appl. Phys. Lett.* **101** 081911
- [12] Brink H A, Barfels M M G, Burgner R P and Edwards B N 2003 A sub-50 meV spectrometer and energy filter for use in combination with 200 kV monochromated (S)TEMs *Ultramicroscopy* **96** 367–84
- [13] Watanabe M, Horita Z and Nemoto M 1996 Absorption correction and thickness determination using the zeta factor in quantitative x-ray microanalysis *Ultramicroscopy* **65** 187–98
- [14] Watanabe M and Williams D B 1999 Atomic-level detection by x-ray microanalysis in the analytical electron microscope *Ultramicroscopy* **78** 89–101
- [15] Watanabe M and Williams D B 2006 The quantitative analysis of thin specimens: a review of progress from the Cliff-Lorimer to the new ζ -factor methods *J. Microsc.* **221** 89–109
- [16] Gubbens A, Barfels M, Trevor C, Twesten R, Mooney P, Thomas P, Menon N, Kraus B, Mao C and McGinn B 2010 The GIF Quantum, a next generation post-column imaging energy filter *Ultramicroscopy* **110** 962–70
- [17] Van Dyck D and Op de Beeck M 1996 A simple intuitive theory for electron diffraction *Ultramicroscopy* **64** 99–107
- [18] Geuens P and Van Dyck D 2005 The s-state model for electron channeling in high-resolution electron microscopy *Adv. Imaging Electron Phys.* **136** 111–226
- [19] Findlay S D, Shibata N, Sawada H, Okunishi E, Kondo Y, Yamamoto T and Ikuhara Y 2009 Robust atomic resolution imaging of light elements using scanning transmission electron microscopy *Appl. Phys. Lett.* **95** 191913
- [20] Okunishi E, Ishikawa I, Sawada H, Hosokawa F, Hori M and Kondo Y 2009 Visualization of light elements at ultrahigh resolution by STEM annular bright field microscopy *Microsc. Microanal.* **15** 164–5
- [21] Findlay S D, Shibata N, Sawada H, Okunishi E, Kondo Y and Ikuhara Y 2010 Dynamics of annular bright field imaging in scanning transmission electron microscopy *Ultramicroscopy* **110** 903–23
- [22] Hytch M, Snoeck F and Kilaas R 1998 Quantitative measurement of displacement and strain fields from HREM micrographs *Ultramicroscopy* **74** 131–46
- [23] Grois A, Devillers T, Li T and Bonanni A 2014 Planar array of self-assembled $\text{Ga}_x\text{Fe}_{4-x}\text{N}$ nanocrystals in GaN : magnetic anisotropy determined via ferromagnetic resonance *Nanotechnology* **25** 395704

12.3 Heusler-films on GaAs

PHYSICAL REVIEW B **83**, 035319 (2011)

Interdiffusion in Heusler film epitaxy on GaAs(001)

C. Gusenbauer,¹ T. Ashraf,¹ J. Stangl,¹ G. Hesser,² T. Plach,² A. Meingast,³ G. Kothleitner,³ and R. Koch¹

¹*Institut f. Halbleiter- und Festkörperphysik, Johannes Kepler Universität, Altenbergerstrasse 69, A-4040 Linz, Austria*

²*Zentrum für Oberflächen- und Nanoanalytik, Johannes Kepler Universität, Altenbergerstrasse 69, A-4040 Linz, Austria*

³*Institute for Electron Microscopy, Graz University of Technology, Steyrergasse 17, 8010 Graz, Austria*

(Received 19 August 2010; published 24 January 2011)

We report the role of interdiffusion in molecular beam epitaxy of the binary Heusler alloy system $\text{Fe}_{1-x}\text{Si}_x/\text{GaAs}(001)$, employing a variety of complementary techniques that, in their combination, provide quantitative insight into the dynamics of the involved processes. The main properties of the investigated $\text{Fe}_{0.84}\text{Si}_{0.16}$ and $\text{Fe}_{0.76}\text{Si}_{0.24}$ films—growth, epitaxy, crystallographic order, interface quality, saturation magnetization, coercive field, and magnetic anisotropy—are in perfect agreement with the literature. Additionally, our results reveal a strong interdiffusion of Fe and Si into the GaAs substrate as well as of As and Ga into the $\text{Fe}_{1-x}\text{Si}_x$ films, creating intermixed layers of 2–3-nm thickness in both film and substrate. Interdiffusion is dominant already at moderate growth temperatures required for crystallographic ordering, thus demanding new concepts including appropriate diffusion barriers for the development of ferromagnet/semiconductor hybrid systems.

DOI: 10.1103/PhysRevB.83.035319

PACS number(s): 68.35.Fx, 68.35.Gy, 68.35.bd

I. INTRODUCTION

Ferromagnetic layers with a high spin polarization on semiconductor substrates are attracting increasing interest as potential spin injectors for spintronics¹ or magnetoresistive elements for magnetoelectronic devices.² High spin-polarization materials commonly are binary or ternary transition-metal compounds such as certain FeCo alloys³ and Heusler compounds (e.g., Fe_3Si or Co_2FeSi). According to theory,⁴ for the latter material class, perfect crystallographic order is essential for attaining high spin polarization. Furthermore, for efficient spin injection the interface has to be abrupt and, even more annoying, it seems to depend dramatically on the type of atoms that participate in the contact layer to the substrate.⁵ Consequently, interface disorder due to interdiffusion or interface reactions between film and substrate is detrimental for technological application. Recently Ramsteiner *et al.*⁶ discovered that during deposition of Co_2FeSi onto GaAs(001) Co, Fe, and Si diffuse about 50 nm deep into the substrate by a thermally activated process. Since the metal atoms may act as paramagnetic spin-scattering centers, the obtained spin injection is low, even though excellent abrupt interfaces have been revealed by high-resolution transmission electron microscopy (HRTEM).⁷

Here we report on interdiffusion processes occurring during molecular beam epitaxy (MBE) of binary, thus experimentally simpler $\text{Fe}_{1-x}\text{Si}_x$ films on GaAs(001). The composition of the films is in the range of the Heusler compound Fe_3Si with $x = 0.25$ (Fig. 1). We employed a variety of complementary experimental techniques that—in their combination—provide quantitative insight into the dynamics of the ongoing interdiffusion processes: (i) *in situ* stress measurements as a real-time technique for monitoring film growth⁸ and interdiffusion;⁹ (ii) a calibrated quartz crystal microbalance (QCM) to directly measure the mass equivalent of deposited Fe and Si for determining film thickness and composition; (iii) x-ray diffraction (XRD) for investigation of structural order and the thickness of the crystallographically ordered layers; (iv) cross-sectional HRTEM for obtaining real-space information on epitaxial growth, crystallographic order, film thickness, and interdiffu-

sion; (v) reflection high- and low-energy electron diffraction (RHEED and LEED) as well as atomic force microscopy (AFM) for investigating surface structure and morphology; (vi) a cantilever beam magnetometer (CBM)¹⁰ for quantitative magnetization measurements; (vii) Auger depth profiling; and (viii) scanning transmission electron microscopy (STEM) in combination with energy dispersive x-ray spectroscopy (EDXS) to detect, identify, and localize interdiffusing species. Our study reveals considerable diffusion of Fe and Si into the GaAs substrate as well as of As and Ga into the $\text{Fe}_{1-x}\text{Si}_x$ films, creating intermixed layers of 2–3-nm thickness in both film and substrate. Diffusion increases with the growth temperature and is dominant already at typical temperatures necessary for crystallographic ordering. Moreover, our study discloses fundamental difficulties in determining the correct composition of binary and ternary compounds prone to interdiffusion from the XRD data, since in that case a direct comparison of the XRD lattice constants with respective bulk constants is not applicable.

The paper is organized as follows: After a short experimental description in Sec. II, the results on two types of $\text{Fe}_{1-x}\text{Si}_x$ films, $\text{Fe}_{0.84}\text{Si}_{0.16}$ and $\text{Fe}_{0.76}\text{Si}_{0.24}$, will be presented in Sec. III and discussed in the context of the current literature. The paper is concluded by a summarizing discussion in Sec. III F.

II. EXPERIMENTAL

The experiments were performed in a multichamber ultrahigh vacuum (UHV) system consisting of separate interconnected growth chambers for III/V semiconductor and metal MBE. The $\text{Fe}_{1-x}\text{Si}_x$ films were deposited onto $c(4 \times 4)$ reconstructed GaAs(001) cantilever-beam substrates prepared in the III/V growth chamber by standard GaAs techniques (low-temperature buffer growth at 480 °C, high-temperature buffer growth at 590 °C, annealing at 605 °C, controlled cooling to 380 °C at constant As_4 flux to form the $c(4 \times 4)$ reconstruction followed by further cooling at reduced As_4 flux). The $c(4 \times 4)$ reconstruction is maintained during sample transfer into the metal growth chamber as checked by RHEED and LEED.

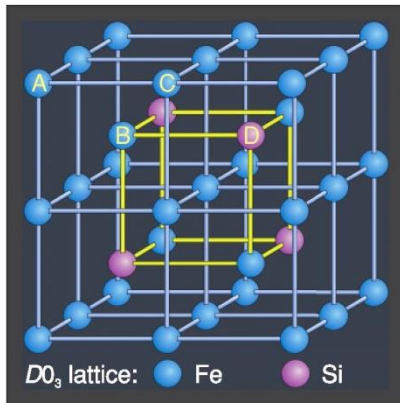


FIG. 1. (Color online) Sphere model of the $D0_3$ lattice of Fe_3Si : It consists of a regular array of body-centered cubes where the corners (A, C) are occupied by Fe atoms and the center atom is alternatingly Fe (B) or Si (D).

The $\text{Fe}_{1-x}\text{Si}_x$ films were deposited at a pressure of 8×10^{-10} mbar and a Si deposition rate of 0.05 nm/min. The Fe deposition rate was adjusted appropriately between 0.5 and 1.5 nm/min according to the respective $\text{Fe}_{1-x}\text{Si}_x$ composition. The deposition rates of Fe and Si were measured and controlled by a quartz crystal microbalance (QCM) calibrated by a QCM in substrate position. From the obtained mass equivalent of deposited Fe and Si composition and nominal thickness of the $\text{Fe}_{1-x}\text{Si}_x$ films were calculated. A CBM¹⁰ was used for measuring the stress of the $\text{Fe}_{1-x}\text{Si}_x$ films in real time during growth as well as their magnetic properties *in situ* after the deposition.

The XRD and HRTEM investigations were performed *ex situ* with a Seifert XRD3003 and a JEOL-2011 TEM, respectively, the AES investigations with a JEOL-JAMP-9500F field emission Auger microprobe. The STEM-EDXS investigations were carried out by a FEI Tecnai F20 electron microscope equipped with an Si(Li) EDX detector from EDAX. Prior to the EDXS-measurements the specimens were oriented into the GaAs[110] zone axis and specimen drift was corrected before each measuring point of a EDXS linescan. To guarantee appropriate resolution and sufficient beam current, a STEM full-width-at-half-maximum beam size 0.36 nm was chosen. For the estimated specimen thickness of ≈ 50 nm the electron beam spread is negligible (with only 1% of the electrons being outside of the nominal beam diameter in GaAs), leading to an overall measurement resolution of 0.5 nm.

III. RESULTS

Growth, structure, and magnetic properties of $\text{Fe}_{1-x}\text{Si}_x$ films on GaAs(001) with compositions close to that of the Heusler compound Fe_3Si have been studied intensively in previous years.^{11–17} Structure and magnetic properties of our $\text{Fe}_{1-x}\text{Si}_x$ films prepared with two compositions, $\text{Fe}_{0.84}\text{Si}_{0.16}$ and $\text{Fe}_{0.76}\text{Si}_{0.24}$, as determined by QCM, are in excellent agreement with these studies. We remark, however, that in order to enhance sensitivity toward interdiffusion effects our films are significantly thinner (~ 7 nm versus typically 20–50 nm).

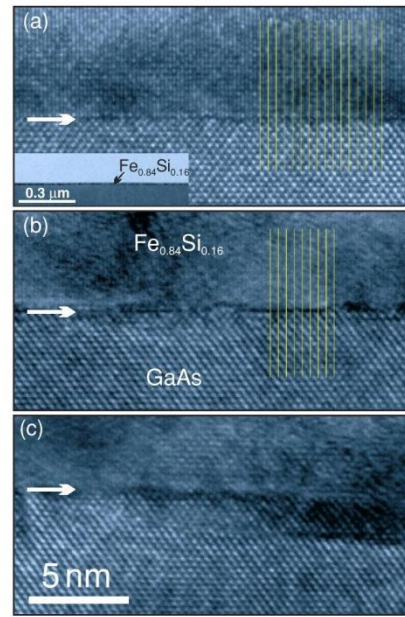


FIG. 2. (Color online) High-resolution TEM images along [110] of the interface region of $\text{Fe}_{0.84}\text{Si}_{0.16}/\text{GaAs}(001)$: (a) $T_G = 150^\circ\text{C}$, (b) 200°C , (c) 250°C . Vertical lines illustrate pseudomorphic growth and arrows mark interface. Inset shows a larger section of the 150°C film.

A. Growth and structure

All films of this study have grown epitaxially with an in-plane lattice spacing equal to that of GaAs(001) as evidenced by HRTEM [e.g., Figs. 2(a) and 2(b) and azimuthal XRD scans (not shown)]. In agreement with the literature, the optimum growth temperature (T_G) turns out to be a tradeoff between realizing good crystallographic order according to the $D0_3$ lattice (i. e., high T_G)¹⁵ and avoiding interdiffusion and chemical reactions at the interface (i. e., low T_G).¹⁷ The compromise is found at $T_G \approx 200^\circ\text{C}$.^{12,15} Figure 3 shows

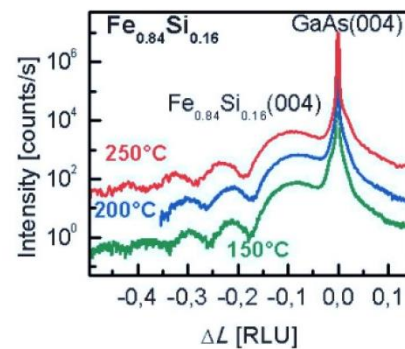


FIG. 3. (Color online) XRD spectra (intensity versus relative x-ray momentum change in reciprocal lattice units) of $\text{Fe}_{0.84}\text{Si}_{0.16}$ films on GaAs(001) deposited at 150°C , 200°C , and 250°C . In addition to the (004) reflection of the $\text{Fe}_{0.84}\text{Si}_{0.16}$ films, pronounced thickness oscillations are observed at all growth temperatures pointing to a good surface and interface quality.

XRD spectra of the $\text{Fe}_{0.84}\text{Si}_{0.16}$ films deposited at different growth temperatures. The out-of-plane (004) reflection of the $\text{Fe}_{0.84}\text{Si}_{0.16}$ films appears at smaller angles than the respective GaAs peak, thus indicating an expanded lattice in the vertical direction and accordingly a compressively strained lattice in the film plane. In agreement with Herfort *et al.*,¹² pronounced thickness oscillations (Pendellösungen) are observed that point to smooth and abrupt interfaces at T_G of 150–250 °C. However, the cross-sectional HRTEM images of Fig. 2 reveal an abrupt interface with a thickness at the absolute minimum of 1–2 ML (monolayers) only for the 150 °C film [Fig. 2(a)]. At $T_G = 200$ °C the transition region between film and substrate broadens to 2–3 ML with distinct steps of lattice-distance height visible in TEM images [Fig. 2(b)]. At $T_G = 250$ °C the interface degrades further exhibiting a roughness of 2–3 nm [Fig. 2(c)]. Figure 4(a) includes the (004) spectra of a $\text{Fe}_{0.76}\text{Si}_{0.24}$ film deposited at 200 °C. The film reflection is shifted closer to the corresponding GaAs peak indicating a decrease of the unstrained lattice constant with higher Si concentration. Notice, however, that the $\text{Fe}_{0.76}\text{Si}_{0.24}$ lattice is still expanded compared to GaAs at a composition very close to that of the Heusler compound Fe_3Si . Interestingly, the thickness oscillations [Fig. 4(a)] are weaker than that of the corresponding $\text{Fe}_{0.84}\text{Si}_{0.16}$ film, although HRTEM [Fig. 4(b)]

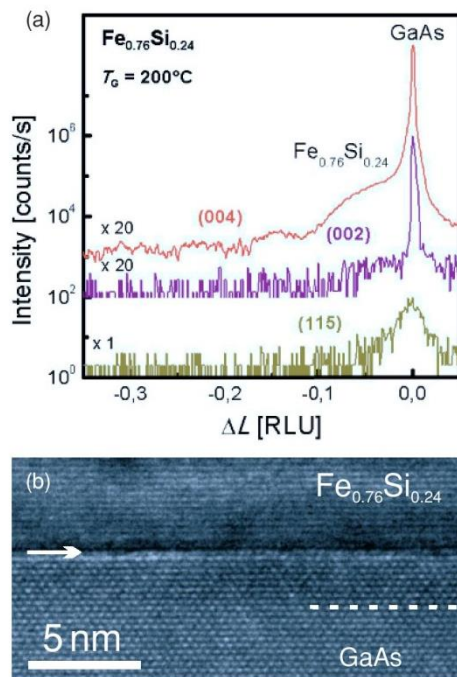


FIG. 4. (Color online) (a) XRD spectra (intensity versus relative x-ray momentum change in reciprocal lattice units) along specific superlattice reflections of a $\text{Fe}_{0.76}\text{Si}_{0.24}$ film deposited at 200° onto GaAs(001). Note that particularly the intensity of the (115) reflection is very low, where even for the GaAs(115) peak less than 10 counts/s are detected (compared to 10^4 counts/s for the GaAs(004) peak). (b) Corresponding HRTEM images along [110] of the interface region of $\text{Fe}_{0.76}\text{Si}_{0.24}/\text{GaAs}(001)$; dashed line indicates affected region in the GaAs substrate (see text).

still seems to indicate the formation of a sharp interface (see below). We remark that the interface to the vacuum investigated by AFM exhibits a root mean square (rms) roughness smaller than 0.5 nm for all films.

As discussed by Jenichen *et al.*,¹⁵ the intensity of specific XRD superlattice reflections provides insight into the crystallographic ordering of the films. $\text{Fe}_{1-x}\text{Si}_x$ is a binary ferromagnetic alloy that crystallizes in the $D0_3$ structure for the Heusler compound Fe_3Si (i. e., $x = 0.25$). The $D0_3$ lattice consists of a regular array of body-centered cubes where the corners (A and C in Fig. 1) are occupied by Fe atoms and the center atom is alternatingly Fe (B) or Si (D). For lower and higher Si concentrations the bcc lattice sites inherently are occupied more and more at random by Fe and Si leading to a disappearance of the (002) and (115) reflections. Indeed we detect no intensity at the angles of the (002) and (115) planes for the $\text{Fe}_{0.84}\text{Si}_{0.16}$ films (not shown) in agreement with Ref. 15. In the case of the $\text{Fe}_{0.76}\text{Si}_{0.24}$ film, on the other hand, both reflections are observed [Fig. 4(a)]. The former confirms a filling of the pure Fe planes of the $D0_3$ lattice (A and C in Fig. 1) preferentially by Fe atoms, the latter appears only when the Fe/Si planes are atomically ordered (B and D in Fig. 1). Compared to the 30-nm films investigated in Ref. 15, the superlattice reflections of our 7-nm films are significantly weaker and remain weak even when measured with intense synchrotrone x-ray sources. The reduced crystallographic order may be explained by the dominant role of interdiffusion observed in the thin films (see in the following).

B. Magnetic properties

The excellent structural quality of our films is further corroborated by the magnetic properties. Magnetic hysteresis loops measured quantitatively at room temperature with the *in situ* CBM are displayed in Fig. 5; the magnetic field was ramped along the [110] direction. Consistent with the results of Ref. 13, the coercive fields particularly of the 150 °C and 200 °C films are extremely low ($H_c < 0.15$ mT), thus confirming the absence of defects which may act as pinning centers for domain-wall motion. For the 250 °C film the coercive field is still low ($H_c \sim 1.0$ mT) but already significantly larger than at lower T_G , which—in agreement with the HRTEM results of Fig. 2(c)—indicates a degrading of the film structure. As discussed in more detail in Sec. III F, the saturation magnetization values (Table I) are in good agreement with literature results. It is noteworthy that the [110] direction is not an easy magnetization axis of the $\text{Fe}_{1-x}\text{Si}_x$ films.¹³ A close inspection of Fig. 5 reveals that for $T_G < 250$ °C the hysteresis loops are not square shaped but exhibit a remanence magnetization well below the saturation magnetization (M_s). In agreement with Lenz *et al.*¹⁴ the easy magnetization axes are directed along [100] and [010]. Due to a small uniaxial anisotropy field the symmetry between the two in-plane $\langle 110 \rangle$ hard axes is broken, thereby transforming the [110] direction to a weak intermediate axis.

C. Film stress

Figure 6 shows the evolution of the film forces (F/w) of various $\text{Fe}_{0.84}\text{Si}_{0.16}$ films normalized to unit film width (w) as a function of the nominal mean film thickness (t) determined by

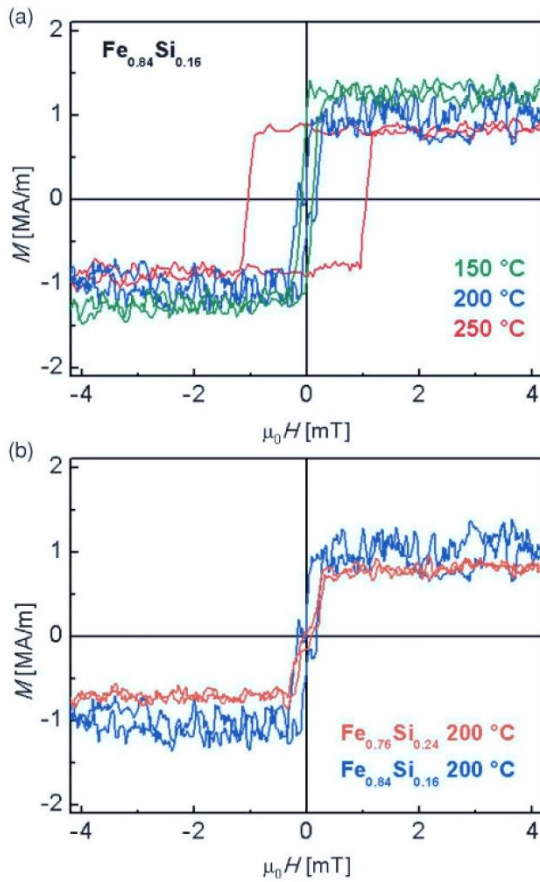


FIG. 5. (Color online) Magnetic hysteresis loops (magnetization M versus magnetic field $H \parallel [110]$) of $\text{Fe}_{1-x}\text{Si}_x/\text{GaAs}(001)$ measured at room temperature: (a) $\text{Fe}_{0.84}\text{Si}_{0.16}$ films deposited at 150 °C, 200 °C, and 250 °C. (b) $\text{Fe}_{0.76}\text{Si}_{0.24}$ films deposited at 200 °C in comparison with the respective $\text{Fe}_{0.84}\text{Si}_{0.16}$ film.

QCM. All force curves exhibit an induction period extending over a thickness of 2–3 nm as well as linearly increasing compressive forces at higher film thickness. Linearly increasing film forces correspond to constant incremental film stress ($F/w = \sigma t$). For comparison, Fig. 6 includes also a force curve of a pure Fe film ($x = 0$) deposited at room temperature. For pure Fe the induction period ends already after deposition of 2–3 ML which is the typical thickness range for surface- and interface-stress effects to dominate. At higher thicknesses the stress is governed by the misfit strain between the lattices of GaAs and Fe. The dashed line in Fig. 6 corresponds to the film forces due to misfit strain of 1.38% calculated by the bulk lattice constants $a_{\text{GaAs}} = 0.5653$ nm and $2 \times a_{\text{Fe}} = 0.5732$ nm. Its slope—corresponding to 2.9 GPa—is in perfect agreement with that of the experimental force curve up to a thickness of about 2–3 nm at which part of the strain is relieved by misfit dislocations.

With increasing Si content ($x > 0$) the lattice constant of $\text{Fe}_{1-x}\text{Si}_x$ films decreases and nearly matches with that of GaAs at the composition of the Heusler compound Fe_3Si ($a_{\text{Fe}_3\text{Si}} = 0.5655$ nm¹⁸). For the $\text{Fe}_{0.84}\text{Si}_{0.16}$ films misfit-

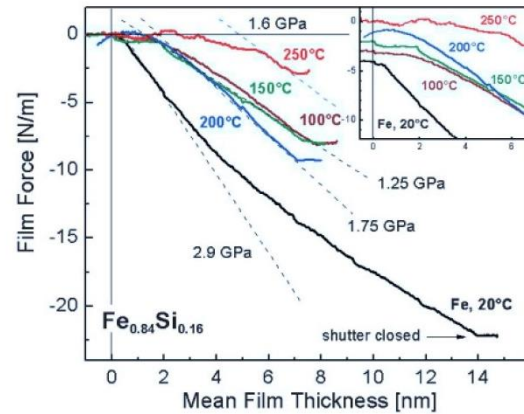


FIG. 6. (Color online) Film force (force per unit film width) as a function of the mean film thickness) evolving during and after MBE growth of various $\text{Fe}_{0.84}\text{Si}_{0.16}$ films deposited onto GaAs(001) at 100 °C, 150 °C, 200 °C, and 250 °C. For comparison, the force curve of a pure Fe film deposited at room temperature is included; slope of dashed lines corresponds to indicated film stress. Film force curves in the inset are subsequently displaced by 1 N/m to enable a better view on the respective induction periods.

induced compressive stress of 1.23–1.38 GPa should be expected (σ_{mf}^T in Table I). Compressive stress indeed is measured experimentally, but only after an induction period of 2–3 nm. At $T_G = 100$ and 150 °C the magnitude of the experimental compressive stress (σ_{exp}^T in Table I) is in very good agreement with the bulk misfit stress. At higher T_G , however, σ_{exp}^T exceeds σ_{mf}^T significantly. At lower thickness the stress is weakly compressive or even tensile. Compared with the room-temperature Fe film, the thickness range of the induction period of the $\text{Fe}_{1-x}\text{Si}_x$ films is decisively increased, from 2–3 ML to 15 ML for $T_G = 100$ and 150 °C, to 20 ML for $T_G = 200$ °C and to 30 ML for $T_G = 250$ °C (inset of Fig. 6). Thus the range of surface- and interface-stress related effects is exceeded by far. Furthermore, strain relief by misfit dislocations can be definitely ruled out. HRTEM reveals perfect pseudomorphic growth up to the maximum deposited thickness of ~ 7 nm consistent with constant stress (indicated by dashed lines in Fig. 6, i.e., no kinks). Moreover, in azimuthal XRD scans only GaAs peaks are observed, thus confirming that the in-plane lattice spacing of GaAs(001) is transmitted without interruption into the entire growing film. These results therefore imply that the compressive misfit stress is not relieved, but rather compensated by the tensile stress contributions of other processes. Figure 7 depicts the film forces of a $\text{Fe}_{0.76}\text{Si}_{0.24}$ film deposited at 200 °C. For this film the stress developing during the induction period is tensile and becomes compressive at a mean thickness of about 2 nm. Compared with the $\text{Fe}_{0.84}\text{Si}_{0.16}$ films the measured compressive stress has decreased to 0.85 GPa, but again it is considerably larger than the calculated misfit stress (Table I). We remark that Fe deposition at 200 °C is accompanied by strong interdiffusion of Fe into GaAs and Ga and As into the Fe film, reflected also by the stress behavior (for details see Ref. 19 and references therein).

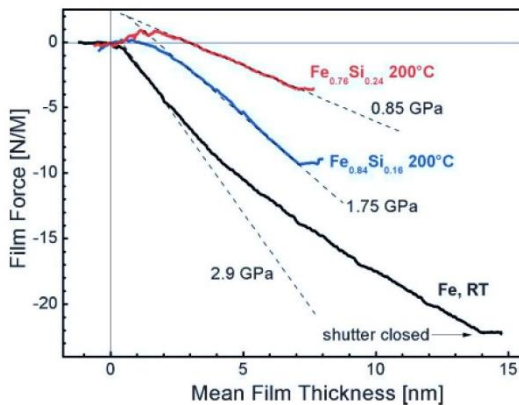


FIG. 7. (Color online) Film force (force per unit film width as a function of the mean film thickness) evolving during and after MBE growth of an $\text{Fe}_{0.76}\text{Si}_{0.24}$ film deposited onto $\text{GaAs}(001)$ at 200°C . For comparison, also the force curves of a respective $\text{Fe}_{0.84}\text{Si}_{0.16}$ film and a pure Fe film deposited at room temperature are included. Dashed lines indicate the film forces evolving due to the maximum misfit stress calculated by bulk lattice constants.

D. AES depth profiling

In order to further elucidate interdiffusion in $\text{Fe}_{1-x}\text{Si}_x/\text{GaAs}(001)$ as suggested by the stress experiments we investigated the 200°C $\text{Fe}_{0.76}\text{Si}_{0.24}$ film by AES depth profiling. Figure 8 displays the relative atomic concentrations of Fe, Si, As, Ga, and O of the surface layer while milling

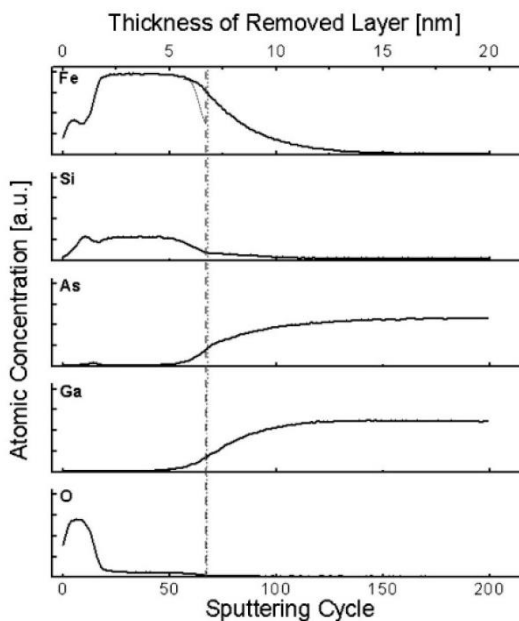


FIG. 8. Auger depth profiles of Fe, Si, As, Ga, and O of the $\text{Fe}_{0.76}\text{Si}_{0.24}$ film deposited at 200°C onto $\text{GaAs}(001)$; dashed line marks the lower film end as indicated by the disappearance of the oxygen signal and used for thickness calibration (upper scale), the expected decay of the Fe signal in the case of a sharp interface, and the kink in the Si signal.

it by Ar sputtering, thus reflecting the depth distribution of these elements. The peaks appearing in the Fe and Si plots at the beginning of Ar sputtering coincide with the maximum in the oxygen plot and originate from a 1–2-nm thick oxide layer due to air exposure of the sample. Upon further milling the signals of Fe and Si become constant and start decaying after about 50 sputtering cycles. At the same time the signals of As and Ga begin to rise. Obviously, the rise of the Fe and Si signals proceeds with a much larger slope than their decay (compare with dotted line in Fe plot), thus indicating a gradual rather than an abrupt decrease of the atomic concentration. The AES signals of As and Ga, on the other hand increases gradually with a small slope. Taking the two findings together, points to the formation of an intermixed layer at the interface, where all four elements, Fe, Si, As, and Ga, are coexisting. Note the remaining small oxygen signal (<5%) up to about 65 sputtering cycles. It can be explained either by a minor oxidation of the $\text{Fe}_{0.76}\text{Si}_{0.24}$ bulk because of air exposure of the sample or by always anew oxide formation at the sputtered surface due to oxygen impurity of the Ar sputtering gas (see Ref. 8). Since the residual oxygen signal is coupled to the presence of a film layer, its disappearance (dashed line in Fig. 8) enables a thickness calibration of the abscissa of Fig. 8 and provides an estimate of the thickness of the intermixed layer (2–3 nm in both film and substrate). Finally we want to remark, that As diffusion into the $\text{Fe}_{0.76}\text{Si}_{0.24}$ film is confirmed by the small peak at about 10 sputtering cycles in the As plot. It lies near the surface of the as-deposited film (i.e., beneath the surface oxide after air exposure), and indicates surface segregation of As during growth analogous to $\text{Fe}/\text{GaAs}(001)$.²⁰

E. EDX spectroscopy

In order to gain a more detailed insight into the diffusion profiles of the four participating elements, STEM-EDXS investigations were performed on both film types as shown in Fig. 9. The distance between subsequent measuring points of the linescans across the $\text{GaAs}/\text{Fe}_{1-x}\text{Si}_x$ interface was 0.4 nm [see insets of Figs. 9(a) and 9(b)]. Figure 9 corroborates the AES depth-profiling results previously mentioned that Fe and Si are diffused into the GaAs substrate and Ga and As into the $\text{Fe}_{1-x}\text{Si}_x$ films. The zone of pronounced interdiffusion has a total width of about 5 nm in both specimens with Fe diffusing more strongly than Si, and Ga more strongly than As (compare normalized spectra; Fig. 9, right). At a distance of about 4 nm away from the interface the concentration of all components has converged to the expected bulk values as indicated by the EDX spectra of Fig. 9 (left), which have been quantified by the k-factor method.²¹ In the GaAs substrate, weak stray signals of Fe, Co, and Si originating from the microscope itself were recorded at higher distances.

F. Discussion

This section provides a comparative discussion of the results obtained by the different experimental techniques. The main finding of this study certainly is the discovery of a broad intermixed region at the interface between the $\text{Fe}_{1-x}\text{Si}_x$ films and the $\text{GaAs}(001)$ substrate that forms already at temperatures necessary for the crystallographic ordering of Heusler films.

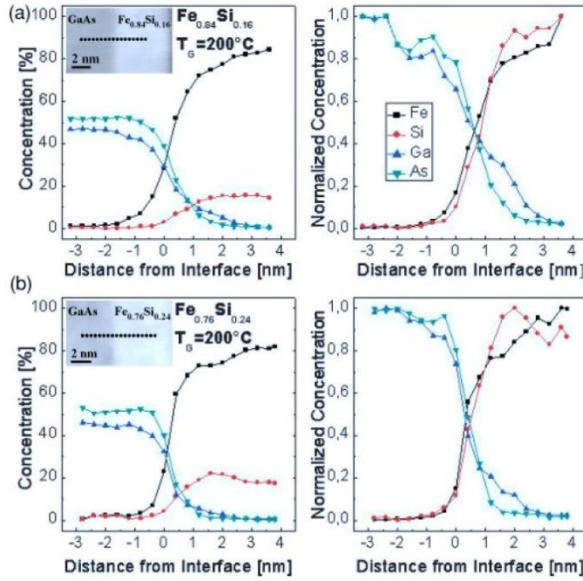


FIG. 9. (Color online) Quantified (left) and normalized (right) STEM-EDXS linescans of Fe, Si, Ga, and As in (a) Fe_{0.84}Si_{0.16}/GaAs(001) and (b) Fe_{0.76}Si_{0.24}/GaAs(001), both deposited at 200 °C; insets show the positions at which the EDX spectra were taken.

Film stress. Whereas XRD and HRTEM indicate pseudomorphic growth up to the total deposited film thickness (~7 nm), the stress measurements reveal an induction period at the beginning of film growth with a thickness of 2–5 nm depending on the growth temperature (t_{ind} in Table II). During this growth stage only weak compressive stress that is significantly smaller than the respective misfit stress (σ_{mf} ; see Table I), or even tensile stress is observed. This result is indeed surprising as pseudomorphic growth conserves the information of the substrate lattice distance. Accordingly, the misfit strain cannot be relieved during the induction period, but is rather compensated by a tensile stress contribution. A very

TABLE I. Bulk misfit stress σ_{mf}^T , experimental stress σ_{exp}^T , and the biaxial elastic constant E_{biax}^T calculated by Eq. (1) as well as the experimental saturation magnetization M_s and coercive field $\mu_0 H_c$ of various Fe_{1-x}Si_x films deposited at different growth temperatures T_G .

Fe _{1-x} Si _x	T_G [°C]	σ_{mf}^T [GPa]	σ_{exp}^T [GPa]	E_{biax}^T [GPa]	M_s [MA/m]	H_c [mT]
Fe _{0.84} Si _{0.16}	20	-1.23		190		
Fe _{0.84} Si _{0.16}	100	-1.27	-1.25	182	1.3	-
Fe _{0.84} Si _{0.16}	150	-1.31	-1.25	178	1.3	0.15
Fe _{0.84} Si _{0.16}	200	-1.36	-1.75	173	1.1	0.10
Fe _{0.84} Si _{0.16}	250	-1.38	-1.60	168	0.9	1.0
Fe _{0.76} Si _{0.24}	20	-0.19		179		
Fe _{0.76} Si _{0.24}	200	-0.37	-0.85	163	0.85	0.1

^athe elastic constants c_{11} and c_{12} for the calculation of E_{biax}^T were obtained by interpolation between the temperature-dependent elastic constants of Fe₃Si and Fe from Ref. 22.

TABLE II. Comparison of film thickness t determined by QCM, XRD, and TEM of various Fe_{1-x}Si_x films deposited at different growth temperatures T_G as well as the respective thickness t_{ind} of the induction period in the film force curves.

Fe _{1-x} Si _x	T_G (°C)	t_{QCM} (nm)	t_{XRD} (nm)	t_{TEM} (nm)	t_{ind} (nm)
Fe _{0.84} Si _{0.16}	100	7.6 ± 0.2	-	-	2.0
Fe _{0.84} Si _{0.16}	150	7.2 ± 0.2	7.6 ± 0.1	7.3 ± 0.2	2.0
Fe _{0.84} Si _{0.16}	200	7.0 ± 0.2	7.2 ± 0.1	6.9 ± 0.2	2.2
Fe _{0.84} Si _{0.16}	250	7.0 ± 0.2	6.6 ± 0.1	6.3 ± 0.5	~5
Fe _{0.76} Si _{0.24}	200	7.1 ± 0.2	7.0 ± 0.1	7.3 ± 0.2	2.0

likely mechanism that generates tensile stress is interdiffusion. It is not immediately detectable by HRTEM and XRD but clearly evidenced by AES depth profiling and STEM-EDXS, which indicate 2–3-nm thick regions in both film and substrate, where Fe, Si, As, and Ga coexist. As proposed in a previous study of Fe(001)/GaAs(001),⁹ tensile stress arises when As or Ga atoms diffuse out of the GaAs matrix and leave voids behind. A net tensile stress remains, even when the voids are refilled by Fe (or here also Si), since the volume of these atoms is smaller compared to Ga or As. Transferring this mechanism to Fe_{1-x}Si_x/GaAs(001) suggests that the “induction period” of the Fe_{1-x}Si_x films is dominated by site exchange processes that do not affect the crystal structure of film and substrate but lead to an intermixed interface region with a reduced net compressive stress. In fact, in the HRTEM image of the Fe_{0.76}Si_{0.24} film a 2–3-nm wide region in the GaAs can be recognized [marked by a dashed line in Fig. 4(b)] that exhibits a darker contrast and may indicate a layer of different strain and/or composition. Furthermore, a clearly disturbed interface region is imaged for the 250 °C Fe_{0.84}Si_{0.16} film [Fig. 2(c)], where additionally also the local crystallographic structure is disturbed (e.g., due to the formation of precipitates). On the other hand, diffusion via interstitial sites leads to compressive stress. This diffusion mechanism seems to dominate in thicker films prepared at $T_G > 150$ °C, which explains the higher compressive stress in the Fe_{0.84}Si_{0.16} and Fe_{0.76}Si_{0.24} films compared with the misfit stress calculated with the lattice constants of respective bulk compounds (Table I).

Magnetic properties. As discussed in Sec. III B and consistent with Lenz *et al.*¹⁴ the easy magnetization axes of our Fe_{1-x}Si_x films are directed along [100] and [010]; $[\bar{1}10]$ and [110] are in-plane hard and intermediate axes, respectively. The coercive fields (Table I), particularly for growth temperatures between 150 °C and 200 °C, are very low (<1.5 mT), thus corroborating the excellent structural quality of the films. In Table I also the saturation magnetization M_s of the Fe_{1-x}Si_x films is listed. M_s of the Fe_{0.84}Si_{0.16} films lies between 0.9 and 1.3 MA/m with the highest values for the optimum T_G range of 150 °C and 200 °C. Reduced structural order at lower temperatures as well as strong interdiffusion and formation of precipitates at higher temperatures may explain the decrease in M_s . Taking the magnetic moments of an *ab initio* study of Kudrnovsky *et al.*²³ and extrapolating them for Fe_{0.84}Si_{0.16} one obtains $\mu_{\text{Fe(A,C)}} = 1.51\mu_B$, $\mu_{\text{Fe(B)}} = 2.39\mu_B$, $\mu_{\text{Fe(D)}} = 2.28\mu_B$, and $\mu_{\text{Si(D)}} = -0.10\mu_B$. With these values a saturation magnetization of 1.25 MA/m is calculated, which is

in good agreement with the experimental values. For comparison, Zareki *et al.*²⁴ report a value of 1.03 MA/m for an 8-nm thick $\text{Fe}_{0.80}\text{Si}_{0.20}$ film deposited at 210 °C onto $\text{MgO}(001)$ and annealed at 630 °C for one hour. M_s of the $\text{Fe}_{0.76}\text{Si}_{0.24}$ film deposited at 200 °C, which is crystallographically ordered according to the $D0_3$ lattice, is 0.85 MA/m. This value is in good agreement with recent experimental (1.02 MA/m,²⁵ 0.74 MA/m,²⁶ 0.79 MA/m,¹⁴ 0.88 MA/m²⁴) and theoretical studies (0.11 MA/m²³).

Film thickness. Commonly, in III/V MBE the thickness of thin films and heterostructures is determined *ex situ* by evaluating respective thickness oscillations in XRD spectra. In the present study three independent experimental techniques have been employed: (i) XRD which senses the thickness of crystallographically ordered phases, (ii) HRTEM which can distinguish different phases in real space, and (iii) QCM which measures the mass equivalent of the deposited components (Fe and Si) from which the thickness of the deposited alloy film can be calculated. The film thickness obtained by the three methods (see Table II) agrees well within experimental error except for the 250 °C film with a broad interface region due to parallel interface reactions. In all other cases a significant “material loss” due to unidirectional diffusion of film atoms into the substrate can be excluded. Diffusion proceeds in both directions and is rather an exchange of atoms.

Comparison XRD/stress measurements. It is worth comparing the results obtained by the two complementary techniques, XRD and stress measurements, as both methods yield values of the unstrained lattice constant a_0^{RT} of the $\text{Fe}_{1-x}\text{Si}_x$ films.

Hooke’s law relates biaxial stress σ in the (100) plane of a cubic lattice to respective strain $\epsilon_{(100)}$ by $\sigma_{\text{exp}} = E_{\text{biax}}\epsilon_{(100)}$. E_{biax} is the elastic constant for biaxial stress:

$$E_{\text{biax}} = \frac{(c_{11} - c_{12})(c_{11} + 2c_{12})}{c_{11}}. \quad (1)$$

Temperature-dependent values E_{biax}^T calculated by interpolation between the temperature-dependent elastic constants, c_{11} and c_{12} , of Fe_3Si and Fe from Ref. 22 are listed in Table I. From $\epsilon_{(100)} = (a - a_0)/a_0^T$ one obtains

$$a_{0,\text{exp}}^T = \frac{a^T}{1 + \epsilon_{(100)}^T} = \frac{a_{\text{GaAs}}^T}{1 + \sigma_{\text{exp}}^T / E_{\text{biax}}^T}. \quad (2)$$

$a_{0,\text{exp}}^T$ is the unstrained lattice constant of the $\text{Fe}_{1-x}\text{Si}_x$ films at the temperature T ; a^T is the strained lattice constant at the temperature T with $a^T = a_{\text{GaAs}}^T$ (pseudomorphic growth!), the respective unstrained lattice constant of the $\text{GaAs}(001)$ plane, all listed in Table III. For $T_G = 100$ °C and 150 °C, $a_{0,\text{exp}}^T$ agrees perfectly with the respective bulk lattice constants $a_{0,\text{bulk}}^T$; at higher temperatures $a_{0,\text{exp}}^T$ is slightly, but significantly expanded.

The values discussed so far refer always to the respective growth temperature, whereas the XRD experiments were performed at room temperature (RT). In order to transform the unstrained lattice constants $a_{0,\text{exp}}^T$ of the $\text{Fe}_{1-x}\text{Si}_x$ films to room temperature, we use a thermal expansion $\alpha = 1.38 \times 10^{-5} \text{ K}^{-1}$ derived from the temperature-dependent bulk lattice constants of Ref. 18. The obtained values are listed in Table III as $a_{0,\text{exp}}^{RT}$. Whereas at $T_G = 100$ °C and 150 °C these

TABLE III. Temperature-dependent lattice constants of $\text{Fe}_{0.84}\text{Si}_{0.16}$, $\text{Fe}_{0.76}\text{Si}_{0.24}$, and $\text{GaAs}(001)$ for the different growth temperatures T_G : $a_{0,\text{bulk}}^T$, bulk values from Ref. 18; $a_{0,\text{exp}}^T$, unstrained lattice constants derived from the experimental stress of Figs. 6 and 7 via Eq. (2); $a_{0,\text{exp}}^{RT}$, respective unstrained values at room temperature calculated from $a_{0,\text{exp}}^T$ with a thermal expansion coefficient $\alpha = 1.38 \times 10^{-5} \text{ K}^{-1}$; $a_{0,\text{XRD}}^{RT}$, unstrained in-plane lattice constant calculated from the XRD data by Eq. (3); $a_{0,\text{GaAs}}^T$, temperature-dependent lattice constants of $\text{GaAs}(001)$ calculated with a thermal expansion coefficient $\alpha = 6.2 \times 10^{-6} \text{ K}^{-1}$.

$\text{Fe}_{1-x}\text{Si}_x$	T_G [°C]	$a_{0,\text{bulk}}^T$ [nm]	$a_{0,\text{exp}}^T$ [nm]	$a_{0,\text{exp}}^{RT}$ [nm]	$a_{0,\text{XRD}}^{RT}$ [nm]	$a_{0,\text{GaAs}}^T$ [nm]
$\text{Fe}_{0.84}\text{Si}_{0.16}$	20	0.5690				0.5653
$\text{Fe}_{0.84}\text{Si}_{0.16}$	100	0.5696	0.5695	0.5689		0.5656
$\text{Fe}_{0.84}\text{Si}_{0.16}$	150	0.5700	0.5698	0.5688	0.5702	0.5658
$\text{Fe}_{0.84}\text{Si}_{0.16}$	200	0.5704	0.5717	0.5703	0.5707	0.5659
$\text{Fe}_{0.84}\text{Si}_{0.16}$	250	0.5708	0.5715	0.5697	0.5710	0.5661
$\text{Fe}_{0.76}\text{Si}_{0.24}$	20	0.5659				0.5653
$\text{Fe}_{0.76}\text{Si}_{0.24}$	200	0.5672	0.5689	0.5675	0.5687	0.5659

^acalculated from the bulk lattice constants of Ref. 18.

values agree nicely with the room-temperature bulk value of 0.5690 nm, they again differ slightly at higher T_G .

$a_{0,\text{XRD}}^{RT}$, on the other hand, is obtained by XRD which measures precisely the in-plane and out-of-plane lattice distances of thin films. Evaluating the relation $\epsilon_{(001)} = -c_{11}/(2c_{12})\epsilon_{\perp}$ with $\epsilon_{(001)}$ being the biaxial strain implied by the substrate one obtains

$$a_{0,\text{XRD}}^{RT} = \frac{a_{\perp,\text{XRD}}^{RT} + (2c_{12}/c_{11})a_{0,\text{GaAs}}^{RT}}{1 + 2c_{12}/c_{11}}. \quad (3)$$

$2c_{12}/c_{11} = 1.27$ for $\text{Fe}_{0.84}\text{Si}_{0.16}$ and 1.33 for $\text{Fe}_{0.76}\text{Si}_{0.24}$ (from Ref. 22). The good agreement between $a_{0,\text{exp}}^{RT}$ and $a_{0,\text{XRD}}^{RT}$, both listed in Table III, confirms the consistency between XRD and the stress experiments.

$\text{Fe}_{1-x}\text{Si}_x$ composition. In the present study the amount of deposited material, Fe and Si, is measured during the film preparation by QCM. We estimate the absolute error of our setup to be about 3%, the relative error of the two sources—relevant for composition—even smaller. The film composition deduced from the QCM data is confirmed by the stress measurements as a further *in situ* technique. For the $\text{Fe}_{0.84}\text{Si}_{0.16}$ films deposited at 100 °C and 150 °C, the derived lattice constants of the unstrained films are in nearly perfect agreement with the respective bulk values of Lihl and Ebel¹⁸ for film concentrations of 16%. For higher T_G (≥ 200 °C) the experimental stress is (significantly) larger than the respective misfit stress. Ignoring other stress mechanisms, the stress results would indicate a decrease of the Si concentration to 13.2%, which contradicts enhanced Fe diffusion indicated by AES depth profiling and STEM-EDXS. Instead, diffusion proceeds preferentially via interstitial sites which gives rise to additional compressive stress. The stress investigations therefore demonstrate the difficulty of determining the composition of a multicomponent system, where other stress mechanisms in addition to misfit contribute to the total stress. *Ex situ* investigations by XRD confirm the stress results. It should be emphasized, however, that also for XRD detailed knowledge

of the origin of the strain state is required for determining composition, since processes other than misfit may modify the unstrained lattice distance. Only when exclusively misfit stress is involved and the film is thick enough for the elastic constants to be bulklike, the unstrained lattice constant can be calculated from the in-plane and out-of-plane lattice constants of the film and compared with respective bulk values if available.

IV. CONCLUSION

We have investigated the role of interdiffusion in MBE of the binary Heusler alloy system $\text{Fe}_{1-x}\text{Si}_x/\text{GaAs}(001)$, employing a variety of complementary techniques: (i) *in situ* stress measurements, (ii) QCM, (iii) x-ray diffraction (XRD), (iv) HRTEM, (v) RHEED, LEED, and AFM, (vi) CBM, (vii) AES depth profiling, and (viii) STEM-EDXS. The main properties of the investigated $\text{Fe}_{0.84}\text{Si}_{0.16}$ and $\text{Fe}_{0.76}\text{Si}_{0.24}$ films—growth, epitaxy, crystallographic order, interface quality, saturation magnetization, coercive field, and magnetic anisotropy—are in perfect agreement with the literature. In their combination, our complementary experimental techniques reveal a strong interdiffusion of Fe and Si into the GaAs substrate as well as of As and Ga into the $\text{Fe}_{1-x}\text{Si}_x$ films, creating intermixed layers of 2–3-nm thickness in both film and substrate. Interdiffusion is dominant already at

moderate growth temperatures required for crystallographic ordering. These findings are not contradictory to previous work. Interdiffusion effects rather have escaped detection by the established, typically *ex situ* characterization techniques of semiconductor research which are not particularly sensitive to interface composition. We remark that the presence of an intermixed interface region of a few nanometers may explain the low spin-injection efficiency (<3%) detected in $\text{Fe}_3\text{Si}/\text{GaAs}(001)$ by a light-emitting-diode configuration,²⁷ although the spin polarization of Fe_3Si is similar to Fe (~45%) as found by Andreev reflection¹⁶ and predicted by theory.^{28–30} In view of our alarming results, future work on ferromagnet/semiconductor hybrid systems needs to focus on the development of appropriate barrier layers inhibiting diffusion that is detrimental for the properties of both ferromagnet and semiconductor.

ACKNOWLEDGMENTS

We thank J. Herfort, O. Brandt, and M. Arndt for helpful discussions, B. Sepiol for providing the lattice-distance data, as well as the Austrian Fonds zur Förderung der Wissenschaftlichen Forschung (Project No. P20650) and the German BMBF under the research program NanoQUIT (Contract No. 01BM463) for financial support.

- ¹S. Datta and B. Das, *Appl. Phys. Lett.* **56**, 665 (1990).
- ²A. Ney, C. Pampuch, R. Koch, and K. H. Ploog, *Nature (London)* **425**, 485 (2003).
- ³S. S. P. Parkin, C. Kaiser, A. Panchula, P. M. Rice, B. Hughes, M. Samant, and S.-H. Yang, *Nat. Mater.* **3**, 862 (2004).
- ⁴D. Orgassa, H. Fujiwara, T. C. Schulthess, and W. H. Butler, *Phys. Rev. B* **60**, 13237 (1999).
- ⁵B. Hülsen, M. Scheffler, and P. Kratzer, *Phys. Rev. Lett.* **103**, 046802 (2009).
- ⁶M. Ramsteiner, O. Brandt, T. Flissikowski, H. T. Grahn, M. Hashimoto, J. Herfort, and H. Kostial, *Phys. Rev. B* **78**, 121303(R) (2008).
- ⁷M. Hashimoto, J. Herfort, A. Trampert, H.-P. Schönherr, and K. H. Ploog, *J. Vac. Sci. Technol. B* **24**, 2004 (2006).
- ⁸R. Koch, *Surf. Coat. Technol.* **204**, 1973 (2010).
- ⁹G. Wedler, B. Wassermann, R. Nötzel, and R. Koch, *Appl. Phys. Lett.* **78**, 1270 (2001).
- ¹⁰M. Weber, R. Koch, and K.-H. Rieder, *Phys. Rev. Lett.* **73**, 1166 (1994).
- ¹¹S. H. Liou, S. S. Malhotra, J. X. Shen, M. Hong, J. Kwo, H. S. Chen, and J. P. Mannaerts, *J. Appl. Phys.* **73**, 6766 (1993).
- ¹²J. Herfort, H.-P. Schönherr, and K. H. Ploog, *Appl. Phys. Lett.* **83**, 3912 (2003).
- ¹³J. Herfort, H.-P. Schönherr, K.-J. Friedland, and K. H. Ploog, *J. Vac. Sci. Technol. B* **22**, 2073 (2004).
- ¹⁴K. Lenz, E. Kosubek, K. Baberschke, H. Wende, J. Herfort, H.-P. Schönherr, and K. H. Ploog, *Phys. Rev. B* **72**, 144411 (2005).
- ¹⁵B. Jenichen, V. M. Kaganer, J. Herfort, D. K. Satapathy, H. P. Schönherr, W. Braun, and K. H. Ploog, *Phys. Rev. B* **72**, 075329 (2005).
- ¹⁶A. Ionescu *et al.*, *Phys. Rev. B* **71**, 094401 (2005).
- ¹⁷J. Herfort, B. Jenichen, V. M. Kaganer, A. Trampert, H.-P. Schönherr, and K. H. Ploog, *Physica E* **32**, 371 (2006).
- ¹⁸F. Lihl and H. Ebel, *Archiv für Eisenhüttenwesen* **32**, 489 (1961).
- ¹⁹T. Ashraf, C. Gusenbauer, J. Stangl, G. Hesser, M. Wegscheider, and R. Koch, *J. Phys.: Condens. Matter* **23**, 042001 (2011).
- ²⁰S. A. Chambers, F. Xu, H. W. Chen, I. M. Vitomirov, S. B. Anderson, and J. H. Weaver, *Phys. Rev. B* **34**, 6605 (1986).
- ²¹O. Eibl, *Ultramicroscopy* **50**, 179 (1993).
- ²²J. B. Rausch and F. X. Kayser, *J. Appl. Phys.* **48**, 487 (1977).
- ²³J. Kudrnovsky, N. E. Christensen, and O. K. Andersen, *Phys. Rev. B* **43**, 5924 (1991).
- ²⁴K. Zakeri, S. J. Hashemifar, J. Lindner, I. Barsukov, R. Meckenstock, P. Kratzer, Z. Frait, and M. Farle, *Phys. Rev. B* **77**, 104430 (2008).
- ²⁵V. A. Niculescu, T. J. Burch, and J. I. Budnick, *J. Magn. Magn. Mater.* **39**, 223 (1983).
- ²⁶A. Ionescu, C. A. F. Vaz, T. Trypiniotis, C. M. Gürtler, M. E. Vicker, H. Garcia-Miquel, and J. A. C. Bland, *J. Magn. Magn. Mater.* **286**, 72 (2005).
- ²⁷A. Kawaharazuka, M. Ramsteiner, J. Herfort, H.-P. Schönherr, H. Kostial, and K. H. Ploog, *Appl. Phys. Lett.* **85**, 3492 (2004).
- ²⁸E. G. Moroni, W. Wolf, J. Hafner, and R. Podloucky, *Phys. Rev. B* **59**, 12860 (1999).
- ²⁹A. Bansil, S. Kaprzyk, P. E. Mijnders, and J. Tobola, *Phys. Rev. B* **60**, 13396 (1999).
- ³⁰N. I. Kulikov, D. Fristot, J. Hugel, and A. V. Postnikov, *Phys. Rev. B* **66**, 014206 (2002).